POLITECNICO
MILANO 1863

SCUOLA DI INGEGNERIA INDUSTRIALE
E DELL'INFORMAZIONE

Numerical Study of Positron Production in Laser-Plasma Interaction with Double-Layer Targets via Nonlinear Breit-Wheeler Process

Tesi di Laurea Magistrale in
Nuclear Engineering - Ingegneria nucleare

Author: **Leonardo Monaco**

Student ID: 995272
Advisor: Prof. Matteo Passoni
Co-advisors: Alessandro Maffini, Marta Galbiati
Academic Year: 2022-23

"If I have seen further
than others, it is by
standing upon the
shoulders of giants"
-Isaac Newton

La mia famiglia,
la roccia su cui ho costruito i miei sogni,
grazie per il vostro amore infinito
che ha illuminato ogni passo della mia vita.

Abstract

High-intensity lasers ionize matter, inducing particle acceleration and various radiation types, like positrons. Laser-driven positron sources offer advantages over conventional ones, including ultra-short duration, higher energy, density, and yield, along with compactness and reduced radioactive risk. The scheme based on non-linear Breit-Wheeler pair production (NBWPP) promises positrons with superior qualities but requires high laser intensities. The unconventional double-layer target (DLT), featuring a low-density near-critical layer and a thin solid-density film, can enhance conditions for NBWPP. This thesis investigates positron production via NBWPP using DLTs and an experimental facilities' laser intensity of $4.75 \times 10^{22}\,\mathrm{W/cm^2}$. Addressing the complexity of laser-plasma interaction requires numerical simulations. For this purpose, codes coupling kinetic plasma simulation using the particle-in-cell (PIC) method with stochastic processes description through a Monte Carlo (MC) approach are established tools. 2D simulations by the open-source PIC-MC code SMILEI are performed to study laser-plasma interaction physics, positron production, and DLT parameter effects. Simulations reveal the critical phases: electron acceleration, laser focusing and reflection, and its interaction with accelerated electrons and produced photons. DLT parameters impact the positron production efficiency and beam properties. An optimal DLT configuration is identified, featuring a micrometer-thick heavy substrate, like lead, and a 40 μm long low-density layer. This produces positrons with temporal spread of 20 fs, divergence of 29°, peak energy of 342 MeV, and average density of 4.4×10^{17} cm^{-3}, confirming the potential of a NBWPP-based positron source. An analysis of the numerical tool performance in simulating NBWPP involves comparing results with theoretical predictions and examining assumptions and approximations. The tool generally provides accurate results, although criticalities in setting parameters, statistics, and non-conserved quantities can become significant in specific circumstances.

Keywords: laser-plasma interaction, plasma physics, non-linear Breit-Wheeler pair production, ultra-intense laser pulse, positron production, positron beams, laser-driven particle acceleration, particle-in-cell Monte Carlo codes, double-layer targets.

Estratto

Lasers ad alta intensità ionizzano la materia causando accelerazione di particelle e generazione di varie radiazioni, tra cui positroni. Le sorgenti di positroni laser-driven offrono, rispetto a quelle convenzionali, durata ultra-corta, maggiore energia, densità e resa, compattezza e minore rischio radioattivo. Lo schema basato sulla produzione di coppie non lineare Breit-Wheeler (NBWPP) promette positroni con qualità superiori ma richiede alte intensità laser. Il target a due strati (DLT), uno a bassa densità quasi-critica e uno sottile a densità solida, offre condizioni favorevoli per NBWPP. Questa tesi indaga la produzione di positroni tramite NBWPP usando i DLT e un'intensità laser di 4.75×10^{22} W/cm^2. Affrontare la complessità dell'interazione laser-plasma richiede simulazioni numeriche. A tal fine, i codici che accoppiano la simulazione cinetica del plasma mediante il metodo particle-in-cell (PIC) alla descrizione di processi stocastici tramite un approccio Monte Carlo (MC) sono strumenti consolidati. Simulazioni 2D con il codice SMILEI sono eseguite per studiare la fisica dell'interazione laser-plasma, la produzione di positroni e gli effetti dei parametri del DLT. Le simulazioni rivelano le fasi critiche: accelerazione degli elettroni, focalizzazione e riflessione del laser, e sua interazione con elettroni accelerati e fotoni prodotti. I parametri del DLT influenzano l'efficienza di produzione dei positroni e le loro proprietà. È individuata una configurazione ottimale del DLT, con substrato pesante, come il piombo, spesso pochi μm e uno strato a bassa densità lungo 40 μm. Ciò produce positroni con spread temporale di 20 fs, divergenza di 29°, energia di picco di 342 MeV, e densità media di 4.4×10^{17} cm^{-3}, confermando il potenziale di una sorgente di positroni basata su NBWPP. Un'analisi delle prestazioni dello strumento numerico nella simulazione di NBWPP coinvolge il confronto tra risultati e previsioni teoriche e la verifica di assunzioni e approssimazioni. Lo strumento fornisce in generale risultati accurati, sebbene criticità nei parametri di settaggio, statistica e quantità non conservate possano diventare significative in circostanze specifiche.

Parole chiave: interazione laser-plasma, fisica dei plasmi, produzione di coppie Breit-Wheeler non lineare, impulsi laser ultra-intensi, produzione di positroni, accelerazione di particelle laser-driven, codici particle-in-cell Monte Carlo, target a doppio strato.

Contents

Introduction

Plasmas, in general, are systems composed of charged particles that evolve accordingly to the self-consistent electromagnetic field. Given the electrical charge within plasmas, it is natural to explore their interaction with external fields, with lasers being a crucial example of systems capable of coherent light amplification. Laser-plasma interaction presents a complex scenario rich in interesting physical phenomena and has important applications in physics, engineering, and beyond. When materials are irradiated by intense lasers, their ionization and plasma formation occur. Its subsequent interaction with the laser field lead to electron and ion acceleration, as well as the generation of various types of radiation. These acceleration mechanisms are thoroughly understood and extensively studied through simulations and experiments, and their applications, such as in the development of compact particle accelerators, have been well-established. The advent of laser facilities capable of generating extremely high-intensity ($> 10^{22}\mathrm{W/cm}^2$) electromagnetic fields has opened up new frontiers in the interaction between light and matter, including high-energy photon emission and positron production through Non-linear Breit-Wheeler Pair Production (NBWPP). As a result, a novel class of laser-driven NBWPP-based positron sources may become accessible in the next period, garnering considerable attention due to their potential unique properties, comprising high density, energy, and short duration, as well as low divergence and reduced retained radioactivity. Positron beams with these characteristics hold promise for a range of applications, such as particle colliders for fundamental research in particle and nuclear physics, synchrotron radiation facilities for material characterization and medical imaging, positron annihilation spectroscopy for defect and phase transition research, and laboratory astrophysics and plasma physics to understand cosmic events. Given the demanding nature in laser intensity of positron production through the NBWPP process, there is a keen interest in exploiting non-conventional, engineered targets to create conditions favorable for NBWPP while reducing the required laser intensity. Double-layer targets (DLTs), which can be produced at Nanolab (Politecnico di Milano) laboratories, show great promise in this regard by offering the ability to optimize various aspects of their interaction with the laser. This thesis aims to investigate and characterize positron production through NBWPP using DLTs under the laser intensity

available in cutting-edge experimental facilities [1], specifically $4.75 \times 10^{22}\mathrm{W/cm^2}$. Given the inherent complexity of the self-consistent dynamics of plasma populations and the electromagnetic field, analytical tools are limited, necessitating a numerical approach, in particular computer simulations. To address this task, the particle-in-cell (PIC) method is employed, chosen for its ability to unravel the intricate physics of the process at a relatively manageable computational cost. The selected laser intensity aligns with the goal of facilitating experimental validation of the simulation results in the present day, using currently available laser technology, with the prospect of realizing a laser-driven NBWPP-based positron source. Due to the importance of accurately simulating positron production during laser-plasma interaction, this thesis also aims to analyze the performance and limitations of the adopted numerical tool in simulating positron production via NBWPP. This additional thesis activity is part of the Honours Programme, an educational path within the Politecnico di Milano high education training strategy, in which the candidate participated.
The topics covered in the thesis follow this structure:

- **Chapter 1** provides an overview of positron production mechanisms and introduces the single-particle picture of the NBWPP process. It then discusses currently available positron sources and applications of positron beams.
- **Chapter 2** introduces the main physical aspects of plasmas, high-intensity lasers, and their interaction, related to NBWPP. In this chapter, the specific target DLT is presented.
- **Chapter 3** discusses the working-principles of PIC codes coupled with a Monte Carlo module for the description of NBWPP, along with the criticalities of these tools.
- **Chapter 4** reports motivations, objectives, and methods of the thesis work.
- **Chapter 5** presents the results obtained from simulations of NBWPP during laser interaction with DLTs, emphasizing the physical processes involved and the characterization of produced positrons. The final part of the chapter discusses the outcomes of the analysis concerning the numerical tool employed to simulate NBWPP.
- **Chapter 6** analyzes the results of a simulation campaign investigating the impact of DLT characteristics on positron production.

The thesis ends with the conclusions and future perspectives. In Chapters 1, 2, and 3, Gaussian units are utilized, while starting from Chapter 4, the International System of Units (SI) is employed for consistency with the units adopted by the simulation tool.

1 | Physics and Engineering relevance of positrons

1.1. Introduction to positrons

In particle physics, the positron is the anti-particle of the electron. It is an elementary particle possessing the same mass and spin of the electron but opposite electric charge. Due to the physics of matter and anti-matter interaction, electrons and positrons can annihilate each other resulting in the production of other particles, such as photons.
Positrons can be naturally produced by specific radioactive elements or in environments with highly energetic particles, such as extremely hot places in the universe like supernovae [2]. Another example is the Earth's atmosphere [3], where cosmic rays colliding with atomic nuclei generate a cascade of particles, including positrons. They can also be produced in laboratories, for instance in accelerators, where collisions between very energetic particles are realized.
Positrons were observed for the first time by Carl David Anderson in 1932 [4] while he was studying particles produced by collisions of cosmic rays with a lead target. The trajectories of these particles were visualized with a cloud chamber, exploiting the ionization of a gas caused by their passage. The chamber was immersed in a magnetic field, causing the particles to deflect in a direction dependent on the sign of their electric charge and with a radius of curvature determined by their mass-to-charge ratio. Anderson observed that some particles had the same mass-to-charge ratio of electrons, indicating that they could not be protons, but with positive charge. This discovery was the first evidence of antimatter.
Few years earlier, after the publication of "The quantum theory of the electron" [5] in 1928 by Paul Dirac and subsequent contributions from Hermann Weyl and Robert Oppenheimer, it was established that the existence of the positron becomes a necessity when aiming to provide a quantum and relativistic description of the electron. When considering the relativistic wave equation for a particle with spin 1/2 and seeking solutions for a free particle, two classes of solutions are found. These solutions have opposite signs

in terms of frequency, and both are indispensable in quantum mechanics. Since states with negative energy are not allowed in physics, states with negative frequency must be interpreted as positive electrons with positive energy [6].

1.2. Fundamental processes to generate positrons

In this section, firstly a general overview of the most important fundamental processes to produce positron is given, and then the Non-linear Breit-Wheeler pair production process will be presented in detail.

1.2.1. General overview

Positrons are charged leptons, and so they interact via the electromagnetic force and the weak force. Therefore the first classification of positron production processes is based on the fundamental force responsible for the process.
In β^+ radioactive elements, represented in Figure 1.1, a proton is transmutated by the weak force into a neutron with the emission of a positron and an electronic neutrino [7].

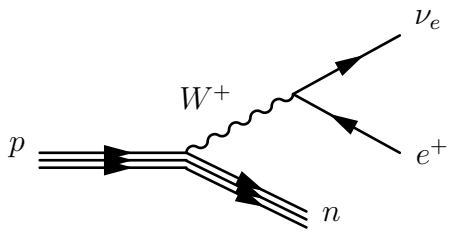

Figure 1.1: Feynman diagram of the β^+ decay, where a proton transform into a neutron emitting a weak boson W^+, which then decays into a positron and electronic neutrino.

Since more than one particles are emitted, the kinetic energy of positrons follow a continuum spectrum [8], and the cutoff energy depends on the specific radio-nuclide.
Consider now positron production mediated by the electromagnetic force, referred to as pair production, where positrons are produced by quanta of the electromagnetic field, known as photons. According to the conservation law of the electron number in particle physics [7], positrons are created (and also annihilated) in pairs with electrons. Since the positron and the electron are produced from vacuum, the energy necessary to create a pair is always greater than two times the electron rest energy. Also, from momentum and energy conservation the pair creation by a single photon is possible only if another particle is present, like a nucleus [9].

Pairs can be created when photons propagate through matter. In particular the Bethe-Heitler pair production process [9] involves an energetic photon interacting with the Coulomb field of a heavy nucleus with charge Z, resulting in the creation of a pair. The Feynman diagram is represented in Figure 1.3. The cross section of the process depends strongly on Z, since it determines the strength of the Coulomb field, and also on the photon energy. When considering a set of target atoms, their concentration and total number determine the overall probability to undergo pair production. Therefore, given a photon impinging into a solid target, the probability of decaying into a pair depends on the material thickness, density and charge Z. Pair production can also occur, in a weaker manner, when photons interact with the Coulomb field of the electrons of the medium. An important property of this process is that the cross-section, which depends on the photon energy, saturates at high energies [9, 10], as shown in Figure 1.2. Therefore, for photons with energy above roughly one hundred times the electron rest mass, fixed a certain material the only possibility to increase the pair production yield is to make the target thicker.

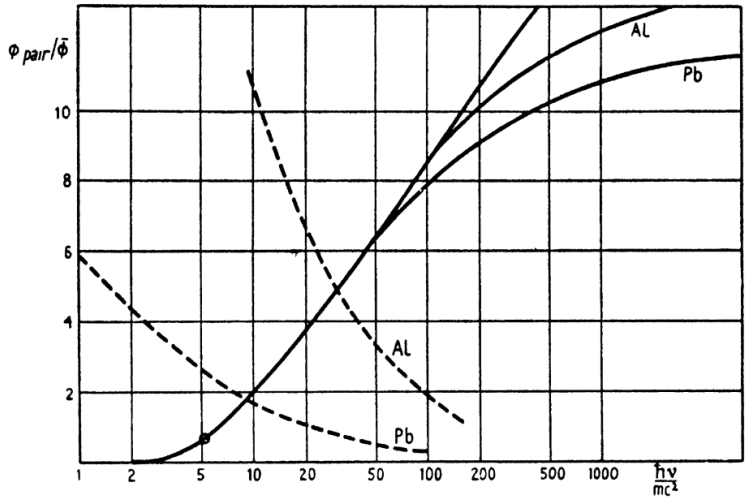

Figure 1.2: The solid lines represent the cross-section for different materials versus the photon energy. The cross section are normalized by $\bar{\phi} = \frac{Z^2 r_0^2}{137}$ where r_0 is the classical electron radius. Taken from [9].

Another possibility of pair creation in matter consists in the trident Bethe-Heitler process, represented in Figure 1.3. Here, a fast electron interacting with the Coulomb field of the nucleus emits a virtual photon and then the last decays into a pair. However, the cross section of this process is very small with respect to the Bethe-Heitler one [9].
Then, completely different mechanisms are the linear Breit-Wheeler pair production and the non-linear one. The linear process, represented in Figure 1.3, involves two photons

that in the collision are converted into a pair [11]. It is important to note that the linear Breit-Wheeler pair creation has not yet been observed in experiments [12], and it is theoretically characterized by a very weak probability. Therefore this process is efficient in setups providing bright sources of collimated, high-energy and counter-propagating photons [12]. The most promising process for abundant pair creation with the advent of high-intensity lasers ($I > 10^{22}\,\mathrm{W/cm^2}$) [13] is the non-linear Breit-Wheeler process, which will be presented in the next subsection.
Concluding, it is worth mentioning the Schwinger mechanism (see Figure 1.4), in which an electron-positron pair is created from the vacuum by a strong constant or oscillating electric field. This process, a prediction of Quantum Electro-Dynamics (QED), requires huge electric fields of the order of 10^{18} V/m, much stronger than any field currently reproducible in laboratories. Consequently, this process is investigated by many theoretical physicists in order to make it observable in the future [14].
Unlike other processes, pair production mechanisms are intrinsically quantum, so they do not have a classic limit, because massive particles are created from the vacuum.

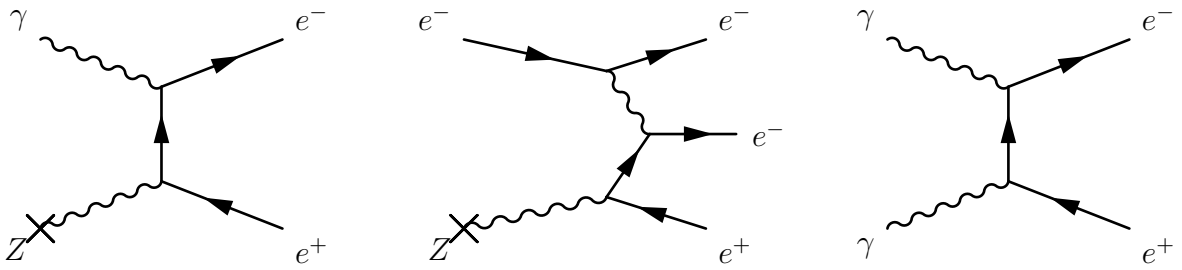

Figure 1.3: From left to right, Feynman diagrams of Bethe-Heitler, trident Bethe-Heitler and linear Breit-Wheeler pair production processes.

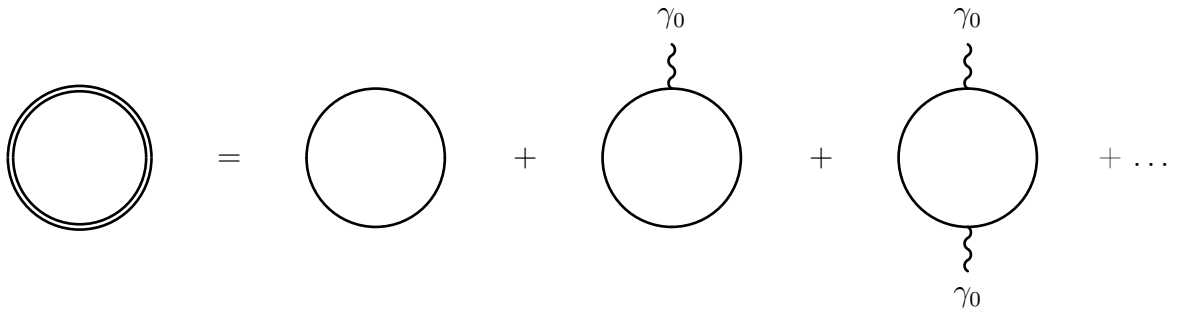

Figure 1.4: Feynman diagram of Schwinger pair production. The double line represents the "dressed" pair, representing the pair interacting with the background field through the absorption of many background photons γ_0 [14].

1.2.2. Non-linear Breit-Wheeler Pair Production (NBWPP)

The Non-linear Breit-Wheeler Pair Production (NBWPP) is a process occurring in a very intense electromagnetic field. Since it involves creation of particles, to be accurately described a quantum field theory is required, in particular the QED, which is the quantum theory of the electromagnetic interaction between charged particles. The Feynman diagram is shown in Figure 1.5. A photon within such a field can interact with multiple background photons undergoing conversion into a pair, thus this process is also referred to as multiphoton Breit-Wheeler pair production. Due to the involvement of many photons of the background field, the dependence of this process on the field amplitude is strongly non-linear [15]. This process, unlike the linear one, has been observed in experiments [16].

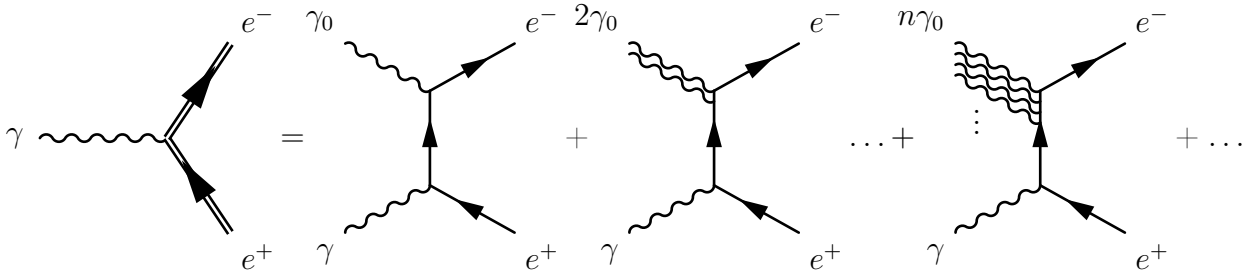

Figure 1.5: Feynman diagram of non-linear Breit-Wheeler pair production. Here γ is the incident photon and γ_0 refers to photons of the background field. The double line in the first one represent the "dressed" pair, i.e. the pair interacting with the background field, meaning that the process occurs with the absorption of many background photons [15].

Firstly, it is useful to introduce a significant, relativistic invariant parameter governing the NBWPP process: the quantum parameter χ. It can be defined for the photon χ_γ, positron χ_+, and electron χ_-, and depends on the corresponding particle velocity $\boldsymbol{v}$ ($\boldsymbol{c}$ for the photon), energy $\mathcal{E}$, and also on the local and instantaneous electric $\boldsymbol{E}$ and magnetic $\boldsymbol{B}$ fields.

$$\chi_\gamma = \frac{\mathcal{E}_\gamma}{E_s m_e c^2}\sqrt{\left(\boldsymbol{E}+\frac{\boldsymbol{c}}{c}\times\boldsymbol{B}\right)^2-\left(\frac{\boldsymbol{c}\cdot\boldsymbol{E}}{c}\right)^2} = \frac{\mathcal{E}_\gamma}{E_s m_e c^2}\frac{F_{\perp,\gamma}}{e} \tag{1.1a}$$

$$\chi_\pm = \frac{\mathcal{E}_\pm}{E_s m_e c^2}\sqrt{\left(\boldsymbol{E}+\frac{\boldsymbol{v}_\pm}{c}\times\boldsymbol{B}\right)^2-\left(\frac{\boldsymbol{v}_\pm\cdot\boldsymbol{E}}{c}\right)^2} \approx \frac{\mathcal{E}_\pm}{E_s m_e c^2}\frac{F_{\perp,\pm}}{e} \tag{1.1b}$$

Here $E_s = m_e^2 c^3/(e\hbar)$ is the Schwinger field, or critical field of QED, m_e is the electron mass, e is the fundamental charge, c is the speed of light and $\hbar$ is the reduced Plank constant. The approximated expression, which is exact for mass-less particles, holds when the particle is ultra-relativistic ($\mathcal{E} \gg m_e c^2$), and shows that the physical meaning of

the quantum parameter is related to the absolute value of the perpendicular component of the Lorentz force $F_\perp = e|\boldsymbol{E}_\perp + \boldsymbol{v}/c \times \boldsymbol{B}|$ acting on the particle. Therefore, the relevant component of the force governing the NBWPP is the perpendicular one, similarly to the emission of radiation [17]. The quantum parameter can also be meaningfully expressed as the ratio between the module of the electric field in the particle rest frame and the Schwinger field. The parameter χ_γ, as shown later, governs both the total probability and the spectrum of the pair. Therefore, it is crucial to note that the quantum parameter, in general, depends strongly on the geometry formed by the particle velocity and the fields. The following argument is proposed by the author of this thesis work. Consider two distinct configurations (see Figure 1.6): the Right-Handed (RH) one, where $(\boldsymbol{E}\times\boldsymbol{B})\cdot\boldsymbol{v} > 0$ and χ is suboptimal, and the Left-Handed (LH) one, where $(\boldsymbol{E} \times \boldsymbol{B}) \cdot \boldsymbol{v} < 0$ and χ is enhanced. The scenario in which $(\boldsymbol{E} \times \boldsymbol{B}) \cdot \boldsymbol{v} = 0$ is possible but not relevant. To understand the impact of the geometry on χ, assume for simplicity the "crossed" geometry $\boldsymbol{E} \perp \boldsymbol{B} \perp \boldsymbol{v}$ (and so $\boldsymbol{E} \cdot \boldsymbol{v} = 0$): in the RH case $\boldsymbol{v} \times \boldsymbol{B}$ and $\boldsymbol{E}$ are oppositely directed and therefore they sum up with opposite sign in χ, whereas in the LH case $\boldsymbol{v} \times \boldsymbol{B}$ and $\boldsymbol{E}$ are aligned and they sum up with the same sign in χ. If the geometry is "crossed" with $|\boldsymbol{E}| = |\boldsymbol{B}|$ and also the particle is ultra-relativistic (or mass-less), χ reduces to:

$$\chi^{\mathrm{RH}} \simeq 0, \quad \chi^{\mathrm{LH}} \simeq 2\frac{\mathcal{E}}{m_e c^2}\frac{|\boldsymbol{E}|}{E_s} \tag{1.2}$$

It is also important to note that the quantum parameter of the photon accounts for the magnitude of the quantum non linear effects [15], as it can be readily expressed as the work, in units of $m_e c^2$, performed by the field over the Compton length in the particle rest system. In principle, quantum effects are important when $|\boldsymbol{E}| \sim E_s$, but according to 1.2, they emerge also when relativistic particles are involved, even if $|\boldsymbol{E}| \ll E_s$. Physically, these particles see $|\boldsymbol{E}| \sim E_s$ in their rest frame. Lastly, the quantum parameter satisfies the conservation law [15]:

$$\chi_\gamma = \chi_+ + \chi_-. \tag{1.3}$$

Moving on, the probability per unit time per unit positron quantum parameter for a photon with energy $\mathcal{E}_\gamma$ and quantum parameter χ_γ to undergo pair production emitting a positron with quantum parameter χ_+, or in other words the NBWPP probability rate spectrum, is given by ([15], elaborated):

$$\frac{d^2N_+}{d\chi_+ dt} = \frac{\alpha_f}{\pi\sqrt{3}}\frac{\left(m_e c^2\right)^2}{\hbar\mathcal{E}_\gamma\chi_\gamma}\left[\int_{2y}^{\infty} K_{1/3}(s)ds - (2-3\chi_\gamma y)K_{2/3}(2y)\right] \equiv \frac{\alpha_f}{\pi\sqrt{3}}\frac{\left(m_e c^2\right)^2}{\hbar\mathcal{E}_\gamma\chi_\gamma}\mathcal{G}(\chi_\gamma,\chi_+) \tag{1.4}$$

where $y = \chi_\gamma/[3\chi_+(\chi_\gamma - \chi_+)]$, $K_{1/3}$ and $K_{2/3}$ are modified Bessel functions of the second kind and α_f is the fine structure constant. The spectrum exhibits clear symmetry when interchanging the positron quantities with those of the electron. Also, once fixed the photon energy, the distribution of χ_γ between χ_+ and χ_- depends on χ_γ itself. Specifically, for low values of χ_γ, it is evenly split between χ_+ and χ_-, whereas as χ_γ increases, a uneven distribution within the pair becomes more probable. The NBWPP total probability per unit time is:

$$\frac{dN_+}{dt} = \int_0^{\chi_\gamma} \frac{d^2N_+}{d\chi_+ dt} d\chi_+ = \frac{\alpha_f}{\pi\sqrt{3}} \frac{(m_e c^2)^2}{\hbar \mathcal{E}_\gamma \chi_\gamma} T(\chi_\gamma), \tag{1.5a}$$

$$T(\chi_\gamma) = \int_0^{\chi_\gamma} \left[\int_{2y}^{\infty} K_{1/3}(s) ds - (2 - 3\chi_\gamma y) K_{2/3}(2y) \right] d\chi_+. \tag{1.5b}$$

The total probability for the photon to undergo NBWPP is governed by χ_γ, and it becomes significant when χ_γ, which is enhanced in the LH geometry, approaches unity.

A simpler, approximated, description in terms of $\mathcal{E}_+$ instead of χ_+ can be derived by assuming that the photon, as well as the positron and the electron, are ultra-relativistic particles ($\mathcal{E} \gg m_e c^2$). Consequently, the emission of the pair is assumed to be collinear with the photon propagation direction, meaning that the photon and the pair share the same direction of propagation. In this case, it is straightforward to show that $F_{\perp,\gamma} \simeq F_{\perp,+}$. By using eqs. (1.1a), (1.1b) and (1.3), the positron energy and the conservation of energy can be derived, along with the spectrum per unit positron energy [18, 19]:

$$\mathcal{E}_+ \simeq \mathcal{E}_\gamma \frac{\chi_+}{\chi_\gamma}, \quad \mathcal{E}_\gamma \simeq \mathcal{E}_+ + \mathcal{E}_- \quad \rightarrow \quad \frac{d^2N_+}{d\mathcal{E}_+ dt} \simeq \frac{\chi_\gamma}{\mathcal{E}_\gamma} \frac{d^2N_+}{d\chi_+ dt} \tag{1.6}$$

It should be noted that the background photons do not enter into this approximated conservation law; this fact is discussed in (1.2.3). The distribution of the available energy, approximately equal to $\mathcal{E}_\gamma$, between the electron and the positron reflects the distribution of χ_γ within the pair. The spectrum per unit positron energy is shown in Figure 1.7.

To conclude, it is worth to mention the trident pair production process in a strong electromagnetic field. In this process, represented in Figure 1.8, an electron in such a field emits a photon, which can be either real or virtual, and then this photon converts into a pair. Consequently, the double-step process in which an electron emits a real photon and then this undergoes NBWPP is included within the trident single-step one. Additionally, it has been observed that the contribution from the virtual photon in the trident process is typically small compared to that from the real photon [19, 20].

Figure 1.6: Left-handed and right-handed geometry for the particle velocity $\boldsymbol{v}$ and the fields $\boldsymbol{E}$ and $\boldsymbol{B}$ in the "crossed geometry".

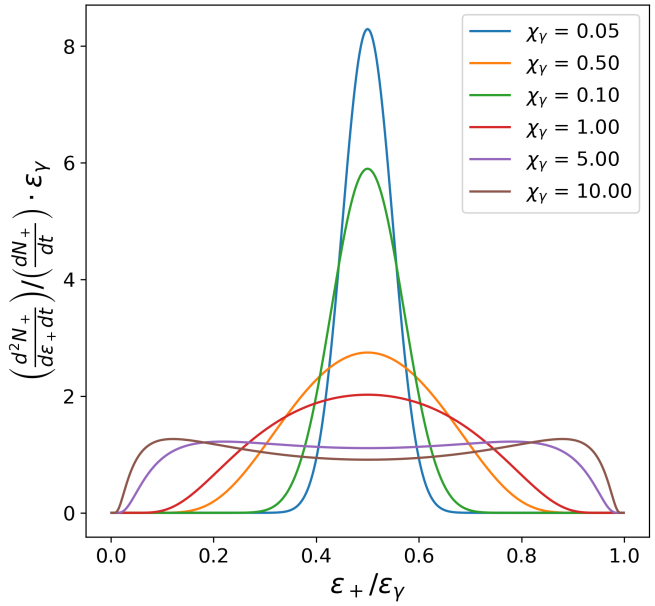

Figure 1.7: Normalized NBWPP spectrum for different values of χ_γ.

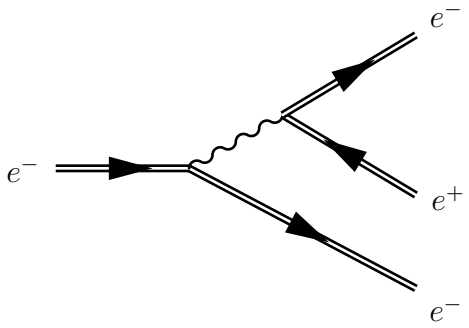

Figure 1.8: Feynman diagram of the trident pair production in a strong electromagnetic field. The double lines mean that both the pair and the initial electron interact non-perturbatively with the background field [15].

1.2.3. NBWPP: theoretical framework and validity conditions

This subsection aims to describe all the hypotheses required to derive the NBWPP spectrum and the total probability rate (eqs. (1.4) and (1.5a)). Actually, the discussion applies as well to high-energy photon emission (see 2.4.1), by considering as emitting particle an electron instead of a photon, and a photon and another electron as the emitted ones.
The calculation of the probability rate, spectrum and angular distribution of NBWPP was performed by Ritus [15] using the perturbation theory in the framework of QED. The analytical expressions are derived considering a photon propagating inside the external field of a plane electromagnetic wave with frequency ω_0. In such a way, the coupling of the positron and electron quantum fields with the electromagnetic background field is treated exactly, i.e. non-perturbatively, while the interaction with the incident photon is treated as a perturbation. The first approximation reduces the description of the process in a plane wave to that in a constant crossed field, in which the electric and magnetic components are perpendicular and equals in magnitude, so $|\boldsymbol{E}| = |\boldsymbol{B}|$ and $\boldsymbol{E} \cdot \boldsymbol{B} = 0$. This is possible when [15]

$$a_0 = \frac{eE}{m_e c w_0} \gg 1 \quad \rightarrow \quad \lambda_0 \gg \frac{m_e c^2}{eE}, \tag{1.7}$$

where E, w_0 and λ_0 are the field magnitude ($E \equiv |\boldsymbol{E}|$), frequency and wavelength. Physically, looking at the second form of this condition, it states that the wavelength of the field, representing the characteristic spatial scale of field variations, is much bigger than the size of the formation region of the process, which scale as the inverse of the field amplitude. An equivalent condition for the frequency of the field can be obtained. Therefore, if the criterion is satisfied, the oscillating nature of the field can be neglected, and a constant crossed field, which is the instantaneous field acting on the emitting particle, can be considered. Another interesting physical interpretation of eq. (1.7) is that the work made by the field over a wavelength is much greater than the rest energy of the electron. This means that if the condition is satisfied, a large number of background photons is absorbed in the process. For this reason, in electrodynamics a_0 is called classical nonlinearity parameter, and it accounts for the number of background photons involved in the process. So, when a_0 is large, the presence of the background field cannot be treated perturbatively. In particular, the number of photons involved in the process is proportional to a_0^3 [14, 15]. Assuming for instance $a_0 = 100$ and $\lambda_0 = 800$ nm, the number of photons involved is roughly 10^6, corresponding to a total background photon energy absorbed in the process of few MeV.
Then, the following assumptions allow to extend the description to an arbitrary electro-

magnetic field, non necessarily crossed [15]:

$$f, g \ll 1, \quad f, g \ll \chi^2 \tag{1.8}$$

where χ is the emitting particle quantum parameter, and $f = \left(|\boldsymbol{B}|^2 - |\boldsymbol{E}|^2\right)/(2E_s^2)$ and $g = (\boldsymbol{B} \cdot \boldsymbol{E})/E_s^2$ are the two Lorentz invariants of the electromagnetic field normalized with the Schwinger field. The physical reason is that when these conditions are met, the field in the emitting particle rest frame is almost a crossed field, and therefore the description of the process in a crossed field can be applied. These conditions depend on the fields but also on the properties of the emitting particle through χ. It should be noted that for both a plane wave and a constant crossed field f and g are exactly zero. Simpler, equivalent conditions are reported in [19] and [21]:

$$\frac{E}{E_s} \ll \chi_\gamma, \quad \frac{E}{E_s} \ll 1. \tag{1.9}$$

Consider now the assumption of considering ultra-relativistic particles and collinear emission, which leads to the approximated expressions for the positron energy, conservation of energy and spectrum per unit positron energy (eq. (1.6)). As mentioned previously, the background photon energy is not included in the energy conservation. However, if the emitting particle is ultra-relativistic, meaning its energy is equal to tens or hundreds of MeV, the previously calculated absorbed background photon energy, which is around few MeV, becomes relatively less significant. According to [19], the energy extracted from the field is $\lesssim m_e c^2$. The extracted background photon energy actually impacts also the field itself, reducing its energy. When the number of QED events becomes significantly large, the energy loss of the field is expected to be non-negligible. In addition, the energy conservation does not conserve momentum. In particular a small fraction of the photon momentum disappears:

$$\mathcal{E}_\gamma = p_\gamma c \simeq \mathcal{E}_+ + \mathcal{E}_- \gtrsim p_+ c + p_- c \quad \rightarrow \quad p_\gamma \gtrsim p_+ + p_- \tag{1.10}$$

The error tends to zero more the particles become ultra-relativistic. This is a general property, consequence of neglecting the correct energy-momentum contribution of the external field: momentum and energy cannot both be exactly conserved. It is worth mentioning that in the description of the process within a plane wave, the conservation of energy and momentum is exact, including also the background field contribution. However, since the background field is treated as an external field, which is assigned, its dynamics, including the loss of photons, is not considered.

As an additional note, QED high-order corrections, such as loop corrections or vertex corrections, are neglected.

1.3. Sources of high-energy positron beams

In this section and in the following one, the engineering aspects of positron production are addressed, with a specific focus on high-energy positron beams rather than positron generation in general. The reason is that in laser-plasma interaction, positrons are produced with beam-like characteristics and MeV energies. Therefore, in the context of this thesis work, the relevant engineering aspects pertain exclusively to high-energy positron beams.
There are two mechanisms to produce positrons, through radioactive sources and by exploiting different types of pair production processes. In this section, the principal setups to produce high-energy positron beams will be presented, together with the main features of the beams produced.

1.3.1. Conventional solutions: accelerators with converters

Conventional schemes are currently employed in today's circular and linear colliders for particle accelerators. These schemes consist in a high-intensity and high-energy electron beam striking a metal target, known as a converter. Charged particles traversing matter lose energy by emitting photons through Bremsstrahlung (see 2.4.1) and by collisions with other electrons [22]. The result of collisions is the ionization and the heating of the material. The energy of the emitted photons can reach the primary electrons' energy. Subsequently, these photons can undergo pair production through the Bethe-Heitler process, presented in 1.2.1. Electrons and positrons produced in this process can emit further photons, which can lead to the creation of additional pairs, initiating a cascade process known as electromagnetic shower [22]. The cross-sections of both Bremsstrahlung and Bethe-Heitler processes depend strongly on the atomic number Z of the target atoms, as they rely on the strength of the Coulomb field. Therefore, high-Z and high-density materials are typically employed for converters.
Once the converter material is fixed, the variable parameters determining the positron production efficiency, or the extension of the electromagnetic shower, are the converter thickness and the primary electrons' energy. Increasing the primary electrons' energy results in higher positron yield and mean energy, since more energy is available for the shower. However, this requires larger electron accelerators, leading to increased costs and complexity. When increasing the converter thickness, there are more target atoms, and so

more photons and hence more positrons are produced. However, once an optimum value is exceeded, the energy of photons and positrons becomes too low to sustain the shower, resulting in no further positron production. Beyond this optimal thickness, the only effect of increasing it is higher positron attenuation, causing the positrons to remain within the target and annihilate there. This behaviour can be observed in Figure 1.9, where lengths are normalized to the radiation length L_{rad}, representing the characteristic distance of energy loss by electrons within a specific material. The optimal converter thickness changes slowly with the converter material and the primary electrons' energy, within the considered energy range [23]. One of the most sophisticated conventional scheme is implemented at SLAC in Stanford, where more than one positron is collected per primary electron. In the other systems, the yield is typically around 1 % when normalized to a primary energy of 1 GeV [23].

The generated positron spectrum is a complex convolution of the spectra of the processes involved and depends on several parameters, such as the primary electrons' energy, the target material and thickness. An example from the positron production system of LEP at CERN is shown in Figure 1.10, considering a primary electrons' energy of 200 MeV and a lead converted with the optimal length. At the converter's output, both positrons and electrons are collected. While the electron spectrum is peaked at 8 MeV, the positron one does not exhibit a maximum but rises toward lower energies [23]. It's worth noting that these spectra are calculated using Monte-Carlo methods. The same study also presents experimentally measured spectra, this time with a primary electrons' energy of 220 MeV. The measured positron spectrum differs from the previous one presenting a low-energy peak around 19 MeV, and extending beyond 70 MeV. Another important characteristic of beams generated by conventional methods is that the electron component dominates over the positron one, as shown in Figure 1.10. In the same picture, the radial distribution of secondary particles, including both electrons and positrons, is reported.

For comprehensive information, a more recent work [24] describes the features of positron beams produced by currently operational facilities. Typically, 10^8-10^{10} positrons per electron bunch are produced, corresponding to yields in the range from 1% to tens of percent, achieving intensities of 10^{10}-10^{12} positron/s. The positron angular-energy distribution, originating from 6 GeV electrons, is depicted in Figure 1.11. The positron spectrum peaks below 10 MeV, although with a cutoff energy extending to several GeV. Moreover, positrons are emitted within a cone with half-aperture of indicatively 50°.

It is worth mentioning another scheme for generating high-intensity positron beams using accelerators in conjunction with a converter. In this setup, an electron beam, accelerated by a circular accelerator, passes through a static magnetic undulator, producing high-energy photons. These photons then enter in a converter producing positrons, since

electromagnetic showers can be initiated by high energy photons as well as by high energy electrons. Among the advantages of this setup [25], the most relevant one is that producing photons in undulators, electrons are not lost, but continues to circulate within the accelerator being accelerated. In this way, electrons do not require to be accelerated each time from low to high energies, which is very expensive, but they are maintained at the required energy. Concluding, the main limitations of conventional schemes are the large size of accelerators, the low positron energy, and the low positron density due to the poor conversion efficiency from electrons to positrons [26, 27].

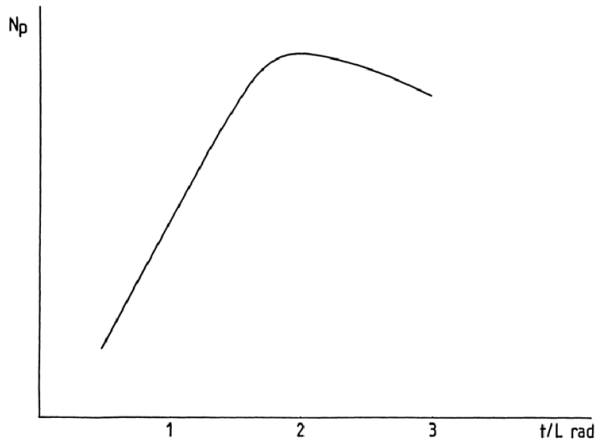

Figure 1.9: Positron yield as a function of the converter thickness for Tungsten ($L_{rad} = 3.5$ mm) and primary electron energy of 200 MeV, obtained by Monte-Carlo calculation [23].

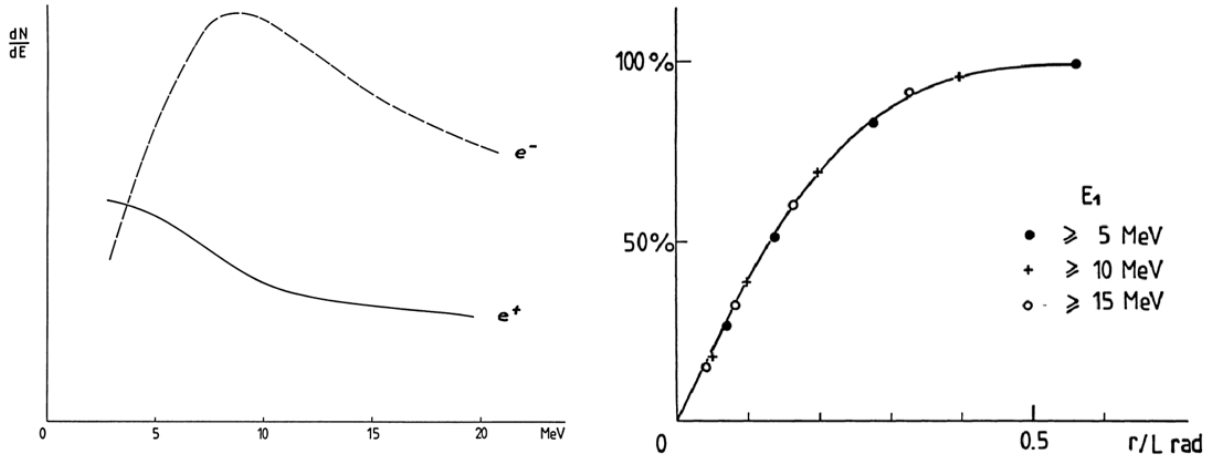

Figure 1.10: On the left the positron and electron spectra and on the right the radial distribution of secondary particles, considering a primary electrons' energy of 200 MeV and a lead ($L_{rad} = 5.6$ mm) converter of thickness equal to $2L_{rad}$. All the results are obtained by Monte-Carlo calculations. Taken from [23].

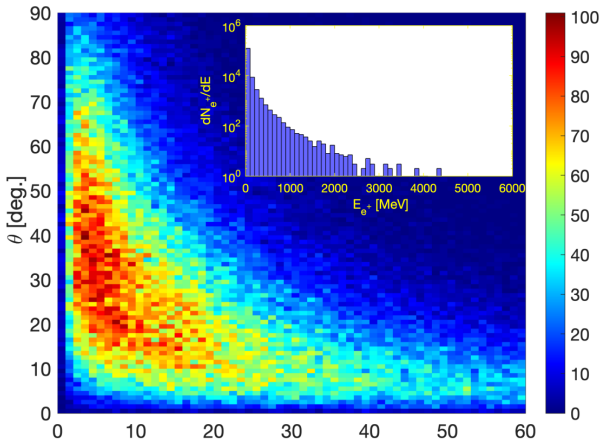

Figure 1.11: Positron angular-energy distribution at the exit of the target-converter for a 6 GeV electron drive beam [24].

1.3.2. Radioactive and nuclear sources

The generation of high-energy positron beams through radioactive and nuclear sources involves complex setups, requiring a series of components for the accumulation, transport, acceleration and eventually bunching of the positrons [24, 28, 29]. This complexity arises because positrons generated by radioactive and nuclear sources have limitations related to the low flux and low density [30]. Therefore accumulation systems are necessary to achieve a high positron density, while accelerator machines allow to reach high energies. Aside these complexities, positron beams generated from radioactive sources offer advantages such as high monochromaticity [28]. Thanks to focusing and accelerating machines, positrons can be arbitrary focused and accelerated to the desired energy. Also, beams from radioactive and nuclear sources are continuum beams, or DC beams, but bunching can be achieved. However, an important limitation of using radioactive sources is the inherent risk associated to radioactivity, particularly when large radioactive sources with high activity are employed to compensate the poor positron yield [30]. In the following, the most relevant schemes to produce slow positrons are presented.

Considering radioactive sources, the choice of the radioactive element depends on the nature of the experiment or task, tempered by cost-effectiveness. Among the sources commercially available, for long-term experiments ^{22}Na is commonly used, offering a reasonable compromise between cost and half-life (2.6 years) [28]. The positron spectrum produced by ^{22}Na peaks at 178 KeV and extends up to 545 KeV. The positron intensity that can be obtained is limited to roughly 10^6-10^8 positrons/s [24, 31]. Immediately after the β^+, this element emits a gamma ray, which has to be shielded for radioprotection and to prevent background signals during the experiment or the activity. In contrast, for

short-term tasks, ^{58}Co is used as β^+-emitter, providing high beam intensity over short periods due to its short life-time [28].
Low-energy positrons can also be generated exploiting the thermal neutron flux from fission reactors [28]. One scheme involves irradiating a copper target, resulting in the $^{63}Cu(n,\gamma)\,^{64}Cu$ reaction, which produces β^+-emitters. This process transforms the initial target into a source of slow positrons with a substantial activity level on the order of tera-Becquerel. Another approach to exploit thermal neutrons is by irradiating a cadmium target, generating gamma rays through the reaction $^{113}Cd(n,\gamma)\,^{114}Cd$. Subsequently, gamma rays enter into a converter and undergo pair production (see 1.3.1). Also, pair production by exploiting directly the gamma rays of a reactor has been employed [29].
A notable setup used in medical applications to produce slow positrons consists in accelerated protons, by a compact cyclotron, impinging on an Aluminium target. Through the $^{27}Al(p,n)\,^{27}Si$ reaction, β^+-emitters are produced. The main advantage of this scheme is that, when the cyclotron is not in operation, the radioactivity of the target decays rapidly. In all of these cases, the use of accumulation and acceleration machines is necessary to produce high-energy positron beams.

1.3.3. Laser-plasma systems

The class of laser-plasma systems for positron production is based on the interaction of a laser pulse with a plasma. A detailed description of both, their interaction, the most promising setups, and the relevant properties concerning the produced positron beams will be provided in the next chapter 2. In this section, the peculiarities, technological advantages, and potentialities of laser-plasma systems are presented.
With the advancement of laser technologies (2.2), culminating in the development of petawatt (PW) class lasers, the pulse duration becomes shorter in the picosecond to femtosecond regime, while the peak intensity gets high up to 10^{22}-10^{23} W/cm^2. These conditions provide the electromagnetic field intensity required to realize QED processes, such as high-energy photon emission (see 2.4.1) and positron production. The role of the plasma is crucial, as it actively participates in the entire dynamics of laser-plasma interaction. The plasma plays a dual role in the interaction: it not only provides the necessary particles to seed these processes efficiently, but also contributes to achieve the conditions for making them possible. While the electric field of nowadays lasers alone cannot create directly pairs from the vacuum (see the Schwinger mechanisms in 1.2.1), exploiting the physics of laser-plasma interaction, it is possible to amplify these fields, reaching extremes conditions. In addition, plasmas can support accelerating electric fields of the order of hundreds of GV/m, which is much higher than the typical MV/m values in

conventional accelerators [26]. This means that in laser-plasma systems, positrons can be produced and also accelerated to energies up to hundreds of MeV or GeV. The generation of positrons takes place within very confined regions and for short times, those associated to the laser pulse, allowing the attainment of high-density and ultra-short duration of the positron beams created. As a result, laser-plasma systems can achieve very high positron intensities, in terms of particles per second. Another significant advantage of laser-plasma systems over conventional methods is their compactness, since the production and acceleration of positrons occur in just few micrometers or millimeters, without the need for a large and expensive accelerator. The overall dimensions of the entire system depends mostly on the laser employed. Furthermore, laser-plasma systems are less affected by radioprotection issues compared to radioactive sources, but these problems are still present due to the activation of materials.
The relevant mechanisms of pair production involved in laser-plasma systems include the Bethe-Heitler process, along with the trident one (see 1.2.1), and the Non-linear Breit Wheeler pair production. These mechanisms have been studied theoretically and demonstrated experimentally [32]. Systems employing the Bethe-Heitler processes utilize the laser field to accelerate electrons into a high-Z converter, leading to electromagnetic showers. Instead, systems based on NBWPP use the laser field to accelerate electrons, generate photons, and provide the external field required for photon conversion into pairs. Currently, laser-plasma systems to generate positrons are very promising due to their technological advantages, including compactness and low radioactivity, and also for the peculiar properties of positrons produces, such as high energy ($>$ MeV), high yield and high density, high intensity ($> 10^{10}$ particles/s), low divergence ($<$ 1 rad) and short duration ($\sim$ fs) [13, 31].

1.4. Applications of high-energy positron beams

Positrons are the most accessible kind of antimatter, and positron beams find applications in a wide range of fields, including high-energy physics (HEP), particle and atomic physics, material science and engineering, medicine and chemistry. Now, the most relevant applications of positron beams will be presented.

1.4.1. Particle colliders for research and Synchrotron Radiation facilities for material science and medicine

Colliders are a type of particle accelerators, and can be ring accelerators or linear accelerators [33]. In electron-positron colliders, beams of electrons and beams of positrons

are accelerated to ultra-relativistic energies and then they are made to collide. In the collisions, pairs of electrons and positrons annihilate releasing their energy to create other subatomic particles, as bosons, leptons, quarks, hadrons and others. These collisions provide a unique opportunity to observe exotic particles that cannot be found in nature due to their short life-time or the high energies required for their existence. Therefore, high energy of the colliding particles is required, but also high density, since the cross-sections of the most exotic processes are typically very small. Advanced detectors play a crucial role in studying the production rates and properties of these particles after the collisions. Physicists utilize colliders to test the Standard Model, the leading theory governing the properties and the behaviour of subatomic particles [34]. Furthermore, accelerators serve as essential tools to search evidences of theories beyond the Standard Model, as the Grand Unification, Supersymmetry and Gravitational theories [34]. The drive to explore new physics is reinforced by observations in astrophysics and cosmology. Additionally, research in physics aims to develop useful applications in engineering and in industry.
Positron beams are employed also in some Synchrotron Radiation (SR) facilities, which are a type of accelerators where electromagnetic radiation is produced by bending energetic charged particles with magnets. The choice of positrons is motivated by the fact that positrons can provide higher brightness compared to electrons [23]. This radiation, principally in the X-rays frequencies, plays a crucial role in the study and characterization of materials [35], and find application in medical imaging and therapeutic technologies [36]. SR radiation is extremely important also in the research in medicine and in basic physics and biochemistry of biological systems.
Electron-positron colliders and synchrotrons require a source of high-density, almost monoenergetic and collimated beam of positrons [23], in order to provide high luminosity and low energy spread. Positron beams typically are produced with conventional methods, and then they are manipulated with spatial and energy focusing systems, beam-lines and accelerating machines. Examples of realistic positron beam sources, considering the complete chain of the required machines, in colliders for HEP and SR are reported in Figure 1.12. An important property of the positron spectrum immediately after the converter is that it does not have a peak but increases toward lower energies (see 1.3.1). This increase of positrons at lower energies is of limited utility, because positrons with too low energies exhibit a wide spread in the time of flight between the source and the accelerating section, resulting in an unacceptable energy spread [23].

	E_e (GeV)	E_p (GeV)	Used for
LAL/Orsay	1	1	SR
LNF/INFN/Frascati	0.09	0.30	SR + HEP
DESY/Hamburg	0.30	0.45	HEP + SR
KEK/Tsukuba-gun	0.20	2.5	HEP + SR
BEPC/Beijing	0.34	1.4	HEP + SR
CERN/LIL/Geneva	0.20	0.60	HEP
SLAC/SLC/Stanford	33	50	HEP

Figure 1.12: Examples of positron beams sources in realistic colliders for HEP research and SR facilities. Here E_e is the primary electron energy and E_p is the positron energy at the end of the beam generation chain. Taken from [23].

1.4.2. Positron annihilation spectroscopy

The discovery of positron's tendency to being trapped in vacancy defects within solids led to the development of Positron Annihilation Spectroscopy (PAS). This technique allows for the characterization of materials at the atomic scale, non-destructive study of the electronic properties of both the bulk and the surfaces of solids, and, most importantly, the realization of defect and void spectroscopy [30, 37]. PAS offers unique advantages compared to other inspection techniques. It is applicable to any type of material, such as crystalline and amorphous, organic and inorganic, biotic and abiotic. PAS excels in identifying sub-nanometers defects with concentrations as low as a part per million, providing detailed information about the type and size of the defects [38]. PAS has found applications in testing disparate systems as turbine, solar cells, and zeolites. PAS also extends to the study of thin films, near-surface regions, magnetic structures of solids, Fermi surfaces of materials, and various other applications [29]. Furthermore, it allows the investigation of mechanical properties of solids, such as plastic deformation at both low and high temperature, or phase transformations in alloys. Moreover, PAS is also employed to investigate the chemical properties of materials and solutions, including bondings and mesomerisms, exploiting the chemical behaviour of positronium, a compound state formed by positrons and host electrons [39]. Additional techniques based on the annihilation physics of positrons have been developed, as doppler broadening of annihilation radiation and angular correlation of annihilation radiation [29]. This research topic is still growing. Consider now the principal PAS technique, the positron annihilation lifetime spectroscopy.

When positrons are injected into a solid body, they penetrate in the material according to their energy, and interact with the host electrons. In materials such as metals or semiconductors where free or nearly free electrons are available, positrons annihilate rapidly. However, in the presence of voids or vacancies, positrons reside inside these defects and annihilate in a longer time. The annihilation of positron-electron pairs releases photons, which can be detected. By measuring the time between the positrons injection and annihilation and the location of annihilation events, it is possible to derive the spatial concentration and distribution of voids and vacancies within the material. Based on the same principle, PAS allows the study of electronic properties of materials: positrons in high electron density regions annihilate faster than the ones in low electron density regions [40]. Positron beams in PAS techniques offer significant advantages over traditional radioelements-based positron systems [29], such as the control of the penetration length of positrons in materials by tuning their initial energy. Additionally, positron beams allow for the separation in time between the injection of positrons and their annihilation, as they need to thermalize through collisions with material atoms before annihilating. In PAS techniques where the timing is important, pulsed positron beam are very desirable. Positron beams are typically produced using radioactive or nuclear sources (see 1.3.2), in combination with beam systems, as positron traps and accelerators, and/or compact cyclotrons [29, 30]. However, the size and complexity of the beam systems, as well as the requirement for a sizable radioactive source in close proximity to the user, have limited the widespread adoption of PAS in industrial laboratories as a routine diagnostic tool. Another approach to provide positron beams, although less commonly used, is through conventional methods (see 1.3.1) with the magnetic transport of positrons in situ [29, 30].
Besides the fact that some PAS techniques, as for the study of surfaces properties, require low-energy positrons in the eV range, positron beams in the MeV energies are employed for measurements on a wide range of materials and are necessary for novel annihilation spectroscopy techniques, such as positron channeling and in-flight annihilation studies, and bulk annihilation measurements [29]. In the last case, high-energy positrons are required to penetrate deep into materials and annihilate within the bulk.

1.4.3. Research in astrophysics and electron-positron plasmas

Some objects in the universe, such as black holes and pulsars, emit violent bursts of gamma-rays, resulting in the production of electron-positron plasmas, in the form of ultra-relativistic winds or jets. These phenomena represent the possibility to test theories of High-Energy Physics (HEP) and astrophysical and cosmological models, including those relates to the origin of our universe [41]. A lot of open questions, such as the mechanisms

of generation of these gamma-bursts, could be addressed in experiments, but currently the extreme difficulties in generating high-density and high-energy positron-electron plasmas are preventing laboratory studies. The high-density requirement is crucial for observing the collective behaviour of such a plasma. Also, the intrinsic symmetry between electrons and positrons within the plasma makes their dynamics significantly different from that of the typical electron-ion plasmas. The fact that the positive and negative species have equal mass introduces peculiarities in the plasma behaviour, for instance in terms of electromagnetic waves propagation and instabilities.

Various approaches to generate high-density and high-energy electron-positron plasmas have been proposed. One method involves using conventional accelerators to generate electron and positron beams separately and then recombining them. Another approach consists in confining low-energy positrons from radioactive sources using traps, and then accelerate them. However, these schemes have some difficulties related to beams recombination. Other methods are proposed, in which electrons and positrons are generated together in situ, but they lack of symmetry in the abundance between positron and electrons, and therefore the produced plasmas are non neutral. In summary, the possibility of generating high-density and high-energy electron-positron beams if of great importance in astrophysics and HEP, but various challenges need to be overcome.

2 | High-intensity laser-plasma interaction for NBWPP

This chapter is devoted to presenting the physical background of non-linear Breit-Wheeler pair production in laser-plasma interaction. Firstly, the main aspects of the two physical systems, laser and plasma, are presented. Then, the physics of their interaction will be detailed, with a particular focus on the most relevant processes related to positron production in a peculiar type of targets, called double-layer targets.

2.1. Plasma

Plasma is a macroscopic aggregation state of matter characterized by the presence of at least one electrically charged population, which can include electrons, ions, nuclei, and even positrons. The peculiarity of a plasma is the presence of a long-range self-consistent electromagnetic field, which mediates the interaction between the charged particles and evolves in time according to their dynamics. Therefore the dynamics of particles and of the field are inherently coupled and cannot be treated separately. The nature of the interaction between particles is primarily electromagnetic, but also other forces can come into play, for instance the nuclear force when nuclear reactions occur.
Plasma is the most abundant form of ordinary matter in the universe, and can be found inside stars, inter-galactic medium and in regions of our atmosphere. A common example of a plasma is a gas that has been completely or partially ionized, resulting in the presence of a free electron population and an ion population. These conditions can be obtained in laboratory, for instance, by heating the gas to a temperature such that the average kinetic energy of particles becomes greater than the ionization potential of atoms or molecules, leading to the breaking of atomic or molecular bonds.
The field of plasma physics cover a huge quantity of topics, the relevant ones to this thesis work will be treated in this section.

2.1.1. Relevant parameters and corresponding properties

A set of parameters and physical quantities can be defined to classify plasmas and obtain information about their behaviour and properties. To begin with, it is necessary to define the species $a = 1, 2 \ldots$ which are present and their properties, such as the mass m_a and electric charge q_a. In the following, a plasma composed primarily of electrons and positive ions will be considered. If the plasma is created through the ionization of a neutral species, the ionization degree describes the amount of ionized atoms with respect to the total number, and it allows for the classification of plasmas as weakly, strongly, or fully ionized.
Subsequently, macroscopic quantities can be introduced, such as the particle density n_a and temperature T_a, which represent the concentration and thermal energy of particles. The overall plasma density n and temperature T are calculated as follows:

$$n = \sum_a n_a, \quad T = \frac{1}{n} \sum_a n_a T_a. \tag{2.1}$$

These parameters can span over a large range of values, and depending on their values, different kinds of plasmas can be classified, each exhibiting distinct physical properties (see Figure 2.1). For plasmas composed of electrons and ions, the substantial difference in their mass results in different inertial properties. At a given plasma temperature, the velocity of ions is significantly lower than the one of electrons.
Considering a single charged particle of the plasma, it repels other particles with the same sign of the charge and attracts the ones with opposite sign. This collective effect, known as polarization [42], leads to the formation of a shielding cloud of particles that tends to neutralize each charge of the plasma. Any charged particle can be considered completely neutralized beyond a certain distance, defined as Debye length λ_D, due to the polarization of other charges. This characteristic length is defined as

$$(\lambda_D)^{-2} = \sum_a (\lambda_{D,a})^{-2}, \quad \lambda_{D,a} = \left(\frac{T_a}{4\pi n_{0,a} q_a^2} \right)^{1/2} \tag{2.2}$$

where q_a, T_a, $n_{0,a}$ are the electric charge, the temperature in energy units, and the average density of the a-population, respectively. For a plasma in which species have charge $q_a = \pm e$, the Debye length can be evaluated numerically as $\lambda_D[\mathrm{cm}] = 740\,(T[\mathrm{eV}]/n[\mathrm{cm}^{-3}])^{1/2}$. Moreover, in plasmas there can be mechanisms, as the thermal motion of particles, acting to separate negative charges from positive ones. However, these separation mechanisms have to contend with the electrostatic attractive force, which acts to cancel the charge unbalance. The Debye length λ_D represents also the characteristic spatial scale of charge

separation, corresponding to the compensation between the thermal kinetic energy of particles and the restoring force.
Another collective phenomenon crucial in plasma physics is the local oscillations of charges. When local charge separation takes place, subsequently the particles involved follow a collective oscillatory motion driven by the long-range charge neutrality restoring field. The frequency of these oscillations is referred to as the plasma frequency ω_p, and it is equal to

$$(\omega_p)^2 = \sum_a (\omega_{p,a})^2, \quad \omega_{p,a} = \left(\frac{4\pi n_{0,a} q_a^2}{m_a}\right)^{1/2}. \tag{2.3}$$

If the plasma is composed by electrons and ions, since $m_e \ll m_i$, the electron contribution dominates in ω_p, meaning that $\omega_p \simeq \omega_{p,e}$. The electron plasma frequency can be numerically evaluated as $\omega_{p,e}[\mathrm{rad/s}] = 2\pi \times 9000(n_e[\mathrm{cm}^{-3}])^{1/2}$.
In plasma physics it is very important the topic of collisions, which are single-particle processes, not a collective effect [42]. In addition to the long-range electromagnetic field, each particle experiences microscopic, or short-range, electromagnetic forces due to the neighbouring charges, leading to scattering-like processes. The inverse of the number of particles contained inside a cube of length λ_D is called plasma parameter g [42], and it quantifies the importance of collisions between particles in terms of their dynamics. Indeed, it can be proven that the plasma parameter is directly proportional to the ratio between the electrostatic potential energy due to neighbour charges and the kinetic energy of thermal origin. Therefore, collisions can be neglected if $g \ll 1$, which is generally valid except for very cold and/or very dense plasmas. It is also useful to introduce the frequency ν at which collisions occur, which depends on the average thermal velocity v_t, the cross section σ of the scattering process, and the average particle density n.

$$g^{-1} = n\lambda_D^3 \sim \sqrt{\frac{T^3}{n}}, \quad \nu = n\sigma v_t = n\sigma \left(\frac{T}{m}\right)^{1/2} \tag{2.4}$$

It is worth mentioning that different collision processes can occur, so σ and ν should be specific to the type of scattering process and the populations under consideration. If considering Coulomb collisions, where $\sigma_c \sim e^4/v_t^4 \sim e^4/T^2$, the following relation is valid:

$$\frac{\nu_c}{\nu_p} \simeq g \tag{2.5}$$

where $\nu_p = \omega_p/2\pi$. Therefore, when $g \ll 1$ the collision frequency is much smaller than the plasma frequency, meaning that collisions are less important than collective effects.
The last interesting quantity is the skin depth, whose physical meaning is related to the

propagation of electromagnetic waves within a plasma and will be detailed in 2.3.1.

$$L_w = \frac{c}{\omega_p} \tag{2.6}$$

In a plasma composed by electrons and ions, since $\omega_p \simeq \omega_{p,e}$ the skin depth can be approximated as $L_w \simeq c/\omega_{p,e}$. Examples of all the parameters introduced for different kinds of plasmas are presented in Table 2.1.

Plasma type	$n[\mathrm{cm}^-3]$	$T[\mathrm{eV}]$	$\omega_{p,e}[\mathrm{s}^{-1}]$	$\lambda_D[\mathrm{cm}]$	g^{-1}	$\nu_{ei}[\mathrm{s}^{-1}]$	$L_w[\mu\mathrm{m}]$
Interstellar gas	1	1	6×10^4	7×10^2	4×10^8	7×10^{-5}	5×10^9
Gaseous nebula	10^3	1	2×10^6	20	8×10^6	6×10^{-2}	1.5×10^8
Solar Corona	10^9	10^2	2×10^9	2×10^{-1}	8×10^6	60	1.5×10^5
Diffusive hot plasma	10^{12}	10^2	6×10^{10}	7×10^{-3}	4×10^5	40	5×10^3
Solar atmosphere, gas discharge	10^{14}	1	6×10^{11}	7×10^{-5}	40	2×10^9	5×10^2
Warm plasma	10^{14}	10	6×10^{11}	2×10^{-4}	8×10^2	10^7	5×10^2
Hot plasma	10^{14}	10^2	6×10^{11}	7×10^{-4}	4×10^4	4×10^6	5×10^2
Thermonuclear plasma	10^{15}	10^4	2×10^{12}	2×10^{-3}	8×10^6	5×10^4	1.5×10^2
Theta pinch	10^{16}	10^2	6×10^{12}	7×10^{-5}	4×10^3	3×10^8	50
Dense hot plasma	10^{18}	10^2	6×10^{13}	7×10^{-6}	4×10^2	2×10^{10}	5
Laser plasma	10^{20}	10^2	6×10^{14}	7×10^{-7}	40	2×10^{12}	5×10^{-1}

Table 2.1: Examples of plasmas existing in nature or produced in laboratory with their key parameters [43]. Here ν_{ei} is the frequency of Coulomb collisions between electrons and ions. The skin depth L_w is calculated using the approximated expression of 2.6.

2.1.2. Kinetic description of a collision-less plasma

The kinetic modeling of a plasma is a non-quantum macroscopic particle description. Among the various macroscopic modeling approaches, the kinetic one is the most detailed because it considers the entire velocity distribution of particles instead of collapsing it into a limited set of fields, as done in the fluid descriptions [42]. In other terms, it takes into account the particle nature of the plasma. Furthermore, the kinetic description becomes necessary when the particle velocity distribution deviates significantly from the one at thermal equilibrium.

The particles are treated as point-like, but instead of studying the position and the velocity of each of them, the intent of a macroscopic description is to determine the average number of particles with position $\boldsymbol{x}$ and velocity $\boldsymbol{v}$ inside corresponding small intervals $d\boldsymbol{x}$ and $d\boldsymbol{v}$. Therefore, the interest is in averaged properties of the plasma, without microscopic fluctuations [42]. Similarly, concerning the electromagnetic field, a macroscopic description aims to determine the average long-range field that exist over a large number of particles, rather than the field acting on each individual constituent. Mathematically, this description is achieved through a spatial filtering procedure that removes all the information below a certain spatial scale. This scale should be chosen to be much greater than the average distance between particles $n_0^{-1/3}$, in order to perform averaging over a sufficiently large number of particles. It should also be much smaller than the Debye length λ_D, which is the characteristic macroscopic length of the plasma.
This model neglects of collisions, making it applicable only when collisional effects are unimportant. This implies that the model is limited to plasmas with plasma parameter $g \ll 1$ and to phenomena characterized by a frequency $w \gg \nu$ [42]. In many cases, the most important collisional process is between electrons and ions, making the relevant collisional frequency ν_{ei}. In ultrashort high-intensity laser-plasma interaction collisions can be neglected, because the dominant process is the coherent electron acceleration, while electron heating, necessary for collisions, is less effective [10].
Lastly, the common feature of all the macroscopic plasma descriptions is the coupling between equations describing the plasma dynamics and Maxwell's equations governing the long-range self-consistent electromagnetic field.
The set of differential equations of the kinetic description, relativistically corrected, of a collision-less plasma, is referred to as the relativistic Vlasov-Maxwell system:

$$\begin{cases} \dfrac{\partial f_a}{\partial t} + \dfrac{\boldsymbol{p}}{\gamma_a m_a} \cdot \dfrac{\partial f_a}{\partial \boldsymbol{x}} + q_a \left(\boldsymbol{E} + \dfrac{\boldsymbol{p}}{\gamma_a m_a c} \times \boldsymbol{B} \right) \cdot \dfrac{\partial f_a}{\partial \boldsymbol{p}} = S_a(\boldsymbol{x}, \boldsymbol{p}, t) \quad a = 1, 2, \dots & \text{(2.7a)} \\ \nabla \cdot \boldsymbol{E} = 4\pi \left(\rho_{ext} + \sum_a q_a \int f_a d\boldsymbol{p} \right) & \text{(2.7b)} \\ \nabla \times \boldsymbol{E} + \dfrac{1}{c} \dfrac{\partial \boldsymbol{B}}{\partial t} = \boldsymbol{0} & \text{(2.7c)} \\ \nabla \cdot \boldsymbol{B} = 0 & \text{(2.7d)} \\ \nabla \times \boldsymbol{B} - \dfrac{1}{c} \dfrac{\partial \boldsymbol{E}}{\partial t} = \dfrac{4\pi}{c} \left(\boldsymbol{J}_{ext} + \sum_a \dfrac{q_a}{m_a} \int \dfrac{\boldsymbol{p}}{\gamma_a} f_a d\boldsymbol{p} \right). & \text{(2.7e)} \end{cases}$$

The time-dependent functions $f_a(\boldsymbol{x}, \boldsymbol{p}, t)$, defined in the phase space, are the distribution functions for the various populations, and they represent the average density of particles in

phase space. In the context of pair production in laser-plasma interaction, the populations involved are electrons, ions, photons and positrons, hence $a = e^-, i, \gamma, e^+$. For photons $q_\gamma = m_\gamma = 0$ and $\boldsymbol{p}/\gamma_\gamma m_\gamma = c\boldsymbol{p}/|\boldsymbol{p}|$. The source term $S_a(\boldsymbol{x}, \boldsymbol{p}, t)$ accounts for the creation and destruction of particles of a-population in phase space, while $\gamma_a(\boldsymbol{p}) = \sqrt{1 + (\boldsymbol{p}/m_a c)^2}$ is the Lorentz factor and depends on m_a. It is worth mentioning that S_a includes also abrupt changes in the velocities of particles. The terms ρ_{ext} and $\boldsymbol{J}_{ext}$ describe external charge densities and external currents. Physically, the Vlasov equation is the continuity equation in phase space for the distribution function, stating that the average number of particles along their trajectory in phase space remains conserved, except for the action of source terms S_a.
Once the distribution function is known, kinetic expressions of macroscopic quantities can be derived as moments of f_a. Examples include temperature, pressure, stresses, conductive and convective fluxes of heat, and others.

2.2. High intensity lasers

Lasers are devices that generate or amplify coherent light within the infrared, visible or ultraviolet frequency ranges. Laser light possesses remarkable properties such as directionality, spectral purity, and intensity [44].
The key process that enabled light amplification and the development of laser technologies is the stimulated emission of radiation. Two operational regimes of lasers are possibles: the continuous-wave regime, where a continuous laser beam is generated with a narrow bandwidth, and the pulsed regime, which produces short pulses of light with a broad bandwidth. The pulsed regime was realized through the development of Q-switching and mode-locking techniques [44]. In conjunction with chirped pulse amplification, short pulses proved to be the gateway to previously unexplored laser field intensities, allowing access to new interaction regimes with matter. Laser field intensities of $10^{15} - 10^{18}$ W/cm^2 were attainable, corresponding to an electric field strength comparable to the Coulomb field within atoms [14]. Subsequently, the advent of optical parametric chirped pulse amplification for amplifying ultra-short pulses led to the achievement of extremely high laser field intensities, currently reaching levels up to 10^{23} W/cm^2. These intensities have extended the applications of lasers into new domains, including nuclear physics, plasma physics and high-energy physics [14]. In laser-matter interaction, electrons are accelerated to ultra-relativistic energies, forming ultra-relativistic plasmas and leading to the emergence of QED strong-field processes. In the next few years, with the incoming 10-Petawatt class lasers, intensities of $10^{23} - 10^{24}$ W/cm^2 are expected to be achieved, allowing for studying QED effects in unexplored domains, such as electromagnetic cascades occurring

in the laser field [19].
In the following, the main parameters and the mathematical modelling of laser pulses will be treated, as well as the mechanisms for generating plasmas using lasers.

2.2.1. Parameters and mathematical modelling

Laser pulses can be characterized by a set of parameters that determine the laser field distribution in time and space.
Important parameters used to describe laser pulses are the pulse energy E_p, the central frequency w_0 (or wavelength $\lambda_0 = 2\pi c/\omega_0$), the temporal duration τ_p, and the spot size σ_p. The pulse energy E_p is the total electromagnetic energy carried by the pulse, which can range from nJ to kJ. To achieve a short finite duration, a wave-packet with a broad spectrum of frequencies is required [45]. The central frequency w_0 is the carrier frequency and depends on the laser and amplification system. Titanium-Sapphire lasers, for instance, generate light with a wavelength $\lambda_0 = 800$ nm. The duration τ_p express the width of the envelope and can range from nanoseconds to tens of femtoseconds. In the context of interaction with matter, a ns-duration pulse is relatively long, almost a continuous wave, while pulses below the ps-duration are considered ultra-short. The spot size σ_p represents the spatial transverse size of the beam, encompassing almost all the pulse energy, and it generally varies during the pulse propagation. In the focal position, where the spot size is minimum, σ_p can reach few micrometers. Assuming a flat temporal and spatial profile and E_0 as the electric field amplitude, it is possible to estimate the energy of the pulse:

$$E_p \simeq \frac{c}{2}\frac{E_0^2}{4\pi}\tau_p(\pi\sigma_p^2) \tag{2.8}$$

Another important parameter is the peak power P_{peak}, representing the maximum energy per unit time crossing a plane transverse to the optical axis. It depends on E_p and τ_p and, for intense lasers, can range from TW to PW. An essential quantity is the peak intensity I_{peak}, which indicates the maximum energy per unit time per unit surface crossing a transverse plane. Both the peak intensity and peak power are considered to be cycle-averaged. The peak intensity depends on P_{peak} and σ_p and can currently reach the regime of 10^{23} W/cm^2, with E_p in the J level. It is important to note that, given P_{peak}, to achieve high intensities the beam should be focused to very small spot sizes. From the peak intensity, the peak value of the electric field $|\boldsymbol{E}|_{peak}$ can be evaluated, and the peak normalized vector potential $a_{0,peak}$ can be defined (see 1.2.3), as follows:

$$|\boldsymbol{E}|_{peak} = \sqrt{2\frac{4\pi}{c}I_{peak}}, \quad a_{0,peak} = \frac{e|\boldsymbol{E}|_{peak}}{m_e c\omega_0}. \tag{2.9}$$

The second one can be evaluated numerically as $a_{0,peak} = 86\lambda_0[\mu\text{m}]\sqrt{I_{peak}[10^{22}\text{W/cm}^2]}$. Then, the polarization identifies the direction of the oscillations of the electric field and is typically linear or circular. When dealing with a train of pulses, the repetition rate ν_{rep} is the inverse of the time between two consecutive pulses and spans from one pulse per day to MHz.

It is worth mentioning that in a photon description of the pulse, $\hbar\omega_0$ is the single photon energy, E_p represents the total energy of the photons in the pulse, and P_{peak} and I_{peak} are related to the maximum photon intensity (photons per unit time) and photon flux (photons per unit time per unit area).

Moving on to the modeling of the field of a laser pulse, it has to satisfy Maxwell's wave equations with the boundary conditions given by the laser cavity [44]. Adopting the paraxial approximation, which assumes that the propagation direction of the beam is near to the optical axis of the laser cavity, and the slowly-varying amplitude approximation, the electric field solution is described by Gaussian Beams $\text{TEM}_{l,m}$ [45]. These are monochromatic functions defined as the product of a Gaussian function and a Hermite polynomial. The lowest order mode $\text{TEM}_{0,0}$ is simply a Gaussian function with frequency ω and wavevector $k_\omega = \omega/c$. Assuming the z-axis as the propagation direction and linear polarization along the x-axis, the electric field can be expressed as follows [44, 45]:

$$\hat{\boldsymbol{E}}_\omega(\boldsymbol{x},t) = \frac{1}{2}E_0\frac{\sigma_{p,0}}{\sigma_p(z)}\exp\left[-\frac{x^2+y^2}{\sigma_p^2(z)} - ik_\omega\left(z+\frac{x^2+y^2}{2R(z)}\right) + i\Phi(z) + iwt\right]\boldsymbol{u}_x + c.c. \tag{2.10}$$

Before the exponential term, E_0 is the amplitude of the electric field, while $\sigma_{p,0}$ is defined as the spot size at the focal position z_0. The first term in the exponential is real and represent the Gaussian distribution of the field in the transverse plane. Subsequently, there are the longitudinal and transverse phase terms, with the latter depending on the radius of curvature of the equi-phase surfaces $R(z)$. The last terms are the Gouy phase shift $\Phi(z)$ and the time oscillations term. In case of free propagation, $\sigma_p(z)$, $R(z)$ and $\Phi(z)$ evolve during the propagation as follows:

$$\sigma_p(z) = \sigma_{p,0}\sqrt{1+\left(\frac{z-z_0}{z_R}\right)^2} \tag{2.11a}$$

$$R(z) = (z-z_0)\left[1+\left(\frac{z_R}{z-z_0}\right)^2\right] \tag{2.11b}$$

$$\Phi(z) = \arctan\left(\frac{z-z_0}{z_R}\right), \tag{2.11c}$$

where $z_R = \pi\sigma_{p,0}^2/\lambda$ is the Rayleigh range, representing the distance from z_0 to where the spot size has increased by a factor $\sqrt{2}$. Therefore, the beam can be considered almost focused between $z_0 - z_R$ and $z_0 + z_R$. It is worth mentioning that in the mode $TEM_{0,0}$ the intensity is concentrated on the optical axis, while other modes distribute the intensity differently.

To achieve a Gaussian beam with finite temporal extension, according to the Fourier theorem, several modes with slightly different frequency around a central one w_0 are superimposed. The result can be expressed as a carrier, in this case the mode $TEM_{0,0}$, evaluated at the central frequency ω_0, modulated by an envelope function, which shape depends on the coefficients of the superposition. For free propagation, both the carrier and the envelope move with velocity c. The complete expression of the electric field of a Gaussian laser pulse with Gaussian envelope in free propagation is:

$$\boldsymbol{E}(\boldsymbol{x}, t) = \hat{\boldsymbol{E}}_{\omega_0}(\boldsymbol{x}, t) \exp\left[-\frac{(t - z/c)^2}{2\tilde{\tau}^2}\right]. \tag{2.12}$$

The pulse duration τ_p is defined as the Full Width Half Maximum (FWHM) of the envelope, and it is related to $\tilde{\tau}$ as:

$$\tau_p \equiv \text{FWHM} = 2\sqrt{\ln 2}\,\tilde{\tau}. \tag{2.13}$$

Different envelope profiles exist, such as the cosine squared profile or super-Gaussian profiles. The description presented is idealized. Actually, realistic pulses exhibits imperfections and distortions. One example is the presence of pre-pulses, which are low-intensity pulses that precede the main pulse.

Examples of the key parameters introduced for realistic lasers are presented in Table 2.2.

Laser name	$\lambda_0[nm]$	$E_p[J]$	τ_p	$\nu_{\text{rep, max}}$	$2\sigma_p[\mu\text{m}]$	$I_{peak}[\text{W/cm}^2]$
ALEPH	400, 800	10, 26	45, 30 fs	3.3 Hz	1.2, 2.4	-
Bella	815	40	30 fs	1 Hz	65	10^{22}
Scarlet	815	10	30 fs	1 per min	2	$> 8 \times 10^{21}$
Hercules	815	15	30 fs	1 per min	0.8, 50	10^{22}
Diocles	805	20	30 fs	0.1 Hz	1, 20	-
Texas Petawatt	1057	186	167 fs	1 per hour	3.9, 2.2, 60	2×10^{22}

Table 2.2: Examples of lasers with key parameters in U.S. [46].

2.2.2. Lasers to generate plasmas

When a high-intensity laser pulse interacts with a solid, the laser field can ionize the solid, generating free electrons and ions leading to the formation of a plasma. Therefore, if the goal is to make a high-intensity laser interact with a plasma, the laser can be used to ionize matter and obtain the plasma. It is also possible to engineer the target material to generate a plasma with the desired density profile.

There are several ionization mechanisms at play, including single-photon ionization, multi-photon ionization, tunneling ionization, and impact ionization. Single-photon ionization, also known as the photoelectric effect or direct ionization, involves a photon being absorbed by an atomic electron, breaking the bonding with the atom and setting the electron free. Despite having the largest cross-section, it cannot occur with standard optical lasers because the energy of a single photon is too small to match the ionization potential, which corresponds to photon energies in the UV range and beyond [47]. Multi-photon ionization, on the other hand, involves the simultaneous absorption of multiple optical photons. Although the cross-section for this process is significantly smaller than the direct ionization, it becomes possible at laser intensities exceeding 10^{10} W/cm^2 [47]. The multi-photon ionization assumes that the Coulomb potential felt by the electron remains undisturbed by the laser field. However, when the laser intensity reaches the level of $I_a \sim 10^{16}$ W/cm^2, the laser field becomes strong enough to distort the Coulomb potential [47]. This leads to the reduction of the potential barrier experienced by the electron, allowing it to be released through tunnel effect. Therefore, at such intensities, tunneling ionization becomes the dominant ionization process. Additionally, another ionization process may occur, which involves free electrons ionizing atoms or other ions through collisions. This is known as impact ionization and becomes competitive with the tunneling process when a significant number of free electrons is created.

In the first stages of the ionization process, when the number of free electrons is still negligible, and assuming a laser intensity sufficiently high, the dominant ionization process is the tunneling one. For a given initial species, the appearance intensity I_{app} at which a certain ion with charge Z starts to appear is given by the formula [47]:

$$I_{app} = \frac{cE_{ion}^4}{128\pi Z^2 e^6}, \tag{2.14}$$

where E_{ion} is the ionization potential of the parent atom or ion with charge $Z-1$. The appearance intensity can be estimated numerically as $I_{app}[\mathrm{W/cm^2}] \simeq 4\times10^9 (E_{ion}[eV])^4 Z^{-2}$, and its value for various ions is reported in Table 2.3.

Ion	$E_{ion}[eV]$	$I_{app}[\mathrm{W/cm^2}]$
H^+	13.61	1.4×10^{14}
N^{5+}	97.9	1.5×10^{16}
O^{6+}	138.1	4×10^{16}
Ne^{7+}	207.3	1.5×10^{17}
Ar^{8+}	143.5	2.6×10^{16}

Table 2.3: Examples of ionization energies and appearance intensities for various ions [47].

When a laser pulse with a peak intensity much larger than I_a, for instance in the range $I_{peak} = 10^{20} - 10^{22}$ W/cm^2, interacts with matter, ionization occurs very rapidly, well before the arrival of the central part of the pulse. The pre-pulses or the initial tail of the main pulse, despite their much lower intensity compared to I_{peak}, are capable of ionizing matter, allowing the central part of the pulse to interact with a fully ionized plasma [47]. In the case of a laser pulse impinging on a solid target, the electron density n_e of the created plasma can be calculated from the mass density ρ and molar mass A of the target, and the ion charge Z:

$$n_e = \frac{ZN_A\rho}{A}. \tag{2.15}$$

Here N_A is the Avogadro number. Then, these electrons are heated by the laser field and expand outwards, resulting in an exponentially decreasing plasma density profile. However, even at electron temperatures of hundreds of eV, the plasma profile remains very steep, if the pulse has ultra-short duration and I_{peak} is in the range considered above [47]. As a result, the electron expansion can be neglected, and the central part of the laser pulse interacts directly with the solid-density plasma which has just formed.
The final remarkable aspect of plasmas generated by a laser field is the regime of electron and ion motion following the ionization process. As a zero-order approximation, the motion of a charged particle in an uniform oscillating electric field of amplitude E_0 is considered. The particle will oscillate in the direction of the field polarization with the same field frequency ω. Its maximum normalized velocity is given by [47]:

$$\frac{v_{osc}}{c} = \frac{eE_0}{mc\omega} = \frac{m_e}{m}a_0, \tag{2.16}$$

where a_0 is the normalized potential as defined in 2.2.1. When $a0 \sim 1$, corresponding to an intensity of 10^{18} W/cm^2, electrons reach relativistic velocities within a laser cycle. Instead, ions require $a_0 \sim m_i/m_e$ to became ultra-relativistic, corresponding to intensities

exceeding 10^{24} W/cm^2. Therefore, plasmas generated by currently available high-intensity lasers are characterized by a relativistic behaviour of electrons, while ions remain in the non-relativistic regime.

2.3. Physics of the non-quantum laser-plasma interaction

In this section, the non-quantum processes of laser-plasma interaction that are relevant for NBWPP in double-layer targets will be discussed. Interaction regimes and target classification will be discussed. Then, an overview of the classical emission of radiation is provided, while the quantum description, which is the important one in the context of pair production, will be presented in the next section. Finally, the main electron acceleration mechanisms are described, followed by the introduction to the double-layer target, highlighting its unique features and potentialities.

2.3.1. Interaction regimes and classification of targets

When an electromagnetic wave interacts with a plasma, it induces collective modes within the plasma, introducing spatial and temporal dispersion [42, 48]. In principle, the collective behaviour of particles, including the dynamics of the self-consistent long-range electromagnetic field, should be addressed by solving the complete relativistic Vlasov-Maxwell system of equations. If collisions cannot be neglected, they must be included with opportune collision terms. Alternatively, simpler descriptions can be employed to study the main properties of collective modes in plasmas, such as the single-fluid or the multiple-fluid descriptions.

According to the non-relativistic linear theory of electromagnetic wave propagation in a collision-less cold plasma [48], the electron density at which the plasma becomes opaque to a wave with frequency ω_0 (or wavelength λ_0) is known as the critical density n_c, defined as:

$$\omega_0^2 = \omega_{p,e}^2 = \frac{4\pi e^2 n_c}{m_e}. \tag{2.17}$$

In practical units, it can be approximated as $n_c[\mathrm{cm}^-3] \simeq 1.1 \times 10^{21} (\lambda_0[\mu\mathrm{m}])^2$. The responsiveness of the plasma depends on its density through $\omega_{p,e}$. The critical density plays a central role in distinguishing the different regimes of wave-plasma interaction. For plasma densities $n_e < n_c$ (or wave frequencies $\omega_0 > \omega_{p,e}$), the plasma is referred to as under-dense, and it is transparent to the electromagnetic wave. The electrons, which are considered the only mobile species, cannot follow the oscillations of the wave field, allowing the wave

to propagate almost undisturbed at nearly the speed of light. Conversely, when $n_e > n_c$ (or $\omega_0 < \omega_{p,e}$), electrons can respond to the wave field, leading to both the reflection and absorption of the wave. In this case, the plasma is called over-dense, and the electromagnetic wave is exponentially dumped within the plasma over a distance equivalent to the skin depth L_w (see 2.1.1). It is essential to note that effective energy transfer from the incident wave to the bulk of the plasma is possible only in under-dense regime. Lastly, the near-critical regime occurs when $n_e \simeq n_c$. This is an interesting and complicated regime, and the energy transfer from the wave to the plasma can still occur (see 2.3.2).
To control the interaction regime, it is important to observe that in laser-plasma experiments, the laser frequency is typically fixed by the optical setup and hardly can be tuned during laser operation. Instead, the plasma density can be quite easily changed by varying the initial material or engineering the target setup. As explained in the previous section, when a laser impinges on a solid target, it ionizes the target, making the central part of the pulse interact with an almost completely ionized, solid-density plasma. This means that if the target is solid, for example metallic, the plasma produced will be over-dense. Otherwise, if an under-dense plasma is desired, gaseous targets are typically employed. In addition, near-critical plasmas can be generated using particular materials like carbon foams, which will be presented later in this section. In conclusion, by properly choosing the target material and its density, it is possible to control the interaction regime between the laser and the generated plasma, allowing or preventing the energy transfer from the laser to the plasma, and thus controlling the outcomes of the interaction.

2.3.2. Relativistic self-induced transparency

When studying the relativistic motion of electrons in a strong transverse electromagnetic wave, this motion can modify the refractive index in a nominally over-dense plasma to permit propagation [47]. In particular, at extreme intensities ($a_0 \gg 1$), the electron inertial properties change due to relativistic motion. In other terms, the effective electron plasma frequency becomes:

$$\omega_{p,e}'^2 = \frac{\omega_{p,e}^2}{\gamma_0} = \frac{4\pi e^2 n_e}{m_e \gamma_0}, \quad \gamma_0 = \sqrt{1 + \frac{a_0^2}{2}}. \tag{2.18}$$

Therefore, the relativistically corrected critical density n_c^{rel} is defined as:

$$n_c^{\text{rel}} = n_c \gamma_0. \tag{2.19}$$

As a result, plasmas with density in the range between n_c and n_c^{rel}, which are nominally over-dense, are relativistically under-dense. This means that a high-intensity laser pulse can propagate in nominally opaque plasmas, provided that a_0 is sufficiently high, allowing also, as a consequence, for effective energy transfer from the laser to the plasma.

2.3.3. Electromagnetic radiation emission

In classical electrodynamics, accelerated charged particles emit electromagnetic radiation, influencing both the electromagnetic field and, through radiation reaction, the particle dynamics. However, this theory does not provide an exact and satisfactory theory of radiation emission, including radiation reaction. Appendix A furnishes the theoretical background for classical radiation emission theory, considering a single charged particle, and discusses its extension to a plasma. The main results derived from this theory are reported in this section. For ultra-relativistic particles, radiation is emitted almost collinear with their velocity, and the primary contribution to the emitted power comes from the perpendicular component of the force acting on the particle. In addition, for a given force, since $m_i \gg m_e$ the power emitted from ions is much lower than that from electrons, as radiation emission depends on the magnitude of the particle acceleration, which is inversely proportional to the mass. Therefore, in a plasma, where the force acting on particles, causing them to emit, is the electromagnetic force, relevant radiation is emitted from light particles, such as electrons and positrons. The radiation carries energy and momentum, and, since these quantities are conserved, emission leads to modifications in the particle energy, momentum, and consequently, its subsequent motion. Since the first phase of laser-plasma interaction is electron acceleration (see 2.3.4), which involves a large number of electrons and results in the emission of significant radiation, strongly affecting the plasma dynamics, the physics of radiation should be appropriately included in an accurate description. In the kinetic collision-less model presented in 2.1.2, the radiation fields are described by Maxwell equations, and therefore they are included in $\boldsymbol{E}$ and $\boldsymbol{B}$ appearing in the Lorentz force term, producing radiation reaction on emitting particles. It is important to underline that, in this description, only the emission, and the corresponding reaction, caused by macroscopic long-range forces are considered. Conversely, radiation emitted due to microscopic forces, such as collisions, is completely neglected in the averaged Maxwell equations, while the corresponding radiation reaction is included only in the collision term, which, in this case, is also neglected.

The classical theory is applicable when the work done by the electromagnetic force over a Compton length is much smaller than mc^2 [15] or, equivalently, when the quantum parameter χ of the emitting particle, which can be defined in both the classical theory

(see Appendix A) and its quantum counterpart (see Section 2.4.1), is much smaller than unity.

2.3.4. Electron acceleration

In this subsection, the main electron acceleration mechanisms in high-intensity laser-plasma interaction are presented, focusing on the acceleration processes that occur during the propagation of a linearly-polarized laser pulse in near-critical relativistically underdense plasmas. As mentioned in 2.1.2, in this interaction regime, thermal heating of electrons is less effective than coherent acceleration, justifying the neglect of thermal motion since the typical energy gained through coherent acceleration is much greater than the temperature [47]. These acceleration mechanisms are complex and not yet completely understood, including the conditions that lead to transition between different acceleration regimes.

To provide useful physical background, the ponderomotive force, a non-linear component of the Lorentz force, is introduced. It comes into play, for instance, when a charged particle oscillates in the field of an electromagnetic wave of frequency ω_0 with non-uniform intensity distribution in the transverse plane relative to the propagation direction. The relativistic expression for the ponderomotive force acting on a particle with charge q and mass m is given by [47]:

$$\boldsymbol{F}_p = \frac{d\boldsymbol{p}_s}{dt} = -mc^2 \frac{\partial}{\partial \boldsymbol{x}} \sqrt{1 + \frac{|\boldsymbol{p}_s(\boldsymbol{x}(t))|^2}{m^2c^2} + \frac{\tilde{a}_0^2(\boldsymbol{x})}{2}}, \quad \tilde{a}_0 = \frac{q}{mc\omega_0} \sqrt{2\frac{4\pi}{c}\bar{I}(\boldsymbol{x})}, \tag{2.20}$$

while in the non relativistic limit $\tilde{a}_0 \ll 1$, $\boldsymbol{p}_s \ll mc$:

$$\boldsymbol{F}_p = \frac{d\boldsymbol{p}_s}{dt} = -mc^2 \frac{\partial}{\partial \boldsymbol{x}} \sqrt{1 + \frac{\tilde{a}_0^2(\boldsymbol{x})}{2}} \simeq -\frac{mc^2}{4} \frac{\partial}{\partial \boldsymbol{x}} \tilde{a}_0^2. \tag{2.21}$$

Here, $\boldsymbol{p}_s$ represents the slow-varying momentum of the particle, which is essentially the particle momentum averaged over the oscillations. The magnitude of this force depends on the spatial variations of the cycle-averaged intensity $\bar{I}$, and its direction is opposite to that of the steepest increase of $\bar{I}$. Physically, the ponderomotive force pushes electrons away from regions of locally higher intensity. It is important to note that this force acts in the same way on positive and negative charges.

In plasmas, a tightly focused and ultra-short laser pulse creates strong radial and longitudinal intensity gradients over few wavelengths. Therefore, as the pulse propagates within the plasma, it pushes particles forward and radially away from itself through the ponderomotive force, leading to the emission of considerable radiation. Due to their larger

inertia, ions respond significantly more slowly than electrons. Consequently, the laser field separates electrons, causing them to accumulate at the front and lateral boundaries of the pulse, from ions, which remain almost in their initial position. This charge separation gives rise to strong electric fields between the pulse edges, where electrons are concentrated, and the inner region, predominantly populated by ions. For electrons, these fields are quasi-static since they follow the slower dynamics of the ions [49].
For under-dense plasmas and pulse duration satisfying the condition $\tau_p < 1/w_p$, the region occupied by the laser pulse forms a cavity that contains only the ions. Once the laser pulse passes, the electrons return toward the axis, behind the pulse, driven by the radial quasi-static electric field, and they become trapped in the wake of the pulse. In this region, they are accelerated by the longitudinal electric field of the plasma wave excited by the pulse itself [47, 49, 50]. This acceleration mechanism is known as Laser Wake-Field Acceleration (LWFA). In idealized LWFA, the laser pulse does not overlap or interact with the trailing trapped electrons [51].
When considering near-critical density plasmas satisfying $\tau_p > 1/w_p$, the sustained ponderomotive force prevents electrons from returning into the depleted region, making LWFA unable to form. In this regime, an ion channel, also referred to as plasma channel, is formed. In addition, the increased ponderomotive force results in a significant rise in the radiation damping force. When these forces become comparable, a significant number of electrons are transversely trapped by the laser field instead of being radially pushed away [52, 53], forming a dense bunch near the laser axis in the high-intensity region due to the action of the quasi-static electric fields. Then, the laser electric field can resonantly drive betatron oscillations of this electron bunch [50, 51], leading to the conversion of transverse momentum, gained from the laser electric field, into longitudinal momentum through the $\boldsymbol{v} \times \boldsymbol{B}$ force. This mechanism, known as Direct Laser Acceleration (DLA) [50, 54, 55], results in longitudinal electron acceleration, with the electrons gaining energy directly from the laser pulse. Moreover, the trapped electrons travel almost along the laser-axis, inducing a strong quasi-static poloidal self-generated magnetic field [52], which further pinches the electrons, causing any escaping electrons to be reinjected into the high-intensity region for further acceleration.
In conclusion, it is worth mentioning the principal electron heating mechanism occurring in over-dense plasmas [56], where the interaction between laser and electrons takes place over a distance comparable to the skin depth. The laser's electric field induces transverse oscillations in surface electrons, while the magnetic component leads to longitudinal acceleration. These accelerated electrons traveling through the plasma constitute an electric current, which is neutralized by a return current consisting of cold electrons.

2.3.5. Advanced targets: Double-Layer Target (DLT)

Double-layer targets are a novel and smart type of multi-layer target composed of a low density layer, in this work referred to as foam, which is attached to a solid metallic foil. Carbon is one possible material used for the foam, and various materials can also be chosen for the metallic substrate, in according to the desired properties and the fabrication method involved. This target has been extensively studied due to its experimentally proven performance in ion acceleration [57]. It is also the subject of theoretical and numerical investigations for the generation of other types of radiation, including radioisotopes, neutrons, and photons [57, 58]. DLT has the potential to serve as multiple-radiation source.

The carbon foam can be produced using Pulsed Laser Deposition (PLD) [59], a technique in which a nano-structured carbon layer is deposited onto the metallic substrate. The peculiarity of this technique is its ability to reach low foam densities, in the range of approximately 10^{21} cm^{-3}. This density corresponds to the critical electron density for a laser with wavelength of 0.8 μm. It is important to note that the mentioned foam density represents an average value. This is because the foams created through PLD are formed by the deposition of clusters of carbon atoms, and so they possess a nano-structure, i.e. nanometer-scale features. Therefore the density profile is not uniform, and the nano-structure can affect the physics and outcomes of laser-plasma interaction. This fact has led to an active research frontier dedicated to the study and realization of engineered targets aimed at controlling various aspects of the interaction, including laser-to-electron absorption mechanisms. PLD excels in providing control over foam density during the growth process, allowing for the realization of micrometer-scale features such as few-micron scale density gradients [60].

The conceptual scheme of a laser pulse interacting with a DLT and the cross-section view of a carbon foam are reported in Figure 2.1.

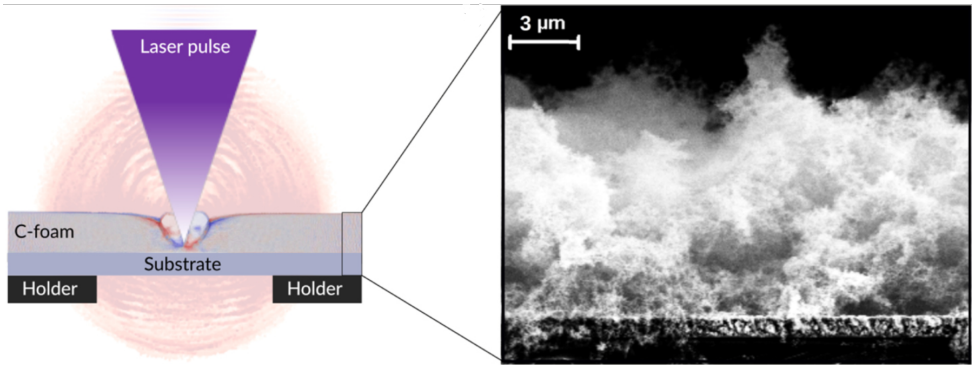

Figure 2.1: Conceptual scheme of laser interaction with a double-layer target and cross section view of a carbon foam on Ti layer [60].

The foam serves in enhancing the efficiency of high-energy electron generation. For a sufficient high-intensity laser pulse, the foam density is relativistically under-dense (see 2.3.2), allowing for the pulse propagation and energy transfer, according to the mechanisms discussed previously. However, the density is considerably higher than what is typically achieved with gaseous targets, leading to a large number of electrons available for acceleration through the mechanisms presented in 2.3.4. This results in an efficient energy conversion from the laser to electrons.
When these accelerated electrons reach the metallic substrate, they pass through the substrate and escape from the rear surface, whereas the ions remains almost in their initial position. This leads to charge separation and the subsequent generation of a strong space-charge electric field on the rear side of the DLT, which can reach extremely high values, even approaching TV/m range. It has the capability to accelerate positive charges, as ions or contaminants, present on the rear surface, resulting in their emission in the direction perpendicular to the target surface. This process is experimentally verified and is known as Target Normal Sheath Acceleration (TNSA).
Another important property of the foam is the realization of relativistic Self-Focusing (SF) of the laser pulse. As discussed in 2.3.2, during its propagation within the foam, the laser pulse induces relativistic oscillations of electrons, leading to an increase in electron inertia and a modification of the electron plasma frequency. Consequently, this results in an increase in the index of refraction n_{ref} of the plasma [56]:

$$n_{ref}^2 = 1 - \frac{w_{p,e}^2}{\gamma_0 \omega_0^2}, \quad \gamma_0 = \sqrt{1 + \frac{a_0^2(I)}{2}}, \tag{2.22}$$

where ω_0 and I represent the laser central frequency and intensity. Since the laser pulse has a Gaussian intensity distribution, γ_0 is higher in the central region and lower in the

outer ones, which is also true for n_{ref}. In addition, the ponderomotive force pushes electrons away from the central region of the pulse, resulting in a reduction of the electron density and, hence, an increase of n_{ref}. In optics, a component with such a refractive index profile acts as a converging lens. Therefore, the low-density foam acts as a lens, focusing the laser pulse. For relativistic intensities, the optical power of this "lens" overcomes the natural diffraction of the laser beam, and SF results in a reduction of the laser spot-size and, consequently, an increase in pulse intensity. Moreover, due to the SF, during propagation the intensity transverse distribution becomes increasingly peaked, enhancing more and more the focusing effect. The limit on the attainable focusing is dictated by the diffraction limit. As the lenses in optics, a focal length can be introduced, representing the distance at which the pulse reaches its minimum spot size. The SF is a very helpful mechanism for processes that require high intensity, such as NBWPP and photon emission, which will be discussed in the next section.

Considering now the substrate, it plays the important role of plasma mirror. When the laser pulse reaches the metallic foil, it cannot propagate inside because the solid-density plasma generated by the ionization of the substrate is opaque. Therefore, upon impinging on the plasma mirror, the pulse is reflected, initially overlapping with the incident one and then propagating backward. During the overlap of the incident and reflected pulses, their intensities sum up, leading to a significant boost in intensity. It is worth mentioning that plasma mirrors in the high-intensity regime are capable of compressing the laser pulse in the temporal domain, generating higher armonics associated to higher single-photon energy, and providing an additional focusing effect due to the curvature induced by the radiation pressure [61]. However, the crucial advantage of the plasma mirror for pair production is the realization of the left-handed geometry (see 1.2.2) for particles propagating in the direction of the incident laser pulse. If photons are emitted in this direction, when they interact with the reflected pulse their quantum parameter is enhanced, maximizing the probability of undergoing pair production. Also, as discussed in the following section, the LH geometry is optimal for the emission of high-energy photons from the accelerated electrons, where photons are emitted in the direction of the incident laser beam, supporting the previous argument.

To conclude, it is possible to estimate the values of the foam properties that optimize certain aspects of the interaction with a laser pulse [62]. In particular, the foam electron density which maximizes the electron mean energy at the SF focal length can be estimated as a function of the properties of the pulse:

$$\frac{n_e^{opt}}{n_{e,c}} \approx 0.91\gamma_0 \left(\frac{\lambda_0}{\sigma_p^{\mathrm{FWHM}}}\right)^2 \left(\tau_p \frac{c}{\lambda_0}\right)^{2/3} \qquad \sigma_p^{\mathrm{FWHM}} = \sqrt{2\ln 2}\,\sigma_p, \tag{2.23}$$

where σ_p is the spot size of the pulse when it impinges on the foam, $\gamma_0 = \sqrt{1 + a_0^2/2}$, and a_0 is the peak normalized potential. Then, the SF focal length can be estimated as a function of the foam electron density and laser properties:

$$L_f(n_e) \approx \sigma_p \sqrt{\gamma_0 \frac{n_c}{n_e}}. \tag{2.24}$$

When the pulse reaches this distance, the absorption mechanisms of laser energy become dominant and prevent a further focusing effect.

2.4. Quantum processes in laser-plasma interaction

In this section, the quantum theory of high-energy photon emission is discussed. Firstly, the single-particle picture is presented, followed by the contextualization of this process and of NBWPP within laser-plasma interaction in DLT. Lastly, an overview of the current research frontier in laser-plasma systems for pair production is provided, with particular focus on the various setups explored and the potentialities of the DLT.

2.4.1. High-energy photon emission

As the strength of the electromagnetic force and the energy of the emitting particles increase significantly, the quantum effects become important and cannot be neglected. In these conditions, the emitted radiation energy becomes a significant fraction of the initial energy of the emitting particle, resulting in a strong radiation reaction. As a result, the stochastic nature of radiation emission emerges, making it a discontinuous process. Emission processes involve the creation of particles, specifically quanta of the electromagnetic field, known as photons. Therefore, its correct description must be performed in the framework of QED, as well as NBWPP. Depending on the type of electromagnetic field causing the emission, the two relevant QED emission processes in laser-plasma interaction are Non-linear Inverse Compton Scattering (NICS) and bremsstrahlung. In the following, as justified in 2.4.2, these two processes are considered, with the focus on NICS. Also, the emission by an electron is considered, but the description applies also for positrons.
When energetic electrons interact with the electrostatic Coulomb field of heavy nuclei, they can emit high-energy photons in a process known as Bremsstrahlung. This mechanism becomes significant and cannot be neglected when heavy elements with large atomic number and high-density targets are involved. Under these conditions, Bremsstrahlung becomes an important source of photons.
In NICS, which Feynman diagram is reported in Figure 2.2, a charged particle emits a

photon due to the action of a strong external electromagnetic field. It is the quantum counterpart of classical synchrotron radiation emission (see Appendix A). Similarly to NBWPP, in NICS the emitting electron absorbs many background photons during the emission process, leading to a strongly non-linear dependence on the amplitude of the background field. It is worth mentioning that in the exact description of NICS [15], accounting for the correct angular distribution of the emitted photon, energy and momentum conservation is derived from first principles, leading to an exact treatment of radiation reaction, in contrast to the classical theory. As with NBWPP, the quantum parameter χ_e of the emitting electron governs NICS:

$$\chi_e = \frac{\mathcal{E}_e}{E_s m_e c^2}\sqrt{\left(\boldsymbol{E}+\frac{\boldsymbol{v}}{c}\times\boldsymbol{B}\right)^2-\left(\frac{\boldsymbol{v}\cdot\boldsymbol{E}}{c}\right)^2} \approx \frac{\mathcal{E}_e}{E_s m_e c^2}\frac{F_{\perp,e}}{e} \tag{2.25}$$

Here, E_s stands for the Schwinger field, $\mathcal{E}_e$ is the energy of the emitting electron, and the approximated expression holds when $\mathcal{E}_e \gg m_e c^2$. All the properties of χ discussed in 1.2.2, including the importance of the geometry and the distinction between left-handed and right-handed configurations, also apply to NICS. Analogously to the classical theory, the relevant component of the force for emission is the perpendicular one. It is possible to define the quantum parameters of the photon emitted χ_γ, as made in 1.2.2, and of the electron after the emission χ'_e, which are related to χ_e by the exact conservation law [15]:

$$\chi_e = \chi_\gamma + \chi'_e. \tag{2.26}$$

The probability per unit time per unit photon quantum parameter for an electron to emit a photon with quantum parameter χ_γ, or in other words the NICS probability rate spectrum, is given by ([15], elaborated):

$$\frac{d^2N_\gamma}{d\chi_\gamma dt} = \frac{\alpha_f}{\pi\sqrt{3}}\frac{\left(m_e c^2\right)^2}{\hbar\mathcal{E}_e\chi_e}\left[\int_y^\infty K_{5/3}(s)ds + \frac{\chi_\gamma^2}{\chi_e(\chi_e-\chi_\gamma)}K_{2/3}(y)\right] \equiv \frac{\alpha_f}{\pi\sqrt{3}}\frac{\left(m_e c^2\right)^2}{\hbar\mathcal{E}_e\chi_e}\mathcal{F}(\chi_e,\chi_\gamma) \tag{2.27}$$

where $y = 2\chi_\gamma/[3\chi_e(\chi_e-\chi_\gamma)]$. The theoretical framework and the hypotheses involved are the same as for NBWPP (see 1.2.3). This explains why the probability rate spectra of NBWPP and NICS share a very similar form. The total probability rate for NICS is expressed as follows [63]:

$$\frac{dN_\gamma}{dt} = \int_0^{\chi_e}\frac{d^2N_\gamma}{d\chi_\gamma dt}d\chi_\gamma = \frac{\alpha_f}{\pi\sqrt{3}}\frac{\left(m_e c^2\right)^2}{\hbar\mathcal{E}_e\chi_e}g(\chi_e), \tag{2.28a}$$

$$g(\chi_e) = \int_0^{\chi_e} \left[\int_y^{\infty} K_{5/3}(s)ds + \frac{\chi_\gamma^2}{\chi_e(\chi_e - \chi_\gamma)} K_{2/3}(y) \right] d\chi_\gamma. \tag{2.28b}$$

If the assumption of ultra-relativistic particles and collinear emission is introduced, the following approximated relations can be derived [18]:

$$\mathcal{E}_\gamma \simeq \mathcal{E}_e \frac{\chi_\gamma}{\chi_e}, \quad \mathcal{E}_e \simeq \mathcal{E}_\gamma + \mathcal{E}_e' \quad \rightarrow \quad \frac{d^2 N_\gamma}{d\mathcal{E}_\gamma dt} \simeq \frac{\chi_e}{\mathcal{E}_e} \frac{d^2 N_\gamma}{d\chi_\gamma dt} \tag{2.29}$$

The collinearity of the emission when particles are ultra-relativistic is also justified in the classical theory or radiation. Both the spectrum, in particular the mean photon energy, and the total probability are governed by χ_e. Therefore, the optimization of the geometry to achieve the left-handed configuration is crucial to maximize high-energy photon emission, which is required for NBWPP. In conclusion, it can be shown that the classical theory of synchrotron radiation is retrieved in the limit $\chi \to 0$.

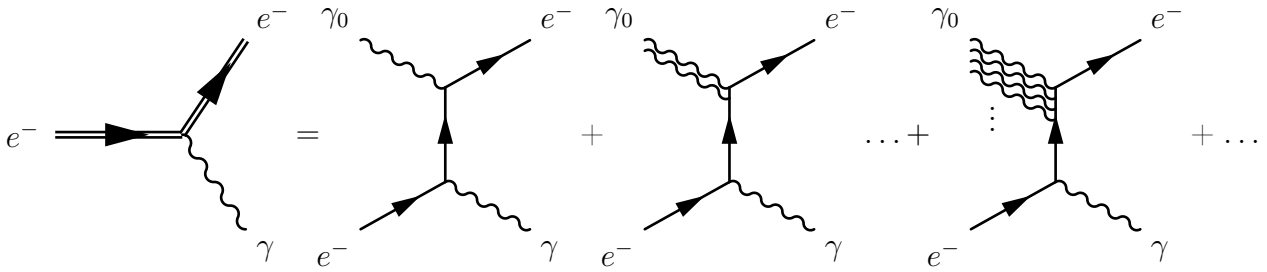

Figure 2.2: Feynman diagram of non-linear inverse Compton scattering. The electron, absorbing many background photons γ_0, emits a photon γ [15].

2.4.2. NBWPP and high-energy photon emission in laser-plasma interaction with DLT

In laser-plasma interaction, the dominant mechanisms of photon emission are NICS and bremsstrahlung. Photons emitted by atomic recombinations or disexcitations can be disregarded because, in strongly or fully ionized plasmas, particles are predominantly in free particle states. Similarly, photons emitted by nuclear processes, such as nuclear disexcitations, and by electron-positron annihilation [20], are not considered due to their relatively low probability. Consider now bremsstrahlung in DLTs. While carbon foams are characterized by low density and a have low atomic number, resulting in a small probability of emission, bremsstrahlung can still occur when accelerated electrons pass through the dense metallic substrate [64], which can have a high atomic number. However, within the scope of this thesis work, bremsstrahlung is not taken into account. This is because the study primarily concerns NBWPP, which takes place in the laser field and not

in the substrate. The photons relevant for NBWPP are those capable of interacting with the laser field, such as photons produced by NICS, which also occurs in the laser field. It is worth mentioning that photons produced by bremsstrahlung in the substrate can undergo pair production through the Bethe-Heitler process (see 1.2.1) producing additional pairs. Appendix B provides some hints on a possible approach to formally incorporate NICS and NBWPP in the kinetic description of the plasma [63] (elaborated).
Consider now the mechanisms in laser-plasma interaction that lead to photon emission and pair production. To generate photons through NICS and pairs through NBWPP exploiting the laser field, energetic electrons are required. In a full-optical configuration, where the plasma is the only source of electrons, excluding external electron beams, the laser field also has to accelerate these electrons. The relevant mechanisms of electron acceleration in high-intensity laser-plasma interaction are discussed in 2.3.4. Electrons reaching the largest energies are located within the high-intensity region of the laser pulse, where they interact with the laser field, and co-propagate with the laser pulse. In this region, electrons oscillate in the laser field and continuously experience the transverse forces exerted by the laser electric and magnetic fields. This leads to the emission of a significant amount of photons through NICS. However, this configuration is not optimal for the generation of high-energy photons, since the fields and the electron velocity form a RH tern (see 1.2.2). The emitted photons are not expected to be capable of efficiently producing pairs, because they would not be so energetic and, since they are emitted almost collinearly with electrons, they in turn form a suboptimal geometry with the laser field. It is important to highlight that the geometry has a "squared" impact on NBWPP, because it influences both the photon emission and the photon conversion steps. Therefore, to efficiently produce positrons, the interaction of the accelerated electrons with the laser field must occur in a LH geometry, producing photons that, in turn, realize the same optimal geometry. One possibility to achieve this is by reflecting the laser pulse after a certain propagation distance. This is accomplished in DLT using the substrate plasma mirror (see 2.3.5). In addition, photons emitted by the accelerated electrons interacting with the reflected pulse are not expected not to be aligned with the laser optical axis. As reported in Figure 2.3, these photons form a certain small angle, which depends on laser and target properties. The reason is that electrons undergo betatron oscillations in the laser field, and at the moment of the emission their momentum direction, as well as the one of emitted photons, is not horizontal. In conclusion, since pairs are also emitted collinearly, the positron distribution, at least at the moment of their generation, will be similar to that of photons. A diagram illustrating the entire laser-DLT interaction, showing the generated photons and pairs, is presented in Figure 2.4.

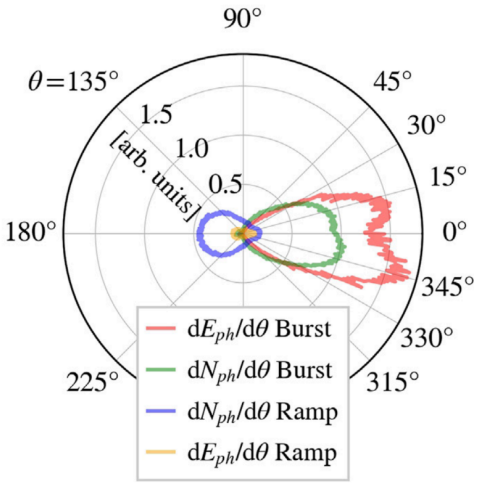

Figure 2.3: Angular distribution of the emitted photon number and photon energy in DLT. "Burst" refers to photons produced by electrons interacting with the reflected laser pulse, while "Ramp" to photons produced during the electron acceleration phase [58].

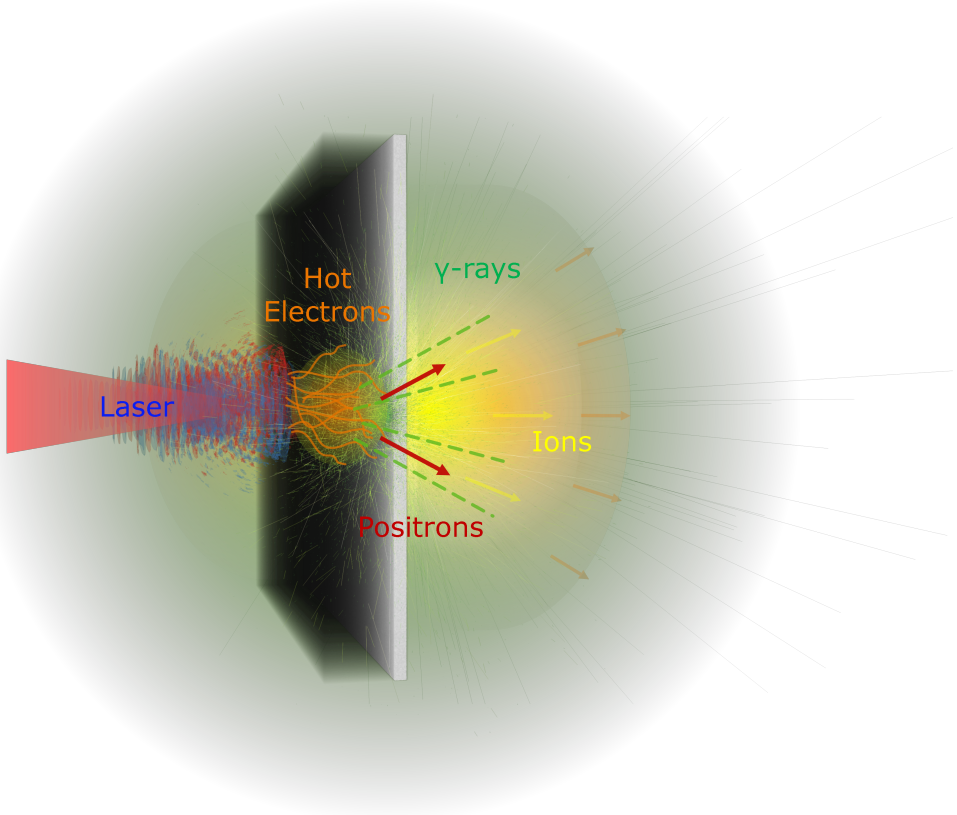

Figure 2.4: Diagram illustrating the phases of laser-DLT interaction: laser impinging on the DLT, electron acceleration, photon emission, and positron production. The diagram indicates the directions of emission for photons and positrons. Additionally, it depicts the ions from the target's rear surface being accelerated by target normal sheath acceleration.

2.4.3. Laser-driven sources and NBWPP: overview of the setups and potential of DLT

Different setups, employing various mechanisms to accelerate electrons and generate photons and positrons, have been proposed in the last two decades. As a consequence, the characteristics of the produced positrons can vary significantly. Some setups have been experimentally validated, while others are currently under investigation through computational simulations (see Chapter 3), as they require laser intensities that are not available nowadays.

Firstly, the setups involving bremsstrahlung to produce photons and the Bethe-Heitler pair production are presented. The experimental work presented in [41] involves the acceleration of electrons through LWFA in a 20 mm wide gas jet employing a laser pulse with $\tau_p = 40$ fs, $\sigma_p = 27$ μm and $I^{peak} = 3 \times 10^{19}$ W/cm^2 ($a_0 = 4$). The resulting electron beam, with a maximum energy of 600 MeV, impinges on a Pb solid target, initiating an electromagnetic shower. Various converter thicknesses t are studied. A maximum positron energy of 600 MeV is achieved for $t = 5$ mm and a maximum positron yield of 10^9 is obtained for $t = 10$ mm. The low divergence ($\theta \sim 10 - 20$ mrad) leptonic beam exiting from the converter consists of electrons and positrons, and reaches a peak density of 10^{16} cm^{-3}. The positron spectrum, which monotonically increases toward lower energies, and the percentage of positrons, ranging from 10% at $t = 5$ mm to 50% above $t = 25$ mm, are reported in Figure 2.5. Another experimental work, described in [65], involves a long and kJ-energy pulse with $\tau_p \sim$ ps, $\sigma_p \sim \mu$m and $I^{peak} = 10^{19} - 5 \times 10^{20}$ W/cm^2 ($a_0 = 3 - 19$), striking a 1 mm thick solid gold target. Here, an oblique laser incidence is employed to optimize the electron acceleration. The positron yield falls in the range $10^{10} - 10^{11}$, with a divergence of $17° - 25°$, and an energy conversion efficiency from laser to ejected positrons of $0.01\% - 0.04\%$. Positrons are accelerated through the TNSA mechanism, resulting in an almost mono-energetic spectrum peaking at $3 - 19$ MeV. In the first work, the laser sole role is to accelerate electrons, while in the second one, it serves also to accelerate positrons.

A remarkable scheme is presented in [66], where a GeV electron beam, produced by LWFA, impinges on a thin converter producing photons through bremsstrahlung up to GeV energies. The photons that do not undergo pair production escape from the converter and interact with a counter-propagating laser pulse, undergoing NBWPP. Using a laser pulse with $\tau_p = 40$ fs, $\sigma_p = 4$ μm, and $I^{peak} = 2 \times 10^{21}$ W/cm^2 ($a_0 = 30$), a positron yield of 5×10^3 per pico-Coulomb of primary electrons is obtained.

In the following, the setups exploiting NICS and NBWPP are treated. The numerical study presented in [21] considers a pulse with $\tau_p = 30$ fs, $\sigma_p = 1$ μm and $I^{peak} =$

4×10^{23} W/cm^2 ($a_0 = 485$), striking 1 μm thick aluminum foil. Positrons are produced during the hole-boring of the pulse into the target and, before escaping, are accelerated by TNSA. The result is a total yield of 10^{10} positrons with average energy of 320 MeV and peak density of 10^{20} cm^{-3}. The laser-positron energy conversion efficiency is 0.01 %. The solid target reflects the laser pulse, doubling the intensity and realizing the optimal geometry for photon and positron emission. Similar setups are presented in the theoretical works [67], where oblique incidence and lower intensity ($\sim 10^{22}$ W/cm^2) are employed, and [68], where the solid target is irradiated symmetrically from both sides by two laser beams. The former investigates the impact of the pre-plasma, a low density layer preceding the solid-density plasma and produced using a pre-pulse, on electron acceleration. The latter uses two-sided irradiation to achieve symmetric compression of the target, confining the solid-density plasma and increasing its reflectivity.

A different approach is investigated using simulations in [13], where a laser pulse with $\tau_p = 30$ fs, $\sigma_p = 3$ μm and $I^{peak} = 2 \times 10^{23}$ W/cm^2 ($a_0 = 384$), propagates in a 30 μm thick Near-Critical Density (NCD) Al plasma, exploiting relativistic transparency. Electrons are accelerated up to 1 GeV and emit photons during their betatron oscillations. Positrons, which are produced in the pulse high-intensity region, are accelerated by DLA similarly to electrons. They are obtained with a total yield of 4×10^{14}, peak density of 3×10^{20} cm^{-3}, a divergence angle of 22°, and a monotonically decreasing spectrum up to the cut-off energy of 1 GeV. This setup does not exploit the reflection of the laser pulse, and the interaction geometry of electrons and photons with the laser field is suboptimal.

In the simulation-based study [52], a 50 μm thick NCD target is irradiated from both sides using two pulses of $I^{peak} = 3 \times 10^{22}$ W/cm^2 (a0=150), $\tau_p = 40$ fs and $\sigma_p = 5$ μm. In this case, the optimal geometry is realized by colliding the electrons accelerated by one pulse with the second, counter-propagating, pulse. Positrons are characterized by a total yield of 10^{11}, peak density of 4×10^{22} cm^{-3}, and a laser-positron energy conversion of 0.14 %. Their spectrum, which decreases almost linearly, extends up to the energy of 1.6 GeV.

The last kind of setups, which includes the DLT, involves both a NCD medium and a solid target. The theoretical works [27, 69, 70] consider a laser pulse impinging on a $20 - 40$ μm thick NCD plasma, produced using a gas-jet, and accelerating electrons up to GeV levels during propagation. The laser pulse is then reflected by a $4 - 5$ μm thick metallic layer, providing the optimal geometry for the accelerated electrons to efficiently generate energetic photons and positrons. A laser pulse with $\tau_p = 15 - 30$ fs, $\sigma_p = 3$ μm, and $I^{peak} = 2 - 5 \times 10^{23}$ W/cm^s ($a_0 = 270 - 581$) is employed. Positrons are generated with total yield of $\sim 10^{10}$ and an almost linearly decreasing spectrum with peak energy of $200 - 300$ MeV and cutoff energy of $1 - 3$ GeV. The reported laser-to-positrons energy

conversion efficiencies are $-, 0.035, 0.2\,\%$, respectively. In addition, the first study reports a positron peak density of 6×10^{21} cm^{-3}. In these works, the solid target is too thick to allow for TNSA, so positrons are not accelerated forward but are instead trapped by the reflected laser pulse and accelerated backward by DLA. It is worth mentioning that a few studies, as [71], investigate the possibility of improving the electron acceleration through an engineered nano- or micro-structure of the NCD layer.

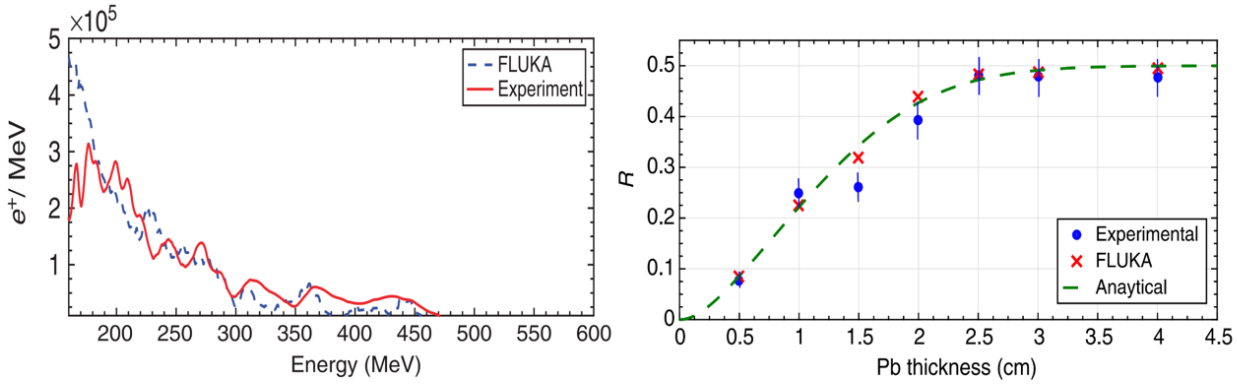

Figure 2.5: The simulated (FLUKA) and experimental positron spectra (left), along with the percentage in the leptonic beam (right), from the LWFA + converter setup presented in [41].

3 | Numerical modeling of NBWPP in Laser-Plasma interaction

Dealing with plasma physics involves tackling complex problems that cannot be solved analytically, except in very basic cases or through strong approximations. For example, in the Maxwell-Vlasov plasma description, the unknowns are the distribution functions, which are defined in the six dimensional phase space, and evolve in time according to a set of coupled and strongly non-linear partial differential equations. Things become even more challenging when QED processes, collisions, or ionization physics are included. These complexities can only be addressed through computational simulations, leveraging the capabilities of computers to handle large amounts of data and perform operations quickly. Simulations essentially implement the equations of interest translated into a series of simpler operations, like multiplications and additions. Unlike experiments, simulations offer the advantage of monitoring the physical system during its evolution, allowing for a deeper understanding of the processes that occur. Furthermore, simulations provide access to comprehensive information without the limitations imposed by the instrumentation required for diagnostics in experiments. Moreover, simulations enable deep understanding of experimental results. Lastly, simulations allow for the exploration of scenarios not yet achievable through experiments and the interpretation. For all these reasons, computer simulations have acquired significant attention in the past and have played an essential role in the development of plasma theory. In addition, they are indispensable tools for investigating and designing various plasma physics applications, such as laser-plasma particle accelerators or fusion reactors. Today, scientific research in this field is highly active in multiple areas, including the massive parallelization of codes for high-performance computers and the implementation of new physical processes.

In the specific case of this thesis work, simulations are essential for studying NBWPP in laser-plasma interaction, mainly because the process involves several intermediate steps, a large number of particles, and the electromagnetic field. The particle-in-cell (PIC)

method that provides a kinetic description of the plasma is considered. In this chapter the central aspects of PIC codes are explained, including their working principles and the implementation of relevant processes.

3.1. Particle-In-Cell (PIC) method for non-quantum plasmas

In this section, a brief overview of the working principles of PIC codes is presented, with the focus on the standard or classical PIC codes, excluding QED processes, which will be addressed in the following section. The main reference textbooks for this section are [72], [73], [74] and [75], which contains valuable insights into the physics behind PIC codes and also numerical aspects. The section discusses the physical equations that are solved, while refer to Appendix C for the discretization procedure of the equations and structure of the PIC algorithm.

3.1.1. PIC approach to Vlasov-Maxwell problem

To provide a kinetic collision-less description of the plasma using a computational algorithm, the system of Vlasov-Maxwell equations should, in principle, be solved. One of the currently available numerical approaches to address this problem is the PIC method. The advantages of this method include its capability to straightforwardly implement both classical mechanics and quantum stochastic processes [20].
A grid representing the spatial domain of the problem is introduced, upon which the electromagnetic field is computed. This means that instead of dealing with fields, the values of the fields evaluated at the grid points are considered, and their evolution according to Maxwell equations is studied. On the other hand, plasma populations are not treated by computing distribution functions on the grid, but they are described by a set of computational particles that move on the grid. In other terms, while an Eulerian approach is used for the electromagnetic field, a Lagrangian approach is used for particles. In particular, the distribution function of each population is sampled using a collection of macro-particles, which are computational objects representing a large number of real particles. Each macro-particle can be considered as a bunch of real particles, and the PIC method studies the dynamics of the plasma by considering the evolution in time of these bunches. Macro-particles are not point-like but have a certain spatial shape and, therefore, a finite extension. The finite size of macro-particles also helps prevent undesired numerical noise. Given the position $\boldsymbol{x}_{p,a}$ of a certain "p" macro-particle of "a" population,

its extensive properties, such as charge, are distributed in space according to a certain shape function $S(\boldsymbol{x}-\boldsymbol{x}_{p,a})$, which is centered on $\boldsymbol{x}_{p,a}$ and normalized to unity. In addition, all real particles in each bunch have same momentum. This can be justified by the averaging procedure of the kinetic description: the dynamics of the macro-particles determine the average properties of the plasma, while the microscopic fluctuations, associated to the motion of the real particles within each bunch, are filtered out. Therefore, given the momentum $\boldsymbol{p}_{p,a}$ and the position $\boldsymbol{x}_{p,a}$ of each macro-particle, the distribution function f_a is replaced by the expression:

$$f_a(\boldsymbol{x},\boldsymbol{p},t) \to \sum_{p}^{N_a} w_{p,a} S(\boldsymbol{x}-\boldsymbol{x}_{p,a}(t))\delta(\boldsymbol{p}-\boldsymbol{p}_{p,a}(t)), \tag{3.1}$$

where N_a is the number of macro-particles introduced for the a-population, δ is the Dirac delta function, and $w_{p,a}$, known as macro-particle weight, is the number of real particles that the macro-particle represents. Then, from Vlasov equation it is obtained that the evolution in time of each macro-particle is dictated by the relativistic Newton equation of motion, where the force term is the average of the Lorentz force over the macro-particle extension, using the shape function as weight:

$$\begin{cases} \dfrac{d\boldsymbol{x}_{p,a}(t)}{dt} = \dfrac{\boldsymbol{p}_{p,a}(t)}{m_a\gamma_{p,a}(t)} \\ \dfrac{d\boldsymbol{p}_{p,a}(t)}{dt} = q_a \displaystyle\int S(\boldsymbol{x}-\boldsymbol{x}_{p,a}) \left[\boldsymbol{E}(\boldsymbol{x},t) + \frac{\boldsymbol{p}_{p,a}(t)}{m_a\gamma_{p,a}(t)c} \times \boldsymbol{B}(\boldsymbol{x},t)\right] d\boldsymbol{x}, \end{cases} \tag{3.2}$$

where q_a is the macro-particle charge and $\gamma_{p,a}(t) = \sqrt{1+(|\boldsymbol{p}_{p,a}(t)|/m_a c)^2}$ is the Lorentz factor. For photons, $q_a = 0$ and therefore their momentum remains constant and they propagate along straight lines according to:

$$\frac{d\boldsymbol{x}_{p,\gamma}(t)}{dt} = c\frac{\boldsymbol{p}_{p,\gamma}}{|\boldsymbol{p}_{p,\gamma}|}. \tag{3.3}$$

The fields on the macro-particle extension are interpolated from their values on the grid. Then, the charge and current density fields, which are the source terms in Maxwell equations, are calculated as follows:

$$\rho(\boldsymbol{x},t) = \sum_{a=1}^{N} q_a \sum_{p=1}^{N_a} w_{p,a} S(\boldsymbol{x}-\boldsymbol{x}_{p,a}(t)) \tag{3.4a}$$

$$\boldsymbol{J}(\boldsymbol{x},t) = \sum_{a=1}^{N} q_a \sum_{p=1}^{N_a} w_{p,a} S(\boldsymbol{x} - \boldsymbol{x}_{p,a}(t)) \frac{\boldsymbol{p}_{p,a}(t)}{m_a \gamma_{p,a}(t)}, \tag{3.4b}$$

where N is the number of populations. These fields are then projected on the grid for solving Maxwell equations.

3.1.2. Emission of electromagnetic radiation in PIC codes

As discussed in Section 2.3.3, the classical description of radiation emission is included within the Maxwell-Vlasov system of equations and, therefore, should be incorporated into the PIC method. However, the spatial domain is discretized, imposing a limitation on the minimum radiation wavelength (or an upper limit to the spectral range) that can be resolved from the Maxwell solver. As a result, electromagnetic radiation with wavelengths equal to or larger than the spatial resolution of the grid is accounted for, while higher frequency components, even in the classical regime, are neglected. Moreover, it is not possible to arbitrarily decrease the grid spacing because the computational cost of the simulation becomes unsustainable. Consequently, an additional physics module is required to correctly simulate the emission of radiation at higher frequencies. In addition to the necessity of a quantum description for radiation emission when quantum effects become non-negligible, the implementation of an additional module for quantum treatment allows for the removal of limitations on high-frequency components of the emitted radiation. Also, the quantum model provides an accurate description of radiation reaction, in the limit of the approximations involved. Furthermore, the quantum description of emitted radiation is necessary to describe NBWPP. Therefore, a dual description of the electromagnetic field is introduced, separating low-frequency components, as the laser field, which are treated by the Maxwell solver, from high-frequency components, as the emission of gamma-rays, that are treated by the additional emission module. This separation is possible due to the wide frequency gap between the radiation characterizing the laser field and plasma dynamics compared to the frequencies emitted in NICS, preventing overlap between the two regimes of interest. However, an overlap at low frequencies is inevitable because both the emission of low frequency components in NICS is theoretically possible, and electrons emitting photons are still a current contribution in the Maxwell equations. Therefore, these electrons are treated as both sources of photons and sources of low-frequency electromagnetic radiation. Nevertheless, this energy deposition in the low-frequency electromagnetic field is negligible and does not significantly affect the simulation [20]. It is worth mentioning that the emission of low-frequency components via NICS can be avoided by appropriately selecting the triggering conditions for the additional module during the simulation.

As mentioned previously, the PIC approach allows for a straightforward implementation of single-particle stochastic processes. The implementation of the additional Monte-Carlo modules for NICS, along with NBWPP, is detailed in the next section.

3.2. PIC method with Monte Carlo (MC) module

Monte Carlo methods are computational algorithms used to simulate stochastic processes such as scattering events, nuclear reactions, photon emission, and more. They are widely employed in physics, engineering and mathematics. These methods rely on repeated random sampling to obtain numerical results and statistical properties of various phenomena [76]. In physics, random sampling is employed to determine the occurrence of a particular process, which is characterized by a probability distribution depending on physical quantities. MC methods are capable of handling problems with numerous coupled degrees of freedom. The fundamental physical model, including interaction mechanisms, is determined by cross-sections. They provide information about the probability of physical processes, the secondary particles produced, the mean free-paths between consecutive interactions, energy loss, angular deflection, and more. Based on this information, particle histories can be generated using suitable sampling methods. By generating a large number of particle histories and averaging over them, quantitative information about the behaviour of particles are obtained.
In PIC codes, MC modules are incorporated to describe physical phenomena that are not accounted by the Vlasov-Maxwell description, such as photon emission, pair production or collisions. In addition, the MC approach aligns well with the quantum, stochastic, nature of high-energy photon emission and NBWPP. Furthermore, integrating MC modules into a PIC code keeps the benefits of the PIC method, such as handling a large number of particles and accurately simulating collective particle behaviour and the self-consistent field. The implementation of MC modules in PIC codes is natural because both adopt the particle approach. In other words, it is natural to perform MC calculations on the macro-particles considered by the PIC algorithm. During each iteration, the MC module determines whether a macro-particle undergoes a specific process. If the process occurs, the module calculates the effect on the macro-particle itself and the properties of the secondary particles produced, through random sampling.
In the following, the implementation of MC modules for high-energy photon emission and NBWPP in PIC-QED codes is discussed. The references for this section are [63], [77], [19] and [20].

3.2.1. MC approach for quantum processes

To simulate quantum processes for macro-particles through the MC module, the probability rates and spectra of the single-particle description are considered. However, the MC module actually does not simulate single-particle processes, since each macro-particle is representative of many real particles. Instead, the MC module involves many particles in each interaction, with each of them having the same probability of undergoing a specific process and, if the process occurs, each one produces the same final state, with the same secondary particles with identical properties. In other terms, an individual macro-particle undergoing a certain process is representative of many real particles undergoing the same process and leading to the same final state. The number of particles involved in each event is equal to the number of particles represented by the initial macro-particle. For photon emission, if a macro-electron (or macro-positron) emits, the macro-photon emitted has a statistical weight, since it represents the sum of the emissions from a large number of real electrons (or positrons). For NBWPP, each macro-photon converts into a macro-positron and macro-electron pair, representing the conversion of many photons into the same electron-positron state.

Consider now the MC procedure for simulating, for a given population, a specific quantum process, characterized by a total probability rate $dN/dt(t) \equiv \lambda(t)$ and spectrum $d^2N/d\chi_s dt$. The objective is to determine, for each macro-particle, if and when this process occurs, along with the quantum parameter χ_s of the secondary particle produced, with $s = e^+/\gamma$. The initial step is to calculate the time interval t between two occurrences, which follows the probability distribution function given by:

$$p(t) = \lambda(t)e^{-\tau(t)}, \quad \tau(t) = \int_0^t \lambda(t')dt', \tag{3.5}$$

where the quantity $\tau(t)$ is known as optical depth. The time t is obtained by sampling this distribution function using the inverse-transform method. This method relies on the fact that, regardless of the shape of $p(t)$, the probability distribution function of the values of its cumulative $P(t)$ is uniform and equal to 1 in the interval $P \in [0, 1]$. Consequently, if ϕ represents random numbers uniformly distributed in $[0, 1]$, the values of $\bar{t} = P^{-1}(\phi)$ are distributed according to $p(t)$. In other terms, sampling a number ϕ from a uniform distribution in $[0, 1]$ and setting $t = P^{-1}(\phi)$ is equivalent to sampling the number t from $p(t)$. The cumulative of $p(t)$, which represents the probability that the next event occurs before or at the time t, is defined as:

$$P(t) = \int_0^t p(t')dt' = 1 - e^{-\tau(t)}. \tag{3.6}$$

Therefore, to sample the time t at which the next event occurs, a number ϕ is generated from a uniform distribution in $[0, 1]$, and it is set such that $P(t) = \phi$:

$$P(t_f) = 1 - e^{-\tau(t_f)} = \phi \quad \rightarrow \quad \tau(t_f) \equiv \tau_f = \int_0^{t_f} \lambda(t')dt' = -\ln(1-\phi), \tag{3.7}$$

where t_f and τ_f indicates the time instant and the corresponding optical depth at which the next process takes place.
For a given population involved in a specific quantum process, the MC module assigns to each macro-particle the final optical depth τ_f, computed as described, and an incremental optical depth τ^n, initialized equal to zero. This step is performed at the beginning of the simulation and after every occurrence of the process (if the particle does not disappear in the process, as for the photon in NBWPP). Subsequently, at each time step, after the field interpolation and before the particle pusher, the incremental optical depth of each macro-particle is updated using a first-order Eulerian integration scheme:

$$\tau^{n+1} = \tau^n + \lambda(t_n)\Delta t = \tau^n + \frac{dN}{dt}(t_n)\Delta t. \tag{3.8}$$

The increment of the optical depth is determined by the probability rate, which depends on the instantaneous macro-particle energy $\mathcal{E}^n$ and quantum parameter χ^n. The latter is computed as:

$$\chi^n = \frac{\mathcal{E}^n}{E_s m_e c^2} \sqrt{\left(\boldsymbol{E}^n(\boldsymbol{x}_p^n) + \frac{\boldsymbol{v}^n}{c} \times \boldsymbol{B}^n(\boldsymbol{x}_p^n)\right)^2 - \left(\frac{\boldsymbol{v}^n \cdot \boldsymbol{E}^n(\boldsymbol{x}_p^n)}{c}\right)^2}. \tag{3.9}$$

Typically, the rate is not calculated at every time step using the analytical formulas eqs. (1.5a) and (2.28a) presented in the previous chapters. Instead, it is obtained by interpolating tabulated values. This is done to avoid computationally expensive calculations, including integrations. Specifically, the functions $T(\chi_\gamma)$ and $g(\chi_e)$, introduced previously, are precomputed and stored for a discrete set of χ values. The values of these functions for arbitrary χ are obtained through interpolation of the precomputed values.
When the incremental optical depth τ^n reaches the final one τ_f, the process occurs, and the secondary macro-particles are initialized. To determine their energy and momentum, their quantum parameter is required. In particular, χ_s is calculated by appropriately sampling the probability rate spectrum $d^2N/d\chi_s dt$ of the considered process, which depends on the emitting particle quantum parameter χ^n. The sampling is performed using the inverse-transform method. Therefore, the cumulative distribution function, representing the probability of emitting a secondary particle s with quantum parameter up to a value

χ_s, is defined as:

$$F(\chi^n, \chi_s) = \frac{\int_0^{\chi_s} \frac{d^2N}{d\chi_s dt} d\chi_s}{\int_0^{\chi^n} \frac{d^2N}{d\chi_s dt} d\chi_s} = \frac{\int_0^{\chi_s} \{\mathcal{F}, \mathcal{G}\}(\chi^n, \chi_s) d\chi_s}{\int_0^{\chi^n} \{\mathcal{F}, \mathcal{G}\}(\chi^n, \chi_s) d\chi_s}, \tag{3.10}$$

where $\mathcal{F}$ is chosen for photon emission, whereas $\mathcal{G}$ for NBWPP. Then, another random number ϕ is sampled from a uniform distribution in $[0, 1]$, and the quantum parameter χ_s is computed by inverting $F(\chi^n, \chi_s) = \phi$. Typically, also the values of $F(\chi^n, \chi_s)$ are tabulated.

From χ_s, the energy and momentum of the secondary particles can be evaluated. In conclusion, if the initial macro-particle survives, its momentum, energy, and optical depths are updated, otherwise the macro-particle is removed. These last steps are different for photon emission and pair production, and they will be detailed in the following subsection.

3.2.2. Implementation of photon emission and NBWPP

The considered photon emission process is non-linear inverse Compton scattering, which is discussed in 2.4.1, and the emitting populations involved are electrons and positrons. For each macro-particle of these populations, when the optical depth reaches its final value τ_f, a photon emission event occurs. A macro-photon with the same position and weight as the emitting macro-particle is created. In PIC-QED codes, it is possible to account for the back reaction on the emitting particle without actually creating the photon, in order to reduce the computational cost. The quantum parameter of the macro-photon χ_γ is sampled according to eq. (3.10). The energy $\mathcal{E}_\gamma$ and momentum $\boldsymbol{p}_\gamma$ are evaluated under the assumption of ultra-relativistic particles and, hence, collinear emission, according to the approximated expression given by eq. (2.29):

$$\mathcal{E}_\gamma = \mathcal{E}_e \frac{\chi_\gamma}{\chi_e}, \quad \boldsymbol{p}_\gamma = \frac{\mathcal{E}_\gamma}{c} \frac{\boldsymbol{p}_e}{|\boldsymbol{p}_e|} \tag{3.11}$$

where χ_e, $\boldsymbol{p}_e$, $\mathcal{E}_e$ are the quantum parameter, momentum, and energy of the emitting particle. Then, the back reaction on the emitting particle is considered. Its momentum, which decreases in magnitude by the photon momentum, is updated as follows:

$$\boldsymbol{p}_e^f = \boldsymbol{p}_e - \boldsymbol{p}_\gamma = \left(1 - \frac{\mathcal{E}_\gamma}{|\boldsymbol{p}_e| c}\right) \boldsymbol{p}_e, \tag{3.12}$$

where $\boldsymbol{p}_e$ and $\boldsymbol{p}_e^f$ are the initial and final momentum of the emitting particle. Although momentum is conserved in the process, the energy is not conserved (see 1.2.3). In particular, the previous equation implies that a small amount of energy is extracted from the laser field during photon emission, and this extracted energy is neglected in the dynamics of the laser field. The following relation can be shown:

$$|\boldsymbol{p}_e^f|^2 = \left(1 - \frac{|\boldsymbol{p}_\gamma|}{|\boldsymbol{p}_e|}\right)^2 |\boldsymbol{p}_e|^2 \quad \rightarrow \quad (\mathcal{E}_e^f)^2 = (\mathcal{E}_e - \mathcal{E}_\gamma)^2 + 2\mathcal{E}_\gamma[\mathcal{E}_e - \sqrt{\mathcal{E}_e^2 - (m_e c^2)}] \tag{3.13}$$

The error in energy conservation decreases as the initial emitting particle becomes increasingly ultra-relativistic. The ratio between the energy extracted from the laser field and the initial emitting particle energy is given by [78]:

$$\frac{\Delta\mathcal{E}_e}{\mathcal{E}_e} = \frac{1}{\mathcal{E}_e}\left|\mathcal{E}_e^f - \mathcal{E}_e + \mathcal{E}_\gamma\right| \simeq \frac{m_e c^2}{2\mathcal{E}_e}\left(\frac{m_e c^2}{\mathcal{E}_e^f} - \frac{m_e c^2}{\mathcal{E}_e}\right), \quad \mathcal{E}_e, \mathcal{E}_e^f >> m_e c^2. \tag{3.14}$$

Subsequently, the created macro-photon and the updated macro-electron (or macro-positron) follow the standard PIC-QED algorithm.
In the case of pair production by NBWPP, which involves the photon population, when a macro-photon reaches the final optical depth, it is removed, and a macro-electron and macro-positron are initialized with same position and weight of the parent photon. The quantum parameter of the positron is computed according to eq. (3.10). The process is symmetrical for the positron and the electron, therefore it is not important which one is considered. The particles are assumed to be ultra-relativistic and, hence, the emission is considered collinear. However, the approximated expression for the positron energy, $\mathcal{E}_+ = \mathcal{E}_\gamma \chi_+/\chi_\gamma$ (see eq. (1.6)), does not account for the photon energy converted into mass. This is because if $\chi_+ = \chi_\gamma$, then $\mathcal{E}_+ = \mathcal{E}_\gamma$, neglecting the electron rest energy. To account for this energy while maintaining the approximated conservation of energy $\mathcal{E}_\gamma = \mathcal{E}_+ + \mathcal{E}_-$, the following expression can be obtained:

$$\mathcal{E}_\pm = m_e c^2 + (\mathcal{E}_\gamma - 2m_e c^2)\frac{\chi_\pm}{\chi_\gamma}. \tag{3.15}$$

As a consequence, if $\mathcal{E}_\gamma < 2m_e c^2$, pair production cannot occur because the energy of the photon is less than the rest energy of the pair. Then, their momentum is calculated as follows:

$$\boldsymbol{p}_\pm = \frac{1}{c}\sqrt{\mathcal{E}_\pm^2 - (m_e c^2)^2}\frac{\boldsymbol{p}_\gamma}{|\boldsymbol{p}_\gamma|} \tag{3.16}$$

However, in this case, while energy is conserved in the process, momentum is not. As discussed in 1.2.3, a fraction of the photon momentum disappears:

$$\mathcal{E}_\gamma = \mathcal{E}_+ + \mathcal{E}_- \quad \rightarrow \quad |\boldsymbol{p}_\gamma| > |\boldsymbol{p}_+| + |\boldsymbol{p}_-| \tag{3.17}$$

The error in momentum conservation decreases as the particles involved become more ultra-relativistic. Then, the created pair follows the usual PIC-QED algorithm.

3.3. Highlights, criticalities and limits of PIC-MC method

PIC-QED algorithms exhibit both strengths and criticalities. In particular, various numerical and physical approximations must be taken into account when studying real physical systems. In this section, the advantages and limitations of these codes are discussed.

3.3.1. Highlights

The PIC method is surely the most used to address the Vlasov-Maxwell problem in plasma physics, especially for laser-plasma simulations. Although the accuracy of PIC codes is lower, they are significantly less computationally intensive than space grid methods, which consider the evolution of the distribution function in phase space. Additionally, the numerical implementation of PIC codes is simpler and more robust, albeit at the cost of some numerical noise. This issue, along with the subsequent emergence of non-physical phenomena, can be managed through careful tuning of the simulation parameters. PIC codes are highly scalable and can be applied to a wide range of plasma scenarios, from micrometer-scale laser-plasma interaction to astrophysical plasmas, which exhibit very different spatial and temporal scales. Moreover, PIC codes are very flexible, since a wide range of materials, geometries, and regimes can be simulated. This quality is further enhanced by the capability of integrating additional physics modules according to specific applications. Previously, Monte Carlo modules for high-energy photon emission and pair creation have been discussed. However, modules for collisions, ionization physics, and other processes can be included. For instance, other mechanisms of pair production, as the trident processes (see 1), or bremsstrahlung have been implemented. As mentioned, the Monte Carlo method naturally merges with the particle-based description of the PIC method. Furthermore, PIC-MC algorithms have been efficiently adapted to parallel computing architectures, resulting in substantial reductions in simulation times.

This capability also allows for simulations with high dimensionality and a high-level of details.

3.3.2. Criticalities and limits

One main limitation of PIC codes is given by the macro-particle description. In PIC codes, the distribution functions are sampled by a limited number of computational particles, each one representing a large number, often millions, of real particles. The tails of the distribution function, which represent small amounts of particles significantly deviating from the average behaviour of the population, are not simulated. As a result, it is not possible to accurately simulate processes involving fewer particles than the weight of macro-particles, even though some phenomena may be strongly affected by the distribution function tails. Therefore, the limited number of macro-particles imposes a minimum resolvable density value, effectively acting as a spatial filter that removes all the density inhomogeneities below that threshold. These limitations in details can be mitigated by selecting a large number of macro-particles. However, the upper limit on this number is determined by the computational cost, which increases exponentially with the number of macro-particles. Typically, when setting up a simulation, the Number of Particles Per Cell (NPPC) is defined. Along with the number of cells in the grid, this value defines the total number of macro-particles in the simulation. A general guideline for setting the NPPC value, basing on the electron density n_e and critical density n_c, suggests the following condition:

$$\text{NPPC} \geq \left\{1,\ \frac{n_e}{n_c}\right\}. \tag{3.18}$$

Actually, this rule cannot be applied for solid density plasmas, where n_e/n_c can be quite large, even in the hundreds, implying an unfeasible number of macro-particles. In these cases, it is sufficient to obtain good results by setting NPPC to a lower value, often in the tens.

Additional critical parameters are the spatial and temporal resolution. They must be chosen sufficiently small to avoid undesired grid effects, meaning non-physical effects that arise from the discretization of the spatial and temporal domains. The spatial resolution must be chosen in order to accurately resolve the characteristic lengths of the relevant processes of the specific regime under consideration. In laser-plasma interaction, the most important phenomena occur at lengths near to the skin depth L_w. Therefore, a rough condition to ensure that the main processes are described is:

$$\Delta x, \Delta y, \Delta z < 3L_w, \tag{3.19}$$

where the skin depth depends on the electron density being simulated. In particular, simulating dense plasmas requires a small resolution, which implies higher computational costs. This imposes a limitation on the densities that can be simulated, especially solid density plasmas, which require unpractical resolutions. Usually, to address this issue, numerical simulations employ lower, non-realistic electron densities, leading to a loss of details and an alteration of the physical properties of the simulated solid density plasma, such as its reflectivity. Moreover, the temporal resolution depends on the spatial one through the CFL condition.

An important limitation of PIC codes is the computational cost required to simulate problems with high-dimensionality. Since three-dimensional simulations are very expensive, typically two-dimensional ones represent a good compromise to significantly reduce computational costs. While these simulations are capable of capturing the essential physics of the problem, certain aspects sensitive to the dimensionality are not described. Also, for obtaining quantitative results, three-dimensional simulations are often required. Nevertheless, to investigate the main physics and perform qualitative studies, two-dimensional simulations are sufficient.

The Monte Carlo module, which is necessary for simulating quantum processes and provides accurate results, significantly contributes to the computational cost of simulations. The largest contribution to the computational load is attributed to photon emission, as pair production events are typically much less numerous at the considered intensities of $10^{22} - 10^{23}\mathrm{W/cm}^2$. At every photon emission, at least one new macro-particle is created, leading to an important increase in the macro-particle number during the simulation. This results in a significant slowdown of the simulation. As a consequence, the simulation run-time cannot be easily estimated in advance. To reduce the computational load, it is possible to avoid the actual generation of low-energy macro-photons, which are useless for pair production. In this case, the back reaction is still considered, but information regarding these photons is lost. Moreover, various theoretical approximations are involved in the description of the processes, and the statistical implications related to the macro-particle description apply to quantum processes as well. These statistical implications and theoretical approximations will be discussed in Chapter 5.

In conclusion, the dual treatment of the electromagnetic field, as argued in 3.1.2, introduces some errors, although they are typically small. In particular, particles emitting photons also deposit a small fraction of their energy in the electromagnetic field, representing a further violation of energy conservation.

4 | Thesis Motivations, Objectives and Methods

4.1. Motivations

The chapters 1 and 2 are devoted to the physical background of Non-linear Breit-Wheeler pair production (NBWPP) in laser-plasma interaction, along with the potential technological implications, while the chapter 3 discusses the necessary computational tools to simulate the process. In this section, the main motivations driving the development of this thesis work, which is dedicated to the numerical investigation of NBWPP during laser-plasma interaction in double-layer targets, are outlined. The work also includes an additional thesis activity as part of the Honours Programme, an educational path within the Politecnico di Milano high education training strategy, in which the candidate participated. This additional part of the thesis work will be defined in the following.
The theoretical description of pair production through NBWPP in an intense electromagnetic field (see 1.2.2), developed in the previous century, is well-established. However, its occurrence in the context of laser-plasma interaction has been explored only in recent decades, thanks to the advent of powerful lasers that can provide the intense electromagnetic field required for the process, without the need of other technologies such as particle accelerators. Beyond the scientific interest in this new regime of laser-matter interaction, it has become evident that a new class of compact, full-optical, low-radioactive sources of ultra-short positron beams with unique properties, such as high yield, energy, density and purity, will be potentially accessible in the next period. As discussed in Chapter 1, positron beams with such characteristics find interesting applications in physics, engineering, and medicine. However, the downside of this new class of sources is the requirement of extremely high laser intensities that can only be provided, currently and in the next future, by the largest and most powerful laser facilities worldwide. In Chapter 1, the limitations of currently available positron beam generation methods are discussed. The accelerator-converter schemes require complex, expensive, and large accelerators, and the positron energy obtained is limited in comparison to the primary electron energy. The

radioactive sources, in addition to the need of accumulation and acceleration machines, are affected by the risk associated to radioactivity. For these reasons and due to the higher positron energy, density and yield, the laser-driven positron beam sources, presented in Chapter 2, have attracted great interest. Within this category, alternative schemes such as the laser wake-field acceleration plus converter solution or the low-intensity long-duration laser pulse plus converter method have been experimentally proven, yielding great results. However, even better positron beam qualities, including higher energy, intensity and density levels, can potentially be achieved through NBWPP-based positron sources, at the cost of significantly increasing the laser intensity. Therefore, the prospect of exploiting this process using lower intensities and advanced targets remains a challenging research topic.

Numerous studies in the literature have explored positron beam sources based on NBWPP in laser-plasma interaction, spanning a wide range of laser intensities and considering various types of targets, which play the fundamental role of providing the plasma with the desired properties. Composite targets, consisting of a low density layer and a metallic substrate, have appeared promising as they provide optimal conditions for enhancing NBWPP. Among these composite targets, the DLT exploits the same physics of electron acceleration, photon emission, and positron production, as well as the reflection of the laser pulse by a solid target to provide the optimal conditions for pair production. The foam density producible with PLD is very similar to the densities of gas-jets considered in previous works, which are around $2-4$ times the critical density. Hence, almost the same efficiency for the electron acceleration is expected. Another advantage of the DLT is the solid low-density layer with accurately tunable density and length, allowing for tailoring of the positrons produced. Moreover, the DLT has the potential to provide a full-optical, multi-radiation source. For these reasons, the DLT has the potential to produce positron beams efficiently and with appreciable properties. However, there is limited existing research on investigating NBWPP in composite targets, and the typical laser intensities considered in these studies are not currently available and will not be in the near future. Therefore, the main purpose of this thesis work is to perform an explorative investigation of NBWPP in a DLT considering laser intensities already achievable in the experimental laser facilities, in the range of $10^{22} - 10^{23}\,\mathrm{W/cm^2}$ [1]. This choice allows for experimental validation of the results obtained in this work in the near future. Analytical tools are limited in addressing this complex problem due to the coupled dynamics of plasma populations and the electromagnetic field. Therefore, the approach for this investigation is through computational simulations. Future experiments have both to confirm the potential of the DLT as a positron source at the considered intensities and validate the results obtained through simulations.

Since the simulation of NBWPP in laser-plasma interaction is still a relatively recent topic, the additional work related to the Honours Programme consists of examining the simulation tool employed. This is motivated by the importance of accurately simulating NBWPP to achieve a comprehensive physical description of laser-plasma interaction. With the advent of the next generation of 10 PW class lasers, positron production is expected to significantly affect the plasma and laser dynamics. Therefore, accurate modeling is essential to capture these effects and reproduce realistic physical systems.

4.2. Objectives

In this section, the objectives of the thesis work are outlined. As anticipated, the main scope is the numerical investigation of pair production via NBWPP in double-layer targets, using PIC-MC codes. This thesis work has entailed an extensive study of the existing literature, and all gathered information has been presented in Chapters 1, 2 and 3. It is already evident that there is significant interest in understanding the physics of pair production occurring in DLT targets and characterizing the positrons produced. Despite the complexity of the subject, which covers multiple aspects of plasma physics, and the necessity of complicated demanding simulations, the problem can be addressed with well-defined objectives.
One point is related to the description of NBWPP process and its implementation in PIC-MC codes:

- Understanding single-particle NBWPP, emphasizing the theoretical assumptions, and its occurrence during laser-plasma interaction. Then, study its implementation in PIC-MC codes, analyzing the additional approximations that are employed. These points are addressed in Chapters 1, 2 and 3.

The following objectives, which pertain to the study of NBWPP during laser-plasma interaction in DLT targets, represent the core of the thesis work:

- Examine the physics of NBWPP, with a particular focus on the various phases of the interaction leading to pair production, and identifying the main properties of the produced positrons. This point is addressed in Chapter 5.
- Investigate the role of the main DLT parameters in NBWPP and their impact on the features of positron production. This is done in Chapter 6.

The last point is related to the analysis of the Monte Carlo module used for simulating NBWPP:

- Evaluate the MC module capability of accurately simulate NBWPP, studying the role of the main setting parameters, and identifying the main limitations, with the help of theoretical and simulation results. This is addressed in Chapter 5.

The points related to the analysis of the MC module, in particular the implementation of NBWPP, the approximations involved, and its performances, constitute the additional thesis activity related to the Honours Programme.
These objectives have been achieved through the use of a specific PIC-MC code for simulations. The following section provides a general description of this tool.

4.3. Methods: numerical tools

The investigation of NBWPP during laser-plasma interaction in DLT targets, as discussed in previous chapters, necessitates a kinetic plasma description that can accurately account for quantum processes, i.e. photon emission and pair production. Analytical tools are limited due to the complexity of the problem. Therefore, a numerical approach is employed, involving simulations that can comprehensively model the entire process. This is achieved through the use of particle-in-cell codes integrated with a Monte Carlo module, allowing for a detailed investigation of the topic.
The PIC-MC code used in this work is SMILEI [74], an open-source, fully relativistic, electromagnetic, and massively parallel PIC code with integrated Monte Carlo packages. It is primarily selected due to all these characteristics and, in practical terms, it is one of the few codes that are freely available and equipped with packages to simulate NBWPP. Furthermore, among the open-source codes, SMILEI has one of the most complete MC module, providing the flexibility to configure and control various useful parameters. This advantage allows for improved control over the NBWPP simulation and a more thorough analysis of the results. Lastly, SMILEI provides particularly accessible diagnostics, allowing for a simpler post-processing of the data. The main limitation of SMILEI is that it is CPU-based, which means that it is not optimized in terms of computational performances compared to some other codes. However, a newly ported GPU version of the code has been recently released, and all MC modules of the code will be ported to GPU in the next months.
The computational load of simulations depends on several factors, including dimensionality, the number of macro-particles, the spatial and temporal resolution, the spatial domain size, and the simulation duration. In addition, the MC module significantly contributes to increasing this load. In general, given the typical requirements for simulating laser-plasma interaction including also quantum processes, PIC-MC simulations are quite demanding

in computational resources, and therefore they are typically run on supercomputers. A cluster setup leverages parallelization of computational operations across numerous CPUs, significantly reducing the real-time needed for simulations. All the simulations in this thesis work are performed on the Galileo100 cluster, hosted by CINECA, the largest Italian computing center and one of the most important worldwide. The cluster, designed and engineered by DELL, is currently equipped with 528 computing nodes, each featuring 384 GB of RAM memory, two Intel Xeon Platinum CPUs with 24 cores each, running at 2.4 GHz.

4.3.1. SMILEI PIC code and simulation setup

SMILEI, which stands for "Simulating Matter Irradiated by Light at Extreme Intensities", is a multi-purpose PIC code developed through a collaboration among various laboratories of the Plateau de Saclay, France. This code finds applications in a wide range of physics studies, spanning from relativistic laser-plasma interaction to astrophysics. Designed for high performances on super-computers, SMILEI has its source code written in C++, with a user interface in Python. Its parallelization is based on an hybrid MPI-OpenMP strategy that allows for dynamic load balancing. For run-time diagnostics, the library HDF5 is employed, while the Python module "happi" is used for the visualization, extraction and post-processing of data from all the diagnostics. SMILEI incorporates additional physics modules for field ionization, binary collisions, impact ionization, high-energy photon emission via non-linear inverse Compton scattering, and pair production through NBWPP.
SMILEI allows for simulations in various dimensions and coordinate systems, including Cartesian 1D, 2D, 3D and cylindrical. Users can choose between different Maxwell solvers, particle pushers, interpolators, projectors, and more. The commonly used Maxwell solver employs a Yee mesh, staggered both in time and space, discretizing with a centered finite difference scheme. Alternative methods, such as a pseudo-spectral analytical time domain solver, are also available. The Boris pusher is frequently used for particle dynamics, although other options are provided. Shape functions of different orders and particle extension can be selected.
SMILEI offers different boundary conditions for fields and particles, including periodic, reflective, and removal (or absorbing) conditions. For particles, also thermalizing conditions, in which the momentum of particles reaching the boundaries is re-assigned in according to the thermal equilibrium distribution function, are available. In addition, users can set different conditions for different directions. For laser pulse injection and absorption in the domain, absorbing conditions, referred to as Silver-Muller conditions,

are required for both particles and fields.
The simulation requires defining the population species, including their physical properties such as mass and charge. Particle initialization typically involves assigning a density profile and the number of particles per grid cell, which determine the particle weights. Among the various possibilities, particles in each cell can be distributed randomly, equispaced, or according to different distributions as set by the user. Particle momenta can be initialized following a uniform distribution or, given the temperature, can be assigned based on the Maxwell-Jünetter distribution, which represents the distribution function at thermal equilibrium. In some cases, particle momenta may be initialized at zero, corresponding to cold particles. Drift velocities can also be assigned if necessary. For field initialization, a Poisson solver is available to compute the initial electric field generated by the charge density corresponding to the initialized particles, if a net charge is present. Laser pulses can be defined specifying their spatial and temporal form, or using a predefined Gaussian profile within the code. In the latter case, the main pulse properties such as duration, spot size, polarization, peak normalized potential, and focal position should be defined. External current sources or fields can be inserted as needed.
Various run-time diagnostics are accessible, including fields, particle data, and scalar (or integrated) quantities. These diagnostics are stored according to specific time intervals or time selection. All these settings and more can be efficiently controlled trough a user-friendly Python interface.
In SMILEI simulations, the international system of units is adopted, even though the code primarily operates using non-dimensional units. All quantities in the code are expressed using units that are proportional to a reference frequency w_r. The units of the main quantities are reported in Table 4.1. Typically, this reference frequency is set at the beginning of the simulation to be equal to a relevant frequency of the problem, such as the plasma frequency or the laser frequency. It is worth mentioning that, when simulating quantum processes using the Monte Carlo module, equations cannot be normalized to dimensionless terms, and explicitly depend on the adopted physical units, which are defined in terms of w_r.
In the following, the common settings employed in all the simulations conducted in this thesis work are discussed. These simulations are two-dimensional, adopt Cartesian coordinates, and the reference frequency used is the laser frequency. The Yee Maxwell solver, Boris pusher, charge-conserving Esirkepov method for current deposition, and second-order shape functions are considered. A laser pulse is injected along the x-axis, so Silver-Muller conditions are applied along that axis, while in the perpendicular direction periodic conditions are adopted for both fields and particles. The density profile of the DLT is assigned, and cold particles are randomly distributed in each cell. The low density

layer, or foam, is made of carbon, and its density profile is considered uniform, neglecting the nano-structure. The laser pulse has a central wavelength of $\lambda_0 = 0.8$ μm and peak intensity equal to $I^{peak} = 4.75 \times 10^{22}$ W/cm^2, corresponding to a peak normalized potential of $a_0^{peak} = 150$. The laser field possesses Gaussian spatial and temporal profiles, is linearly polarized along the y-axis, and propagates along the x-axis, with normal incidence with respect to the DLT surface. The pulse duration is set to $\tau_p = 30$ fs, and its focal position is located at the starting position of the carbon foam, where the spot size is $\sigma_p = 3$ μm. The peak of the laser pulse enters within the simulated domain 50 fs after the beginning of the simulation. In conclusion, collisions are neglected. The motivations supporting the main choices are discussed in 5.1.1.

Physical quantity	**units**	**Physical quantity**	**units**
velocity	c	**number density**	$n_r = \epsilon_0 m_e w_r^2 / e^2$
charge	e	**current density**	ecn_r
mass	m_e	**pressure**	$m_e c^2 n_r$
momentum	$m_e c$	**electric field**	$m_e c w_r / e$
energy, temperature	$m_e c^2$	**magnetic field**	$m_e w_r / e$
time	w_r^{-1}	**Poynting flux**	$m_e c^3 n_r / 2$
length	c / w_r		

Table 4.1: List of normalization units used inside the code SMILEI [74]. Here, ϵ_0 is the vacuum permittivity.

4.3.2. MC module for photon emission and NBWPP in SMILEI

SMILEI offers several options for simulating classical radiation emission, such as the Landau-Lifshitz model, while its incorporated MC module enables the simulation of photon emission via non-linear inverse Compton scattering. In this thesis work, photon emission MC module is employed. SMILEI provides the possibility to set a photon energy threshold above which a macro-photon is created, while macro-photons below that energy are not created, still accounting for radiation reaction. Furthermore, SMILEI allows for setting the photon sampling parameter, which determines the number of macro-photons created at each emission event, conserving the total weight of macro-photons emitted. Two additional thresholds are defined on the emitting particle quantum parameter. Below a certain given value, the Monte Carlo photon emission is replaced by a classical radiation emission model. Moreover, a minimum value for the quantum parameter can be set, below which radiation reaction in not taken into account.

The MC module of SMILEI enables the simulation of pair production via NBWPP. Users can define two sampling parameters, similarly for photon emission, to specify the number of macro-electrons and macro-positrons created at each event, conserving their total weights, which are equal to the weight of the parent macro-photon.
For both photon emission and pair production, the tables of total rates and cumulative functions, required in eqs. (3.8) and (3.10), are embedded in the SMILEI code. However, users can implement customized tables. Interpolation is adopted for values of the emitting particle quantum parameter falling between two table points, while for values outside the tables, the values at the boundaries are used. In the default tables, the quantum parameter of both the emitting particle χ and the secondary particle produced χ_s (photon and positron for photon emission and pair production, respectively), are evaluated at 128 values on a logarithmic scale. For photon emission, χ ranges from 10^{-3} to 10^{3}, whereas for NBWPP it ranges from 10^{-2} to 10^{2}. Considering the cumulative distribution function for χ_s given by eq. (3.10), the lower bound of χ_s is determined by imposing, for each value of χ, the condition $F(\chi, \chi_{s,min}) < \epsilon$, where $\epsilon = 10^{-3}$ for photon emission and $\epsilon = 10^{-8}$ for pair production. These values guarantee that the remaining portion of χ_s has a negligible importance (10^{-3} and 10^{-8}) in terms of total emission or conversion probability, respectively. The upper limit of χ_s always equals χ.
In the simulations of this thesis work, the photon energy threshold is set to $2m_ec^2$. The photon sampling, except when explicitly indicated, is chosen equal to 3. When the quantum parameter of the emitting particle is greater than 10^{-4}, the MC module for photon emission is used, while when it is below that value, radiation reaction and photon emission are neglected. For NBWPP, the sampling parameters for electrons and positrons is set to 1. For both processes, the default tables are employed.

5 | Numerical investigation of NBWPP physics in DLTs

In this chapter, the results of a series of 2D simulations related to NBWPP during laser-plasma interaction in a DLT are discussed. Firstly, the physical processes leading to pair production, along with the characterization of positrons produced, are considered. Subsequently, the analysis of the SMILEI MC module for simulating NBWPP is presented.

5.1. Analysis of physical processes and features of positrons produced

The description of NBWPP in DLT cannot be separated from the phenomena occurring within the plasma populations and the laser field. Understanding the physical processes during laser-plasma interaction is not only of scientific interest but is also crucial for comprehending the key parameters and physical quantities that influence positron production. This knowledge is essential for optimizing or tailoring positron characteristics. Therefore, to perform subsequent scans of DLT attributes, it is indispensable to have a clear understanding of the role of each of these quantities to determine the ranges for the scan. Moreover, previous literature studies of NBWPP in laser-target interaction outlined that this process requires high laser intensities. The typical intensities considered in these works are considerable higher than the value adopted in this work. The reason for this choice, as explained previously, is to guarantee the feasibility of experiments to validate the obtained results in the present or next few years. The consequence of the reduced intensity considered in this thesis work is that eventual suboptimal parameters can significantly deteriorate positron production via NBWPP. This underscores the importance of understanding all the physical steps and parameters governing NBWPP.
Characterizing the positrons produced is essential for evaluating the features of a potential positron beam source based on NBWPP using a DLT. This evaluation is necessary to assess the advantages of this source compared to others, especially those requiring much lower laser intensities. The physical properties of positrons depend on various processes

and interaction regimes involving different populations, and therefore also the positron characterization can be addressed by a proper understanding of all the implicated processes and parameters.

5.1.1. Simulations setup

Two 2D simulations have been performed: one aimed at studying the NBWPP physics and related processes, and another devoted to characterize produced positrons and analyze the MC module in the final part of this chapter. These simulations share similar settings, with the main difference being the number of particles per cell (NPPC) for the electrons within the foam. The first simulation adopts a standard value for this parameter, while the second employs a significantly higher NPPC value. The specific parameters of these simulations are detailed in Tables 5.1 and 5.2. In this section, the results of the first simulation are presented, while the second one will be discussed in the section related to the MC module. Figure 5.1 provides a snapshot of the full box size and the location of the target inside it. Here, some space is dedicated to motivate the simulations setup.

- **Dimensionality** The choice of conducting 2D simulations is motivated by the need to perform an exploratory study of a new process and gain insights into its most important physical aspects while keeping the computational load manageable. Extensive simulation campaigns in three dimensions would be computationally expensive, particularly when considering the additional computational requirements of the MC module. While 2D simulations do not capture high dimensionality effects, they provide a reasonable compromise by describing the primary physical processes and producing qualitative results, even though they do not yield reliable quantitative data. In 2D simulations, translational symmetry along the non-simulated axis is assumed, meaning for instance that particles actually are described as infinite wires. Therefore, the 2D approach leads to important physical implications that must be treated carefully. An approximate indication of realistic three-dimensional quantities can be obtained from the corresponding quantities per unit length, obtained from 2D simulations, by multiplying with the laser spot-size [67].
- **Laser properties** The chosen laser properties are representative of high-intensity lasers typically used in experimental facilities. The peak intensity is selected to activate the NBWPP process while still making experiments feasible in the present day. To concentrate the pulse energy in a small region and a short time window, which is necessary for achieving high peak intensities, a duration of tens of femtoseconds

and a micrometric spot size at the focal position are employed. For simplicity, the laser is set to normal incidence on the target, even if in experiments a small angle of incidence is introduced to prevent back-scattering which can damage the laser equipment. The chosen polarization direction aligns with the 2D geometry, where the electric field is oriented along the y-axis, and the magnetic component is along the z-axis, which is the non-simulated direction. Consequently, both the electric and magnetic forces act within the simulated plane when a particle moves inside it.

- **Box size and simulation duration** The spatial and temporal scales of the laser-plasma interaction are determined by the size of the target and the properties of the laser pulse. The box should be large enough to contain the DLT and the laser pulse. Specifically, the length of the box is dictated by the overall thickness of the DLT, which is in the micrometer range. In the transverse direction, since the DLT can have arbitrary width, the box size depends on the pulse spot size, ensuring it fully contains the Gaussian shape of the laser field. Extra space is also included to mitigate boundary effects and non-physical phenomena, such as particle recirculation, and to contain the expansion of the target and all the secondary particles produced for sufficient simulation time. The duration of the simulation depends on the time required for the pulse to reach the target and the time scale of the interaction, which is governed by the laser pulse duration.

- **Collisions** As discussed in Section 2.1.2, collisions can be safely neglected when the characteristic frequency of the problem significantly exceeds the collisional frequency ν_{ei}. In this context, the characteristic frequency is defined by the laser frequency, which is approximately $\nu_0 = w_0/2\pi \simeq 10^{14}$ Hz, while the typical collisional frequency for laser-generated plasma is around $\nu_e i \simeq 10^{12}$. Consequently, during the relevant time scale of the interaction, the impact of collisions can be disregarded. By neglecting collisions, the problem is simpler, and the additional computational load required for simulating collisions is avoided, resulting in reduced simulation time.

- **Target simulation** The substrate of the DLT is represented as a 1 μm thick slab of aluminum with an electron density of 450 n_c, while the low density layer, or the foam, is simulated as a 15 μm thick slab of carbon with density of 2 n_c. The carbon for the foam and the aluminum for the substrate are the typical materials employed in DLTs. The selected foam thickness optimizes the average photon energy considering a peak normalized potential of $a_0 = 60$ [58]. The substrate thickness of one micrometer is chosen because it can be ordinarily reproduced and ensures an effective Target Normal Sheath Acceleration (TNSA) field. The target is consid-

ered to be completely ionized. This can be justified by calculating the appearance intensity (see 2.2.2) for Al^{13+}, which is 6.67×10^{20} W/cm^2, and for C^{6+}, which is 6.41×10^{18} W/cm^2. Both values are orders of magnitude lower than the considered laser intensity. Considering the impact ionization not significant due to the minor role of collisions, the non-negligible tunneling ionization process by the pulse low-intensity tail is not simulated. This choice avoids the additional computational cost associated with simulating ionization processes. For the substrate, the realistic density is adopted, since the role of this layer is to efficiently reflect the laser pulse, enhancing the intensity and realizing the optimal geometry for photon emission and pair production (see 1.2.2 and 2.4.1). The reflectivity depends on the density, and a lower, non realistic density would be suboptimal. However, the condition 3.18 for the NPPC for substrate electrons cannot be satisfied, as it predicts an unfeasible NPPC value. As a consequence, the dynamics of substrate electrons will not be accurately simulated, but this is a reasonable compromise because the dynamics inside the substrate is not of great interest. The NPPC for ions is slightly lower than that of electrons in both the DLT materials, as ions are less numerous than electrons. Lastly, the nanostructure of the foam is not taken into account, mainly because it is a three-dimensional feature, and at high-intensity the nanostructure is expected to be destroyed and homogenized by the prepulse or the front edge of the pulse. The effect of the nanostructure, as discussed in [79], compared to an uniform density profile, mainly contributes an additional level of chaos in the electron motion.

- **Resolution** The spatial resolution is chosen according to the criterion 3.19. The smallest skin depth is given by the higher electronic density simulated, which is the one of the substrate. With three times the skin depth in the substrate totaling $3L_w = 18$ nm, a grid resolution of 64 grid points per micron is selected in both directions, resulting in a grid spacing of 15.6 nm. The time-step is determined by imposing $\Delta t = CFL\Delta x$, assigning $CFL = 0.95$. This value satisfies the CFL criterion while preventing an excessively small time-step, thus reducing the computational load.

- **Radiation emission** The photon energy threshold is set to $2m_ec^2$, since only photons with energies greater than the pair creation threshold are relevant for this work. When the quantum parameter of the emitting particle falls below 10^{-4}, radiation reaction and photon emission are neglected. These choices alleviate the computational load of the MC module in the non-interesting regime of low-energy emission. The photon sampling, which is discussed in the final part of the chapter, is set to 3, while the pair sampling is set to 1.

In the high-NPPC simulation, the number of macro-particles per cell for foam electrons is

increased by a factor ten to enhance the statistics of photon emission and pair production. This results in a reduction of the weight of these macro-electrons and, since in quantum processes the weight is conserved, also of the photons and positrons produced. The increased statistics allows for a deeper exploration of the tails of the distribution functions of the populations and their impact on the physical processes under consideration. In addition, the number of macro-positrons will be larger, providing more information and statistics for their characterization. However, this important increase in NPPC, along with the non-indifferent length of the foam, significantly raises the computational load. Therefore, some adjustments are performed in order to mitigate this increase, such as a slight reduction in the box size, duration of the simulation, and the NPPC value for the substrate electrons. The spatial and temporal resolution remains unchanged.

Exploration of NBWPP in DLT - standard NPPC			
Box size ($x \times y$)	70 μm $\times$ 50 μm	Grid points ($x \times y$)	4480 $\times$ 3200
Time duration	350 fs	CFL	0.95
Substrate properties			
Z	13	Density n_e	450 n_c
A	27	Thickness	1 μm
NPPC electrons	30	NPPC ions	6
Carbon foam properties			
Density n_e	2 n_c	Thickness	15 μm
NPPC electrons	5	NPPC ions	1

Table 5.1: Parameters of the 2D simulation performed to study the physics of NBWPP in DLT and the features of positrons produced. This simulation employs a standard NPPC value for the foam electrons.

Exploration of NBWPP in DLT - high NPPC			
Box size $(x \times y)$	50 μm $\times$ 40 μm	Grid points $(x \times y)$	3200 $\times$ 2560
Time duration	280 fs	CFL	0.95
Substrate properties			
Z	13	Density n_e	450 n_c
A	27	Thickness	1 μm
NPPC electrons	25	NPPC ions	6
Carbon foam properties			
Density n_e	2 n_c	Thickness	15 μm
NPPC electrons	50	NPPC ions	1

Table 5.2: Parameters of the 2D simulation performed to analyze the Monte Carlo module capability to simulate pair production. This simulation employs a ten times greater NPPC value for the foam electrons with respect to the standard value.

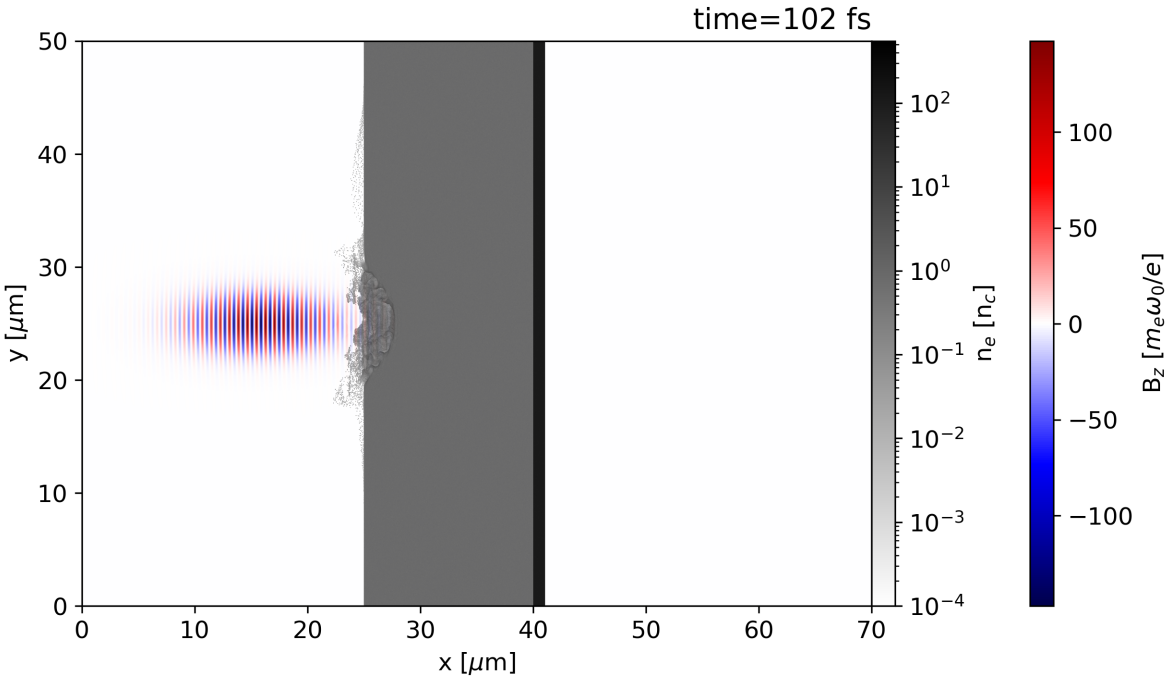

Figure 5.1: Laser pulse impinging on the DLT. The pulse is represented through the magnetic filed component B_z, while the target appears through its electronic density. SMILEI units are adopted, where w_0 is the central frequency of the laser pulse.

5.1.2. Evolution of the electromagnetic field

The global dynamics of the simulation can be understood by examining the energy transfer between the electromagnetic field and the plasma populations, as depicted in Figure 5.2. As the laser pulse impinges on the DLT and propagates into the foam, energy transfer from the laser field to the plasma populations initiates. First, due to their low inertia, electrons are rapidly accelerated absorbing energy from the laser. Subsequently, the electron energy drives photon emission and pair production, transferring in turn their energy to photons and pairs. The efficiencies of these energy conversion processes ultimately determine the number of positrons produced and their energy. The figure provides an order of magnitude for the amount of laser energy absorbed by each population. Notably, photon emission and pair production processes, coupled with a strong laser energy absorption, occur within a very short time window, corresponding to the reflection of the laser pulse. This section focuses on the behavior of the electromagnetic field, while subsequent sections delve into the dynamics of other plasma populations.

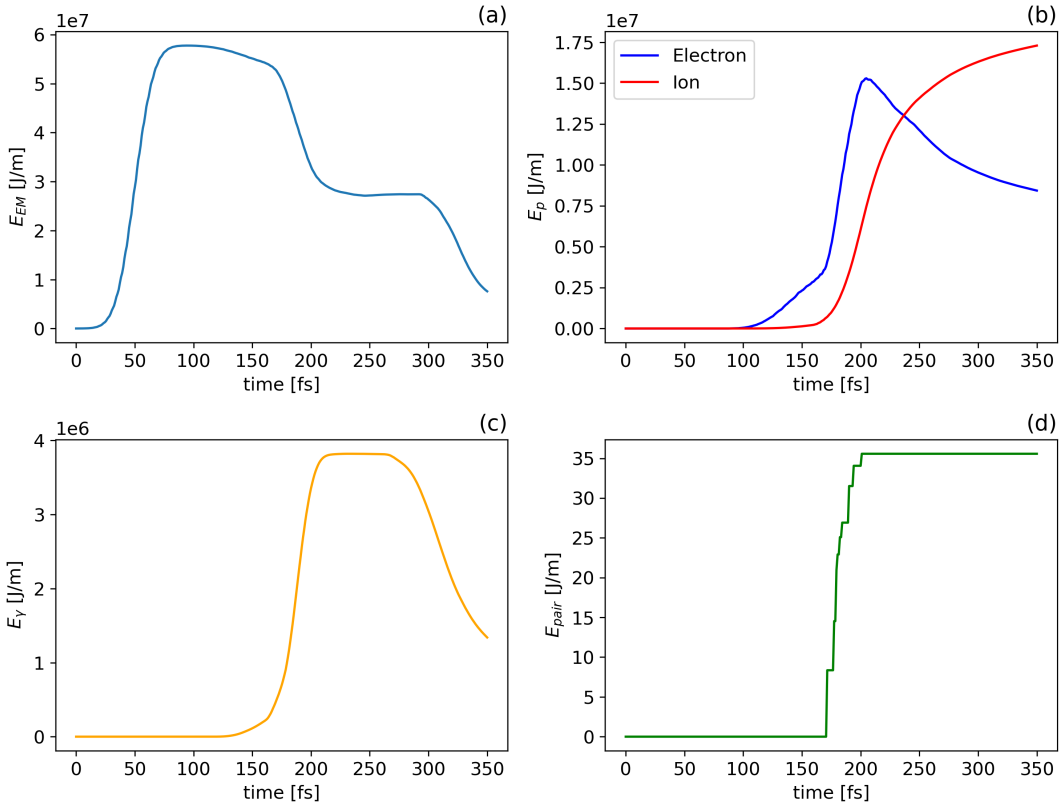

Figure 5.2: Evolution in time for the energy of the electromagnetic field (a), electron and ion populations (b), photons emitted (c), and converted into pairs (d).

Before reaching the DLT, the laser pulse follows the free propagation law of Gaussian beams, as discussed in Section 2.2.1. Since the focal position is initially located at the front of the DLT, the spot size decreases, reaching the set focal spot size of 3 μm. During this phase, the laser field is the only relevant electromagnetic field present in the simulation. As outlined in Section 2.3.5, when the laser pulse enters the foam it experiences self-focusing, leading to a further reduction in spot size and increase in peak intensity. Simultaneously, electrons are accelerated, absorbing energy from the pulse. Figure 5.3 provides a comprehensive view of all the components of the electromagnetic field, including the evolution of their integrated energy and their maximum values.

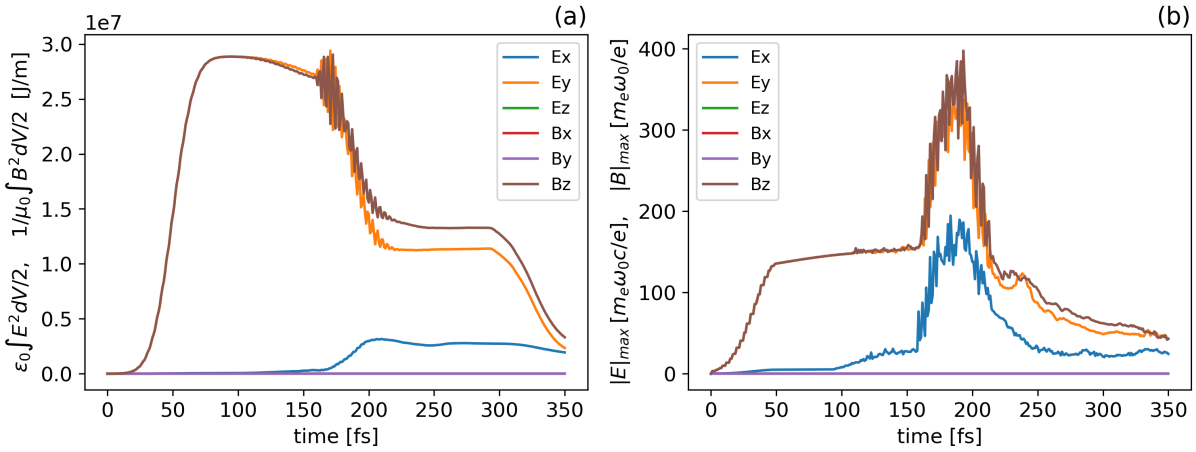

Figure 5.3: Evolution in time of the integrated energy (a) and maximum value (b) of each component of the electromagnetic field. In picture (b) SMILEI units are adopted.

At the beginning of the simulation, the field of the initial laser pulse is visible, described only by the B_z and E_y components. Notably, due to the adopted normalization, the quantities plotted on the ordinate axis of Figure 5.3 (b) related to the electric field can be interpreted as contributions to the normalized vector potential a_0. Consider the time window indicatively between 70 fs and 160 fs, corresponding to the interval between the complete entrance of the pulse into the simulated box and its reflection. During this time, the energy of the field remains constant until the pulse reaches the front of the DLT. Subsequently, it decreases due to energy absorption by electrons. In contrast, the peak values of the B_z and E_y components slightly increase from the beginning up to the reflection point. Before entering the DLT, whose front coincides with the focal position, the pulse is naturally focused. Then, instead of diverging, which would lead to a decrease of $B_{z,max}$ and $E_{y,max}$, they continue to increase, despite the laser energy absorption by electrons. The reason is the Self-Focusing (SF) effect, which was discussed in Section 2.3.5

and can be visualized in Figure 5.4. As the pulse propagates in the foam, it creates a channel of depleted density and relativistic electrons, leading to the SF effect. This effect results in a reduction of the laser spot size and an enhancement in the pulse intensity. The increased intensity is beneficial for both photon emission and pair production. Using eq. (2.24), it is possible to estimate the self-focusing focal length, obtaining $L_f \simeq 22$ μm, which is greater than the foam length. This suggests that stronger focusing and higher intensities can be achieved with longer foams. In Figure 5.5, at $t = 147$ fs, a weak steepening of the pulse profile can be noted, where the pulse leading edge is slightly absorbed from the central part. This phenomenon is caused by the same non-linear effects that arise in a dispersive medium leading to the SF. In this case, the steepening is induced by the modulation of the refractive index in time, driven by the temporal profile of the pulse intensity. When considering a longer foam, the steepening is expected to become more pronounced, potentially resulting in a quasi-step pulse envelope.
In the same time window (70 fs − 160 fs), the E_x component becomes significantly non null. This component is likely the quasi-static longitudinal field generated by the separation of electrons from ions, driven by the strong ponderomotive force (see Section 2.3.4).

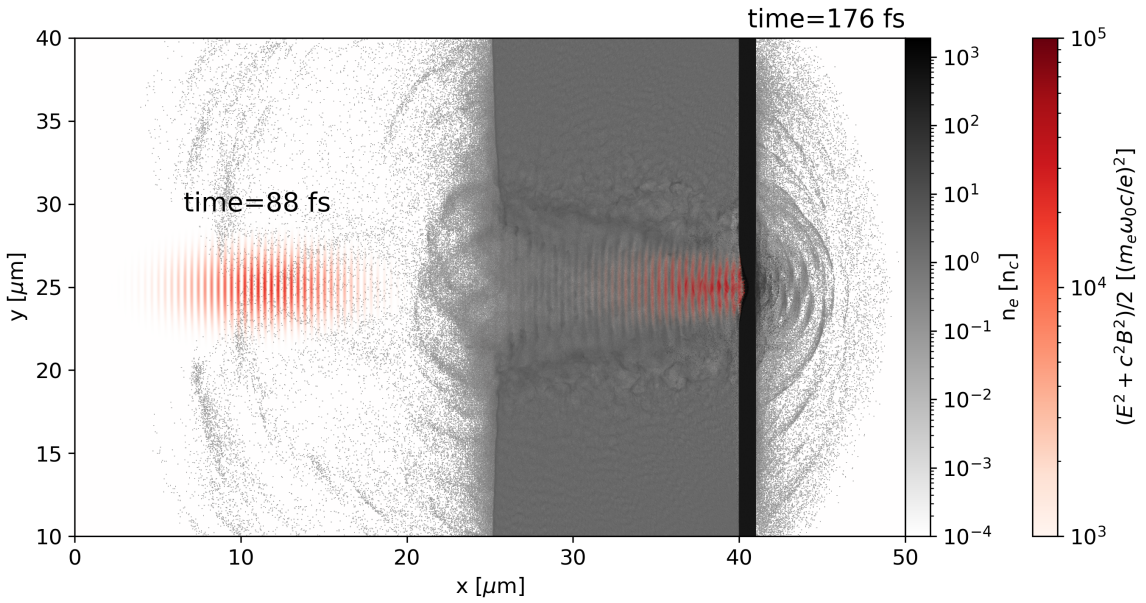

Figure 5.4: Snapshot of the quantity $(E^2 + c^2B^2)/2$ and DLT electronic density at the reflection ($t = 162$ fs). The same quantity $(E^2+c^2B^2)/2$ before the pulse enters the target ($t = 88$ fs) is superimposed. SMILEI units are adopted.

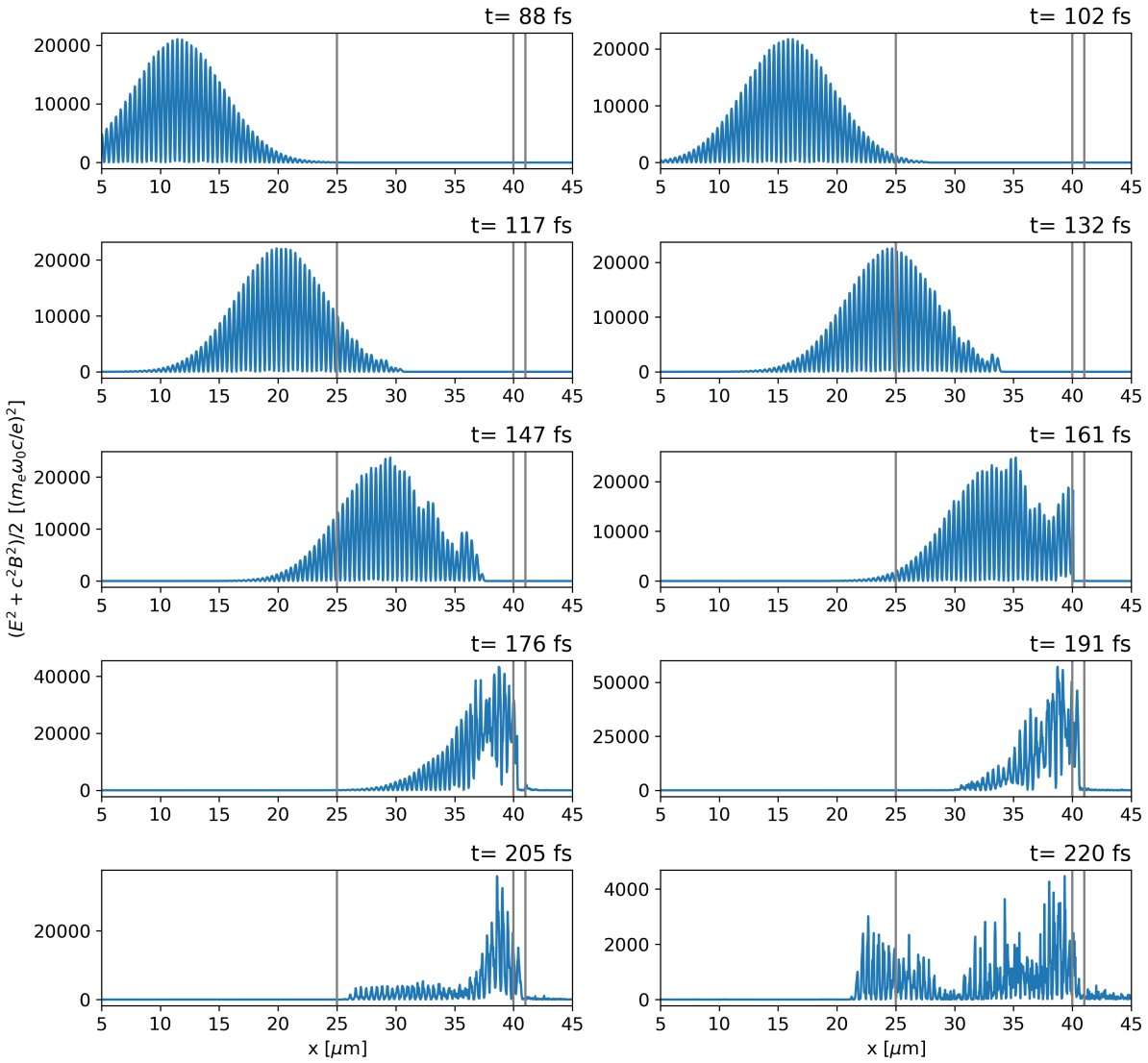

Figure 5.5: Snapshots of the quantity $(E^2 + c^2B^2)/2$ at $y = L_y/2$ during the propagation of the laser pulse, up to its reflection. The gray lines represent the unperturbed DLT, and SMILEI units are adopted.

Subsequently ($t \gtrsim 160$ fs), the laser pulse reaches the solid substrate and, approximately between 170 fs and 200 fs, is reflected, resulting in a significant amplification of the field maximum values and intensity, as shown in Figures 5.3 and 5.5. The values of $B_{z,max}$ and $E_{y,max}$ almost double, indicating a nearly perfect superposition of the incident and reflected pulses. The amplification in instantaneous intensity, which more than doubles, can be visualized in Figure 5.5, where this quantity is evaluated at $y = L_y/2$ during the reflection. This superposition corresponds to the formation of a quasi-stationary wave, although not ideal, as laser pulses are considered rather than plane waves. During

reflection, a non-negligible fraction of pulse intensity penetrates into the solid-density substrate. This is an initial indication of suboptimal reflectivity of the substrate, a point that will be emphasized in the following parts.
During the time interval, the E_x component is also significantly amplified, corresponding to the formation of the TNSA field (see 2.3.5). This longitudinal field is generated by the electrons escaping the rear side of the target. The TNSA field, formed on the target rear side during the pulse reflection, is shown in Figure 5.6. It is interesting to note that the maximum value of this field is comparable to the initial transverse field of the laser pulse.

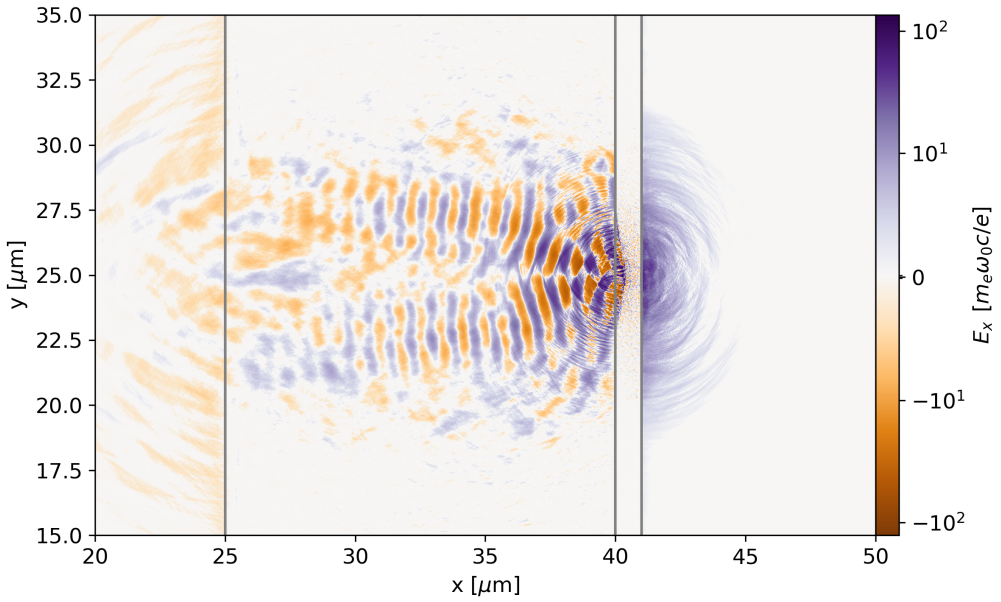

Figure 5.6: Snapshots of E_x at the reflection of the laser pulse, at $t = 176$ fs. The gray lines represent the unperturbed DLT, and SMILEI units are adopted.

To conclude this part, Figure 5.7 shows the B_z component at the pulse reflection. The intense currents produced by the electron motion magnetize the channel, generating a strong poloidal magnetic field. This leads to the formation of two symmetric regions within the channel with opposite sign of B_z.
After the reflection, the laser pulse diverges while back-propagating outside the target.

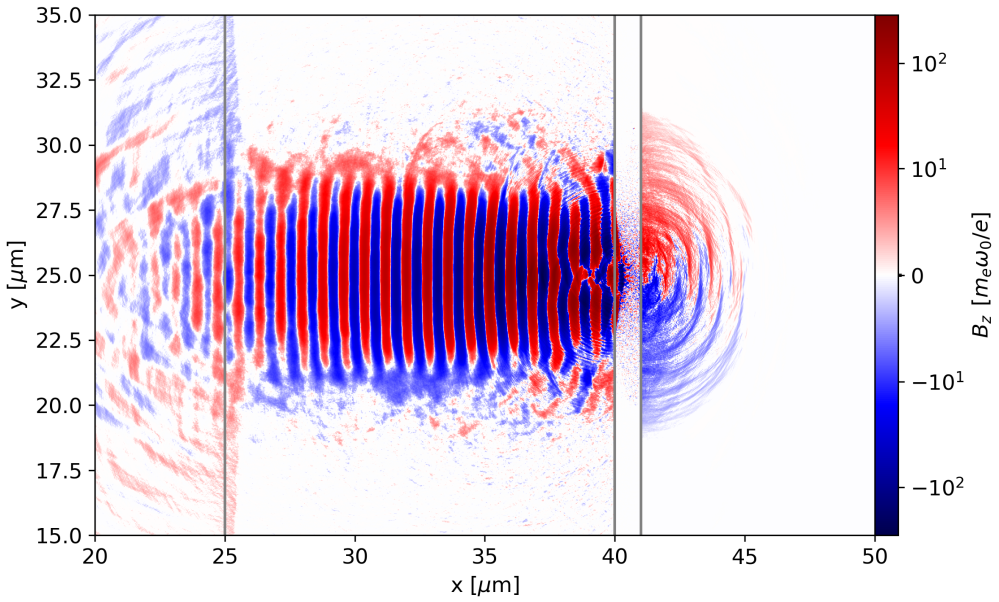

Figure 5.7: Snapshots of B_z at the reflection of the laser pulse, at $t = 176$ fs. The gray lines represent the unperturbed DLT, and SMILEI units are adopted.

5.1.3. Particle dynamics

When the laser pulse impacts the foam, the first population to absorb energy from the laser field is the foam electrons, which are accelerated through the mechanisms explained in 2.3.4. Figure 5.8 illustrates how the leading edge of the pulse pushes these electrons radially and forward, leading to the creation of an almost fully depleted region and an accumulation of electrons on the frontal and lateral boundaries of the channel. This process results in charge separation due to the different inertia of ions, whose dynamics will be discussed in the following. However, some electrons are trapped by the laser pulse due to radiation friction and the charge separation field, and they fall into the high-intensity region of the pulse. In this region, trapped electrons co-move with the laser pulse and undergo betatron oscillations driven by the laser electric field, thus getting accelerated longitudinally by the $\boldsymbol{v} \times \boldsymbol{B}$ force. This mechanism, known as direct laser acceleration (DLA), involves electrons being accelerated directly by the laser field. Figure 5.8 also shows that electrons moving along the lateral edges of the pulse cannot return toward the optical axis, preventing the formation of the laser wake-field acceleration. Trapped electrons are further confined within the pulse by the magnetization of the channel, which is illustrated in Figure 5.7. All these trapping mechanisms discussed are essential for generating a bunch of energetic electrons moving in the forward direction, efficiently seeding the photon emission and pair production processes.

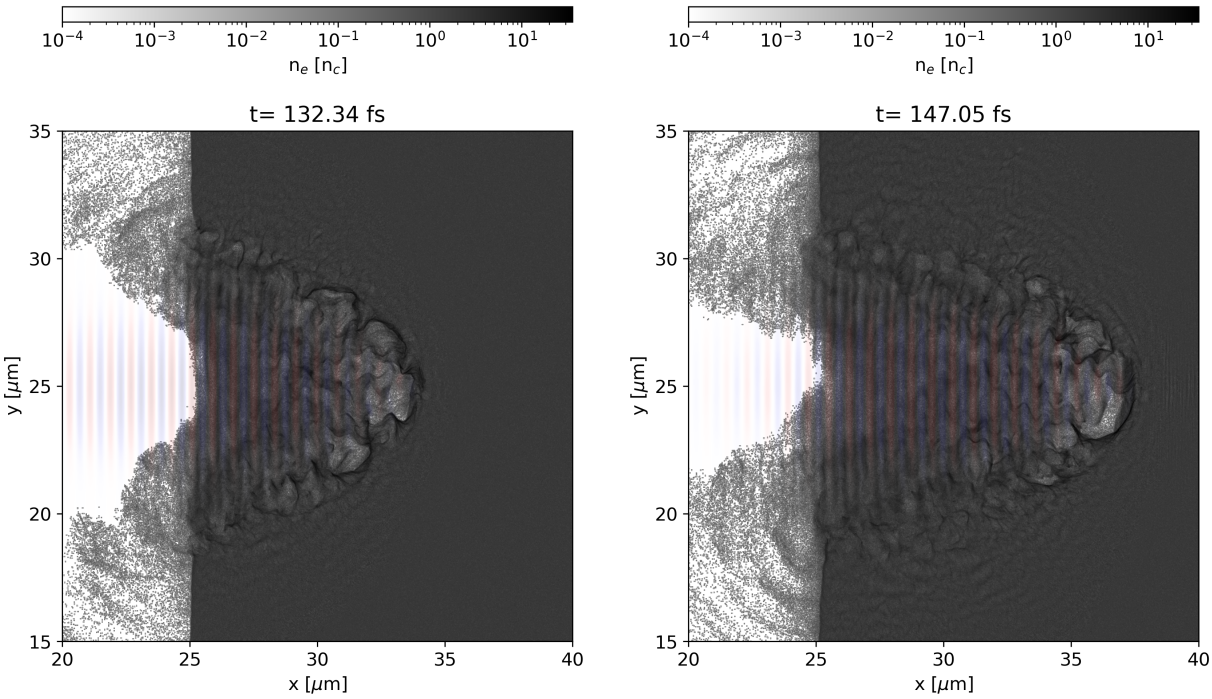

Figure 5.8: Snapshots of the electron density within foam while it is crossed by the laser pulse. For clarity, the shadow of the laser pulse is superimposed. SMILEI units are adopted.

Figure 5.9 illustrates the time evolution of the integrated energy of the foam (a) and substrate (b) electrons. The former exhibit almost linear energy absorption from the laser field. At the reflection point, there is a discontinuity in the foam electron energy, where it slightly decreases due to photon emission. After reflection, the foam electrons are accelerated backward by the back-propagating laser pulse, but no longer contribute to pair production. In contrast, the substrate electrons, during laser reflection, absorb a large amount of laser energy, much more compared to the foam electrons. The reasons are the electron density in the substrate, which is hundreds of times larger than that of the foam, and the fact that the laser is weakly absorbed within the foam, with almost all its energy impinging on the substrate and heating its electrons. However, substrate electrons do not significantly contribute to pair production because they interact only with the leading edge of the laser pulse. Consequently, the photons emitted by these electrons do not experience the central high-intensity region of the pulse, resulting in a low probability of conversion into pairs. The seeding of photon emission, and hence pair production, only by foam electrons will be further explained in the discussion of the photon emission process. Therefore, the laser energy absorbed by the substrate electrons is essentially wasted, leading to a reduction of the laser field intensity acting on photons

emitted by foam electrons. This strong energy absorption in the substrate indicates poor reflectivity because the laser pulse partially penetrates the substrate, instead of being perfectly reflected, accelerating electrons and deposing energy. It suggests that aluminum might not be the most suitable choice as plasma mirror because it wastes laser energy and has limited reflectivity, both of which reduce the laser field intensity available for pair production. It is important to stress that the reflected field is essential since it provides the optimal geometry for photon emission and pair production, as discussed in 1.2.2 and 2.4.1. The reflectivity of different substrate materials will be discussed in the next chapter.

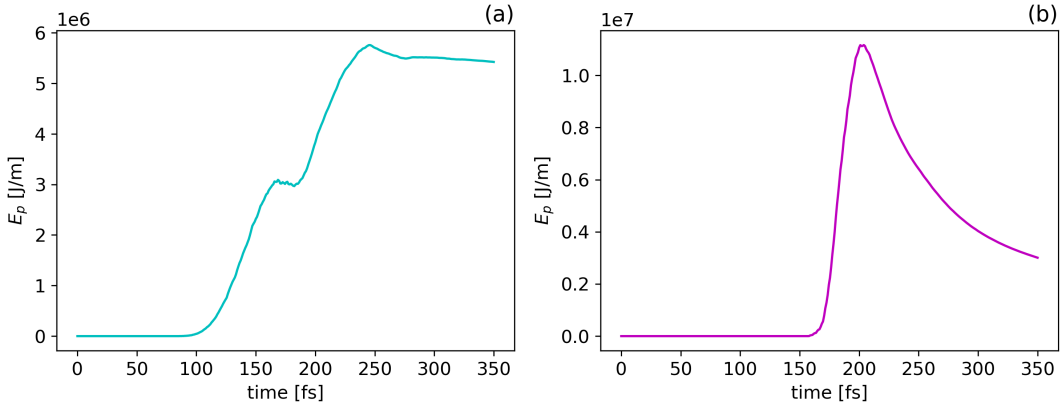

Figure 5.9: Energy evolution of the electrons belonging to the foam (a) and substrate (b).

To efficiently produce positrons, numerous and energetic photons are required. Photon emission is primarily governed by two parameters: the electron energy and the quantum parameter χ. The behaviour in time of these parameters for the foam electrons during the acceleration phase is illustrated in Figure 5.10 (a) and (b), respectively. The energy spectrum of foam electrons progressively increases during the pulse propagation within the foam, reaching a cut-off value of almost 750 MeV at $t = 167$ fs. Throughout the acceleration phase, the quantum parameter remains constant around 0.1. However, as the laser pulse begins to reflect at $t = 167$ fs, χ experiences a strong increase, extending up to 0.8. Evidently, the foam electrons reaching such energies and χ values are those accelerated by DLA within the laser pulse. During reflection ($t \geq 167$ fs), these electrons interact with the reflected laser field, realizing the optimal left-handed (LH) geometry, and leading to χ enhancement. Since the electron quantum parameter approaches unity, efficient photon emission is expected. Therefore, during the reflection, the high-energy region of the electron spectrum decreases because photon emission, and consequently the quantum parameter also decreases, as the two are related.

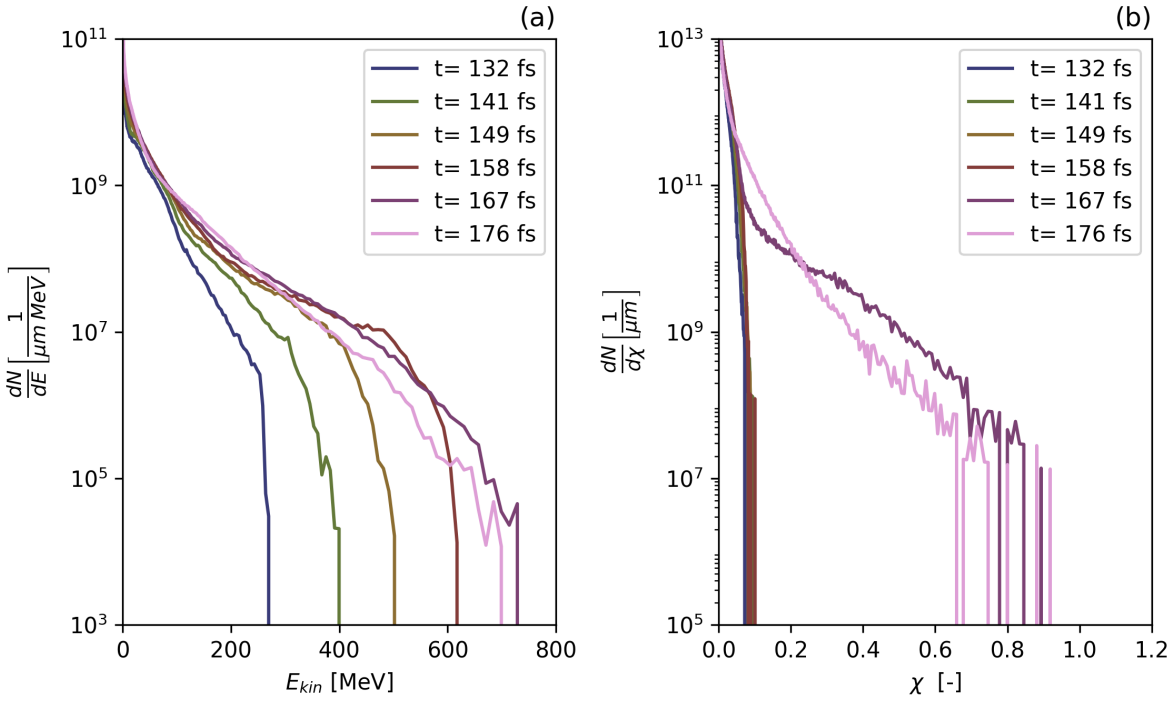

Figure 5.10: Spectra as a function of the kinetic energy (a) and quantum parameter (b) for foam electrons evaluated at different times during the acceleration stage, up to the first stages of laser reflection ($t \gtrsim 167$ fs) from the substrate.

The spectra of substrate electrons, as functions of their kinetic energy and quantum parameter, reported in Figure 5.11 (a) and (b) respectively, show that their acceleration is delayed compared to foam electrons. In particular, the electrons belonging to the substrate are accelerated to interesting energies during the laser reflection ($t \geq 167$), and therefore they do not interact efficiently with the reflected pulse. This is motivated by their lower quantum parameter, extending up to 0.4, the half compared to foam electrons. Furthermore, the acceleration mechanisms for substrate electrons, which in general are not DLA due to the different interaction regime, occurring during laser reflection are less efficient, leading to less energetic electrons. The lower energy levels and quantum parameter values in the substrate prevent an efficient high-energy photon emission. Another important aspect related to substrate electrons concerns the low-energy region of their spectrum, which is much more populated than that of foam electrons, due to the higher density. This property justifies the large values assumed by their integrated energy.

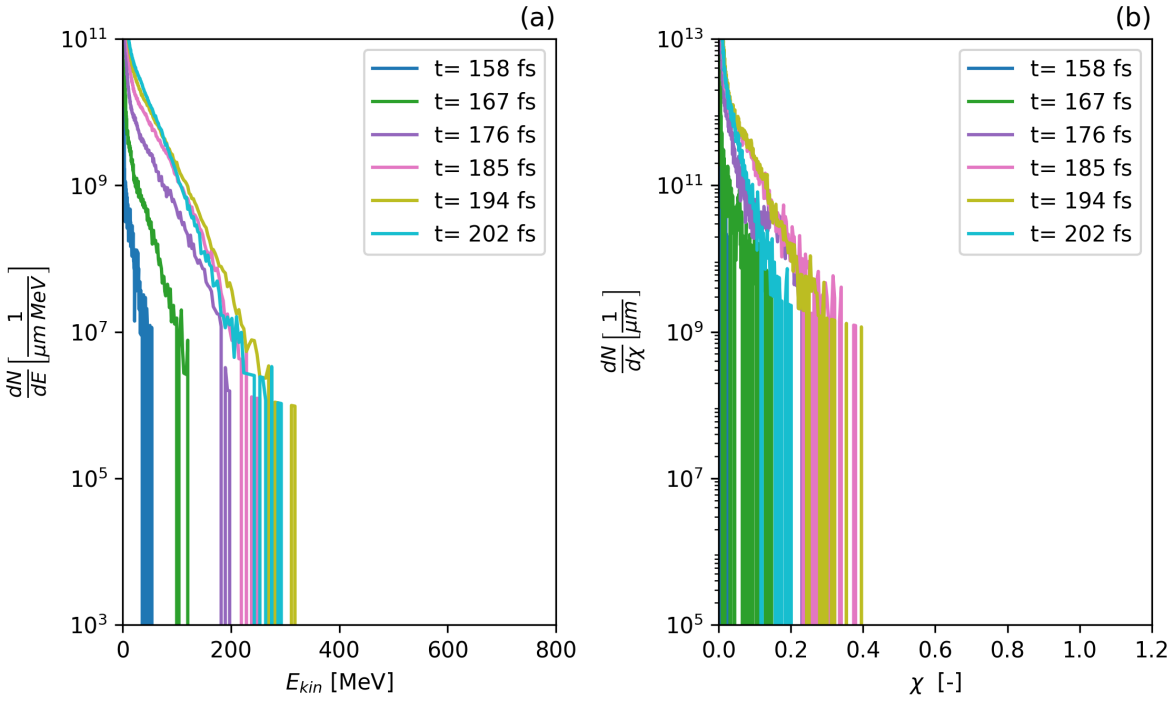

Figure 5.11: Spectra as a function of the kinetic energy (a) and quantum parameter (b) for substrate electrons evaluated at different times during and after the laser reflection.

The ion dynamics is much slower than that of electrons and less interesting for the purpose of studying pair production. As anticipated, their slower motion results in charge separation, which gives rise to quasi-static electric fields. These fields, acting on the electrons, determine the diameter of the depletion channel within the foam by reaching equilibrium with the laser ponderomotive force. They also contribute to the injection of some electrons into the high-intensity region of the pulse, contributing to the trapping effect. However, despite their bigger inertia, ions experience the laser ponderomotive force, being slowly pushed in the radial direction, as shown in Figure 5.12. Plot (a) illustrates that the ion depletion in the channel directly caused by the pulse is relatively weak when compared to the electron depletion. Then, as shown in plot (b), after the passage of the pulse, ions expand outwards the target, driven by the repulsive Coulomb force that arises from the concentration of positive charge within the channel. In the same figure it is possible to observe ions on the rear surface of the substrate being accelerated by the TNSA field. The laser energy absorbed from ions within the foam, reported in Figure 5.13 (a), is roughly one order of magnitude less than that absorbed by foam electrons, supporting what stated previously. On the other hand, laser energy is strongly absorbed by ions belonging to the substrate during the reflection of the pulse, as depicted in Figure 5.13 (b). The reason is once again the poor reflectivity of the aluminum substrate, causing a partial transmission

of the pulse into the plasma mirror and the subsequent acceleration of electrons and ions within the substrate. It is crucial to recognize that the substrate electrons and ions together absorb almost one third of the total laser energy. This results in a weaker reflected pulse and the reduction in the available laser intensity to seed photon emission and pair production.

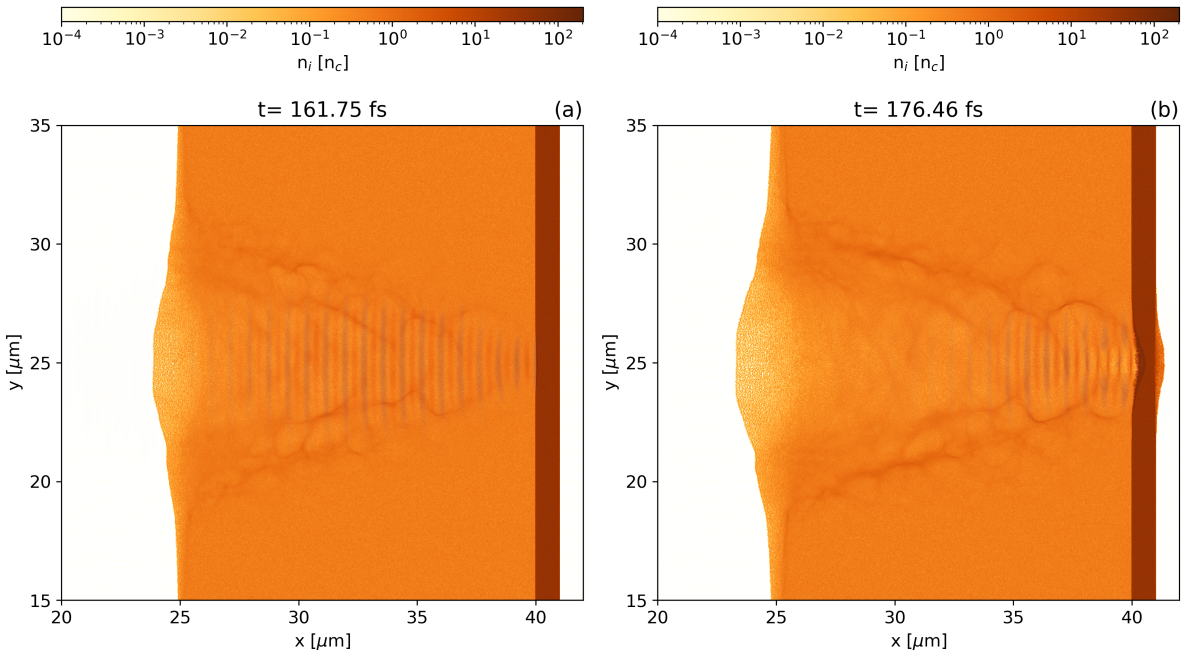

Figure 5.12: Snapshots of the ion number density during pulse propagation in the foam (a) and its reflection from the substrate (b). For clarity, the shadow of the laser pulse is superimposed. SMILEI units are adopted.

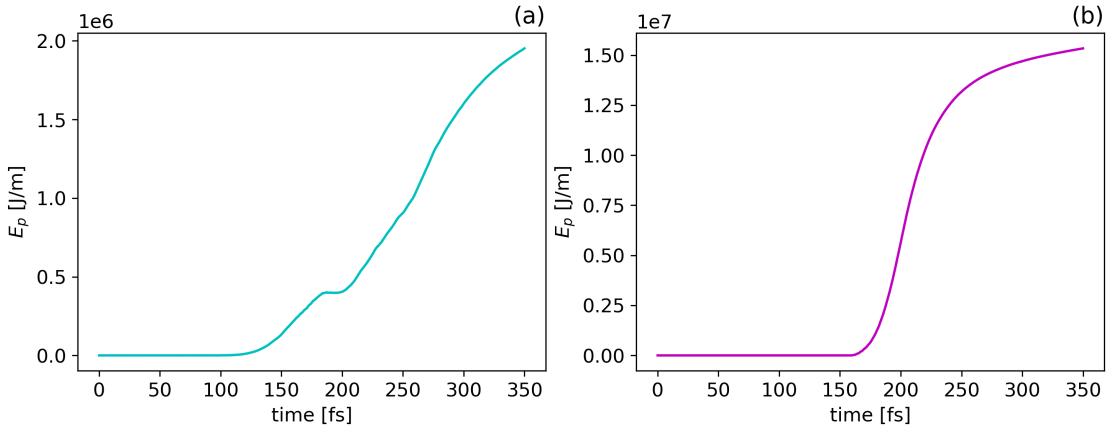

Figure 5.13: Evolution in time of the integrated energy of ions belonging to the foam (a) and substrate (b).

5.1.4. Photon emission

In this context, photons are produced through the non-linear inverse Compton scattering process, which is explained in Section 2.4.1. Figures 5.2 (c) and 5.14 describe the behaviour over time of the integrated photon energy and its derivative. They show a sharp increase in photon energy, indicating that the effective photon production mechanisms are confined to a very limited time interval. A weak photon emission occurs during the formation of the channel within the foam ($t \leq 170$ fs) while electrons are being accelerated, resulting in a small ramp in photon energy. These electrons emit low-energy photons (see Figure 5.15 and 5.18) as they oscillate in the laser field due to their interaction with the field itself. However, the photon energy produced during this period is very small, and these photons are not relevant for pair production. The reason is that they do not interact with the reflected pulse, preventing the realization of the optimal interaction geometry and resulting in a suboptimal photon quantum parameter. These properties are illustrated in Figure 5.18, where the photon quantum parameter spectrum before reflection is almost zero. Almost all the energy stored in the photon population is emitted during the reflection of the pulse, indicatively between 170 fs and 210 fs. During this time window, the most numerous and energetic photons are emitted, and these are the ones relevant for seeding pair production. After this strong emission phase, the photon energy remains almost constant at the peak value, and the subsequent decreasing trend corresponds to the photons escaping from the simulated box. By considering the maximum value of integrated photon energy, it is possible to estimate the conversion efficiency from laser energy to photon population, resulting in approximately 6.6%.

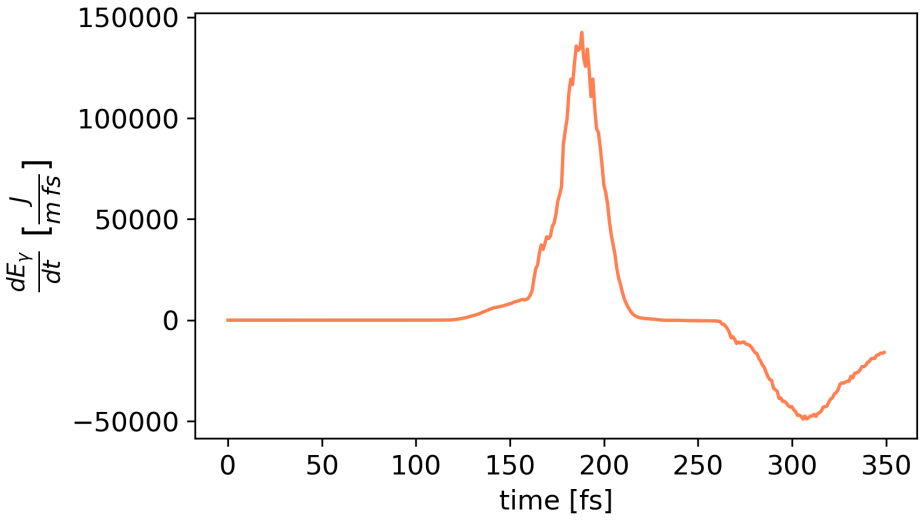

Figure 5.14: Evolution over time of the derivative of the integrated photon energy.

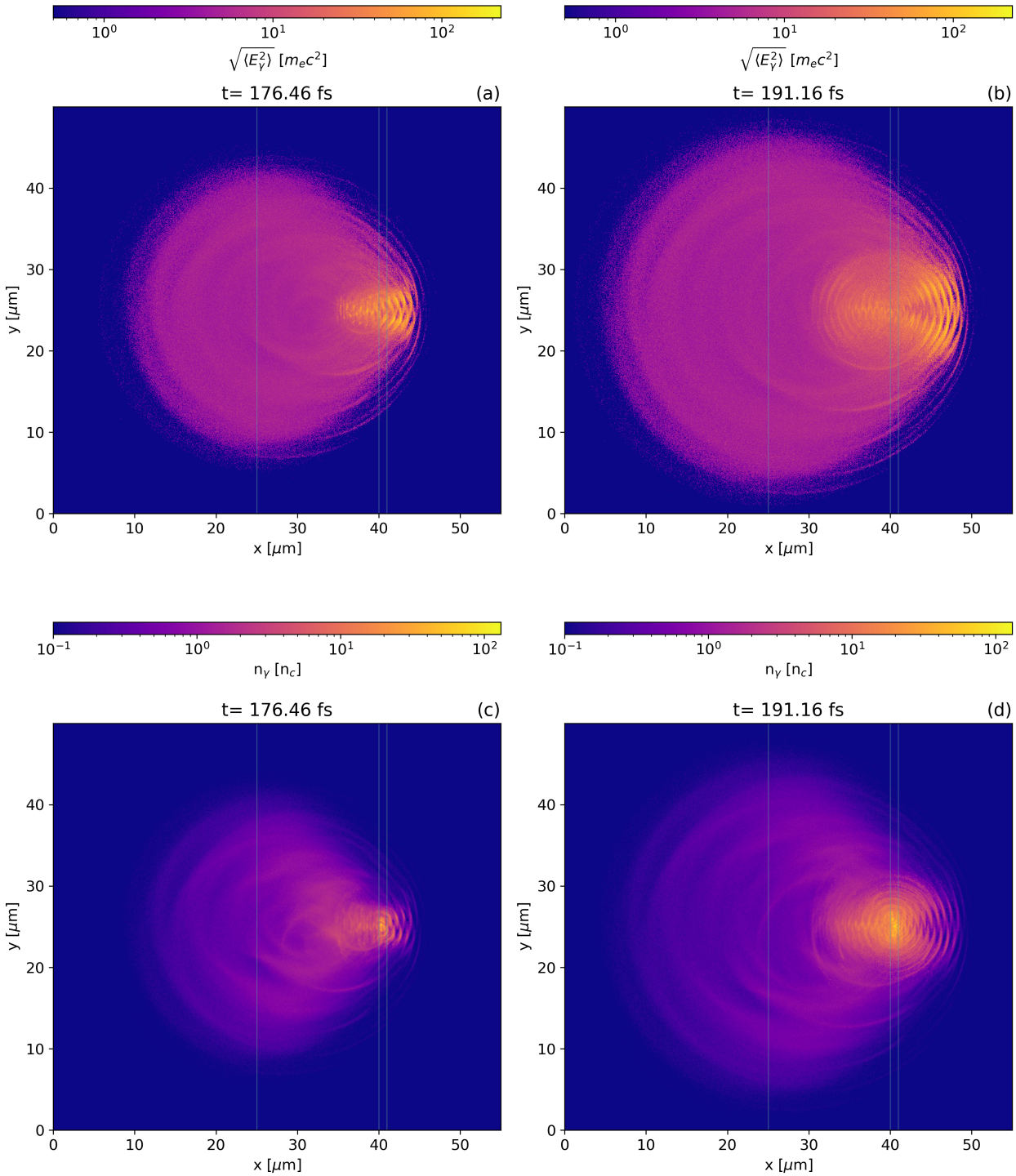

Figure 5.15: Maps of the photon energy, calculated as the root mean square $\sqrt{\langle E_\gamma^2 \rangle}$ and at each grid point, (a,b) and density (c,d), at different times during the reflection of the laser pulse by the substrate. Only photons with energy greater that $2m_e c^2$ are considered. The unperturbed DLT is represented through semi-transparent vertical lines, and SMILEI units are adopted.

The panels (a) and (b) of Figure 5.15 show the photon energy map, calculated as the root mean square value $\sqrt{\langle E_\gamma^2 \rangle}$ at each grid point, at different times during the pulse reflection. Aligned with the previous arguments, the most energetic photons are emitted in a very limited region on the front of the substrate, dominating over a background of non-interesting low-energy photons. At $t = 176$ fs, when the pulse impinges on the substrate and initiates reflection, the foam electrons, accelerated by DLA, interact with the reflected laser field, realizing the optimal LH geometry and therefore emitting energetic photons. The intensity enhancement due to the superposition of the incident and reflected pulses, along with the self-focusing effect, boosts photon emission by these electrons. These observations emphasize the crucial role of foam electrons in seeding the photon emission and pair production processes. Notably, the most energetic photons are emitted forward, but not uniformly in angles. Instead, they are emitted along two specific directions that are clearly visible in the figure and are symmetric with respect to the laser axis. This angular distribution is due to the fact that, as discussed in Section 2.4, electrons oscillate in the laser field. Consequently, photons are not emitted along the optical axis but form a small angle of approximately 15°. An intriguing property of these energetic photons propagating along such specific directions is their coherence. In the energy map (b), it is possible to observe the distribution of the considered photons during their propagation, which resembles the wave-fronts of a spherical wave. It is remarkable how photons, which are simulated as point-like particles, manifest a coherent wave-like behaviour, similar to an electromagnetic wave. Furthermore, the photon energy map shows that some energetic photons are also emitted backwards. They are probably produced by electrons that are accelerated from the reflected pulse and interact with the trailing tail of the still incoming pulse. Also these backward-emitted photons are not interesting for the purpose of pair production, both because they have a lower probability of undergoing NBWPP and eventual positrons would be produced in the opposite direction to the primary beam.
The panels (c) and (d) of Figure 5.15 displays the photon density map, including all the photons with energy greater than $2m_ec^2$, during the reflection of the laser field. The photon density resembles their spatial energy distribution, with two prominent directions characterized by a much higher concentration which stand out the lower photon density background produced during the pulse propagation within the foam. Moreover, the coherent behaviour of forward-propagating photons can be noted. An important feature shown in the density maps is a significant concentration of photons inside the substrate. However, this concentration does not appear in the energy maps, meaning that the large number of photons produced in the substrate have limited energy, further emphasizing that these photons are not relevant in terms of pair production. They represent a mere waste of laser energy, consequence of the poor reflectivity of the substrate, which dimin-

ishes the efficiency of pair production. The inability of the photons to generate pairs is supported by the distribution of the photon quantum parameter in space, as depicted in Figures 5.16 and 5.17. The former shows the map of the quantum parameter, calculated as $\sqrt{\langle \chi_\gamma^2 \rangle}$ at each grid point, at different times during the pulse reflection, while the latter presents the same quantity evaluated at $y = L_y/2$ for various times from the channel formation to the end of the reflection. The photon quantum parameter within the substrate is significantly lower compared to the values assumed in the final part of the foam, where the geometry of photon interaction with the laser field and the intensity enhancement are optimal. Similar arguments apply to photons produced during the pulse propagation within the foam, as they experience irrelevant χ values. From these figures it is evident that the photon quantum parameter assumes its highest values in the initial part of the pulse reflection, constraining the effective time window for pair production indicatively between 170 fs and 190 fs. This aligns with the time evolution of the integrated positron energy reported in Figure 5.2. Another interesting feature in Figure 5.16 is that the distribution of photons with the highest values of χ resembles the distribution of electrons oscillating in the laser field. This reinforces the idea that these electrons are responsible of the most significant photons in terms of pair production.

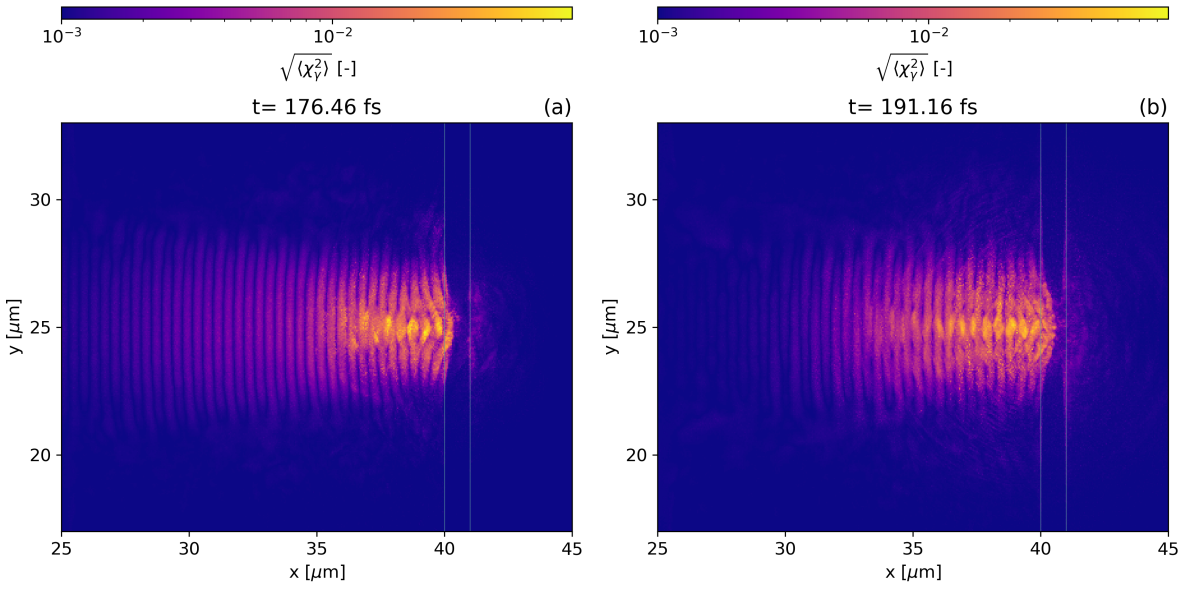

Figure 5.16: Maps of the photon quantum parameter, calculated as the root mean square $\sqrt{\langle \chi_\gamma^2 \rangle}$ at each grid point, for different times during the reflection of the laser pulse. Only photons with energy greater that $2m_e c^2$ are included. The unperturbed DLT is represented through semi-transparent vertical lines.

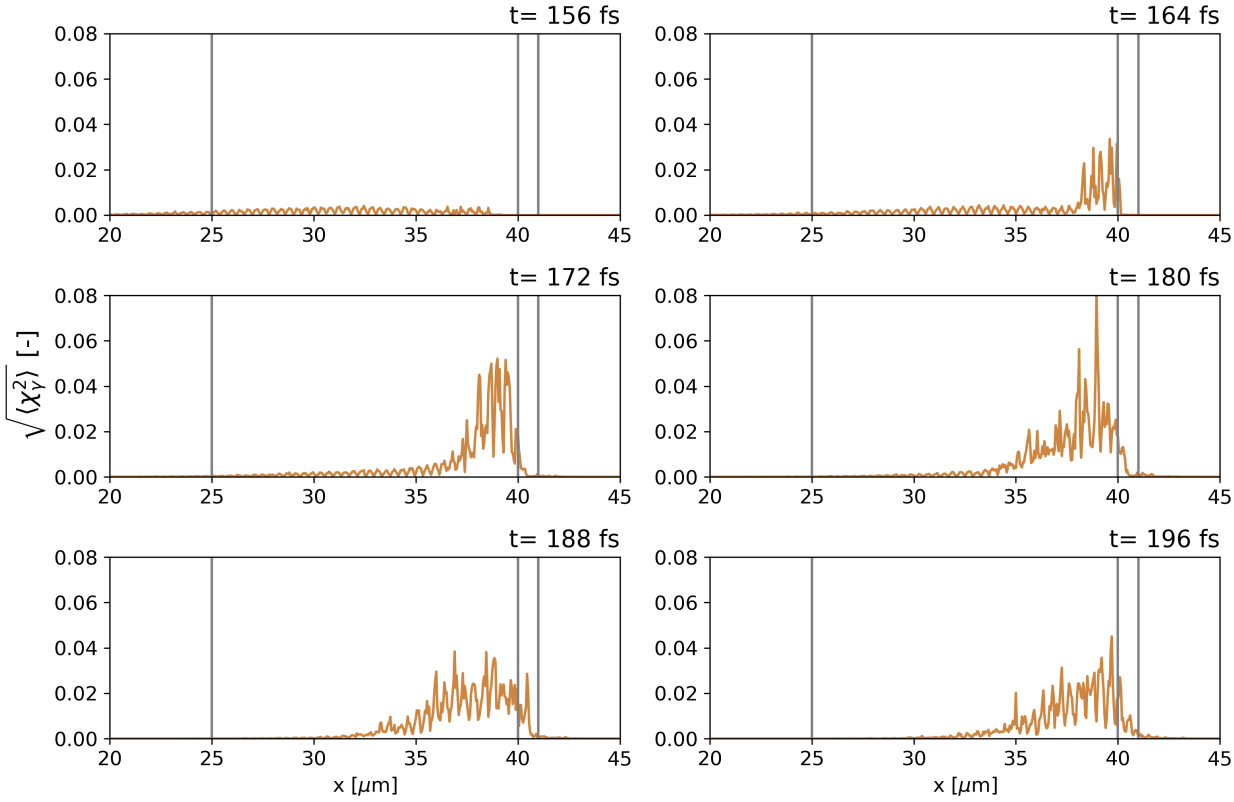

Figure 5.17: Snapshots of the photon quantum parameter, calculated as the root mean square $\sqrt{\langle\chi_\gamma^2\rangle}$ for each grid point, at $y = L_y/2$ during the pulse propagation inside the foam and its reflection. Only photons with energy greater that $2m_ec^2$ are included. The grey lines represent the unperturbed DLT.

Whereas the previously presented values of the photon quantum parameter are averaged, not representing the highest values assumed, these last can be visualized in Figure 5.18, which shows the photon spectra as a function of the energy (a) and χ (b) for several times during the pulse reflection. As discussed earlier, the most energetic photons with the highest χ values are those produced during the laser reflection. These photons reach energies up to nearly 500 MeV and their quantum parameter extends to around 0.5. These values suggest that positron production might not be very abundant, as the quantum parameter is not very close to unity. It is interesting to note how the low-energy region of the spectrum becomes much more populated during the reflection, corresponding to the abundant low energy photons produced in the substrate. In the final phase of the reflection ($t > 190$ fs), energetic photons are produced by the last delayed electrons, but they only interact with the trailing edge of the reflected pulse, resulting in lower values of the photon quantum parameter.

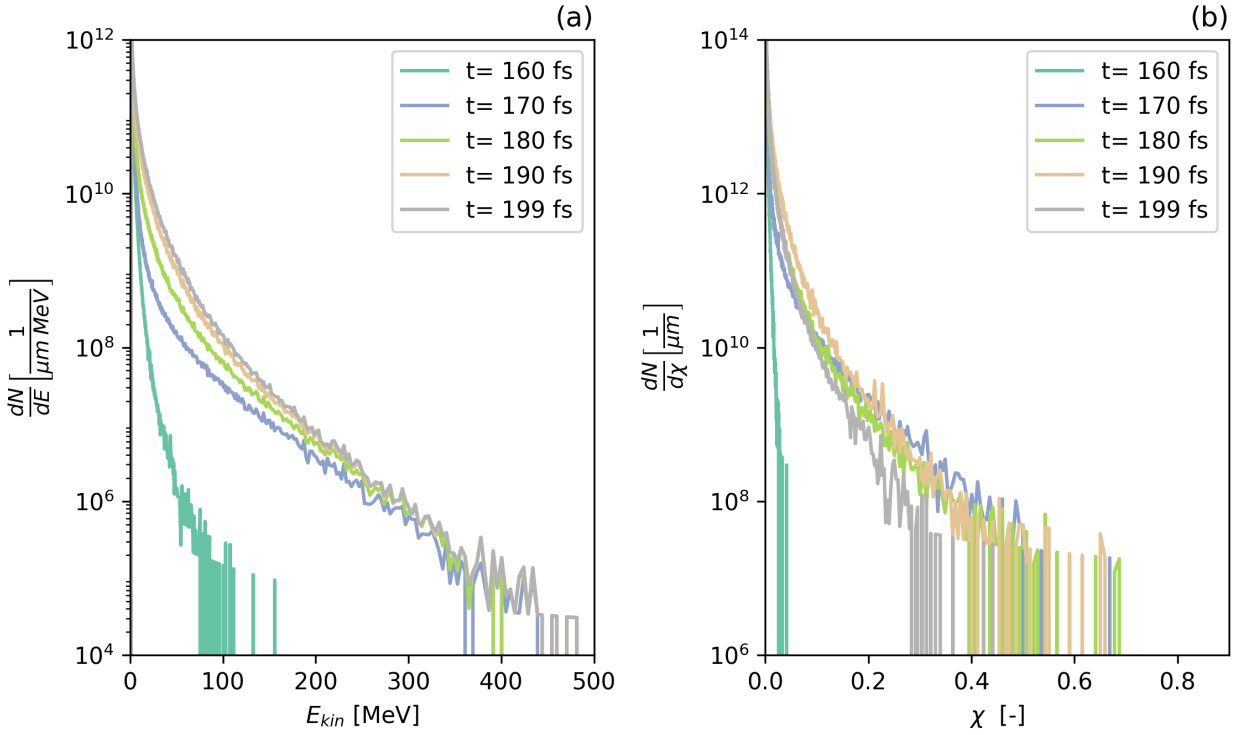

Figure 5.18: Spectra as a function of the kinetic energy (a) and quantum parameter (b) for photons evaluated at different times during the pulse reflection.

5.1.5. Positron production and dynamics

In this context, pairs are produced through the non-linear Breit-Wheeler pair production process. In this part, to characterize the positrons produced, the results of both the "standard NPPC" and "high NPPC" simulations are employed. The setup of these simulation is presented in Section 5.1.1, while differences in the results provided by the two will be discussed in the final part of this chapter. It is helpful for the following to recall that the size of the simulated box in the "high-NPPC" simulation is slightly smaller, and therefore all the processes, including the pulse reflection and positron production, occur at lower times. A first comprehensive picture of the positron and electrons production through NBWPP and their subsequent dynamics is presented in Figures 5.19 and 5.20. The figures represent the last stage of the laser-DLT interaction for the two simulations, where the reflected pulse is leaving the hole-bored DLT, with the trajectories of pair positrons and electrons superimposed. Pairs are produced at the front of the substrate, in the limited region associated with the superposition between the incident and reflected pulse. The majority of positrons, after the generation, are forward-accelerated by the strong longitudinal fields present in their formation region (see Figure 5.6), including the TNSA field,

which significantly increases the positron total energy, as shown in Figure 5.21, leading them to follow straight trajectories. It is evident from their trajectories that these energetic positrons form a beam propagating in the forward direction. A fraction of the produced positrons are trapped and backward-accelerated by the reflected pulse across the plasma channel dug within the foam. These positrons do not benefit from the TNSA field, and therefore their energy remains limited, as can be observed from their curved trajectories. Figure 5.19 shows that the back-propagating positrons are initially emitted in the forward direction, but due to certain mechanisms they lose energy and are trapped from the reflected pulse. The reason, as discussed in the following, is probably photon emission. A minor number of positrons are channelled within the substrate, following trajectories inside its thickness. The pair electrons, instead, are drastically slowed down from the longitudinal TNSA field and are unable to escape the target, forming a cloud of chaotic trajectories, which are visible in Figure 5.20. Therefore, the electron component of the beam is removed from the TNSA field itself. Because of the uninteresting motion of pair electrons and the thesis purpose, the following discussion will center on the positrons.

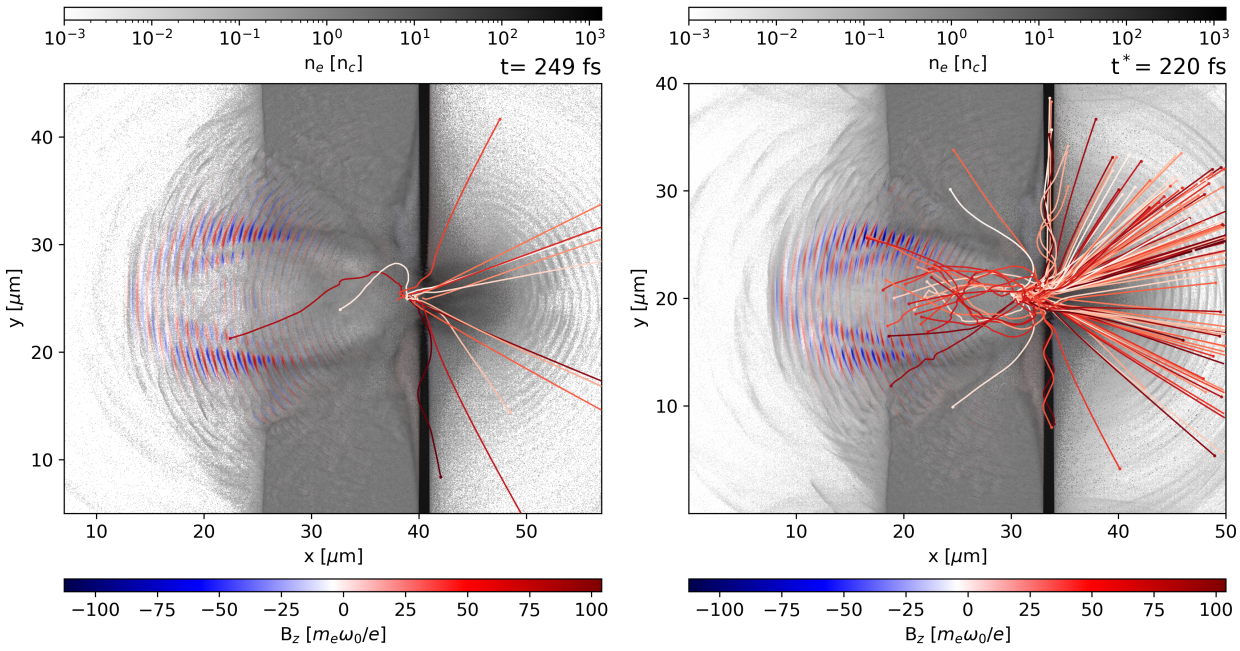

Figure 5.19: Snapshot of the laser-DLT interaction at the final stage for the two simulations characterized by a standard NPPC value (left) and an higher NPPC value (right) for the foam electrons. The DLT is represented though its electronic density, the pulse through the B_z component and the red lines represent the macro-positron trajectories from their production by NBWPP to the time considered. SMILEI units are adopted.

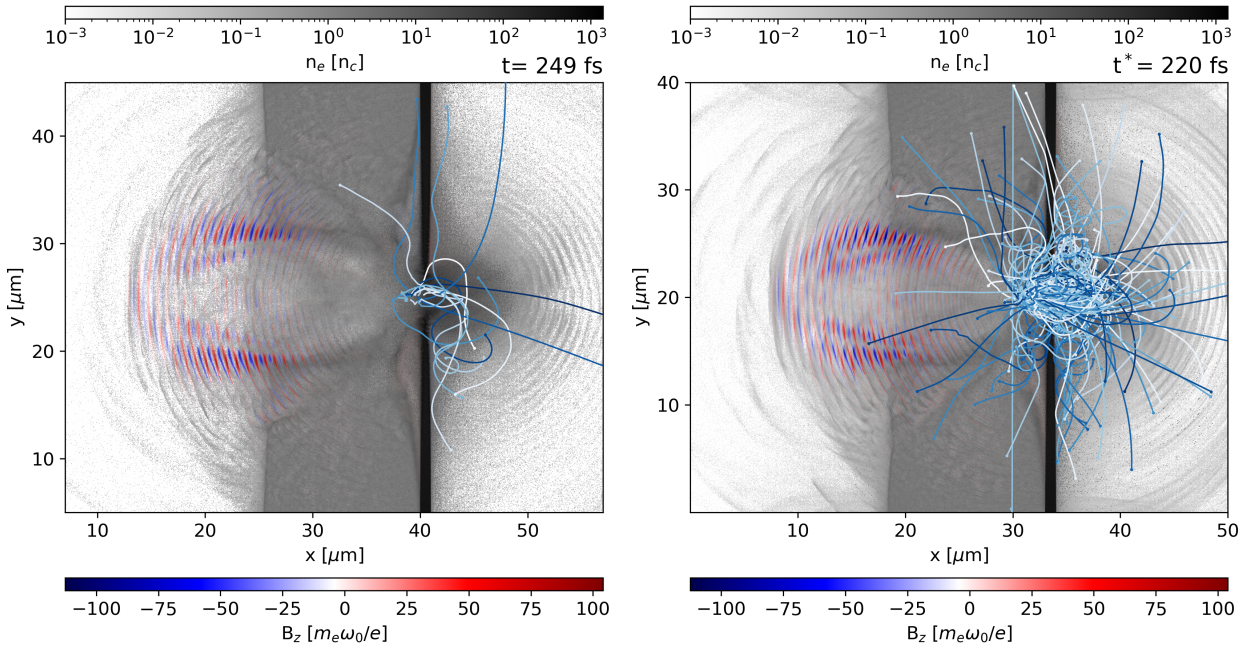

Figure 5.20: Snapshot of the laser-DLT interaction at the final stage for the two simulations characterized by a standard NPPC value (left) and an higher NPPC value (right) for the foam electrons. The DLT is represented though its electronic density, the pulse through the B_z component and the blue lines represent the macro-electron trajectories from their production by NBWPP to the time considered. SMILEI units are adopted.

Figure 5.21 presents the time behaviour of integrated quantities that are significant for NBWPP, such as the total converted energy into pairs (a), its time derivative (b), and the individual integrated energy of the pair electrons and positrons (c,d). From the integrated converted energy displayed in panel (a), it is possible to estimate the conversion efficiency from laser energy to pairs, which is roughly 5×10^{-5} %. This integrated energy, and hence the calculated conversion efficiency, includes only the energy converted into pairs at their creation, not considering eventual energy gained during their following dynamics. Nevertheless, this low conversion efficiency supports the investigation of an optimized setup, which is performed in the last chapter of this work, capable of providing better performances in terms of positron production. It can be anticipated that an increment of two orders of magnitude will be obtained by optimizing the DLT properties. Pictures (a) and (b) illustrate that, as discussed in the previous sections, photon conversion into pairs occurs in a limited time frame associated with the first stage of laser reflection by the substrate. For the "standard NPPC value" simulation, picture (b) indicates that the ef-

fective time window for NBWPP is between 170 fs and 200 fs, aligning with the arguments presented in the previous parts. Panels (c) and (d) show that positrons, after their production, are accelerated, as their integrated energy increases from the generation instant throughout their propagation time. Electrons, on the contrary, are decelerated, and their energy becomes significantly lower compared to that of positrons. It is interesting to note that positrons, immediately before leaving the box, possess an integrated energy above 40 J/m, which is larger than the total converted energy (above 30 J/m). This means that the energy gained by positrons after their production surpasses the energy lost by pair electrons. It is worth mentioning that in picture (d), due to the decreased box size in the high-NPPC simulation, positrons rapidly leave the box, truncating the simulation of their acceleration phase by the TNSA field and resulting in a lower final positron energy.

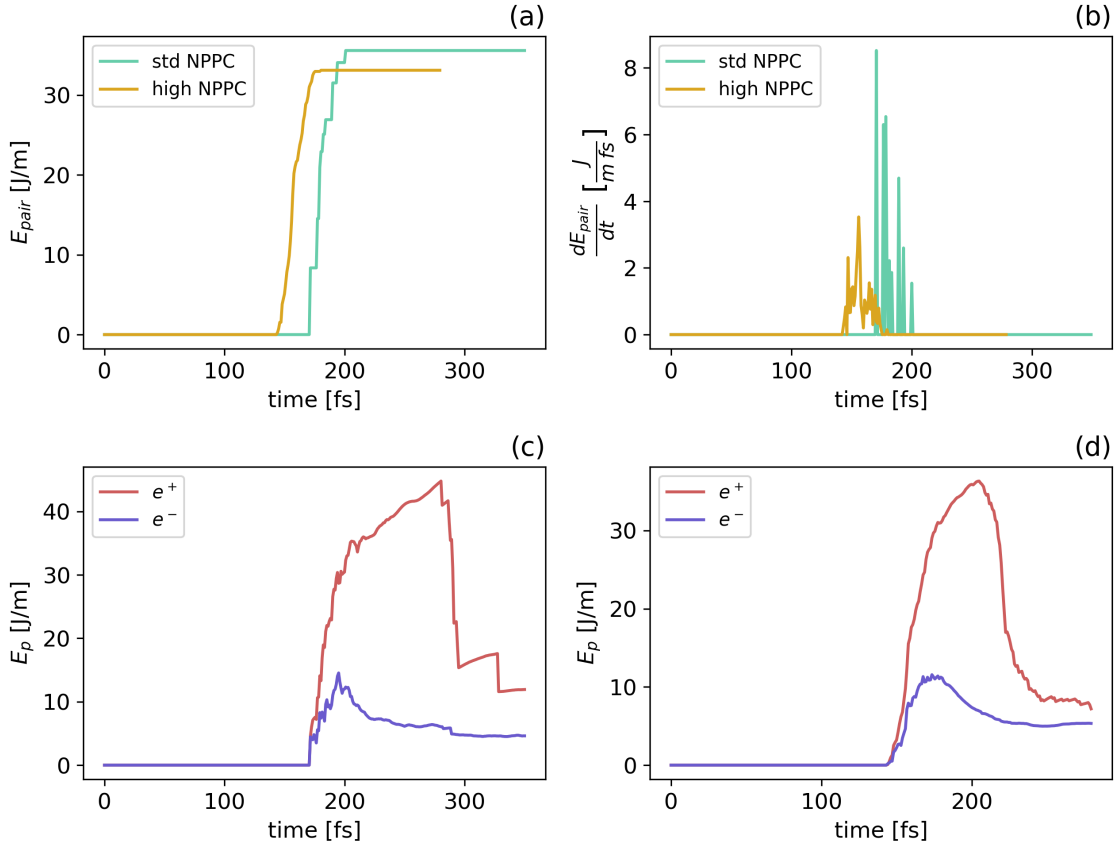

Figure 5.21: Integrated quantities associated to the produced pairs for the two simulations characterized by a standard NPPC value and an higher NPPC value for the foam electrons. The upper panels represent the time evolution of the total energy converted into pair (a) and its time derivative (b) for the two simulations. Panel (c) represents the integrated energy of pair electrons and positrons separately for the "standard NPPC" simulation, while panel (d) describes the same quantities but for the "high NPPC" simulation.

Figure 5.22 displays the distribution of energy and quantum parameter within each pair of macro-electrons and macro-positrons at their creation instant. These quantities, on average, are symmetrically distributed within the pairs, in accordance with the theoretical model, and strong deviations from even subdivision have low probability. A relevant number of particles are produced with high quantum parameter, indicating that as pairs are created, they have a high probability of emitting photons, decreasing their energy. This explains why some positrons are unable to escape the formation region and get trapped by the reflected pulse. The obtained values for the quantum parameter at the creation are explained by the fact that only photons with χ_γ approaching unity have a significant probability of converting into pairs, and at the conversion χ_γ is distributed within the produced particles. Notably, positrons and electrons are generated with energies in the hundreds of MeV. The physics of NBWPP prevents the generation of positrons with very low energies, as these events have very weak probability (see Figure 1.7).

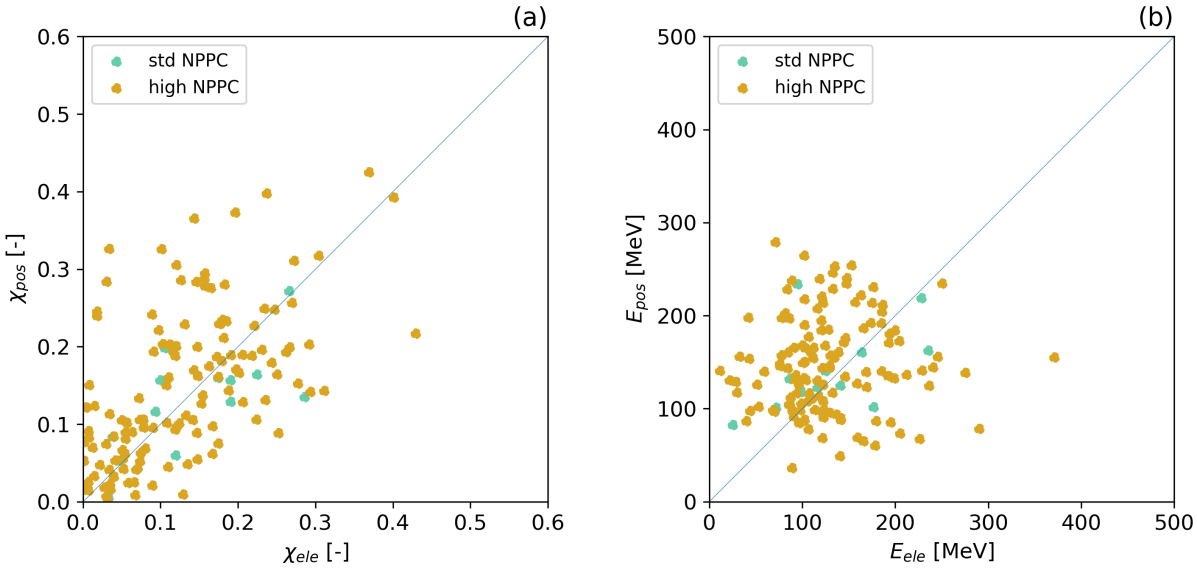

Figure 5.22: Distribution of the quantum parameter (a) and energy (b) within each macro-electron and macro-positron pair, which is represented as a dot, for the two simulations characterized by a standard NPPC value and an higher NPPC value for the foam electrons. The blue lines correspond to even distribution within the pair.

In the following, to characterize the forward-propagating positron beam, only positrons that cross a plane located at 10 μm ahead of the unperturbed substrate rear surface are considered. This choice excludes positrons that back-propagate or diverge too rapidly. Figure 5.23 shows the time behaviour of the main integral quantities associated with the positron beam. Picture (a) reports the time behaviour of the integrated number of

positrons crossing the considered plane, indicating a final value of approximately 5.8×10^5 positrons per micron. Picture (c) illustrates that the fraction of the total positron energy (see Figure 5.21) carried by the forward-propagating beam is around 95%. Panels (b) and (d) report, respectively, the number of positrons and the corresponding energy crossing the considered plane per unit time. These quantities determine the temporal duration of the positron beam and the particle intensity, which reaches levels of 10^4 positrons/fs, corresponding to 10^{19} positrons/s (per unit length).

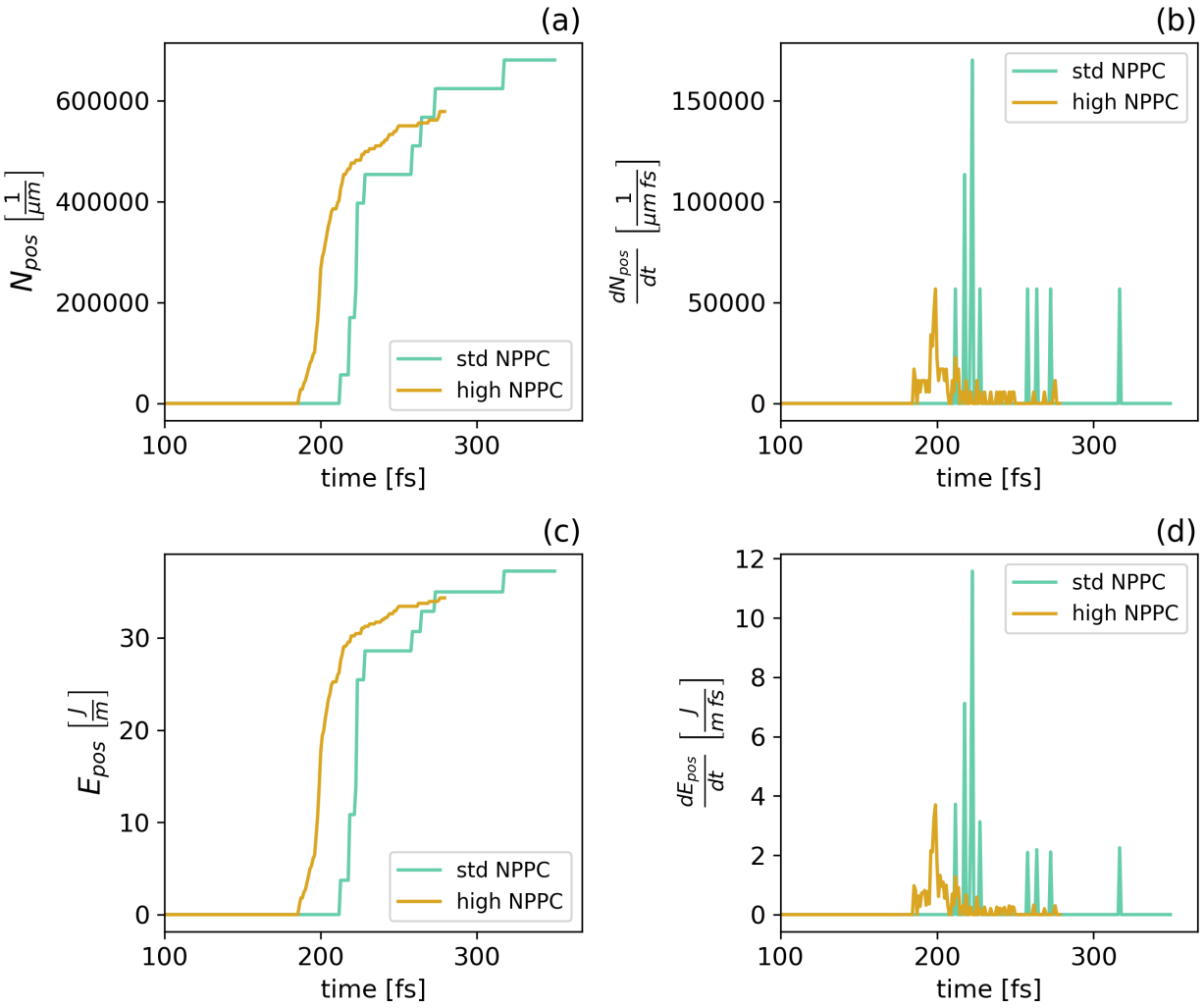

Figure 5.23: Integral quantities associated to the positrons surpassing a plane located 10 μm ahead of the unperturbed substrate rear surface for the two simulations characterized by a standard NPPC value and an higher NPPC value for the foam electrons. Pictures (a) and (c) represent the time evolution of, respectively, the total number of positrons and the total positron energy crossing that plane, while panels (b) and (d) report the time derivative of these quantities or, equivalently, the associated rates.

In the following part, some numerical estimations of physical quantities are provided, referring to the simulation with NPPC of 50. The temporal duration can be estimated as twice the root mean square of the positron time displacements from the average time $\langle t \rangle$ in which they cross the considered plane, resulting in $\tau = 2\sqrt{\langle (t - \langle t \rangle)^2 \rangle} = 33.6$ fs. The weight used in the averaging procedure is the positron energy rate shown in Figure 5.23. Figure 5.24 displays the radial distribution of the positron beam at the specified distance from the target. Positrons are confined to a micrometric transverse region, and there is a small depleted region exactly along the laser axis. The transverse dimension of the beam can be calculated as twice the mean square root of positron displacements from the laser axis y_0, resulting in $2\sqrt{\langle (y - y_0)^2 \rangle} = 15.4$ μm. Here, the weight used in the averaging procedure is the positron energy transverse distribution. Now, the average density of the beam can be estimated dividing the total number of positrons per unit length by the transverse and longitudinal ($c\tau$) dimensions of the beam, obtaining 3.7×10^{15} cm^{-3}.

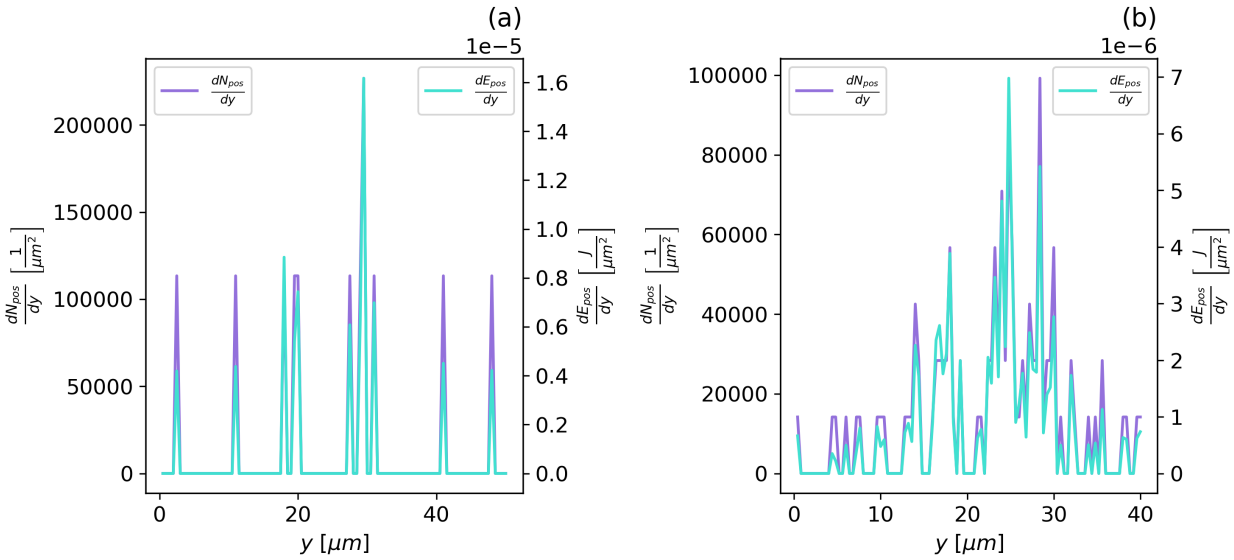

Figure 5.24: Transverse distribution in particle number and in energy of the produced positron beam for the two simulations characterized by a standard NPPC value (a) and higher NPPC value (b) for foam electrons.

The positron beam angular distribution is depicted in Figure 5.25, in terms of particle number and energy. Positrons are mainly concentrated in a cone with a half-aperture of 45°, and exhibit a wider angular spread compared to the directions of emission of the most energetic photons. The reason possibly is that photons emitted with higher angles propagate a larger distance within the laser field, and therefore possess an higher probability to convert. The divergence, calculated as the root mean square of the positron

angles using as weight the angular energy distribution, is $\sqrt{\langle\theta^2\rangle} = 0.51$ rad, corresponding to 29.2°. Then, Figure 5.26 illustrates the energy spectrum of the produced positron beam. All positrons have energy in the range of hundreds of MeV, with their spectrum peaking at 324 MeV and extending above 700 MeV. The energy spread of the spectrum is $2\sqrt{\langle(E - E^{peak})^2\rangle} = 235.4$ MeV. Here, the weight used in the averaging procedure is the positron energy spectrum. In conclusion, it is worth mentioning some results, reported in Figure 5.27, obtained for the optimal configuration of DLT parameters, which will be discussed in the next chapter. The angular distribution shows two prominent peaks at ±25° and a strongly depleted region at small angles, and possesses a divergence of $\sqrt{\langle\theta^2\rangle} = 0.5$ rad, corresponding to 28.6°. The transverse dimension of the beam 10 μm after the substrate is $2\sqrt{\langle(y - y_0)^2\rangle} = 17.2$ μm, while the temporal duration is $\tau = 2\sqrt{\langle(t - \langle t\rangle)^2\rangle} = 19.6$ fs, much shorter than the previous case. The obtained laser-to-positron energy conversion efficiency is 0.005%. The total number of positrons, belonging to the beam, per unit length is 4.5×10^7 $1/\mu$m, resulting in an average density of 4.4×10^{17} cm^{-3}, two orders of magnitude bigger than the suboptimal case. The energy spectrum is peaked at 342 MeV, extends to 800 MeV, and possess a spread of $2\sqrt{\langle(E - E^{peak})^2\rangle} = 215$ MeV. Therefore, the positron beam is more energetic and also more monochromatic.

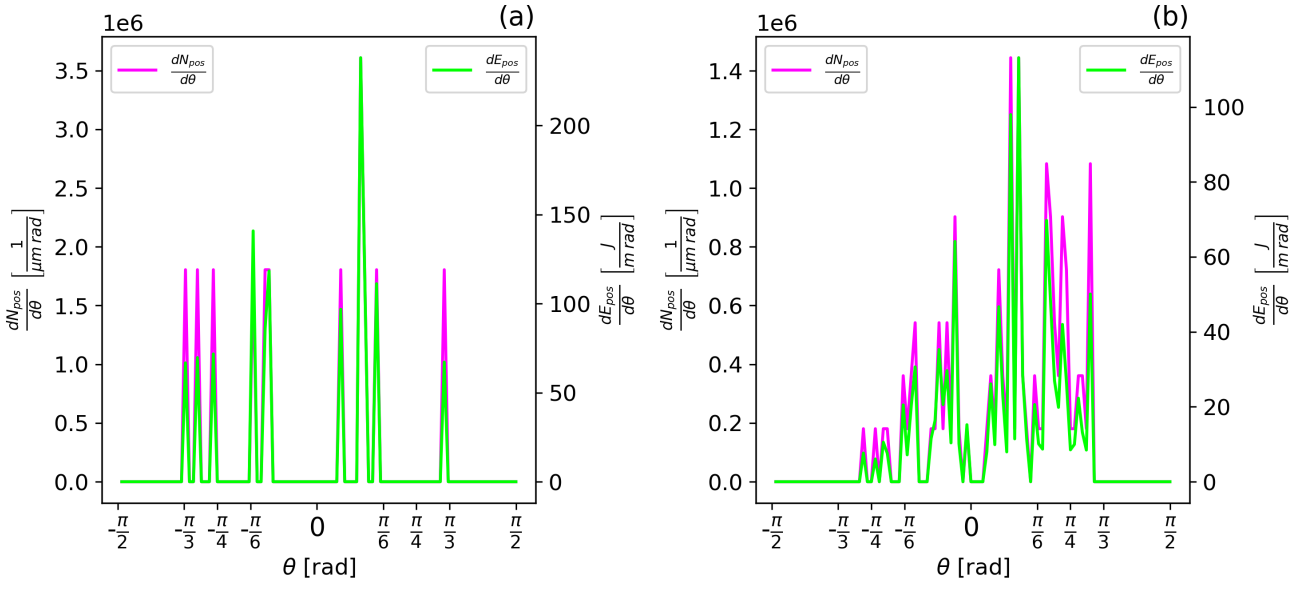

Figure 5.25: Angular distribution in particle number and in energy of the produced positron beam for the two simulations characterized by a standard NPPC value (a) and higher NPPC value (b) for foam electrons.

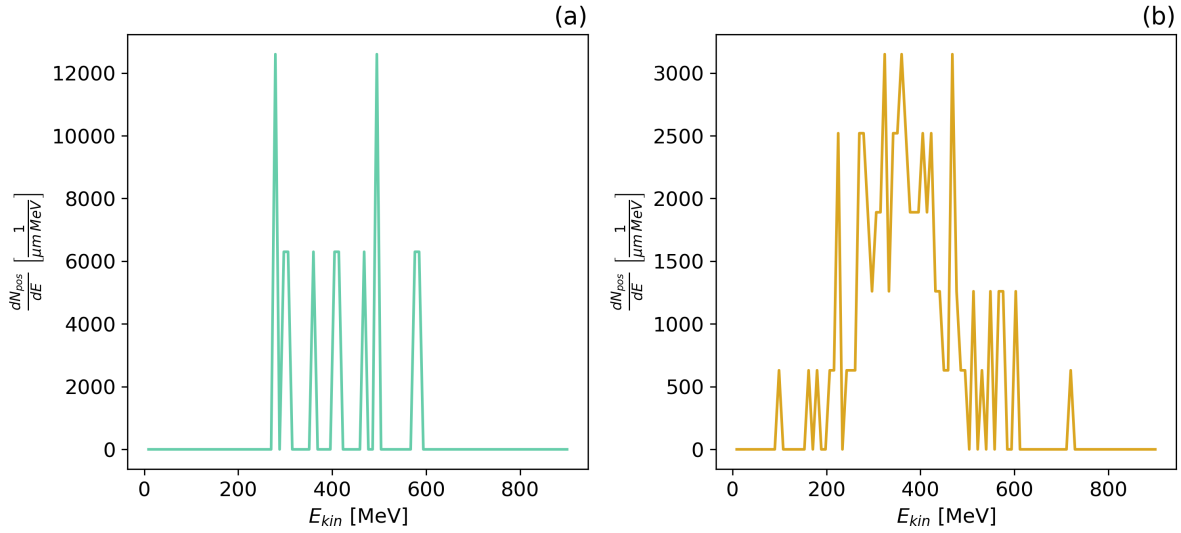

Figure 5.26: Energy spectrum of the positron beam for the two simulations characterized by a standard NPPC value (a) and higher NPPC value (b) for foam electrons.

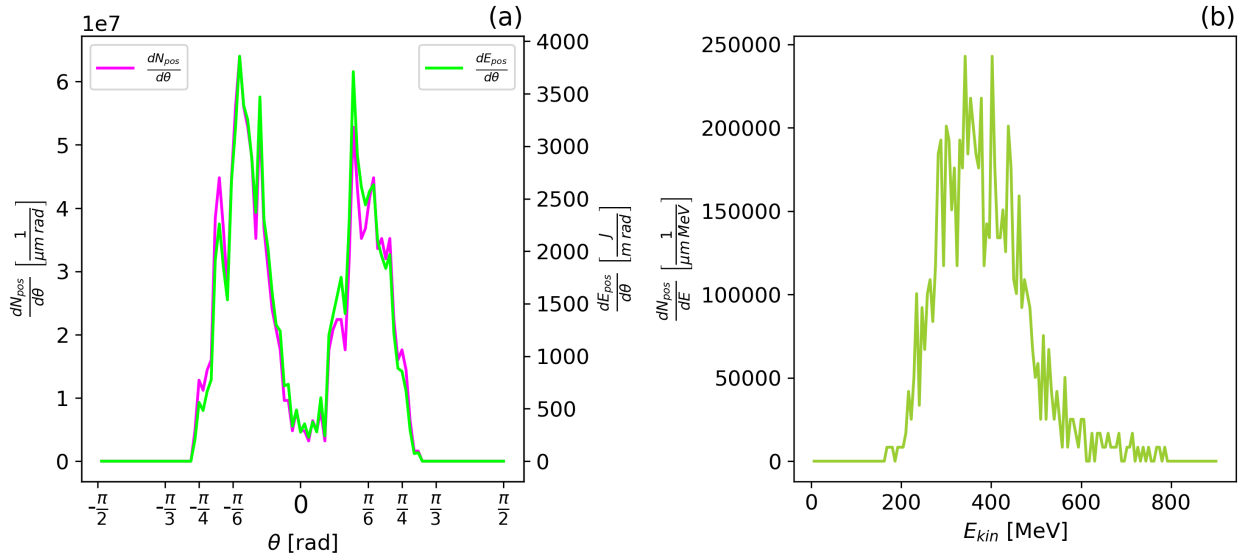

Figure 5.27: Angular distribution in particle number and energy (a) and energy spectrum (b) of the positron beam for the simulation adopting the optimal DLT parameters, which are discussed in Chapter 6.

At this point, it is possible to compare a potential NBWPP-based positron source using DLTs and a laser intensity of 4.75×10^{22} W/cm^2 with other sources presented in previous chapters. This comparison is made using the rule explained in 5.1.1 to estimate three-dimensional quantities from 2D simulation quantities per unit length. The

obtained total positron yield of 10^8 is two orders of magnitude lower than that of conventional accelerator-converter solutions explained in 1.3.1. However, since the conventional scheme spectrum peaks below 10 MeV and extends to several GeV, the obtained positron peak energy and energy spread are clearly superior, implying a higher monochromaticity and a reduced spread in time of flight, a key aspect for the eventual successive focusing of the beam. The obtained positron intensity is 7-10 orders of magnitude higher compared to conventional schemes, strongly enhanced by the femtosecond duration of the produced beam. The divergence is appreciably reduced when considering the low-energy component of beams by conventional schemes, while it is higher if considering the high-energy tail of the spectrum, which possesses a divergence of $10 - 20°$. In addition, that scheme produces beams presenting an important electron component, which is absent in the investigated case thanks to the TNSA field removing electrons. Radioactive sources, which depend on accumulation and acceleration machines, provide positron intensities 12-14 orders of magnitude lower. Consider now a comparison with other laser-plasma positron sources discussed in 2.4.3, focusing on those experimentally proven. Compared to the LWFA-converter scheme, where the positron spectrum peaks below 200 MeV and extends up to 470 MeV, the obtained positron peak energy of 350 MeV and maximum energy of 800 MeV are larger, indicating more energetic positrons. Although the obtained total positron yield is one order of magnitude lower, the average positron density of 10^{17} cm^{-3} is one order of magnitude higher than the peak density by LWFA-converter solution. Similar to conventional schemes, this setup also presents a significant electronic component (not below 50% of the beam). The scheme employing a long kJ-energy pulse ($I^{peak} = 10^{19} - 5 \times 10^{20}\,W/cm^2$) and converter produces a quantity of positrons 2-3 orders of magnitude larger than the analyzed setup, corresponding to a laser-to-positron conversion efficiency 2-10 times higher, and a divergence of 5-10° less. However, the positron spectrum of that scheme peaks at 3-19 MeV, much less energetic than the obtained one. To conclude, the numerically investigated schemes employing much more intense lasers ($I^{peak} \sim 10^{23} W/cm^2$) generally provide a 2-3 orders of magnitude larger positron yield and 2-10 times higher conversion efficiency, while maintaining a similar positron divergence and positron spectrum peak energy.

5.2. Discussion of the criticalities of MC module for NBWPP

This section is devoted to the analysis of the most critical aspects and limitations when simulating NBWPP using the Monte Carlo module of available open-source PIC-MC

codes. Firstly, the theoretical and numerical approximations are summarized and discussed, followed by the investigation of the role of the most important setting parameters and the intrinsic statistical limitations of PIC-MC codes, with supporting arguments based on the results of 2D simulations.

5.2.1. Theoretical approximations

Several assumptions are introduced within the theoretical model to achieve a description which is applicable to realistic scenarios, while other approximations are employed to simplify the implementation of the processes in simulation codes. In addition, a series of low-probability processes is not included into the codes to prevent an excessive demand on computational resources.

Consider now the assumptions made in the description of NBWPP and photon emission processes, which were discussed, along with their physical significance, in Section 1.2.3. The analytical calculations of the rates and spectra were performed by considering the processes occurring in the field of a plane wave. While such a field is not realistic for various reasons, including its implied infinite power, under certain conditions the description of the processes in any field becomes equivalent to that in a plane wave. This equivalence ensures the validity of the expressions for rates and spectra. The first assumption pertains to the field strength or intensity, requiring that $a_0 \gg 1$, where $a_0 \sim 1$ for $I \sim 10^{18}$ W/cm^2. However, pair production by NBWPP is activated at intensities well above this threshold value, because high-energy photons are necessary, and such photons require strong fields to convert into pairs. Therefore, if pair production occurs, the first condition is broadly satisfied. The second assumption can be expressed in terms of the relativistic invariants of the electromagnetic field normalized by the Schwinger field. These invariants are required to be much smaller than unity and the quantum parameter of the emitting particle. To verify this assumption, the two invariants are calculated at the reflection of the laser pulse ($t = 176$ fs) for the simulation with the standard value of NPPC . The first normalized invariant $g = (c\boldsymbol{B} \cdot \boldsymbol{E})/E_s^2$, where E_s is the Schwinger field, is found to be zero, indicating that the fields are always almost perpendicular. This is reasonable because even when the reflected and incident pulses overlap, resulting in a standing wave, the fields remain orthogonal. Additionally, since B_x is always null, E_x does not contribute to the scalar product. The other normalized invariant $f = (c^2|\boldsymbol{B}|^2 - |\boldsymbol{E}|^2)/2E_s^2$ at the reflection is shown in Figure 5.28. Even if it is not exactly zero, since the standing wave formation leads to fields amplitudes that are different due to their half-period phase shift, the values assumed are very small. This is because the fields at play are much weaker than the Schwinger field.

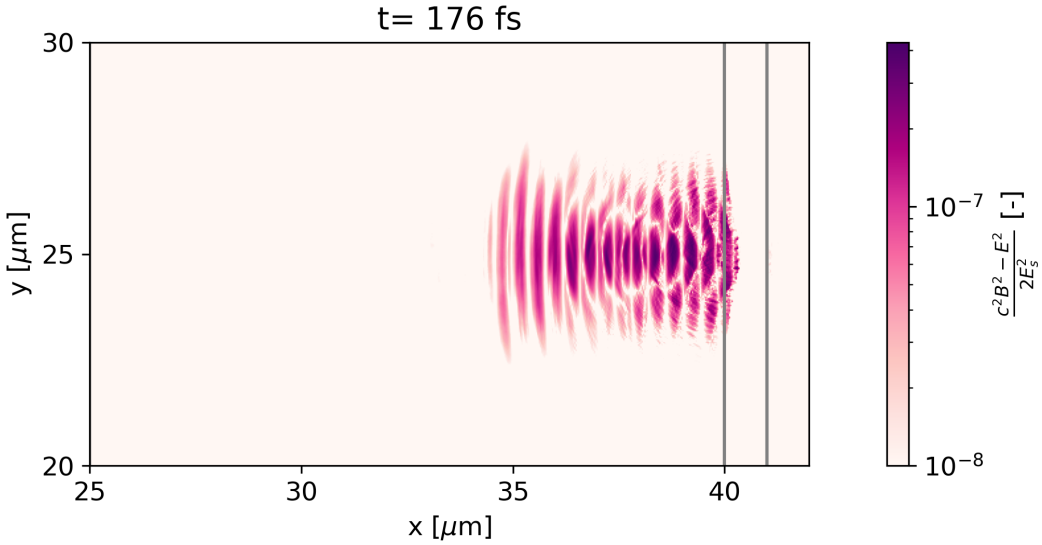

Figure 5.28: Relativistic invariant, normalized by the Schwinger field, associated to the electromagnetic field, evaluated at the reflection of the laser pulse for the simulation with standard NPPC value for foam electrons. The gray lines represent the unperturbed substrate.

Then, in order to simplify the formulas relating particle kinematic quantities and reduce the complexity of implementation in numerical codes, the assumption of relativistic particles is introduced, which implies collinear emission. In general, this assumption is valid, as demonstrated by the energies of photons and particles produced through NBWPP presented in previous sections. The reason is that only photons with energies in the range of hundreds of MeV have significant probability to convert, and subsequently their energy is distributed within the created pair, resulting in positrons and electrons having energies in the same range. As explained in Sections 1.2.2 and 1.2.3, using the ultra-relativistic assumption, an approximate energy conservation law can be derived, which is then implemented in simulation codes. However, this law is affected by two problems: the non-conservation of momentum and the disregard of energy and momentum contributions from the external field. In particular, the error in momentum conservation tends to zero when particles mass becomes zero, meaning that the more ultra-relativistic the particles are, the smaller the error becomes. Assuming that $\mathcal{E}_{\pm} \gg m_e c^2$, the photon momentum that disappears in a NBWPP event is estimated as:

$$\frac{\Delta p}{p_\gamma} \equiv \frac{p_\gamma - p_+ - p_-}{p_\gamma} \simeq 2\frac{(m_e c^2)^2}{\mathcal{E}_+ \mathcal{E}_-} \tag{5.1}$$

The neglect of energy and momentum contributions from the field can be justified by considering that, when particles possess ultra-relativistic energies, the field contribution to their energy and momentum becomes irrelevant. The energy extracted from the field was estimated in 1.2.3 as in the order of a few MeV, supporting the previous argument. While these two approximations are insignificant for individual processes, errors may accumulate when a large number of QED processes occur, potentially leading to non-negligible effects. Similar arguments apply to photon emission as well, see Section 3.2.2. As a result, the total energy and momentum in simulations are not exactly conserved. Nevertheless, in the considered regime where QED events are not highly numerous, these sources of errors can be neglected for both particles and the field.
On the other hand, several processes are typically neglected in PIC-MC codes due to their low probability and additional computational load required for their simulation. In the context of pair production, these processes include the Bethe-Heitler (BH) process, along with its trident version, which are described in Section 1.2.1. As anticipated in 2.4.2, these processes require dense and high-Z materials, and therefore in principle they can occur in the substrate. However, in all the positron sources based on the BH processes, discussed in 1.3.1 and 2.4.3, typically employ millimeter-range thick converters. The DLTs considered in this thesis work have an overall thickness of tens of μm, making BH processes ineffective and justifying their neglect. Additional non-simulated processes involving positrons consist in single-photon absorption and pair annihilation. Their neglect is motivated by their low probability, except for very specific situations [20]. For the same reason, the trident NBWPP, presented in 1.2.2, is also neglected. Finally, higher-order QED corrections, such as loop corrections, are not considered in the simulation codes.

5.2.2. Role of the sampling parameter

The first important setup parameter affecting the simulation of NBWPP is the photon sampling. It is a numeric parameter, without physical meaning, that determines the number of macro-photons created at each photon emission event, ensuring the conservation of the total weight of the emitted macro-photons. To qualitatively investigate this numerical parameter, a series of "low-resolution" 2D simulations have been performed. These simulations do not aim to study physical aspects of pair production, so the criterion for spatial resolution is not strictly satisfied, and lower densities are considered to reduce also the NPPC values. These choices significantly reduce the computational load, making it possible to execute them using very few computational resources. The main differences compared to the simulations in the rest of the chapter are briefly described. The simulation duration is 290 fs, and the peak of the laser pulse enters the box after 20 fs from

the beginning. The size of the box is reduced to 60 μm $\times$ 40 μm, maintaining the same target materials, dimensions, and position within the box, except for the substrate density which is set to 130 n_c. The spatial resolution is 20 points per micron, the CFL is 0.95, and the NPPC values are 2 for both electrons and ions of the foam, and 15 for those of the substrate. Other secondary differences in the photon emission module are present but not relevant for the purpose of this part. Four simulations are performed, each with a different value of the photon sampling, and the chosen values are 1,3,6,9. In the following, the results of these simulations are considered.

Figure 5.29 displays snapshots of the final stage of the interaction for the four simulations, showing the positron trajectories, from their creation to the time considered, as red lines. The first evidence is that increasing the photon sampling parameter results in an increased number of macro-positrons produced, especially when the sampling parameter changes from 1 to 3. Considering higher values of the parameter, this increase becomes less pronounced. Creating more photons with lower weight enhances the statistics of pair production, since the sampling of NBWPP occurrence is made over a larger population of macro-photons. As a result, the number of NBWPP events is boosted, leading to the generation of more macro-positrons but with lower weight, meaning that they represent a lower number of real positrons. According to the results obtained, the number of NBWPP events is strongly affected by the photon sampling when it is low, and this sensitivity reduces when increasing the parameter. Figure 5.30 illustrates the time behaviour of the energy converted into pairs and the integrated positron energy. In this case, when increasing the photon sampling from 1 to 3, these physical quantities are significantly affected, while above a photon sampling of 3, their variations due to the sampling parameter are not distinguishable from statistical fluctuations. It is crucial for physical quantities like these not to depend on numerical parameters, otherwise the simulated physical system would not be realistic. This argument justifies the choice of setting the photon sampling to 3 in all the other simulations presented in this thesis work. A further increase would improve the statistics of positron creation and the subsequent dynamics, since more macro-positrons are produced and simulated, without affecting the physics of the simulated system. Even if an increase in the photon sampling beyond 3 allows for a better characterization of the produced positrons, it comes at the cost of significantly increasing the computational load, since the number of photons generated and considered by the particle pusher and MC module becomes several times larger. Therefore, the value of 3 represents a good compromise between avoiding non-physical effects and utilizing computational resources efficiently.

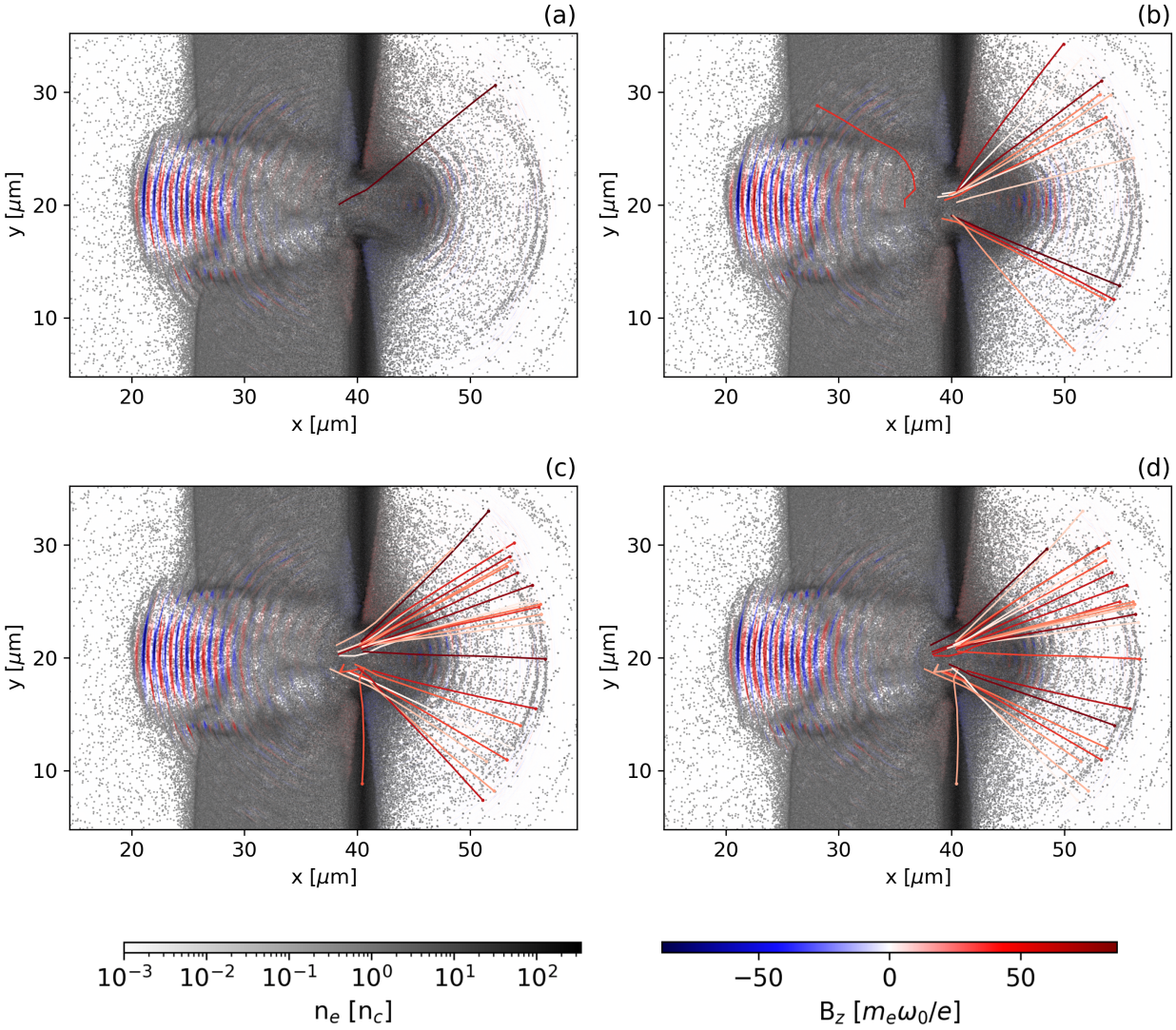

Figure 5.29: Snapshot of the laser-DLT interaction at the final stage ($t = 210$ fs) for the four simulations at low resolution aimed to the study of the photon sampling parameter, which is set to 1 (a), 3 (b), 6 (c) and 9 (d). The DLT is represented through its electronic density, the pulse through the B_z component and the red lines represent the macro-positron trajectories from their production by NBWPP to the time considered. SMILEI units are adopted.

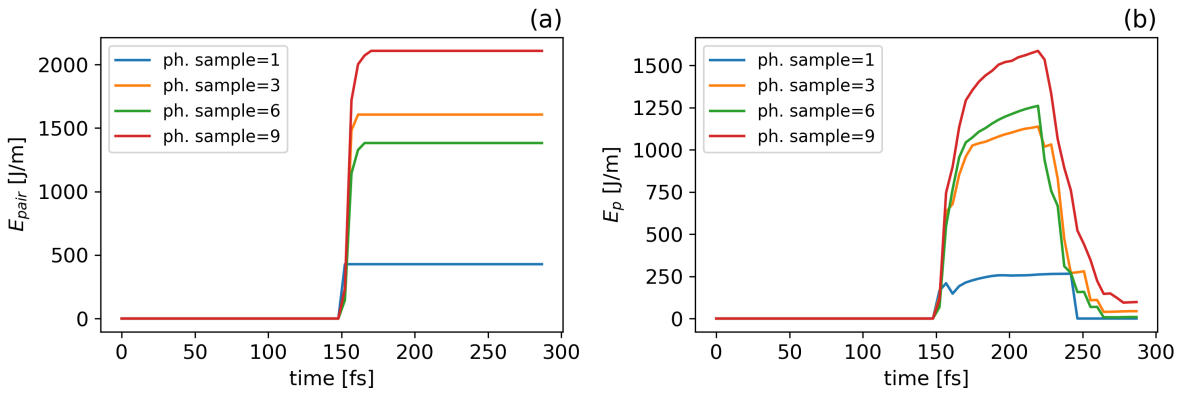

Figure 5.30: Time evolution of the energy converted into pairs (a) and the integrated positron energy (b) for the four simulations at low resolution aimed to the study of the photon sampling parameter.

It is worth mentioning that some PIC-MC codes, such as SMILEI, provide the option to set the sampling parameters for the macro-electrons and macro-positrons generated at each NBWPP event. Increasing this parameter for positrons would improve the statistics of their dynamics by simulating more positrons with lower weights, but not in terms of their generation properties. To conclude about the photon sampling, it does not impact the photon distribution function, and therefore it does not improve the exploration of the tails. To achieve that, as discussed in the following section, the initial number of macro-electrons must be increased.

5.2.3. Statistics limitations and impact of the number of particles per cell

The macro-particle description in PIC-MC codes presents significant limitations related to the statistics of the simulated processes, and these limitations becomes even more pronounced for single-particle processes like photon emission and pair production. As discussed in Section 3.3.2, simulating processes that involve a small number of real particles, fewer than the macro-particle weights, is prevented. Consequently, the tails of the distribution functions are not simulated. Each event, along with its outcome, represents a large number of particles undergoing the same process at the same time and producing the same secondary particles. For example, PIC-MC codes are unable to simulate photon emission by a small number of electrons, and in each event millions of electrons emit simultaneously, producing an equal number of photons with the same energy and momentum. The same applies to pair production, where in each NBWPP event millions of photons

undergoing conversion produce an equal number of positrons in the same state. This discrepancy also contradicts the quantum nature of the processes, where in principle each particle should have different probabilities of undergoing a certain event. As a result, the spectra of the emitted secondary particles are not continuous but discretized, especially near the tails, where the probability of emission is lower, and the tails are truncated. For example, refer to the electron, photon, and positron spectra shown in Figures 5.10, 5.18 and 5.26, respectively. In the context of positron production, the limited statistics affecting the high-energy and high-χ regions of the photon spectra can substantially impact the number of positrons generated and their characteristics.

Improved statistics can be achieved by increasing the initial number of particles per cell, hence simulating more macro-particles with lower weights. This results in each process being representative of a smaller number of particles and, consequently, better exploration of the distribution function tails. It is interesting to analyze how the electron and photon spectra, represented in Figures 5.10 and 5.18, modify when the NPPC value is increased. Figure 5.31 reports relevant spectra for foam electrons and photons in the two simulations with a standard and higher NPPC values. With an increased NPPC value, electron cutoff energy at the onset of reflection does not change significantly, while the electron quantum parameter tail extends to higher values. Consequently, more energetic photons with increased quantum parameter are emitted, as shown in panels (c) and (d), demonstrating the improved exploration of the photon spectra tails. Increasing the NPPC value results in a significant enhancement in the number of NBWPP events, as depicted in Figure 5.22. While this increase in statistics maintains the energy converted into pairs and the final total positron energy almost unaffected, as seen in Figure 5.21, it allows for a better positron characterization, including their energy, angular, and transverse distribution, as displayed in Figures 5.24, 5.25 and 5.26. However, the benefit of increasing the NPPC value, in terms of NBWPP simulation, is more pronounced when the number of macro-positrons produced is small, as in the low-NPPC simulation. It is important to note that while increasing NPPC improves statistics, it also exponentially increases the computational load of the simulation.

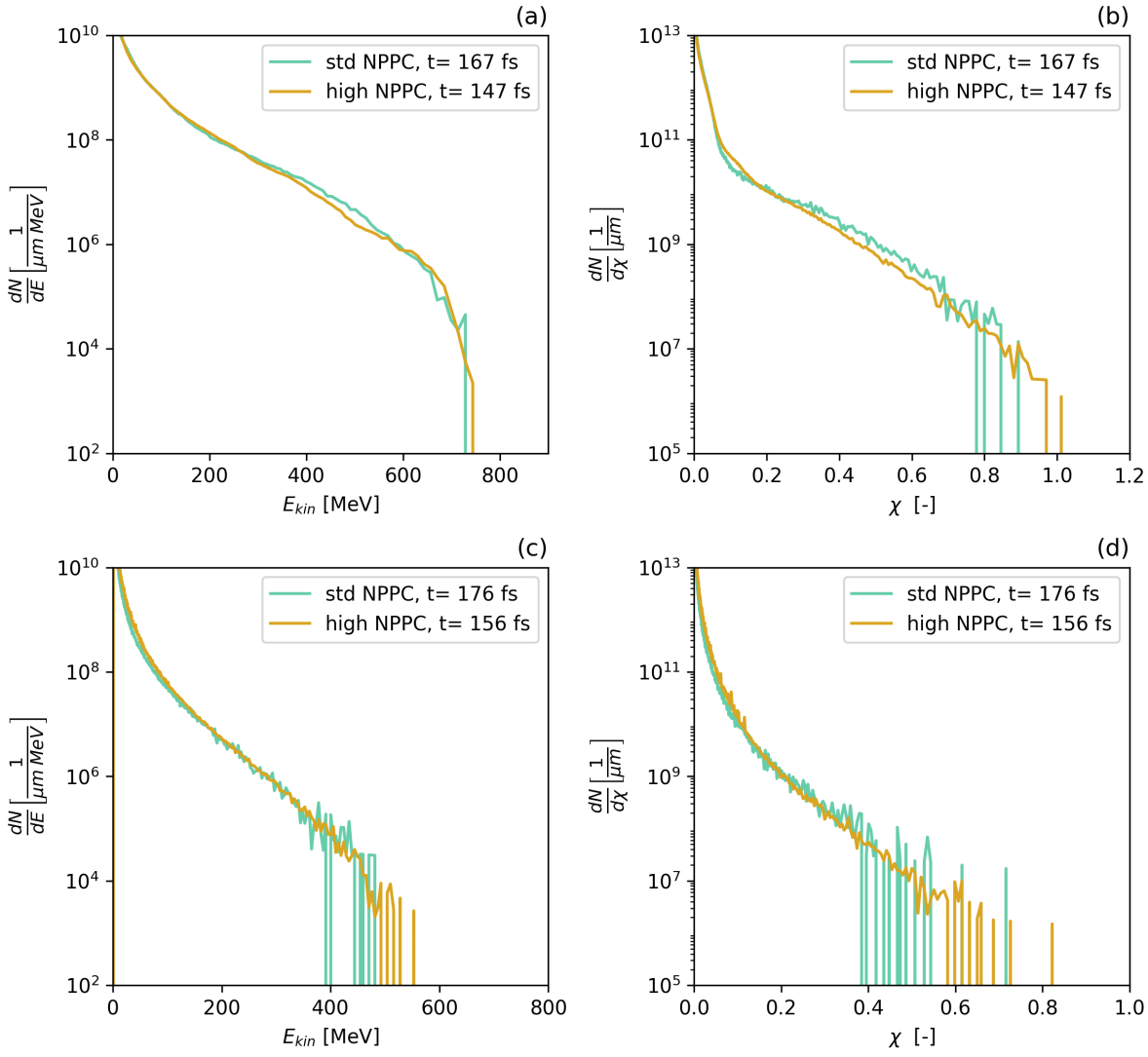

Figure 5.31: Spectra as a function of the kinetic energy and quantum parameter for the foam electrons (a,b) and photons (c,d) for the two simulations characterized by a standard NPPC value and an higher NPPC value for the foam electrons. The electron spectra are evaluated at the onset of reflection, while the photon ones during reflection.

Since the number of simulated macro-particles cannot be increased arbitrarily, and the adopted NPPC values are typically lower than the value used in the high-NPPC simulation, statistics limitations arising from the macro-particle description are unavoidable. It is interesting to compare the results obtained from the simulation with improved statistics to the theoretical predictions. To achieve this, the theoretical positron generation spectrum and energy converted into pairs are calculated, by using the NBWPP spectrum and total rate, presented in Section 1.2.2, along with the time evolution of the photon population given by the high-NPPC simulation. The back-effects of pair production on the

photon population are taken into account by the simulation itself, through the simulated NBWPP events. The theoretical positron generation spectrum and the energy converted into pairs can be expressed as follows:

$$\frac{dN_+}{d\mathcal{E}_+} = dt \sum_{t_n} \sum_{\gamma} w_\gamma^n \frac{d^2 N_+}{d\mathcal{E}_+ dt}\bigg|_{t_n,\gamma} = dt \sum_{n} \sum_{\gamma} w_\gamma^n \frac{\chi_\gamma^n}{\mathcal{E}_\gamma^n - 2m_e c^2} \frac{d^2 N_+}{d\chi_+ dt}(\chi_\gamma^n, \mathcal{E}_\gamma^n, \chi_+) \tag{5.2a}$$

$$E_{pair} = dt \sum_{t_n} \sum_{\gamma} w_\gamma^n \mathcal{E}_\gamma^n \frac{dN_+}{dt}\bigg|_{t_n,\gamma} = dt \sum_{n} \sum_{\gamma} w_\gamma^n \mathcal{E}_\gamma^n \frac{dN_+}{dt}(\chi_\gamma^n, \mathcal{E}_\gamma^n) \tag{5.2b}$$

where w_γ^n represents the weight of the photon γ at time t_n, and a summation over all time-steps t_n and all photons γ is performed. The adopted relation between the positron quantum parameter χ_+ and energy $\mathcal{E}_+$ is that implemented in PIC-MC codes, which is discussed in Section 3.2.2. The comparison between the simulation results and theoretical prediction is presented in Figure 5.32. On average, the simulated generation spectrum follows the shape of the theoretical one. However, its discrete nature due to limited statistics leads to important deviations, in both excess and defect, compared to the theoretical predictions. The peak positions are in good agreement, while the cut-off energy is underestimated in simulations, once again because the tails are not accurately simulated. On the other hand, the total energy converted into pairs matches quite well, with deviations not distinguishable from statistical fluctuations. In conclusion, it can be stated that the Monte Carlo module of PIC-MC codes generally provides accurate results for integrated quantities, while lacks of limited statistics for the characterization of the populations, particularly when the number of macro-particles is restricted due to low-probability of generation or suboptimal conditions for their production.

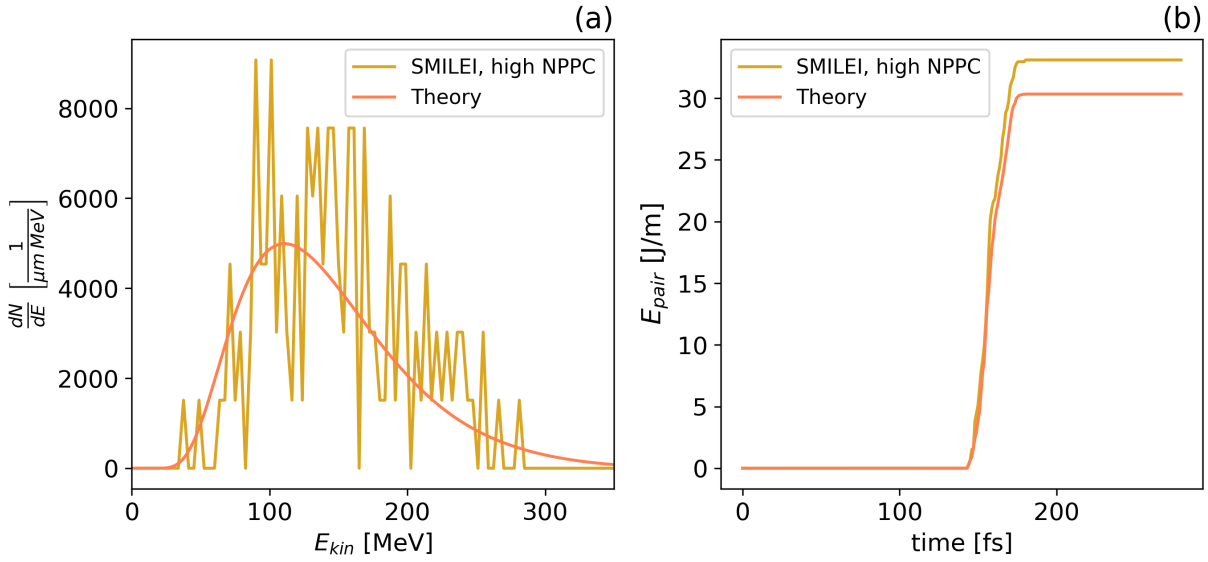

Figure 5.32: Comparison between theoretical predictions and simulation results in the positron generation spectrum (a) and the total energy converted into pairs (b). The simulation characterized by the higher value of NPPC value for foam electrons is considered.

It is worth mentioning a modified PIC-MC algorithm in which the macro-particle weights change dynamically during the simulation [10]. For each macro-particle involved in quantum processes, the MC algorithm is performed multiple times n_q simultaneously, and if the particle emits, a secondary particle with a weight n_q times smaller than that of the parent particle is created. To prevent a dramatic increase in the total number of macro-particles, a minimum weight for secondary particles is introduced. This approach allows a simulation with a lower number of initial macro-electrons to provide the same photon or positron distribution as a simulation with a higher initial particle number. However, also this method significantly increases the utilization of computational resources.

6 | DLT parameter optimization for a NBWPP positron source

The final chapter of this thesis work delves into the results of a parametric campaign of 2D simulations, performed to examine the impact of the DLT parameters concerning positron production and its characteristics. Initially, the parameters of the solid-density metallic layer are analyzed, followed by an exploration of those pertaining to the low-density layer. The laser properties are maintained constant. The primary objective of this chapter is to identify an optimal target configuration that maximizes positron production efficiency, while maintaining the laser intensity considered in the previous chapters.

6.1. Impact of the metallic layer's parameters

The analysis performed in Chapter 5 outlined the role of the metallic layer, or substrate. It serves as plasma mirror to efficiently reflect the laser pulse, enhancing the intensity during the superposition between the incident and reflected components, and providing the optimal interaction geometry of electrons and photons with the laser field. This creates the optimal conditions for high-energy photon emission and subsequent photon conversion into pairs. A critical property of the substrate is its reflectivity, as it influences the laser intensity distribution and its availability for interaction, crucial for efficient photon emission and pair production. An improved reflectivity limits the laser energy deposition within the substrate, preventing unnecessary heating of electrons and ions and the generation of photons which are inefficient in pair production. The reason, as anticipated in the previous chapter, is the low energy and interaction efficiency affecting these photons. It is important to stress that the laser reflected component is more important than the incident one, due to interaction geometry reasons, supporting the primary role of substrate reflectivity in positron production. The analysis of particle dynamics and photon emission presented in the previous chapter demonstrated that the aluminum substrate's reflectivity might not be optimal due to the high energy deposition within it. This realization prompts the exploration of alternative substrate configurations with superior reflectivity.

This investigation involves examining various substrate properties, including the density, atomic mass, and thickness, independently, in order to individuate the key factors for optimizing positron production. The results of this analysis will help to identify the best materials for the substrate. In this section, after the discussion of simulation setups, the differences in the substrate behaviour, concerning laser reflection and pair production, by changing separately each substrate property are analyzed. The results from the simulation, featuring a standard NPPC value (= 5) for foam electrons, discussed in Chapter 5 are used in this part as basis of comparison for the effects of different substrate properties.

6.1.1. Simulation setup

Compared to the "standard NPPC" simulation settings detailed in the previous chapter, specific adjustments are made to investigate, individually, the substrate density, atomic mass, and thickness. Consequently, three additional 2D simulations are performed, each delving into a distinct substrate parameter: the first adopts a reduced substrate electron density of 100 n_c, the second employs a non-realistic atomic mass for substrate ions set to 197, and the last simulation involves an increased thickness of 5 μm. The selected value for the atomic mass is equivalent to that of gold, a typical material used in literature as plasma mirror in composite targets. Laser properties, box dimensions, spatial and temporal resolutions, NPPC values, and MC module settings remain unchanged. The setups of these three simulations are summarized in Table 6.1.

Impact of substrate parameters			
Box size ($x \times y$)	70 μm $\times$ 50 μm	Grid points ($x \times y$)	4480 $\times$ 3200
Time duration	350 fs	CFL	0.95
Substrate properties			
Z	13	Density n_e	$100 - 450$ n_c
A	$27 - 197$	Thickness	$1 - 5$ μm
NPPC electrons	30	NPPC ions	6
Carbon foam properties			
Density n_e	2 n_c	Thickness	15 μm
NPPC electrons	5	NPPC ions	1

Table 6.1: Parameters of the 2D simulations performed to study the impact of substrate density, atomic mass, and thickness on NBWPP.

6.1.2. Discussion of the results

In this section, the capability of the four different substrates, including the reference one considered in Chapter 5 and those with altered density, atomic mass, and thickness, to reflect the laser pulse and efficiently produce pairs, is analyzed. Since the foam and laser properties are unchanged with respect to the reference simulation, the initial electron and field dynamics up to the laser reflection, including the pulse impinging on the target and propagating within the foam, accelerating electrons, remains identical. Therefore, the electron energy spectrum and field distribution remain consistent with those presented in Chapter 5. When the laser impacts the substrate and begins reflection, the distinct substrate properties come into play. Initial insights into the differences in reflectivity among the four substrates can be derived from the energy evolution in time of the electromagnetic field, photons, and substrate populations, depicted in Figure 6.1. The first evidence consists in the strong reduction of the energy deposited within the substrate as the atomic mass increases. Specifically, the energy transferred to substrate electrons nearly halves, while for substrate ions it decreases to less than one third compared to the reference case. As a result, the total electromagnetic energy retained during reflection remains considerably higher. This illustrates how high reflectivity reduces energy deposition within the substrate, redirecting it to the pulse superposition region to support pair production. Increased thickness leads to a notable decrease in the energy transferred to ions, while the energy absorbed by electrons is higher, likely due to the larger number of electrons in a thicker substrate. Then, the energy converted to photons is notably lower for both the heavier and thicker substrates, signifying a reduction in the energy wasted on low-energy photon emission within the substrate. Conversely, the low-density substrate demonstrates a substantial energy conversion into photons, indicating the penetration of the pulse within the substrate and the resulting low-energy photon emission by a significant quantity of electrons. It is essential to note that the integrated photon energy primarily represents the amount of low-energy, non interesting photons, rather than the most energetic ones. This is due to the many orders of magnitude higher number of photons in the MeV range than the ones in the hundreds of MeV, as visible in the photon spectra in Figure 5.18. These observations suggest that reflectivity is enhanced by increasing substrate thickness and atomic mass, with the latter having the most pronounced beneficial effect. Instead, in line with the theory of interaction regimes discussed in 2.3, reducing density results in lower reflectivity.

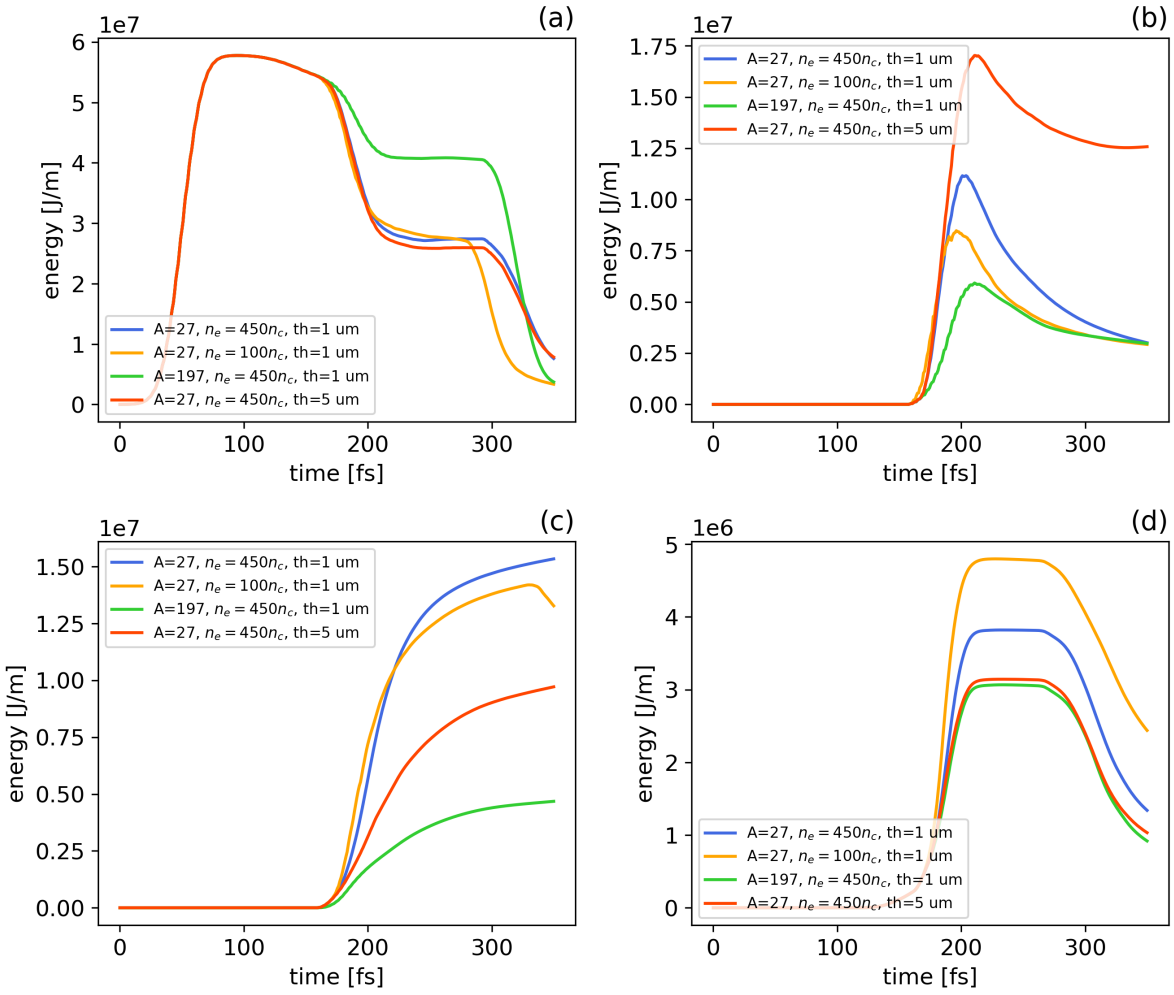

Figure 6.1: Evolution in time of the integrated energy of the electromagnetic field (a), substrate electrons (b), substrate ions (c), and photons (d) for the four simulations devoted to the investigation of the impact of substrate properties on laser reflection and NBWPP.

Figure 6.2 illustrates the electromagnetic intensity distribution at $y = L_y/2$ during the laser reflection. In the early stages of reflection ($t = 176$ fs), it is already evident that the low-density substrate fails to reflect the laser pulse. Instead, the pulse penetrates and traverses this substrate due to its relativistic under-critical density for the given intensity, resulting in degraded reflectivity. When increasing the thickness, there are not substantial differences in the intensity distribution, except for lower values within the substrate. On the other hand, a higher atomic mass significantly enhances the intensity at the front of the substrate, specifically in the superposition region, throughout the duration of laser reflection. In the final stage of reflection ($t = 191$ fs), the pulse partially penetrates the "reference" and thicker substrates, while it is almost perfectly reflected by the substrate

with higher atomic mass. This explains the notable reduction in energy deposited within the substrate for this latter case. Remarkably, the high-intensity region for the heavier substrate is not only more pronounced but also more extended compared to the other cases.

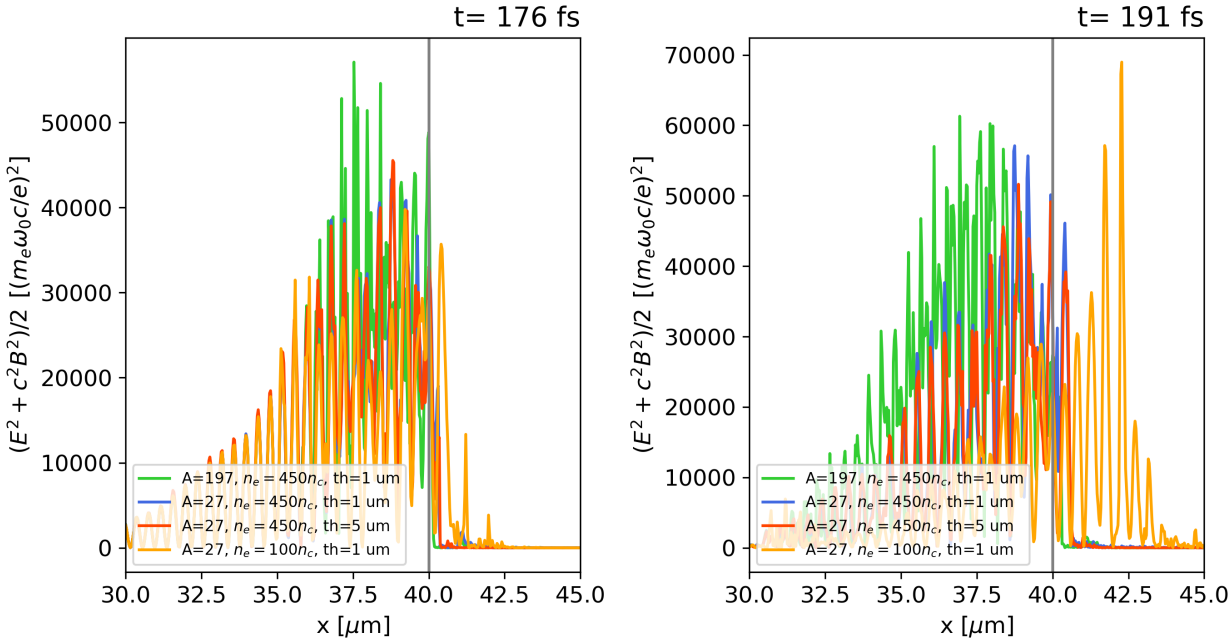

Figure 6.2: Snapshots of the quantity $(E^2 + c^2B^2)/2$ at $y = L_y/2$ at different times during the reflection of the laser pulse for the four simulations devoted to the investigation of the impact of substrate properties on laser reflection and NBWPP. The gray line represents the beginning of the unperturbed substrate. SMILEI units are adopted.

Figure 6.3 displays the photon density profile and the average photon quantum parameter at $y = L_y/2$ during the laser reflection. Once again, from the photon quantum parameter distribution it is evident that the region providing the conditions for pair production coincides with the superposition region between the incident and reflected laser pulses. In contrast, photons produced within the substrate do not contribute to positron generation, and represent only a waste of laser energy. The low-density substrate results in a significantly higher concentration of produced photons compared to other cases, yet the average photon quantum parameter remains globally smaller. This occurs because the pulse traverses the substrate without significant reflection, leading to suboptimal interaction conditions for the produced photons. On the other hand, a thicker substrate results in a reduction of photon density produced within it, accompanied by a considerable increase in the average photon quantum parameter within the laser field's superposition region.

These beneficial effects are even more pronounced in the case of a substrate with higher atomic mass, where both quantities are optimized, minimizing laser energy wastage and enhancing photon conversion into pairs. These observations align with the behaviour of the integrated photon energy for the different substrates discussed earlier.
The relevant photon spectra as a function of energy and quantum parameter are illustrated in Figure 6.4. While clear distinctions in the energy spectrum are obscured by poor statistics affecting the high-energy tail, notable differences appear in the χ spectrum. Both the thicker and heavier substrates enhance the high χ tail, increasing its population and extending it toward higher values. Conversely, the low reflectivity of the substrate with reduced density leads to a degradation in the values of the photon quantum parameter. It is important to remember that the photon quantum parameter spectrum accounts for the effectiveness of both the photon emission phase and their subsequent interaction with the laser field.

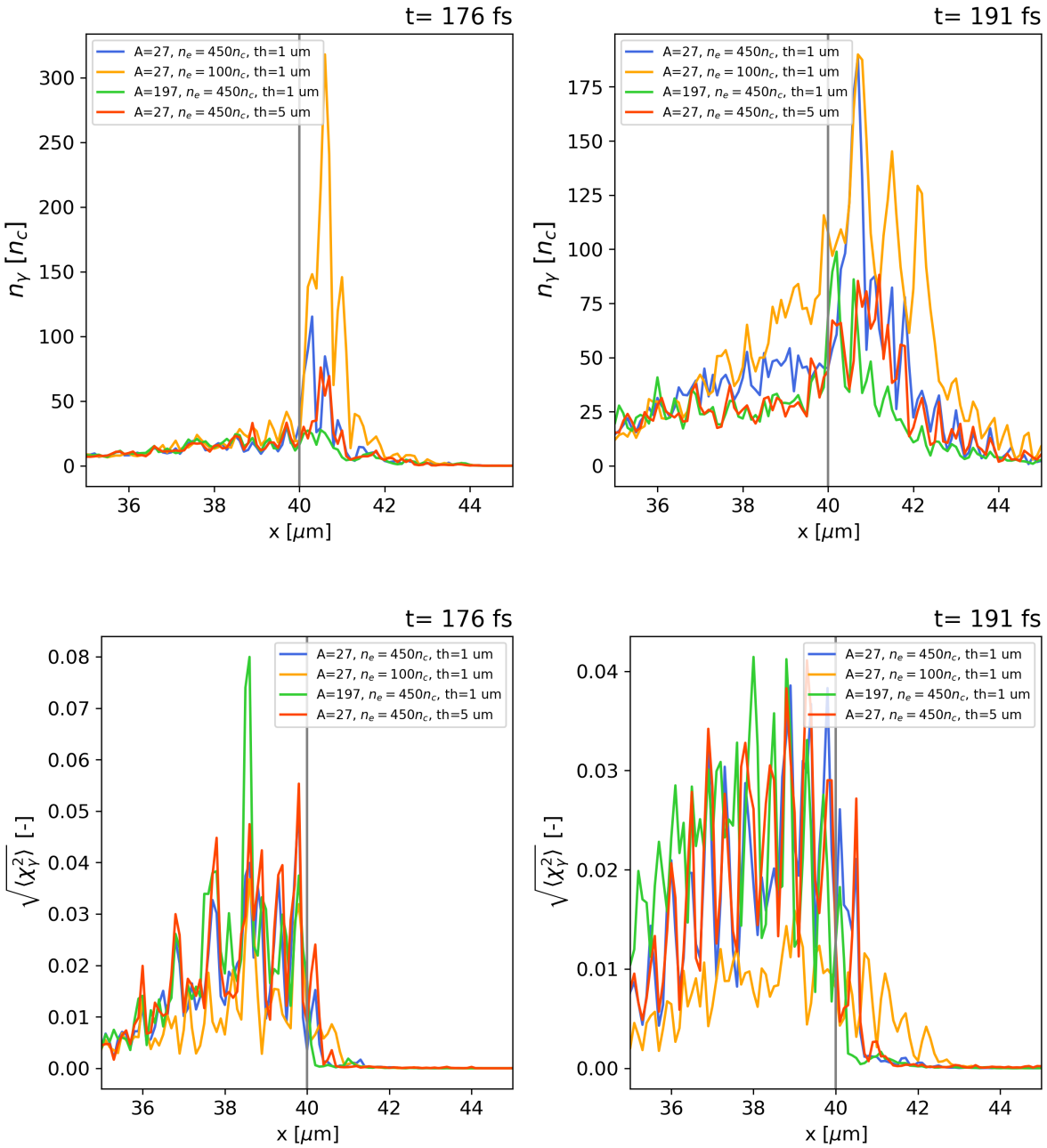

Figure 6.3: Snapshots of the photon density (upper panels) and quantum parameter, calculated as root mean square $\sqrt{\langle \chi^2 \rangle}$, (lower panels) at $y = L_y/2$ and different times during the reflection of the laser pulse for the four simulations devoted to the investigation of the impact of substrate properties on laser reflection and NBWPP. The gray line represents the beginning of the unperturbed substrate. SMILEI units are adopted.

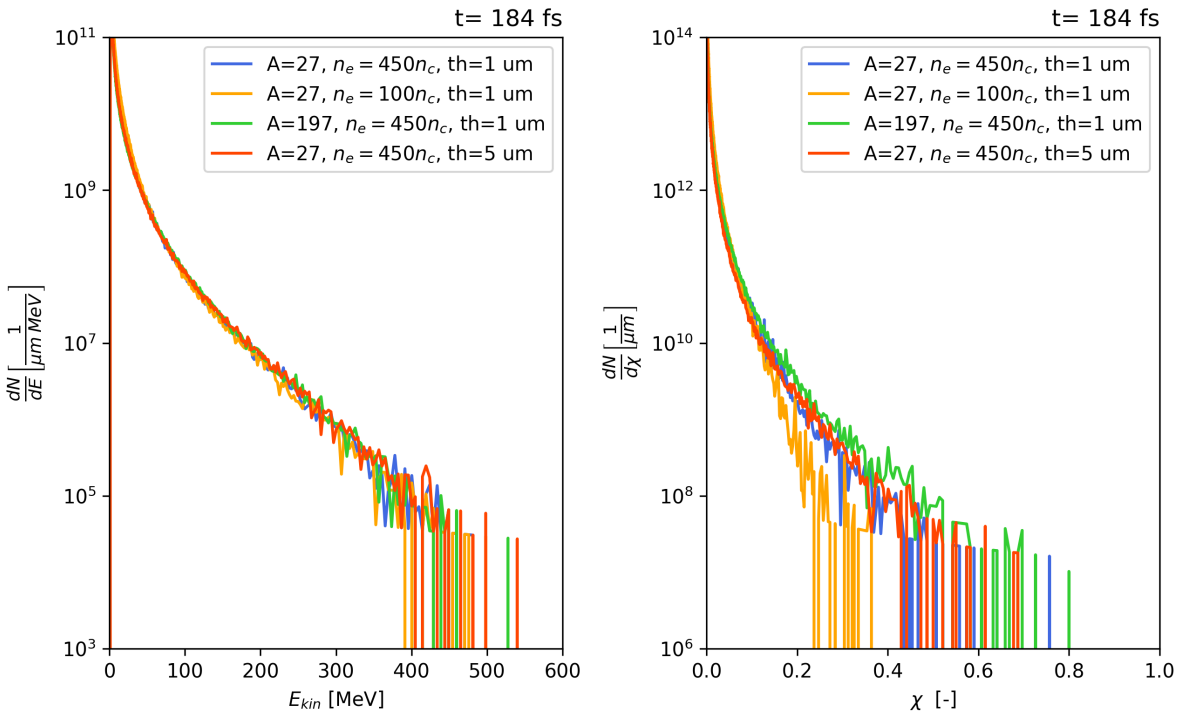

Figure 6.4: Photon spectra as a function of the kinetic energy (a) and quantum parameter (b) during the reflection of the laser pulse for the four simulations devoted to the investigation of the impact of substrate properties on laser reflection and NBWPP. They are evaluated at the time in which the higher quantum parameter values are achieved.

Examining the features of positron production concerning different substrate properties, Figure 6.5 reports the time behavior of the energy converted into pairs (a), representing the total pairs' energy at their generation, and integrated positron energy (b), characterizing the subsequent positron acceleration phase. As anticipated, these quantities peak with substrate configurations offering higher reflectivity. The increase in energy converted into pairs is almost 50% when increasing the thickness, while it is about 160% for the higher atomic mass. In terms of final positron energy, a 50% gain is obtained with the thicker substrate, while the heavier one leads to an 180% increase. Therefore, higher thickness and atomic mass are both beneficial for pair generation and positron acceleration. Notably, the TNSA field does not deteriorate with the considered higher thickness, rather it accelerates positrons with at least the same efficiency. The lower energy transferred to substrate ions might enhance the charge separation leading to the TNSA field. The significantly reduced energy converted into pairs for the low-density substrate clearly demonstrates its inability to efficiently produce positrons.

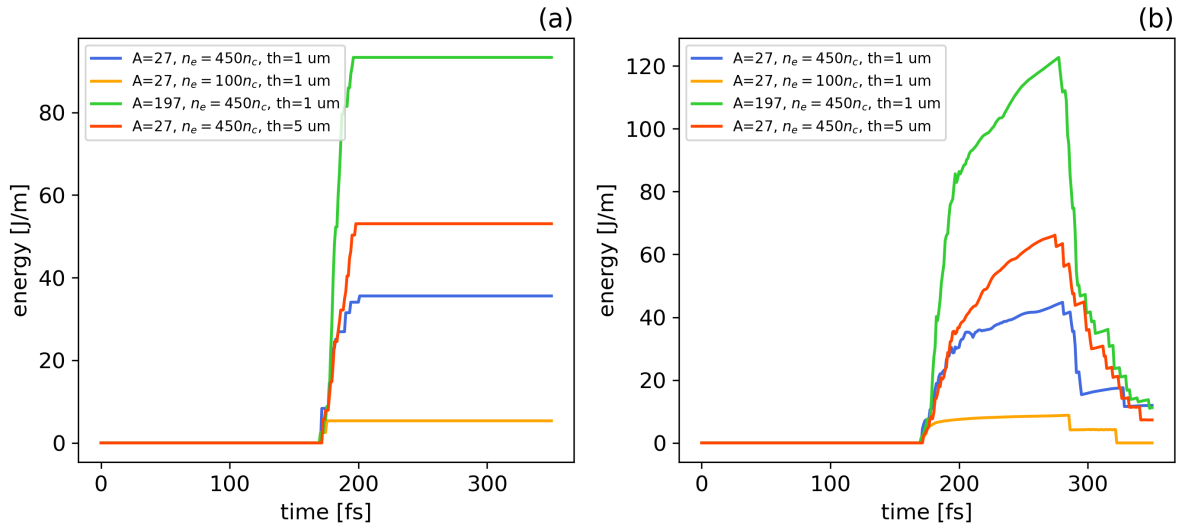

Figure 6.5: Time behaviour of the energy converted into pairs (a) and integrated positron energy (b) for the four simulations devoted to the investigation of the impact of substrate properties on laser reflection and NBWPP.

Figure 6.6 presents a comparison of the number of generated macro-positrons and their dynamics after the creation between the four different substrates. The substrate with higher atomic mass results in a larger number of macro-positrons populating the forward-propagating beam, which exhibits also a lower divergence compared to the reference case. However, there is a rise in the number of positrons trapped by the reflected pulse without contributing to the primary beam. Another significant observation is the lower electron density traveling in the same direction as the positron beam in the case of heavier substrate. Notably, while the laser pulse clearly traverses the low-density substrate, it is almost perfectly reflected from the heavier one. The thicker substrate, aside the generation of a higher number of macro-positrons, does not significantly impact the beam's divergence and the fraction of back-propagating positrons. Further comprehensive analysis is detailed in Table 6.2, evaluating the positron beam characteristics 10 μm ahead of the rear surface of the substrate for the reference, thicker, and heavier substrates. The latter provides the largest number of positrons and significantly lower divergence, transverse size, and temporal duration. However, the fraction of the total positron energy carried by the forward-propagating beam is considerably reduced, along with monochromaticity and the positron peak energy. It can be anticipated that these drawbacks are mitigated by optimizing foam properties, as will be demonstrated in the next section of this chapter. The thicker substrate results in a considerably higher number of positrons within the beam, even if with reduced peak energy and fraction of the total positron energy carried

by the beam. In conclusion, by properly choosing the substrate properties it is possible to tailor several aspects of the produced positron beam. In the subsequent analysis of foam properties, a slightly thicker lead substrate, featuring a higher atomic mass (A=207) and electronic density, is employed. The beam properties guiding this choice are the total number of positrons and its transverse, longitudinal, and angular spreads.

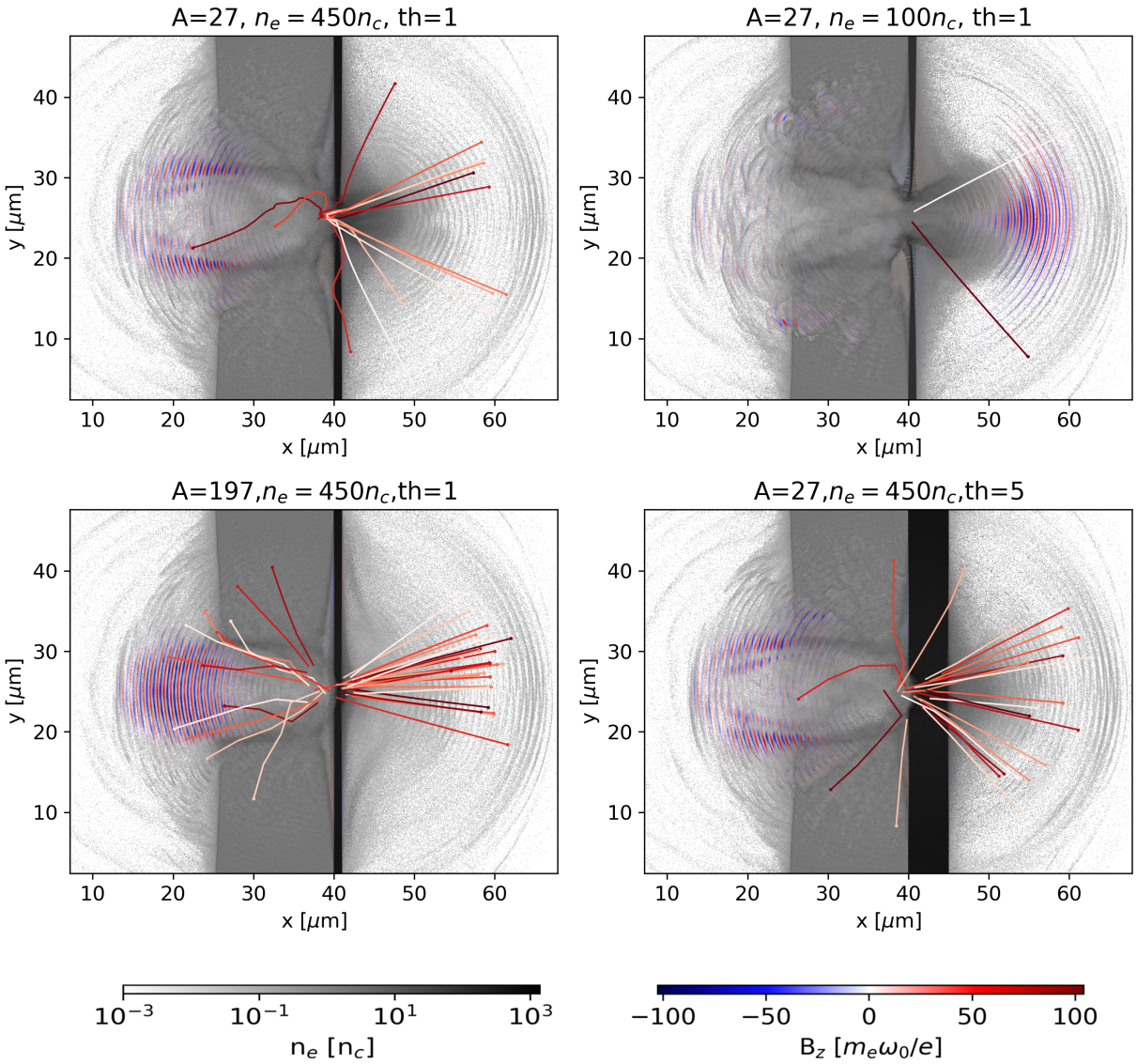

Figure 6.6: Snapshot of the laser-DLT interaction at the final stage (t = 249 fs) for the four simulations devoted to the investigation of the impact of substrate properties on laser reflection and NBWPP. The DLT is represented though its electronic density, the pulse through the B_z component and the red lines represent the macro-positron trajectories from their production by NBWPP to the time considered. SMILEI units are adopted.

Substrate	Δy [μm]	Δt [fs]	$\Delta\theta$ [rad]	ΔE [MeV]
A=27, n_e=450n_c, th=1 μm	15.4	33.6	0.51	235
A=197, n_e=450n_c, th=1 μm	8.8	14.8	0.26	312
A=27, n_e=450n_c, th=5 μm	16.6	31.2	0.48	232
Substrate	E_{peak} [MeV]	N_{beam} [1/μm]	E_{beam} [J/m]	E_{beam}/E_{pos} [%]
A=27, n_e=450n_c, th=1 μm	324	5.8×10^5	34.3	95
A=197, n_e=450n_c, th=1 μm	234	1.5×10^6	84.3	69
A=27, n_e=450n_c, th=5 μm	252	1×10^6	66.2	84

Table 6.2: Properties of the produced positron beam considering three of the four different analyzed substrates. The transverse size Δy, temporal duration Δt, divergence $\Delta\theta$ and energy spread ΔE are calculated as the root mean square, as described in Chapter 5. N_{beam} and E_{beam} are the total number and energy of positrons belonging to the beam (per unit length), and E_{beam}/E_{pos} is the fraction of the total positron energy carried by the forward-propagating beam. The values for the "reference" substrate properties (A=27, n_e=450n_c, th=1μm) are derived from the "high-NPPC" simulation results, which are discussed in Chapter 5.

6.2. Impact of the parameters of the low density layer

As revealed by the analysis in Chapter 5, the near-critical low-density layer's role involves the Self-Focusing (SF) of the laser pulse, enhancing the available laser intensity for high-energy photon emission and pair production, and the generation of energetic electrons moving in the direction of the laser axis, seeding these processes. The boost in intensity due to the SF is more prominent in the region at the front of the substrate, both due to the superposition with the reflected pulse and the maximum utilization of the SF, corresponding to reaching the minimum laser spot size. The foam density and length play a central role in determining both the magnitude of the SF and the quantity and energy of seed electrons at the end of the acceleration phase. Additionally, foam parameters govern the laser energy absorption and dissipation during the electron acceleration phase by determining the quantity of electrons heated through their interaction with the laser field, as well as the consequent emission of photons. These photons, due to their low energy and suboptimal interaction geometry with the laser field, are unimportant for pair production, representing a waste of laser energy. Unfortunately, this wastage is unavoidable as the pulse is required to propagate within the foam. All the mentioned aspects controlled by

foam properties, which are crucial for pair production, drive the parametric investigation presented in this final part of the chapter, focusing on foam density and length. Multiple combinations of these quantities are considered to identify the optimal configuration for pair production and its related features. Initially, the selected foam parameters and the simulation setup are discussed, followed by an analysis of the most significant differences in laser absorption, electron acceleration, photon emission, and pair production.

6.2.1. Simulation setup

As anticipated in Section 5.1.3, the foam length (15 μm) used previously is less than the calculated SF focal length (22 μm) for the considered density ($n_e = 2n_c$), which implies an underutilization of the focusing effect. This suggests a potential, significant enhancement in pair production by fully exploiting the SF effect. By using eq. (2.23), the foam density that optimizes the electron average energy at the focal distance is estimated to be $n_e = 24.8n_c$. However, while considering this, the laser energy absorption must be factored in since it reduces the intensity available for pair production. Therefore, higher densities than the one considered earlier are explored, but still kept below the estimated value. Lower densities are not investigated due to limitations in producing carbon foams using the PLD technique. Specifically, the chosen foam electron densities are $n_e = 2 - 6 - 12n_c$. For each selected density, foam length values are chosen from slightly below the focal length to abundantly above it, concluding when too much laser energy absorption deteriorates positron production. The focal lengths for the considered densities, calculated using eq. (2.24), are $22 - 13 - 9$ μm, respectively. The NPPC value for foam electrons is adjusted according to the density, while for ions it remains fixed. As for the substrate, basing on the results discussed in Section 6.1.2, a fully ionized lead slab with a thickness of 2 μm and non-realistic electron density of $n_e = 568n_c$ is considered. Actually, this density value is derived from the consideration of partially ionized lead in the Pb^{30+} state, characterized by an appearance intensity of 5.4×10^{18} W/cm^2, which is well below the intensity considered. Three times the skin depth related to this density is $3L_w = 16$ nm, which motivates the adopted spatial resolution of 76 grid points per micron, corresponding to a spacing of 13.2 nm. Laser properties, NPPC values for the substrate, and MC module settings remain constant, while adjustments are made in box dimensions and simulation duration in accordance with the total length of the target. The simulation setups are detailed in Table 6.3.

Impact of foam parameters			
Box size $(x \times y)$	(38μm+foam length)×40 μm	Grid points per μm $(x \times y)$	76×76
Time duration	$1.5 *$ Box size in x/c	CFL	0.98
Substrate properties			
Z	82	Density n_e	568 n_c
A	207	Thickness	2 μm
NPPC electrons	30	NPPC ions	6
Carbon foam properties			
Density n_e	$2-6-12$ n_c	Thickness	$6-9-12-15-18-21-27-33-39$ μm
NPPC electrons	if $n_e/n_c < 10$: $2n_e/n_c$, else: n_e/n_c	NPPC ions	1

Table 6.3: Parameters of the 2D simulations performed to study the impact of foam density and length on NBWPP.

6.2.2. Discussion of the results

Important insights into the behaviour of the considered foams emerge from the temporal evolution of integral quantities related to populations and the electromagnetic field during the electron acceleration phase, up to the start of reflection. As depicted in Figure 6.7, the fraction of laser energy transferred to foam electrons (a) and ions (b) escalates for longer and denser foams. This increase is attributed to the larger number of particles interacting with the laser field, absorbing energy through their heating. Although the energy transferred to ions remains several times smaller than that of electrons, it is non-negligible, especially for dense foams. It becomes apparent that excessively increasing the foam density is not advantageous as the laser energy absorbed by particles rises rapidly, significantly limiting the energy available to seed photon emission and pair production. Moreover, during the acceleration phase, electrons emit low-energy, non-interesting photons, further wasting laser energy. Figure 6.8 (a) illustrates the photon energy emitted during this phase, which is comparable to, or even greater than, the energy transferred to ions. Consequently, photon emission represents a considerable waste of laser energy, particularly in denser foams. The collective impact of these factors results in the fraction of laser energy remaining until the start of reflection, shown in Figure 6.8 (b). Notably,

lower foam density implies a gentler decrease in the remaining laser energy with increasing length, enabling the utilization of longer foams. Conversely, in denser foams, even a small increase in length, just a few microns, causes a rapid decline in laser energy.

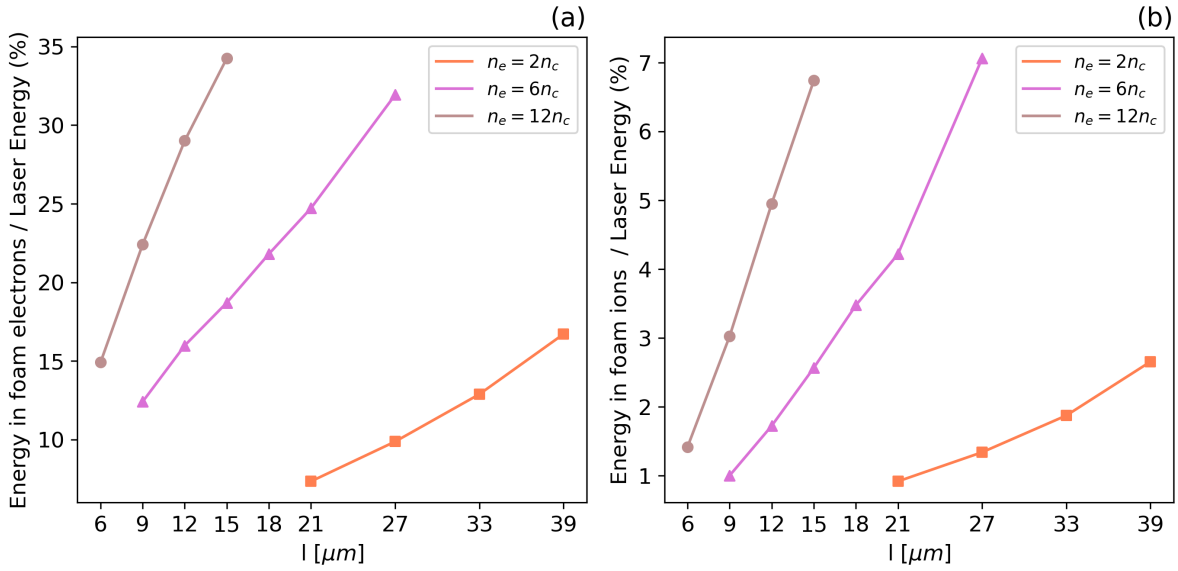

Figure 6.7: Fraction of laser energy absorbed by electrons (a) and ions (b), during the acceleration phase up to the start of reflection, as functions of foam electron density n_e and length l. Each mark corresponds to a simulation.

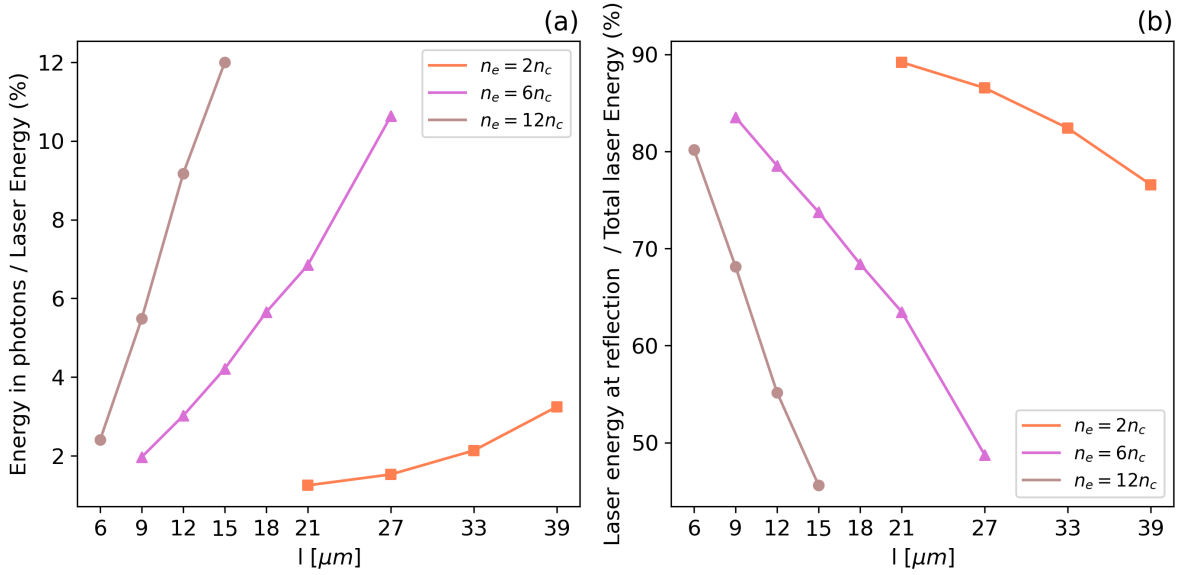

Figure 6.8: Fraction of laser energy emitted as photons during the acceleration phase up to the start of reflection (a), and available laser energy at the start of reflection (b), as functions of foam electron density n_e and length l. Each mark corresponds to a simulation.

Relevant quantities concerning electron acceleration include their average energy and quantum parameter, which, as illustrated in panels (a) and (b) of Figure 6.9, assume significantly higher values for longer, less dense foams. These quantities, as functions of foam length, exhibit a parabolic trend, suggesting an optimal condition that depends on the density. For the less dense case, where the optimal foam length is expected to be greater than 39 μm, longer foams beyond this value are not included in the simulation campaign due to the considerable computational resources required. The curvature of these parabolas decreases as the density decrease, meaning that the ideal condition becomes less stringent. It is important to note that, in general, the optimal foam length for electron energy and χ surpasses the self-focusing focal length, indicating that the latter is not optimal. Optimizing laser intensity alone is not sufficient, it is also critical to consider the distance within the foam available for electron acceleration. More energetic electrons generate higher-energy photons, enhancing the probability of conversion. Hence, longer foams are preferable, making a balance between electron acceleration and laser energy absorption. Optimal cases with the lowest density show that, upon exceeding the SF focal length, the pulse undergoes filamentation while maintaining the minimum spot size. Conversely, foam lengths less than the focal distance rapidly deteriorate electron acceleration performance, underscoring the importance of adopting foams longer than this distance. This aspect can be directly observed in results for higher densities and, for the lower one, by considering those reported in Chapter 5.
Figure 6.10 displays the laser energy converted to photons during the reflection phase, where the most energetic photons are generated. Although lower densities lead to a reduction in energy converted into photons during reflection, the decrease in the same quantity during the acceleration phase is more pronounced. Therefore, less dense longer foams prove to be more efficient in photon emission. This is supported by the evaluation of the average photon energy and quantum parameter during reflection, presented in panels (a) and (b) of Figure 6.11. Once more, less dense longer foams exhibit superior performance, producing more energetic photons while preserving laser energy, resulting in higher χ. Furthermore, these quantities demonstrate a behaviour akin to the parabolic trend observed in electrons, albeit somewhat distorted. Across considerations of electron acceleration, laser absorption, and photon emission, they all align with the optimal foam properties, favoring longer less dense configurations.

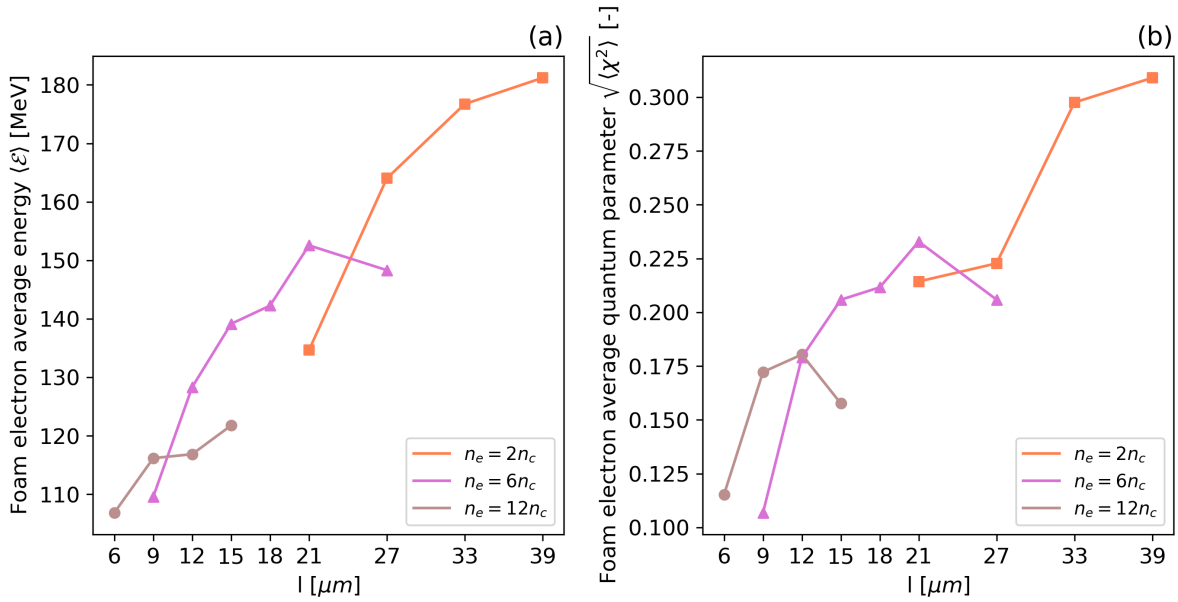

Figure 6.9: Average energy $\langle\mathcal{E}\rangle$ (a) and quantum parameter $\sqrt{\langle\chi^2\rangle}$ (b) for foam electrons as functions of foam electron density n_e and length l. Each mark represents a simulation where these values are calculated during the reflection, at the point where the average quantum parameter reaches its maximum. Only electrons contributing with $\mathcal{E} > 50$ MeV and $\chi > 0.05$ are included.

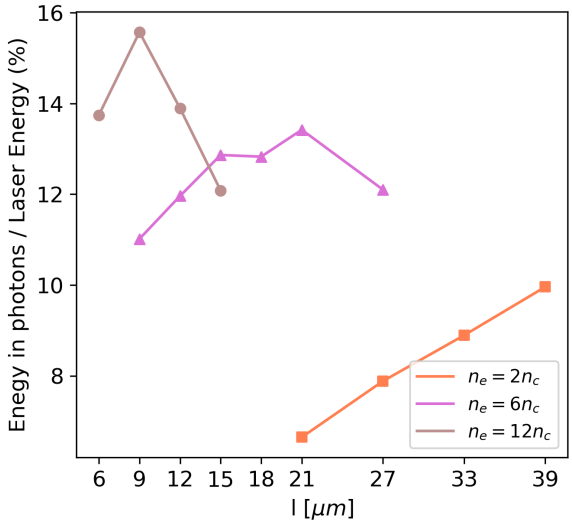

Figure 6.10: Fraction of laser energy emitted as photons during reflection as a function of foam electron density n_e and length l. Each mark corresponds to a simulation.

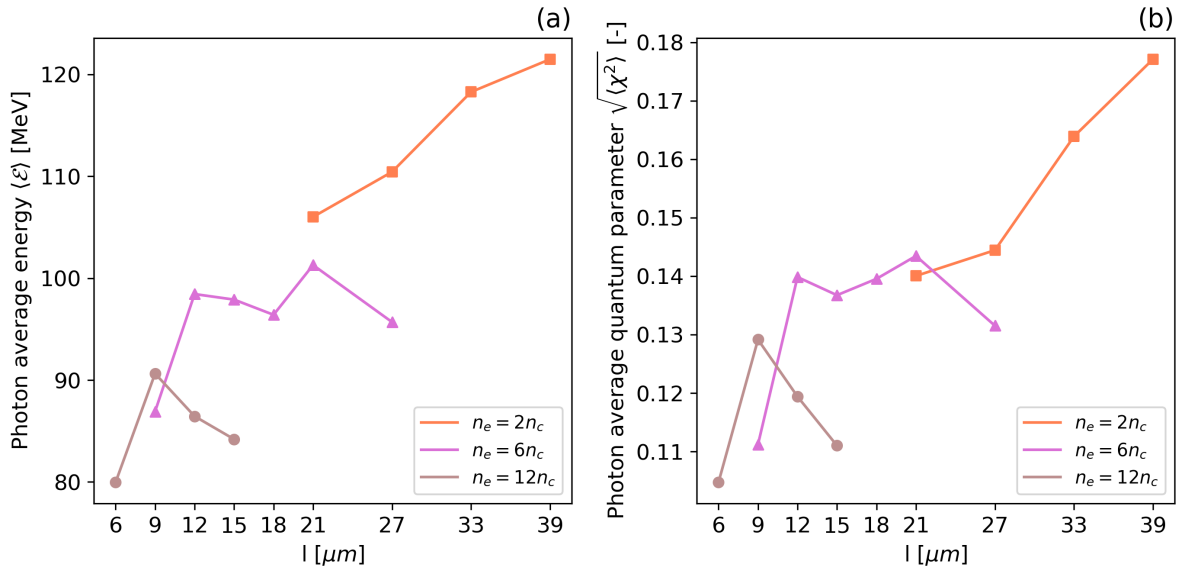

Figure 6.11: Average energy $\langle\mathcal{E}\rangle$ (a) and quantum parameter $\sqrt{\langle\chi^2\rangle}$ (b) for photons as functions of foam electron density n_e and length l. Each mark represents a simulation where these values are calculated during the reflection, at the point where the average quantum parameter reaches its maximum. Only photons contributing with $\mathcal{E} > 50$ MeV and $\chi > 0.05$ are included.

Figure 6.12 illustrates that the energy converted into pairs (a) and the maximum total positron energy (b) align with the behaviours observed in electron and photon characteristic quantities. It highlights the existence of an optimal foam length for each density value, particularly noting that, for the lowest density case, this optimal length exceeds 39 μm, leading to an energy conversion into pairs of about 0.01%. The results underscore the necessity for long, near-critical low-density foams to optimize positron production, showcasing notably superior performance compared to other configurations. It is interesting to note that, for lower density foams, the final positron energy can be lower then the energy converted into pairs, indicating that the energy gained by positrons during their dynamics is less than the energy converted into electrons at their generation events. The characterization of the produced positron beam is performed 10 μm ahead of the target's rear surface and detailed in Figures 6.13, 6.14, 6.15 and 6.16. The number of positrons within the beam, reported in 6.13 (a), follows a similar trend to the energy converted into pairs, significantly favoring longer low-density foams. The energy carried by the beam, shown in 6.13 (b), consistently comprises almost the entire total positron energy, with a fraction fluctuating between $94 - 99\%$. It is worth noting that, in one instance where the energy of the beam exceeds the total positron energy, this is attributed to a wide

temporal duration of the beam, resulting in some positrons continuing acceleration while others leave the simulated box. When examining the divergence and transverse dimension of the beam, depicted in panels (a) and (b) of Figure 6.14, the two higher densities exhibit better results with shorter foams, while for the lower density, more collimated and less divergent beams are produced with longer foams. This is advantageous as the same configuration not only yields the highest number of positrons but also minimizes beam divergence and transverse size. The peak energy and energy spread of the beam, illustrated in panels (a) and (b) of Figure 6.15, are affected by statistical fluctuations, oscillating between $325 - 425$ MeV for the former and $180 - 200$ MeV for the latter. The time duration of the beam, shown in Figure 6.16, also fluctuates in the range of $20 - 30$ fs. The trend of all these quantities, considering the most interesting low-density case, suggests that a further increase in the length would result in a more populated beam with even lower transverse dimension and reduced angular and temporal spread.

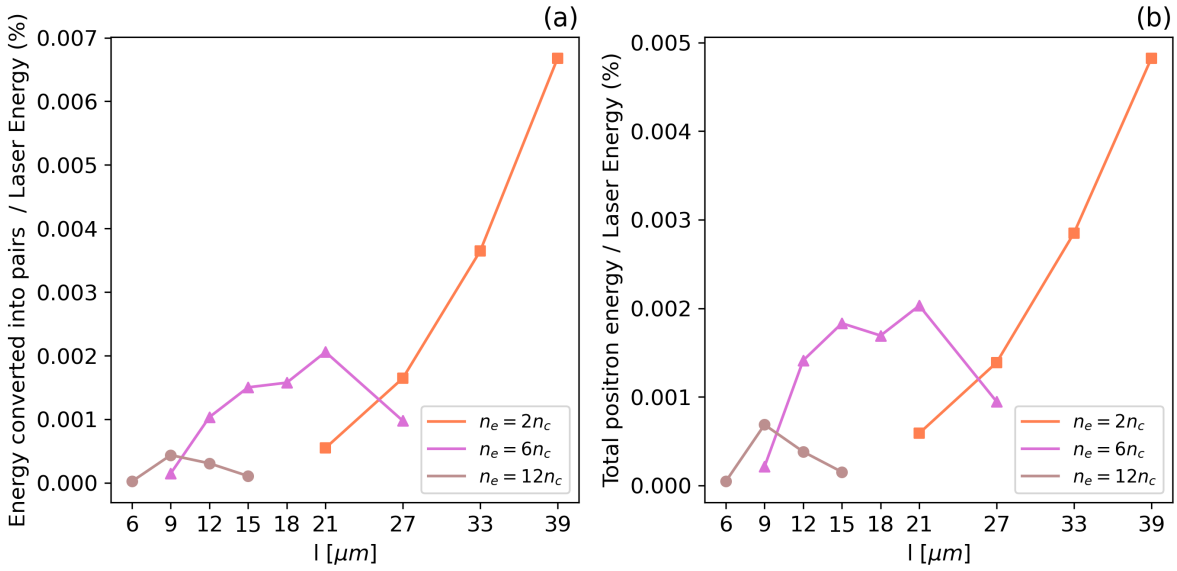

Figure 6.12: Fraction of laser energy converted into pairs (a) and the ratio between the maximum total positron energy and the laser energy (b) as functions of foam electron density n_e and length l. Each mark corresponds to a simulation.

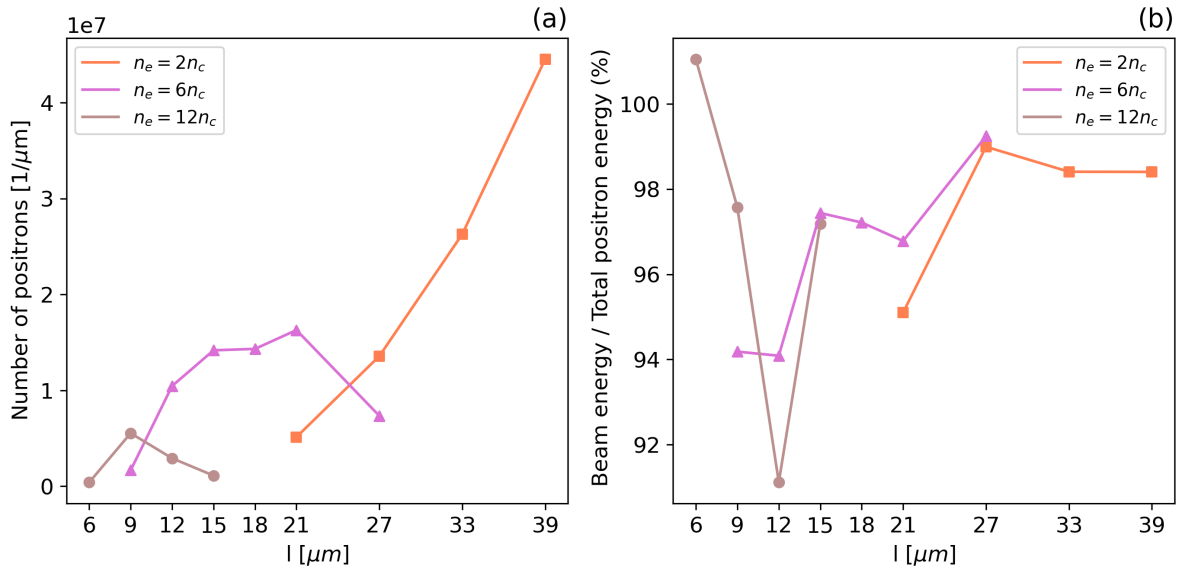

Figure 6.13: Number of positrons per unit length within the produced beam (a) and the ratio between their carried energy and the total positron energy (b), assessed 10 μm ahead of the target, as functions of foam electron density n_e and length l. Each mark corresponds to a simulation.

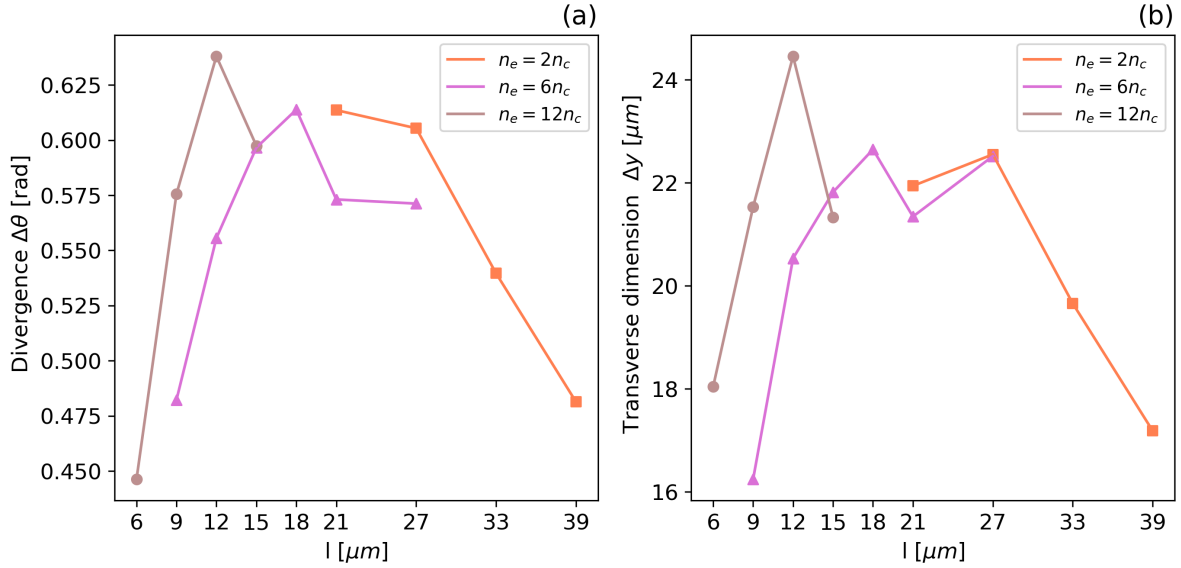

Figure 6.14: Divergence, or half-aperture, (a) and transverse dimension (b) of the produced positron beam, assessed 10 μm ahead of the target, as functions of foam electron density n_e and length l. These quantities are calculated as explained in Section 5.1.5. Each mark corresponds to a simulation.

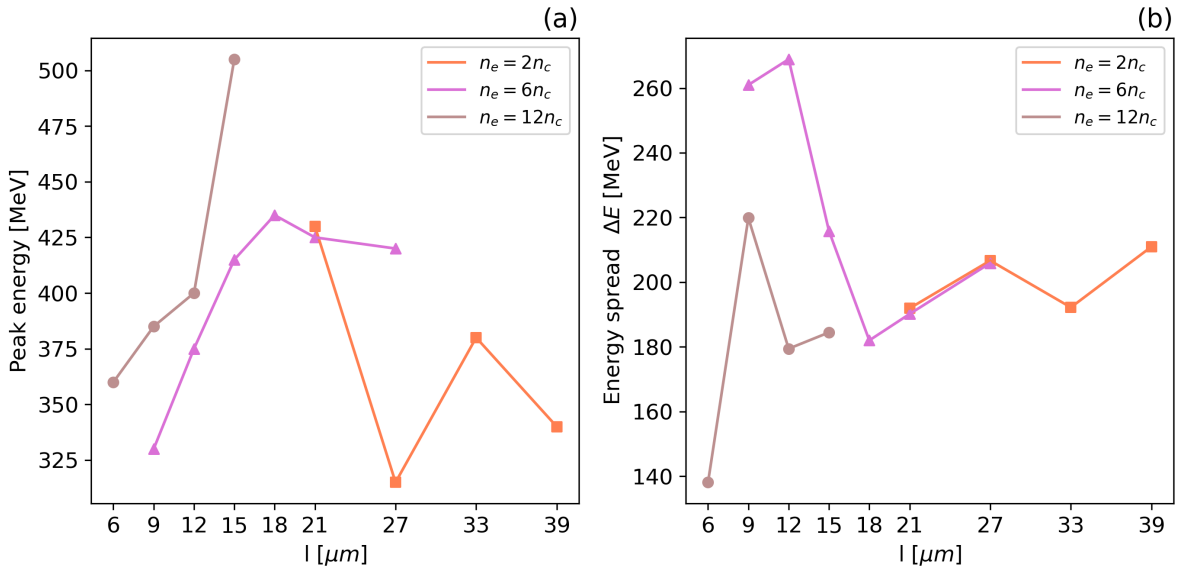

Figure 6.15: Peak energy (a) and energy spread (b) of the produced positron beam, assessed 10 μm ahead of the target, as functions of foam electron density n_e and length l. These quantities are calculated as explained in Section 5.1.5. Each mark corresponds to a simulation.

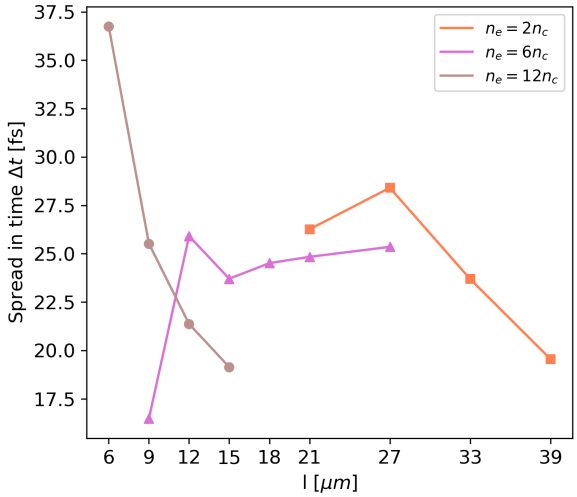

Figure 6.16: Spread in time, or temporal duration, of the produced positron beam, assessed 10 μm ahead of the target, as a function of foam electron density n_e and length l. This quantity is calculated as explained in Section 5.1.5. Each mark corresponds to a simulation.

Conclusions and perspectives

The results presented in Chapters 5 and 6 enable to draw conclusions regarding the potential realization of a positron source based on non-linear Breit-Wheeler pair production (NBWPP) using double-layer targets (DLTs) and laser technology currently available in experimental laser facilities, specifically adopting a wavelength of 0.8 μm, peak intensity of 4.75×10^{22} W/cm^2, spot size of 3 μm, and pulse duration of 30 fs.
As discussed in Chapter 2, high-intensity lasers can ionize matter, generating plasmas. Depending on target properties, different laser-plasma interaction regimes can be achieved, providing control over electron acceleration, laser field evolution, and generation of various types of radiation. Laser-driven positron sources, as discussed in Section 1.3.3, has garnered significant interest due to several advantages over conventional and radioactive sources. These advantages include higher positron energy, density, and yield, as well as the elimination of the need for accelerator machines and reduced risk associated with radioactivity. As detailed in Section 2.4.3, within the class of full-optical sources, the NBWPP-based scheme promises, in the next period, of producing positron beams with enhanced qualities, including femtosecond duration, higher positron density and intensity levels, and a spectrum peaking in the hundreds of MeV. However, this scheme requires the utilization of significantly higher laser intensities due to the demanding nature of NBWPP in intense electromagnetic fields. Non conventional, engineered composite targets, such as the double-layer target described in Section 2.3.5, can be used to provide the necessary conditions favoring NBWPP. With the purpose of investigating NBWPP during laser-plasma interaction in DLTs, various topics have been covered in this thesis. In Section 1.2.2, the NBWPP single-particle process was described, emphasizing the key physical quantities governing its occurrence and outcomes. To contextualize it in laser-plasma interaction, a point addressed in Chapter 2, numerical tools are essential, and particle-in-cell (PIC) codes integrated with a Monte Carlo (MC) module are the most suitable. The working principles of these codes, along with the implementation of NBWPP in their algorithm, were explained in Chapter 3. In this thesis, the open-source PIC-MC code SMILEI was employed to perform 2D simulations of pair production through NBWPP during laser-plasma interaction following the irradiation of a DLT.

The study primarily focused on understanding the physical processes involved in the interaction leading to pair production, identifying key parameters and relevant physical quantities for NBWPP, and describing the main properties of the produced positrons. It has been recognized that crucial phases include the acceleration of electrons to energies of several hundreds of MeV, the focusing and reflection of the laser field, and its interaction with the accelerated electrons and subsequently produced photons. All these aspects should be optimized to provide seed energetic electrons and the required laser intensity in the interaction region, and realize their optimal interaction geometry, resulting in the enhancement of photon emission and pair production processes. An important characteristic of DLTs has been demonstrated to be the target normal sheath acceleration (TNSA) of the generated positrons, improved by the reduced thickness of the solid-layer. The TNSA field not only accelerates positrons in the forward direction but also decelerates electrons, leading to a high level of purity of the produced positron beam. It emerged that the DLT parameters, including both the near-critical and solid-density layers, strongly affect the laser-to-positron conversion efficiency and the positron beam characteristics. This motivated the parametric study of DLT properties, analyzing their impact on the different phases of the interaction. Specifically, the investigation of the solid layer parameters underlines the importance of having high density and atomic-mass to achieve high-reflectivity, leading to a more efficient utilization of the available laser energy and boosting the laser intensity in the interaction region. It also emerged that thickness of the solid layer plays an important role, and various configurations of these parameters can be employed to tailor positron production features. On the other hand, the study of the impact of density and length of the low-density layer indicates the existence of an optimal configuration, exhibiting better results in laser-to-positron conversion efficiency, divergence, transverse size, and temporal spread. This optimal configuration consists in a DLT formed by a micrometer thick, dense, heavy substrate, such as lead, and a low-density layer with $n_e = 2n_c$ and length around 39 μm. The positron beam features obtained in this optimal case, including a temporal duration of 19.6 fs, a divergence of 28.6°, peak and maximum energies of 342 MeV and 800 MeV, energy spread of 215 MeV, and a total number and average density of 4.5×10^7 $1/\mu$m and 4.4×10^{17} cm^{-3}, respectively, confirm the potential of a NBWPP-based positron source. The obtained laser-to-positron energy conversion efficiency is 0.005%. As expected, the electronic component in the beam is removed from the TNSA field, leading to a high-level of purity.

One of the conclusions of this thesis work is that the DLT configuration allows for the generation of a significant number of positrons at the considered laser intensity, confirming the interest in further investigating NBWPP in DLTs. Few works are available in the literature concerning NBWPP in composite targets, and the used laser intensities

are considerably higher, preventing experimental validation of the results in the near future. Therefore, this thesis work constitutes a new contribution to understanding the main physical processes related to NBWPP in laser-plasma interaction and the investigation of NBWPP-based positron beam sources. Another interesting conclusion is the confirmation of the orders of magnitude of the main positron beam features expected from NBWPP-based sources, specifically related to the temporal duration, average density, and positron spectrum. The obtained laser-to-positron conversion efficiency, which obviously depends on the considered laser intensity, features the same order of magnitude as the other experimentally-proven laser-driven positron sources (see 2.4.3).
Concerning the additional thesis activity as part of the Honours Programme in which the candidate participated, a comparison between simulation results and theoretical predictions for relevant physical quantities was performed, obtaining good agreement. Then, an analysis of the theoretical assumptions and numerical approximations involved in the implementation of NBWPP in PIC-MC codes, along with the main setting parameters, has been conducted. The theoretical assumptions are abundantly satisfied in the regime of interaction considered, while the numerical approximations lead to momentum and energy non-conservation during the simulation. However, further studies are needed to evaluate their global importance, especially when the number of photon emission and pair production events becomes large, like in laser-plasma interaction regimes accessible in the next future with the advent of the next generation of multi-PW class-lasers. MC module setting parameters have statistical implications, but in certain conditions of poor statistics due to limited number of secondary particles produced, they must be properly chosen to avoid influencing physical quantities. Then, statistical limitations arising from the PIC description are inevitable and can influence the characterization of secondary particles produced through the processes accounted for by the MC module, especially when these processes have a low probability due to suboptimal conditions for their occurrence. Similarly, the tails of the spectra are not simulated, expecting a significant impact on processes depending on them, such as NBWPP.
Possible further developments have emerged throughout this thesis work, addressing open questions and limitations in the adopted analysis approach:

- Further investigation of DLT parameters that have not been explored in this work. Specifically, the impact of further reducing the density of the low-density layer, which could potentially be achieved through techniques other than pulsed laser deposition. Additionally, delving into the substrate properties and their role in tailoring positron production is of interest, especially when considering the optimal configuration of the low-density layer. Another aspect requiring exploration is the influence of laser

parameters, such as spot size, duration, polarization, and energy, as well as different spatial and temporal profiles.

- Conduct 3D simulations in order to validate the obtained results and generate more quantitative information regarding the produced positron beam. This point is particularly important to investigate potential effects arising from the three-dimensionality of the problem, such as the nanostructure of the low-density layer, and understand their impact on positron production.
- Design an experiment to be conducted at a laser facility capable of providing the specified laser parameters, such as the Extreme Light Infrastructure (ELI), based on the results of this thesis and the extended numerical campaign as described in previous perspectives.
- Explore an alternative DLT configuration by substituting the thin solid layer with a thicker converter, in order to exploit different positron production processes, specifically the Bethe-Heitler pair production and the trident one. This modified setup is expected to generate positrons also at lower laser intensities. The study should comprise a comparative analysis of the features of the produced positron beam.
- Improvements of PIC-MC algorithms to restore energy-momentum conservation when modeling photon emission and NBWPP processes, and enhance their statistics. Additionally, conduct further analysis on the implications of assuming collinearity in these processes instead of their correct angular distribution.

Finally, experimental validation in current and forthcoming laser facilities is essential to substantiate the viability of a positron beam source based on NBWPP with DLTs and to characterize the produced positrons through their experimental detection. Subsequent developments should be focused on the dedicated design of these positron sources, taking into account all aspects related to their realization.

Bibliography

[1] J. W. Yoon, Y. G. Kim, W. I. Choi, J. H. Sung, H. W. Lee, S. K. Lee, and C. H. Nam. Realization of laser intensity over 1023 w/cm2. *Optica*, 2021. doi: 10.1364/OPTICA.420520.

[2] P. Milne, M. Leising, and L. The. Galactic positron production from supernovae. 1999. doi: 10.48550/arXiv.astro-ph/9911517.

[3] T. Stanev. Cosmic rays and extensive air showers. *INSPIRE HEP*, 2010.

[4] C. Anderson. The positive electron. *Physical Review Letters*, 1933. doi: 10.1103/PhysRev.43.491.

[5] P. Dirac. The quantum theory of the electron. *Proceedings of the Royal Society A*, 1928. doi: 10.1098/rspa.1928.0023.

[6] A. Akhiezer and V. Berestetskii. *Quantum Electrodynamics*. Interscience Publishers, 1965.

[7] B.R Martin and G Shaw. *Particle Physics*. Wiley, 2008.

[8] Bertulani. *Nuclear Physics in a Nutshell*. Princeton University Press, 2007.

[9] Heitler. *The Quantum Theory of Radiation*. Oxford University Press, 1944.

[10] Z. Lecz and A. Andreev. Minimum requirements for electron-positron pair creation in the interaction of ultra-short laser pulses with thin foils. *Plasma Physics and Controlled Fusion*, 2019. doi: 10.1088/1612-202X/ab83fe.

[11] G. Breit and J. Wheeler. Collision of two light quanta. *Physical Review Letters*, 1934. doi: 10.1103/PhysRev.46.1087.

[12] Y. He, T. Blackburn, T. Toncian, and A. Arefiev. Dominance of $\gamma - \gamma$ electron-positron pair creation in a plasma driven by high-intensity lasers. *Communications Physics*, 2021. doi: 10.1038/s42005-021-00636-x.

[13] J. Liu, Y. Ma, J. Zhao, T. Yu, X. Yang, L. Gan, G. Zhang, J. Yan, H. Zhuo, J. Liu, Y. Zhao, and S. Kawata. High-flux low-divergence positron beam generation from

ultra-intense laser irradiated a tapered hollow target. *physics of Plasmas*, 2015. doi: 10.1063/1.4932997.

[14] A. Di Piazza, C. Muller, K. Hatsagortsyan, and C. Keitel. Extremely high-intensity laser interactions with fundamental quantum systems. *Reviews of Modern Physics*, 2012. doi: 10.1103/RevModPhys.84.1177.

[15] Ritus. Quantum effects of the interaction of elementary particles with an intense electromagnetic field. *Journal of Soviet Laser Research volume*, 1985. doi: 10.1007/BF01120220.

[16] D. Burke, R. Field, G. Horton-Smith, J. Spencer, D. Walz, S. Berridge, W. Bugg, K. Shmakov, A. Weidemann, C. Bula, K. McDonald, E. Prebys, C. Bamber, S. Boege, T. Koffas, T. Kotseroglou, A. Melissinos, D. Meyerhofer, D. Reis, and W. Ragg. Positron production in multiphoton light-by-light scattering. *Physical Review Letters*, 1997. doi: 10.1103/PhysRevLett.79.1626.

[17] Jackson. *Classical Electrodynamics*. Wiley, 1999.

[18] M Lobet, E. Humières, M. Grech, C. Ruyer, X. Davoine, and L. Gremillet. Modeling of radiative and quantum electrodynamics effects in pic simulations of ultra-relativistic laser-plasma interaction. *Journal of Physics: Conference Series*, 2016. doi: 10.1088/1742-6596/688/1/012058.

[19] N. Elkina, A. Fedotov, I. Kostyukov, M. Legkov, N. Narozhny, E. Nerush, and H. Ruhl. Qed cascades induced by circularly polarized laser fields. *Physical Review Letters*, 2011. doi: 10.1103/PhysRevSTAB.14.054401.

[20] A. Gonoskov, S. Bastrakov, E. Efimenko, A. Ilderton, M. Marklund, I. Meyerov, A. Muraviev, A. Sergeev, I. Surmin, and E. Wallin. Extended particle-in-cell schemes for physics in ultrastrong laser fields: Review and developments. *Physical Review E*, 2015. doi: 10.1103/PhysRevE.92.023305.

[21] C. Ridgers, C. Brady, R. Duclous, J. Kirk, K. Bennett, T. Arber, and A. Bell. Dense electron-positron plasmas and bursts of gamma-rays from laser-generated quantum electrodynamic plasmas. *Physics of Plasmas*, 2013. doi: 10.1063/1.4801513.

[22] R. Chehab. laboratoire de l'accélérateur linéaire, 1989.

[23] K. Hübner. Positron production for particle accelerators. *Hyperfine Interactions*, 1988. doi: 10.1007/BF02398667.

[24] I. Chaikovska, R. Chehab, V. Kubytskyi, S. Ogur, A. Ushakov, A. Variola, P. Sievers,

P. Musumeci, L. Bandiera, Y. Enomoto, M.J. Hogan, and P. Martyshkin. Positron sources: from conventional to advanced accelerator concepts-based colliders. *Journal of Instrumentation*, 2022. doi: 10.1088/1748-0221/17/05/P05015.

[25] P. Csonka. Undulators for efficient positron production. *Radiation Physics and Chemistry*, 2003. doi: 10.1016/S0969-806X(03)00196-8.

[26] G. Sarri, W. Schumaker, A. Di Piazza, M. Vargas, B. Dromey, M. Dieckmann, V. Chvykov, A. Maksimchuk, V. Yanovsky, Z. He, B. Hou, J. Nees, A. Thomas, C. Keitel, M. Zepf, and K. Krushelnick. Table-top laser-based source of femtosecond, collimated, ultrarelativistic positron beams. *Physical Review Letters*, 2013. doi: 10.1103/PhysRevLett.110.255002.

[27] Jian-Xun Liu, Yan-Yun Ma, Tong-Pu Yu, Jun Zhao, Xiao-Hu Yang, Long-Fei Gan, Guo-Bo Zhang, Yuan Zhao, Shi-Jie Zhang, Jin-Jin Liu, Hong-Bin Zhuo, Fu-Qiu Shao, and Shigeo Kawata. Enhanced electron-positron pair production by ultra intense laser irradiating a compound target. *Plasma Physics and Controlled Fusion*, 2016. doi: 10.1088/0741-3335/58/12/125007.

[28] P. Coleman. *Positron Beams and their applications*. Word Scientific, 2000. doi: 10.1142/3719.

[29] P. Coleman. Positron spectroscopy. *digital Encyclopedia of Applied Physics*, 2009. doi: 10.1002/3527600434.eap355.pub2.

[30] P. Coleman. Positron beams: The journey from fundamental physics to industrial application. *Nuclear Instruments and Methods in Physics Research Section B: Beam Interactions with Materials and Atoms*, 2002. doi: 10.1016/S0168-583X(02)00710-3.

[31] Y. Yan, Y. Wu, Z. Zhao, J. Teng, J. Yu, D. Liu, K. Dong, L. Wei, W. Fan, L. Cao, Z. Yao, and Y. Gu. Monte carlo simulation study of positron generation in unltra-intense laser-solid interactions. *Physics of Plasmas*, 2012. doi: 10.1063/1.3686109.

[32] Hui Chen, S. C. Wilks, D. D. Meyerhofer, J. Bonlie, C. D. Chen, S. N. Chen, C. Courtois, L. Elberson, G. Gregori, W. Kruer, O. Landoas, J. Mithen, J. Myatt, C. D. Murphy, P. Nilson, D. Price, M. Schneider, R. Shepherd, C. Stoeckl, M. Tabak, R. Tommasini, and P. Beiersdorfer. Relativistic quasimonoenergetic positron jets from intense laser-solid interaction. *Physical Review Letters*, 2010. doi: 10.1103/PhysRevLett.105.015003.

[33] Wiedemann. *Particle Accelerator Physics*. Springer, 2019.

[34] David Griffiths. *Introduction to Elementary Particles*. Wiley, 2008.

[35] C. Fan and Z. Zhao. *Synchrotron Radiation in Materials Science: Light Sources, Techniques, and Applications*. Wiley, 2018. doi: 10.1002/9783527697106.

[36] P. Suortii and W. Thomlinson. Medical applications of synchrotron radiation. *Physics in Medicine & Biology*, 2003. doi: 10.1088/0031-9155/48/13/201.

[37] F. Tuomisto and I. Makkonen. Defect identification in semiconductors with positron annihilation: Experiment and theory. *Reviews of Modern Physics*, 2013. doi: 10.1103/RevModPhys.85.1583.

[38] Thomas L. Audet, Aaron Alejo, Luke Calvin, Mark Hugh Cunningham, Glenn Ross Frazer, Gagik Nersisyan, Michael Phipps, Jonathan Richard Warwick, Gianluca Sarri, Nasr A. M. Hafz, Christos Kamperidis, Song Li, and Daniel Papp. Ultrashort, mev-scale laser-plasma positron source for positron annihilation lifetime spectroscopy. *Phys. Rev. Accel. Beams*, 2021. doi: 10.1103/PhysRevAccelBeams.24.073402.

[39] H. Ache. Chemistry of the positron and of positronium. *Angewandte Chemie International Edition in English*, 1972. doi: 10.1002/anie.197201791.

[40] Y. Kobayashi, K. Ito, T. Oka, C. He, H.F.M. Mohamed, R. Suzuki, and T. Ohdaira. Application of positron beams to the study of positronium-forming solids. *Applied Surface Science*, 2008. doi: 10.1016/j.apsusc.2008.05.278.

[41] G. Sarri, K. Poder, J. Cole, W. Schumaker, A. Di Piazza, B. Reville, T. Dzelzainis, D. Doria, L. Gizzi, G. Grittani, S. kar, C. Keitel, K. Krushelnick, S. Kuschel, S. Mangles, Z. Najmudin, N. Shukla, L. Silva, D. Symes, A. Thomas, M. Vargas, J. Vieira, and M. Zepf. Generation of neutral and high-density electron-positron pair plasmas in the laboratory. *Nature Communications*, 2015. doi: 10.1038/ncomms7747.

[42] Dwiht R. Nicholson. *Introduction to Plasma Theory*. Wiley, 1983.

[43] J. Huba. Nrl plasma formulary, 2004.

[44] A. Siegman. *Lasers*. Optica, 1986.

[45] M. Zavelani-Rossi and F. Vismarra. *High-Intensity Lasers for nuclear and physical applications*. Euscalpi, 2021.

[46] Colin N. Danson, Constantin Haefner, Jake Bromage, Thomas Butcher, Jean-Christophe F. Chanteloup, Enam A. Chowdhury, Almantas Galvanauskas, Leonida A. Gizzi, Joachim Hein, David I. Hillier, and et al. Petawatt and exawatt class lasers worldwide. *High Power Laser Science and Engineering*, 2019. doi: 10.1017/hpl.2019.36.

[47] P. Gibbon. *Short Pulse Laser Interactions with Matter: an introduction.* Imperial College Press, 2005.

[48] William L. Kruer. *The physics of Laser Plasma Interactions.* Westview Press, 2003.

[49] A. Hussein, A. Arefiev, T. Batson, H. Chen, R. S. Craxton, A. S. Davies, D. H. Froula, Z. Gong, D. Haberberger, Y. Ma, P. Nilson, W. Theobald, T. Wang, K. Weichman, G. J. Williams, and L. Willingale. Towards the optimisation of direct laser acceleration. *New Journal of Physics*, 2021. doi: 10.1088/1367-2630/abdf9a.

[50] M. Jirka, M. Vranic, T. Grismayer, and L. O. Silva. Scaling laws for direct laser acceleration in a radiation-reaction dominated regime. *New Journal of Physics*, 2020. doi: 10.1088/1367-2630/aba653.

[51] K. Miller, J. Palastro, J. Shaw, F. Li, F. Tsung, V. Decyk, C. Joshi, and W. Mori. Accurate simulation of direct laser acceleration in a laser wakefield accelerator. *Physics of Plasmas*, 2023. doi: 10.1063/5.0152383.

[52] X. Zhu, T. Yu, Z. Sheng, Y. Yin, I. Turcu, and A. Pukhov. Dense gev electron–positron pairs generated by lasers in near-critical-density plasmas. *Nature Communications*, 2016. doi: 10.1038/ncomms13686.

[53] L. Ji, A. Pukhov, I. Kostyukov, B. Shen, and K. Akli. Radiation-reaction trapping of electrons in extreme laser fields. *Physical Review Letters*, 2014. doi: 10.1103/PhysRevLett.112.145003.

[54] A. V. Arefiev, A. P. L. Robinson, and V. N. Khudik. Novel aspects of direct laser acceleration of relativistic electrons. *Journal of Plasma Physics*, 2015. doi: 10.1017/S0022377815000434.

[55] A. Pukhov, Z. Sheng, and J. Meyer-ter Vehn. Particle acceleration in relativistic laser channels. *Physics of Plasmas*, 1999. doi: 10.1063/1.873242.

[56] A. Macchi. *A Superintense Laser–Plasma Interaction Theory Primer.* Springer, 2013.

[57] M. Passoni, A. Zani, A. Sgattoni, D. Dellasega, A. Macchi, I. Prencipe, V. Floquet, P. Martin, T. Liseykina, and T. Ceccotti. Energetic ions at moderate laser intensities using foam-based multi-layered targets. *Plasma Physics and Controlled Fusion*, 2014. doi: 10.1088/0741-3335/56/4/045001.

[58] M. Galbiati, A. Formenti, M. Grech, and M. Passoni. Numerical investigation of non-linear inverse compton scattering in double-layer targets. *Frontiers in Physics*, 2023. doi: 10.3389/fphy.2023.1117543.

[59] A. Zani, D. Dellasega, V. Russo, and M. Passoni. Ultra-low density carbon foams produced by pulsed laser deposition. *Carbon*, 2013. doi: 10.1016/j.carbon.2013.01.029.

[60] M. Passoni, F. Arioli, L. Cialfi, D. Dellasega, L. Fedeli, A. Formenti, A. Giovannelli, A. Maffini, F. Miriani, and A. Pazzaglia. Advanced laser-driven ion sources and their applications in materials and nuclear science. *Plasma Physics and Controlled Fusion*, 2019. doi: 10.1088/1361-6587/ab56c9.

[61] L. Fedeli, A. Sainte-Marie, N. Zaim, M. Thévenet, J. L. Vay, A. Myers, F. Quéré, and H. Vincenti. Probing strong-field qed with doppler-boosted petawatt-class lasers. *Physical Review Letters*, 2021. doi: 10.1103/PhysRevLett.127.114801.

[62] A. Pazzaglia, L. Fedeli, A. Formenti, A. Maffini, and M. Passoni. A theoretical model of laser-driven ion acceleration from near-critical double-layer targets. *Communications Physics*, 2020. doi: 10.1038/s42005-020-00400-7.

[63] C.P. Ridgers, J.G. Kirk, R. Duclous, T.G. Blackburn, C.S. Brady, K. Bennett, T.D. Arber, and A.R. Bell. Modelling gamma-ray photon emission and pair production in high-intensity laser–matter interactions. *Journal of Computational Physics*, 2013. doi: 10.1016/j.jcp.2013.12.007.

[64] A. Formenti, M. Galbiati, and M. Passoni. Modeling and simulations of ultra-intense laser-driven bremsstrahlung with double-layer targets. *Plasma Physics and Controlled Fusion*, 2022. doi: 10.1088/1361-6587/ac4fce.

[65] Hui Chen, S. C. Wilks, D. D. Meyerhofer, J. Bonlie, C. D. Chen, S. N. Chen, C. Courtois, L. Elberson, G. Gregori, W. Kruer, O. Landoas, J. Mithen, J. Myatt, C. D. Murphy, P. Nilson, D. Price, M. Schneider, R. Shepherd, C. Stoeckl, M. Tabak, R. Tommasini, and P. Beiersdorfer. Relativistic quasimonoenergetic positron jets from intense laser-solid interactions. *Physical Review Letters*, 2010. doi: 10.1103/PhysRevLett.105.015003.

[66] T. Blackburn and M. Marklund. Nonlinear breit–wheeler pair creation with bremsstrahlung γ rays. *Plasma Physics and Controlled Fusion*, 2018. doi: 10.1088/1361-6587/aab3b4.

[67] Z. Lecz and A. Andreev. Diagnostics of peak laser intensity by pair production from thin foil target. *Laser Physics Letters*, 2020. doi: 10.1088/1361-6587/aafe59.

[68] Wen Luo, Yi-Bo Zhu, Hong-Bin Zhuo, Yan-Yun Ma, Ying-Ming Song, Zhi-Chao Zhu, Xiao-Dong Wang, Xing-Huo Li, I. C. E. Turcu, and Min Chen. Dense electron-

positron plasmas and gamma-ray bursts generation by counter-propagating quantum electrodynamics-strong laser interaction with solid targets. *Physics of Plasmas*, 2015. doi: 10.1063/1.4923265.

[69] Y. Gu, O. Klimo, S. Bulanov, and S. Weber. Brilliant gamma-ray beam and electron positron pair production by enhanced attosecond pulses. *Communications Physics*, 2018. doi: 10.1038/s42005-018-0095-3.

[70] Y. Gu, M. Jirka, O. Klimo, and S. Weber. Gamma photons and electron-positron pairs from ultra-intense laser-matter interaction: A comparative study of proposed configurations. *Matter and Radiation at Extremes*, 2019. doi: 10.1063/1.5098978.

[71] Y. Wang, Y. Yin, W. Wang, D. Zou, W. Miao, T. Yu, and F. Shao. Copious positron production by femto-second laser via absorbtion enhancement in a microstructured surface target. *Nature*, 2020. doi: 10.1038/s41598-020-61964-6.

[72] R. Hockney and J. Eastwood. *Computer Simulations Using Particles*. CRC Press, 1988. doi: 10.1201/9780367806934.

[73] J. Boris and R. Shanny. *Proceedings, Fourth Conference on the Numerical Simulation of Plasmas : November 2, 3, 1970, Naval Research Laboratory, Washington, D.C.* 1971.

[74] J. Derouillat, A. Beck, F. Pérez, T. Vinci, M. Chiaramello, A. Grassi, M. Flé, G. Bouchard, I. Plotnikov, N. Aunai, J. Dargent, C. Riconda, and M. Grech. Smilei: a collaborative, open-source, multi-purpose particle-in-cell code for plasma simulation. *Computer Physics Communications*, 2017. doi: 10.1016/j.cpc.2017.09.024.

[75] C. Birdsall and A. Langdon. *Plasma Physics via Computer Simulations*. CRC Press, 1991. doi: 10.1201/9781315275048.

[76] W. Dunn and J. Shultis. *Exploring Monte Carlo Methods*. Elsevier, 2022. doi: 10.1016/C2017-0-01717-2.

[77] Igor V. Sokolov, Natalia M. Naumova, Igor V. Nees, John A.Sokolov, Natalia M. Naumova, and John A. Nees. Numerical modeling of radiation-dominated and quantum-electrodynamically strong regimes of laser-plasma interaction. *Physics of Plasmas*, 2011. doi: 10.1063/1.3638138.

[78] R. Duclous, J. G. Kirk, and A. R. Bell. Monte carlo calculations of pair production in high-intensity laser-plasma interactions. *Plasma Physics and Controlled Fusion*, 2011. doi: 10.1088/0741-3335/53/1/015009.

[79] T. W. Huang, C. M. Kim, C. T. Zhou, C. M. Ryu, K. Nakajima, S.C. Ruan, and C.H. Nam. Tabletop laser-driven gamma-ray source with nanostructured double-layer target. *Plasma Physics and Controlled Fusion*, 2018. doi: 10.1088/1361-6587/aadbeb.

[80] L. Landau and E. Lifshitz. *The Classical Theory of Fields*. Pergamon Press Ldt., 1971.

[81] K. Yee. Numerical solution of initial boundary value problems involving maxwell's equations in isotropic media. *IEEE Transactions on Antennas and Propagation*, 1966. doi: 10.1109/TAP.1966.1138693.

[82] T. Esirkepov. Exact charge conservation scheme for particle-in-cell simulation with an arbitrary form-factor. *Computer Physics Communications*, 2001. doi: 10.1016/S0010-4655(00)00228-9.

[83] G. Lapenta. Kinetic plasma simulation: Particle in cell method. 2015. doi: 10.13140/RG.2.1.3319.2801.

A | Theory of classical emission of radiation: single charge and plasma

If the motion ($\boldsymbol{r}(t)$, $\boldsymbol{\beta}(t) = \boldsymbol{v}(t)/c$) of a particle with charge q is known, it is possible to calculate the electromagnetic field corresponding to the emitted radiation using Maxwell equations. This field takes the form [17]:

$$\boldsymbol{E}(\boldsymbol{x},t) = \frac{q}{c}\left[\frac{\boldsymbol{n}\times\left[(\boldsymbol{n}-\boldsymbol{\beta})\times\dot{\boldsymbol{\beta}}\right]}{(1-\boldsymbol{\beta}\cdot\boldsymbol{n})^3 R}\right]_{t_r} \qquad \boldsymbol{B}(\boldsymbol{x},t) = \left[\boldsymbol{n}\times\boldsymbol{E}\right]_{t_r}, \tag{A.1}$$

where $\dot{\boldsymbol{\beta}} = d\boldsymbol{\beta}/dt$ represents the acceleration, $R(t) = |\boldsymbol{x} - \boldsymbol{r}(t)|$ is the distance between the observation point $\boldsymbol{x}$ and the emitting particle, and $\boldsymbol{n}(t) = (\boldsymbol{x} - \boldsymbol{r}(t))/R(t)$ is the unit vector pointing from the emitting particle to the observation point. The fields at time t are determined by the charge motion at time $t_r = t - R(t_r)/c$, referred to as retarded time, accounting for the finite velocity of radiation propagation. The angular distribution of the instantaneous emitted power and the total one are given by the following expressions:

$$\frac{d\mathcal{P}(t_r)}{d\Omega} = \frac{q^2}{4\pi c}\frac{|\boldsymbol{n}\times[(\boldsymbol{n}-\boldsymbol{\beta})\times\dot{\boldsymbol{\beta}}]|^2}{(1-\boldsymbol{\beta}\cdot\boldsymbol{n})^5} \tag{A.2a}$$

$$\mathcal{P}(t_r) = \frac{2}{3}\frac{q^2}{m^2c^3}\gamma^2\left[\left(\frac{d\boldsymbol{p}}{dt}\right)^2 - |\boldsymbol{\beta}|^2\left(\frac{d|\boldsymbol{p}|}{dt}\right)^2\right], \tag{A.2b}$$

where the second one is known as relativistic Larmor formula. Here, $\boldsymbol{p} = mc\gamma\boldsymbol{\beta}$ and $\gamma = \sqrt{1+(|\boldsymbol{p}|/mc)^2}$ are the particle momentum and Lorentz factor. From equation A.2a it can be shown that for relativistic velocities, the radiation is emitted in a narrow cone in the direction of the velocity, with half-aperture of $1/\gamma$. Therefore for $\gamma \gg 1$ the radiation is emitted almost collinear with the velocity. Then, from A.2b it is straightforward to prove that for linear acceleration ($d\boldsymbol{p}/dt \times \boldsymbol{p} = 0$) the emitted power is $\mathcal{P} \sim (d\boldsymbol{p}/dt)^2$, while for circular acceleration ($d\boldsymbol{p}/dt \cdot \boldsymbol{p} = 0$ and $d|\boldsymbol{p}|/dt = 0$) the power is $\mathcal{P} \sim \gamma^2(d\boldsymbol{p}/dt)^2$.

Therefore, for relativistic and ultra-relativistic particles, the primary contribution to the emitted power comes from the perpendicular component of the forces. It is also observed that, given a certain force, since $m_i \gg m_e$ the power emitted from ions is much lower than that of electrons. Physically, the radiation emission depends on the magnitude of the particle acceleration, which is inversely proportional to the mass. Successively, the spectrum of the radiation emitted for a generic particle motion can be derived. However, to simplify calculations, a specific type of motion, the circular one, is considered. The choice is motivated by the fact that perpendicular forces dominate the emission by ultra-relativistic particles. Additionally, any force can be decomposed into perpendicular and parallel components. Therefore, by neglecting the parallel component of forces, any general motion can be thought as instantaneously circular in the context of radiation emission. If the force causing the emission is the Lorentz force, the process is referred to as synchrotron radiation emission. In this case, the spectrum of the instantaneous power emitted by an electron is given by:

$$\frac{d\mathrm{P}}{d\omega} = \frac{\sqrt{3}}{2\pi}\frac{e^2 m_e c}{\hbar\gamma}\chi\left[y\int_y^\infty K_{5/3}(x)dx\right], \quad y = \frac{2}{3}\frac{\hbar}{m_e c^2}\frac{\omega}{\gamma\chi}. \tag{A.3}$$

Here, χ is the quantum parameter of the electron (see 1.2.2).
Up to this point, the motion of the particle has been assumed as assigned a priori. However, it is important to consider that the radiation emitted carries energy and momentum. Since these quantities are conserved, the emission leads to modifications in the particle energy, momentum, and consequently, its subsequent motion. To account for radiation reaction, an appropriate friction force must be included in the equation of motion of a particle in a given electromagnetic field. The Abraham-Lorentz-Dirac radiation reaction force, in covariant form, is expressed as [80]:

$$m\left.\frac{du^\alpha}{d\tau}\right|_{rad} = \frac{2}{3}\frac{q^2}{c^3}\left(\frac{d^2u^\alpha}{d\tau^2} - \frac{u^\alpha u^\beta}{c^2}\frac{d^2u_\beta}{d^2\tau}\right), \tag{A.4}$$

where $u^\alpha = \gamma(c, \boldsymbol{v})$ is the four-velocity and $d\tau = dt/\gamma$ is the differential of the proper time. By substituting the particle zero-order motion, which corresponds to the acceleration due to the Lorentz force without radiation reaction, in the second-order derivatives of u^α, the Landau-Lifschitz (LL) radiation reaction force can be obtained. In the ultra-relativistic limit, the LL force in Newton mechanics notation becomes:

$$\frac{d\boldsymbol{p}}{dt} = -\mathcal{P}\frac{\boldsymbol{v}}{c^2}. \tag{A.5}$$

This force is oppositely directed to the velocity and proportional to the total radiated power $\mathcal{P}$. It is important to note that these models for radiation reaction are approximated, not derived from first principles. The current approach is entirely classical, as it considers deterministic particle trajectories, and the emission of radiation is treated as a continuous process both in time, in opposition to the stochastic nature of quantum physics, and in frequency, since the entire radiation spectrum, which depends on the instantaneous force, is emitted at each time instant.
In a plasma, integral quantities can be derived from the single-particle description. Given a single-particle quantity $\mathcal{O}(\boldsymbol{x}, \boldsymbol{p})$, which depends on the individual momentum and position, the corresponding integral quantity for the plasma $\mathcal{O}_p(\boldsymbol{x})$ can be obtained by integrating over the particle momentum distribution, represented by the distribution function of the population involved:

$$\mathcal{O}_p(\boldsymbol{x}) = \int \mathcal{O}(\boldsymbol{x}, \boldsymbol{p}) f_a(\boldsymbol{x}, \boldsymbol{p}, t) d\boldsymbol{p}. \tag{A.6}$$

As an example, to calculate the density of power emitted by a certain population at a given position $\boldsymbol{x}$, the single-particle quantity is given by the relativistic Larmor formula $\mathcal{O} = \mathcal{P}(\boldsymbol{p}, d\boldsymbol{p}/dt)$, where $d\boldsymbol{p}/dt$ depends, though the equation of motion, on $\boldsymbol{p}$ and the fields $\boldsymbol{E}(\boldsymbol{x})$ and $\boldsymbol{B}(\boldsymbol{x})$.

B | NBWPP and photon emission in kinetic Vlasov-Maxwell description

In principle, the classical theory of radiation is included in Maxwell equations. To avoid double-counting the radiation process in both classical and quantum descriptions, one option is to select a reference frequency for the radiation, chosen appropriately, and consider radiation below this frequency as classical and above it as quantum. This approach aligns with the spatial filtering in the kinetic description, where small wavelengths are filtered out, and it is commonly done in computational simulations. The creation of photons and positrons and the abrupt change in the electron or positron momentum due to the emission, represent source and sink terms in the phase space. Therefore, opportune source terms can be introduced in the Vlasov equation for the electron, positron and photon populations. For electrons (and positrons), the source term associated to the emission of photons is given by:

$$S_e^{\mathrm{NICS}}(\boldsymbol{x},\boldsymbol{p}_e,t) = -\frac{dN_\gamma}{dt}(\boldsymbol{x},\boldsymbol{p}_e) f_e(\boldsymbol{x},\boldsymbol{p}_e,t) + \int_{\mathcal{E}'_e>\mathcal{E}_e} \frac{d^2N_\gamma}{d\mathcal{E}_\gamma dt}\frac{d\mathcal{E}_\gamma}{d\mathcal{E}_e}(\boldsymbol{x},\boldsymbol{p}'_e,\boldsymbol{p}_e,t)\frac{d\mathcal{E}_e}{d\boldsymbol{p}_e} f_e(\boldsymbol{x},\boldsymbol{p}'_e,t)d\boldsymbol{p}'_e \tag{B.1}$$

The first term represents the sink due to emission, while the second term is a production term accounting for electrons changing energy after emission. The dependence on the fields is included in the position dependence $\boldsymbol{x}$. The prime notation refers to the emitting electron. The NICS spectrum multiplied by $d\mathcal{E}_\gamma/d\mathcal{E}_e$ represents the spectrum per units energy of the final electron instead of the photon. Therefore, it is a function of the momenta of the electron after and before the emission. The gradient of the energy relation with respect to the momentum is given by $d\mathcal{E}_e/d\boldsymbol{p}_e = \boldsymbol{v}_e$ from Hamilton equations. Electrons (and positrons) are also generated in NBWPP, so an additional source term is required:

$$S_e^{\mathrm{NBWPP}}(\boldsymbol{x},\boldsymbol{p}_e,t) = \int_{\mathcal{E}_\gamma>2m_ec^2} \frac{d^2N_e}{d\mathcal{E}_e dt}(\boldsymbol{x},\boldsymbol{p}_\gamma,\boldsymbol{p}_e,t)\frac{d\mathcal{E}_e}{d\boldsymbol{p}_e} f_\gamma(\boldsymbol{x},\boldsymbol{p}_\gamma,t)d\boldsymbol{p}_\gamma. \tag{B.2}$$

Here, the NBWPP spectrum, which is symmetric for electrons and positrons, appears. Considering now the photon population, a sink term for NBWPP and a production term for NICS are present:

$$S_\gamma(\boldsymbol{x}, \boldsymbol{p}_\gamma, t) = -\frac{dN_e}{dt}(\boldsymbol{x}, \boldsymbol{p}_\gamma) f_\gamma(\boldsymbol{x}, \boldsymbol{p}_\gamma, t) + \int_{\mathcal{E}_e > \mathcal{E}_\gamma} \frac{d^2 N_\gamma}{d\mathcal{E}_\gamma dt}(\boldsymbol{x}, \boldsymbol{p}_e, \boldsymbol{p}_\gamma, t) \frac{d\mathcal{E}_\gamma}{d\boldsymbol{p}_\gamma} f_e(\boldsymbol{x}, \boldsymbol{p}_e, t) d\boldsymbol{p}_e \tag{B.3}$$

It is important to emphasize that the presented kinetic description accounts for QED processes mediated by the self-consistent long-range electromagnetic field, while fluctuations and microscopic forces are neglected. Additionally, the particle dynamics is classical, they follow deterministic trajectories, while only the processes are quantum. In conclusion, the method to obtain integral quantities for the plasma starting from single-particle ones, which was discussed in Appendix A, applies to QED processes as well.

C | PIC simulation algorithm

PIC codes employ a discretized spatial domain known as grid $\boldsymbol{x}_{ijk}$ and a discretized temporal axis t_n. With spatial spacings Δx, Δy, Δz, and temporal interval Δt, the grid points and the time steps are defined as:

$$\boldsymbol{x}_{ijk} = i\Delta x\hat{\boldsymbol{u}}_x + j\Delta y\hat{\boldsymbol{u}}_y + k\Delta z\hat{\boldsymbol{u}}_z \qquad t_n = n\Delta t \tag{C.1}$$

where i, j, k and t are spatial and temporal indices, and they can take on both integer and half-integer values. The continuous fields and macro-particle kinematic quantities are replaced by their discretized counterparts:

$$\boldsymbol{E}(\boldsymbol{x},t),\ \boldsymbol{B}(\boldsymbol{x},t) \rightarrow (\boldsymbol{E})^n_{i,j,k} \equiv \boldsymbol{E}(\boldsymbol{x}_{i,j,k},t_n),\ (\boldsymbol{B})^n_{i,j,k} \equiv \boldsymbol{B}(\boldsymbol{x}_{i,j,k},t_n), \tag{C.2a}$$

$$\boldsymbol{x}_{p,a}(t),\ \boldsymbol{p}_{p,a}(t) \rightarrow (\boldsymbol{x}_{p,a})^n \equiv \boldsymbol{x}_{p,a}(t_n),\ (\boldsymbol{p}_{p,a})^n \equiv \boldsymbol{p}_{p,a}(t_n). \tag{C.2b}$$

The discretization of spatial and temporal derivatives typically employs a second-order finite difference scheme. For a generic function $A(x,t)$, the discretized derivatives can be expressed as:

$$\left.\frac{dA}{dt}\right|_{t=t_n} = \frac{A(t_{n+1/2}) - A(t_{n-1/2})}{\Delta t}, \quad \left.\frac{dA}{dx}\right|_{x=x_i} = \frac{A(x_{i+1/2}) - A(x_{i-1/2})}{\Delta x} \tag{C.3}$$

This approach allows Maxwell equations and the equations of motion to be written as algebraic equations.

The structure of a PIC code involves an iterative procedure executed at every time step t_n for the entire duration of the simulation. The goal is to compute macro-particle positions and momenta as well as the electromagnetic field values on the grid points. Starting from the assigned initial conditions, this iterative procedure comprises four steps in the following order: the evaluation of the current density on the grid nodes from macro-particle kinematic quantities, determination of the discretized electromagnetic field by solving the Maxwell equations, the interpolation of the fields from the grid to macro-particle positions, and the update of macro-particle positions and momenta. In the following, the

term "macro" to refer to macro-particles is omitted.
Particles position, momentum, and weight, along with the fields, should be properly initialized and, typically, several options are available in usual PIC codes.
Assuming that the current density on grid points is known, the electric and magnetic fields can be updated. The charge density is not required for this purpose because only the Ampère-Maxwell and Faraday equations need to be solved during each time-step. This is because if the two Maxwell divergence equations are satisfied at the initial time, they are automatically satisfied at the following times, provided that electric charge is conserved over time. Several solvers can be used to solve Maxwell equations, such as spectral solvers or others that solve the integral form of Maxwell equations. In this work, the Yee [81] solver based on finite differences is considered. It adopts the leap-frog scheme, which utilizes a staggered grid, consisting of two separates grids shifted by half a cell, both in time and space. Practically, this means that some fields are evaluated at integer indexes while others are evaluated at half-integer indexes along a specific axis. For example, since the time derivative of $\boldsymbol{E}$ depends on the curl of $\boldsymbol{B}$, the former is evaluated at integer time steps $n = 0, 1, 2\ldots$ and the latter on half integer time steps $n = 1/2, 3/2, 5/2, \ldots$. The update of fields from one time step to the next is determined by:

$$\boldsymbol{E}^{n+1} = \boldsymbol{E}^{n} + \Delta t[\, c(\boldsymbol{\nabla} \times \boldsymbol{B})^{n+1/2} - 4\pi \boldsymbol{J}^{n+1/2}] \tag{C.4a}$$

$$\boldsymbol{B}^{n+1/2} = \boldsymbol{B}^{n-1/2} - c\Delta t(\boldsymbol{\nabla} \times \boldsymbol{E})^{n}, \tag{C.4b}$$

where n and $i,\ j,\ k$ assume by convention only integer values. Introducing spatial discretization, the electric field and current components along each axis are shifted by half cell with respect to the magnetic component along the same axis. The arrangement of all the components and of the charge density is represented in Figure C.1. With this scheme and discretizing the spatial derivatives, the algebraic equations for updating the fields can be obtained. For example, considering the equation for the x component of the electric field:

$$(E_x)^{n+1}_{i+1/2,j,k} = (E_x)^{n}_{i+1/2,j,k} + \Delta t \left[c\,(\partial_y B_z)^{n+1/2}_{i+1/2,j,k} - c\,(\partial_z B_y)^{n+1/2}_{i+1/2,j,k} + (J_x)^{n+1/2}_{i+1/2,j,k} \right] \tag{C.5a}$$

$$(\partial_y B_z)^{n+1/2}_{i+1/2,j,k} = \frac{(B_z)^{n+1/2}_{i+1/2,j+1/2,k} - (B_z)^{n+1/2}_{i+1/2,j-1/2,k}}{\Delta y} \tag{C.5b}$$

$$(\partial_z B_y)^{n+1/2}_{i+1/2,j,k} = \frac{(B_y)^{n+1/2}_{i+1/2,j,k+1/2} - (B_y)^{n+1/2}_{i+1/2,j,k-1/2}}{\Delta z}. \tag{C.5c}$$

To guarantee numerical stability, the spatial and time steps must satisfy the Courant-Friedrichs-Lewy condition:

$$c\Delta t\sqrt{\frac{1}{\Delta x^2}+\frac{1}{\Delta y^2}+\frac{1}{\Delta z^2}} \equiv CFL < 1 \tag{C.6}$$

This condition ensures that for an electromagnetic wave moving on the grid, the time spacing between two iterations is less than the time needed for the wave to travel the distance corresponding to one cell of the grid.
Once the fields on the grid are known, they need to be interpolated on the particle positions. To compute particle kinematic quantities at integer times t_n, the fields must be evaluated at the same times. The electric field is already known at t_n, therefore can be interpolated as follows:

$$\boldsymbol{E}^n(\boldsymbol{x}^n_{p,a}) = \int \boldsymbol{E}^n(\boldsymbol{x})S(\boldsymbol{x}-\boldsymbol{x}^n_{p,a})d\boldsymbol{x}. \tag{C.7}$$

The magnetic field is computed by the Maxwell solver at half-integer times, so firstly it must be evaluated at the correct time. This can be done by approximating it as the average between the two adjacent half-integer times, and then it can be interpolated:

$$\boldsymbol{B}^n = \frac{\boldsymbol{B}^{n+1/2}+\boldsymbol{B}^{n-1/2}}{2}, \quad \boldsymbol{B}^n(\boldsymbol{x}^n_{p,a}) = \int \boldsymbol{B}^n(\boldsymbol{x})S(\boldsymbol{x}-\boldsymbol{x}^n_{p,a})d\boldsymbol{x}. \tag{C.8}$$

To perform the integration, the shape function must be chosen. It should be a symmetric function, centered in the particle position, and normalized to unity. The three-dimensional shape function $S^m(x,y,z)$ of order m can be factorized into one-dimensional shape functions $\hat{S}^m(x)$,$\hat{S}^m(y)$,$\hat{S}^m(z)$, each one expressed as a piece-wise polynomial function of order m and with extension of m times the grid spacing in the corresponding direction. See [74] for their explicit expressions, and Figure C.2 for some graphical examples. The fields can be reconstructed from the grid as follows:

$$\boldsymbol{E}^n(\boldsymbol{x}) = \sum_{i,j,k}(\boldsymbol{E})^n_{i,j,k}\theta(x-x_i)\theta(y-y_j)\theta(z-z_k), \tag{C.9}$$

where $\theta(x) = 1$ if $|x| <= \Delta x/2$ and $\theta(x) = 0$ otherwise, and similarly for the other directions. Here, the indices are generalized to both integer and half-integer values. Now the fields at particle positions can be explicitly computed. For example, the electric field

is interpolated as:

$$\begin{aligned}\boldsymbol{E}^n(\boldsymbol{x}^n_{p,a}) &= \int \boldsymbol{E}^n(x,y,z)\hat{S}^m(x-x^n_{p,a})\hat{S}^m(y-y^n_{p,a})\hat{S}^m(z-z^n_{p,a})dxdydz \\ &= \sum_{i,j,k}(\boldsymbol{E})^n_{i,j,k}\,\hat{S}^{m+1}(x^n_{p,a}-x_i)\hat{S}^{m+1}(y^n_{p,a}-y_j)\hat{S}^{m+1}(z^n_{p,a}-z_k)\end{aligned} \tag{C.10}$$

The same expression holds for the magnetic field as well.
With the interpolated fields, particle kinematic quantities can be updated using the leap-frog scheme. The relativistic Boris pusher is implemented to solve the following equations:

$$\boldsymbol{p}^{n+1/2}_{p,a} = \boldsymbol{p}^{n-1/2}_{p,a} + q_a\Delta t\left[\boldsymbol{E}^n(\boldsymbol{x}^n_{p,a}) + \frac{\boldsymbol{p}^n_{p,a}}{m_a c\gamma^n_{p,a}} \times \boldsymbol{B}^n(\boldsymbol{x}^n_{p,a})\right] \tag{C.11a}$$

$$\boldsymbol{x}^{n+1}_{p,a} = \boldsymbol{x}^n_{p,a} + \Delta t\frac{\boldsymbol{p}^{n+1/2}_{p,a}}{m_a\gamma^{n+1/2}_{p,a}} \tag{C.11b}$$

Since the momentum is known only at half-integer times, it is approximated at the integer ones as:

$$\boldsymbol{p}^n_{p,a} = \frac{\boldsymbol{p}^{n+1/2}_{p,a} + \boldsymbol{p}^{n-1/2}_{p,a}}{2}, \quad \gamma^n_{p,a} = \sqrt{1+\left(\frac{|\boldsymbol{p}^n_{p,a}|}{m_a c}\right)^2}. \tag{C.12}$$

The momentum equation can be rewritten as:

$$\boldsymbol{p}^n_{p,a} = \boldsymbol{p}^{n-1/2}_{p,a} + \frac{q_a}{2}\Delta t\left[\boldsymbol{E}^n(\boldsymbol{x}^n_{p,a}) + \frac{\boldsymbol{p}^n_{p,a}}{m_a c\gamma^n_{p,a}} \times \boldsymbol{B}^n(\boldsymbol{x}^n_{p,a})\right] \tag{C.13}$$

To make it explicit, the following definitions and approximations are introduced:

$$\tilde{\boldsymbol{p}} = \boldsymbol{p}^{n-1/2}_{p,a} + \frac{q_a\Delta t}{2}\boldsymbol{E}^n(\boldsymbol{x}^n_{p,a}), \quad \boldsymbol{b} = \frac{q_a\Delta t}{2m_a c\gamma^n_{p,a}}\boldsymbol{B}^n(\boldsymbol{x}^n_{p,a}) \tag{C.14a}$$

$$\gamma^n_{p,a} = \sqrt{1+\frac{\boldsymbol{p}^n_{p,a}\cdot\boldsymbol{p}^n_{p,a}}{(m_a c)^2}} \backsimeq \sqrt{1+\frac{\tilde{\boldsymbol{p}}\cdot\tilde{\boldsymbol{p}}}{(m_a c)^2}}, \tag{C.14b}$$

where terms proportional to Δt^2 are neglected, and it is assumed that the momentum direction does not change significantly from one time step to the next. Multiplying $\times\boldsymbol{b}$ the equation C.13, the explicit momentum updating equation can be written as:

$$\boldsymbol{p}^n_{p,a} = \frac{1}{1+|\boldsymbol{b}|^2}[\tilde{\boldsymbol{p}} + \tilde{\boldsymbol{p}}\times\boldsymbol{b} + \boldsymbol{b}(\tilde{\boldsymbol{p}}\cdot\boldsymbol{b})] \tag{C.15}$$

For photons, whose momentum remains constant, the position is updated as:

$$\boldsymbol{x}_{p,\gamma}^{n+1} = \boldsymbol{x}_{p,\gamma}^{n} + c\frac{\boldsymbol{p}_{p,\gamma}^{n+1/2}}{|\boldsymbol{p}_{p,\gamma}^{n+1/2}|} \tag{C.16}$$

The last missing step is the current density deposition on the grid. The direct deposition onto a grid point $\boldsymbol{x}_{i,j,k}$ consists in considering the projected current as the amount of current contained in the cell located around this grid point:

$$\begin{aligned}(\boldsymbol{J})_{i,j,k}^{n} &= \sum_{a=1}^{N} q_a \sum_{p=1}^{N_a} w_{p,a}\frac{\boldsymbol{p}_{p,a}^{n}}{m_a\gamma_{p,a}^{n}} \int S^{m}(\boldsymbol{x}-\boldsymbol{x}_{p,a}^{n})\theta(x-x_i)\theta(y-y_j)\theta(z-z_k)dxdydz \\ &= \sum_{a=1}^{N} q_a \sum_{p=1}^{N_a} w_{p,a}\frac{\boldsymbol{p}_{p,a}^{n}}{m_a\gamma_{p,a}^{n}} \hat{S}^{m+1}(x_i-x_{p,a}^{n})\hat{S}^{m+1}(y_j-y_{p,a}^{n})\hat{S}^{m+1}(z_k-z_{p,a}^{n})\end{aligned} \tag{C.17}$$

However, this current deposition method does not guarantee charge conservation. For this reason, more sophisticated methods for the deposition of currents that ensure charge conservation are usually employed, such as the Esirkepov [82] method. This method computes the current density on grid points by forcing the continuity equation to each cell.
In conclusion, to solve this algorithm, boundary conditions for both the fields and the particles are needed. Commonly used boundary conditions include periodic, absorbing, and reflective boundary conditions. Periodic conditions mean that particles exiting from one side of the domain reappears from the opposite side with the same momentum, whereas fields assume the same values along opposite sides of the domain. In this case, to prevent unphysical phenomena such as recirculation, the domain must be chosen sufficiently large. Absorbing conditions remove particles and electromagnetic waves exiting from the domain, while reflective conditions reflect both particles and electromagnetic waves according to the specular reflection rules.
Throughout the iterations of this algorithm, data from the particles and fields are saved, in order to be analysed after the simulation.

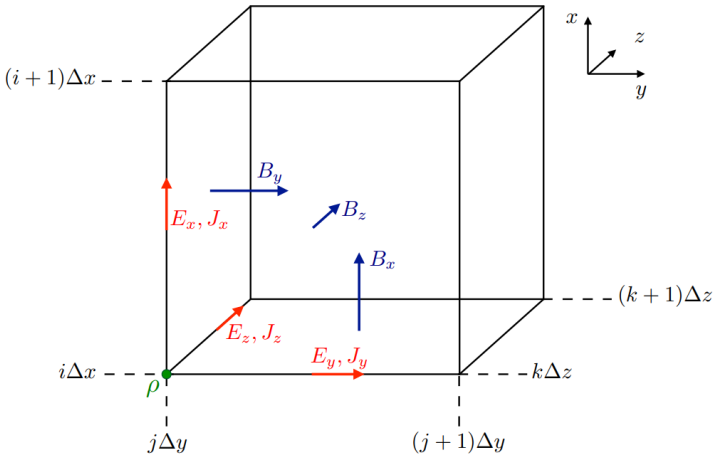

Figure C.1: Representation of the cell of the Yee 3D grid with the positions at which $\boldsymbol{E}$,$\boldsymbol{B}$,$\boldsymbol{J}$ and ρ are computed [74].

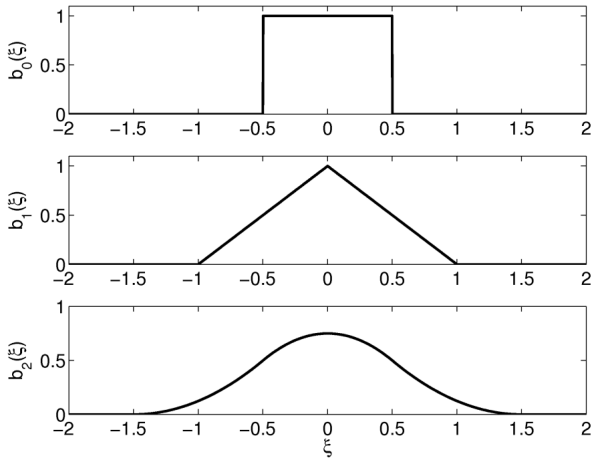

Figure C.2: Shape functions for orders $m = 1, 2, 3$, assuming a unitary cell length [83].

List of Figures

List of Tables